Title
Methods of Generating High-Quality Beams in Laser Wakefield Accelerators through Self-Injection

Author
Davidson, Asher Warren

Publication Date
2016

Peer reviewed|Thesis/dissertation

University of California
Los Angeles

Methods of Generating High-Quality Beams in Laser Wakefield Accelerators through Self-Injection

A dissertation submitted in partial satisfaction
of the requirements for the degree
Doctor of Philosophy in Physics

by

Asher Warren Davidson

2016

Abstract of the Dissertation

Methods of Generating High-Quality Beams in Laser Wakefield Accelerators through Self-Injection

by

Asher Warren Davidson

Doctor of Philosophy in Physics

University of California, Los Angeles, 2016

Professor Warren B. Mori, Chair

In the pursuit of discovering the fundamental laws and particles of nature, physicists have been colliding particles at ever increasing energy for almost a century. Lepton (electrons and positrons) colliders rely on linear accelerators (LINACS) because leptons radiate copious amounts of energy when accelerated in a circular machine. The size and cost of a linear collider is mainly determined by the acceleration gradient. Modern linear accelerators have gradients limited to 20-100 MeV/m because of the breakdown of the walls of the accelerator. Plasma based acceleration is receiving much attention because a plasma wave with a phase velocity near the speed of light can support acceleration gradients at least three orders of magnitude larger than those in modern accelerators. There is no breakdown limit in a plasma since it is already ionized. Such a plasma wave can be excited by the radiation pressure of an intense short pulse laser. This is called laser wakefield acceleration (LWFA). Much progress has been made in LWFA research in the past 30 years. Particle-in-cell (PIC) simulations have played a major part in this progress. The physics inherent in LWFA is nonlinear and three-dimensional in nature. Three-dimensional PIC simulations are computationally intensive.

In this dissertation, we present and describe in detail a new algorithm that was introduced into the OSIRIS[1, 2] Particle-In-Cell Simulation Framework. We subsequently use this new quasi three-dimensional algorithm to efficiently explore the parameter regimes of LWFA that

are accessible for existing and near term lasers. This regimes cannot be explored using full three-dimensional simulations even on leadership class computing facilities. The simulations presented in this dissertation show that the nonlinear, self-guided regime of LWFA described through phenomenological scaling laws by Lu et al., in 2007 is still useful for accelerating electrons to energies greater than 10 GeV.

Fortunately, in many situations the physics of LWFA is nearly azimuthally symmetric and the most salient three-dimensional physics is captured by the inclusion of only a few azimuthal harmonics. Recently, it was proposed[3] to model LWFA by expanding the fields and currents in azimuthal harmonics and truncating the expansion. The complex amplitudes of the fundamental and first harmonic for the fields were solved on an r-z grid and a procedure for calculating the complex current amplitudes for each particle based on its motion in Cartesian geometry was presented using a Marder's correction to maintain the validity of Gauss's law. In this dissertation, we describe in detail the implementation of this algorithm into OSIRIS using a rigorous charge conserving current deposition method to maintain the validity of Gauss's law. We show that this algorithm is a hybrid method which uses a particles-in-cell description in r-z and a gridless description in ϕ (which we have subsequently coined the 'quasi-3D' method). We include the ability to keep an arbitrary number of harmonics and higher order particle shapes. Examples for laser wakefield acceleration, plasma wakefield acceleration, and beam loading are also presented.

In almost all of the recent experiments progress on LWFA the plasma wave wake has been excited in the nonlinear blowout regime. A phenomenological description of this regime was given in ref. [4]. This included matching conditions for the laser spot size and pulse length so that the laser evolution and wake excitation would be stable and the laser would self-guide. Scaling laws for the electron electron energy (self or externally injected) in terms of the laser and plasma parameters was also given. The parameters for the supporting simulations were limited due to the computational demands for such simulations particularly for higher electron energy.

The recent implementation of the quasi-3D algorithm into OSIRIS including the charge conserving current deposit, now make it possible to study these scaling laws and examine

how well they still hold for higher laser intensities and laser energies. We have studied in detail how well the nonlinear, self-guided regime works for existing and near term 15-100 Joule lasers. We demonstrate that the scaling laws do capture the key phenomenological characteristics LWFAs under a wide range of different laser and plasma parameters, but are not meant to give exact predictions for a choice of parameters. The simulations indicate that the self-injected particles reach slightly higher energies than estimated by the scaling laws, although the evolution of the maximum energy looks similar when scaled to the dephasing time. We also find that shape of the evolution of the energy, spot size, and wake amplitude scales if the normalized vector potential, and transverse and axial profile shapes remain fixed. If the normalized vector potential is changed then the scaling laws are still useful but the shape of energy evolution curve changes. We also used the scaling laws to optimize the energy gain for a fixed laser energy. We then use the quasi-3D OSIRIS code to study study in detail how to optimize the energy gain for fixed laser energy including how to optimize the axial laser profile. We find that shortening the pulse length and reducing the plasma density is effective in producing a higher energy beam with a low energy spread, given a fixed laser energy.

The dissertation of Asher Warren Davidson is approved.

Chandra J. Joshi

George Morales

Troy Carter

Warren B. Mori, Committee Chair

University of California, Los Angeles

2016

To those

who were there for me

when I needed them

the most

Table of Contents

List of Figures

List of Tables

Acknowledgments

I would like to express my gratitude to Prof. Warren Mori for his support and guidance over the course of my study at UCLA. Without his valuable intuition regarding potential developments in simulation code and plasma theory, this dissertation would not have been possible.

I would also like to thank Prof. Chan Joshi for our collaboration early on in my study at UCLA regarding staged ionization injection. Although I have moved on to primarily study pre-ionized plasmas, this provided valuable experience and insight into the world of plasma experimentation.

I would like to thank Viktor Decyk for introducing me to the fascinating world of plasma simulation in the summer preceding my research at UCLA. The hospitality, instruction, and support during this time was a key instigator in my subsequent pursuit of computational physics.

I would also like to thank my valued colleagues, including Adam Tableman, Peicheng Yu, Weiming An, Xinlu Xu, Benjamin Winjum, Josh May, Frank Tsung, and Wei Lu, and our collaborators as IST, including Ricardo Fonseca, Jorge Vieira, and Luis Silva. I would like to thank all of the staff, researchers, and students who I have the pleasure of working with for making UCLA such a friendly and welcoming place.

Vita

2008	B.A., Physics
	Reed College
2010	M.S., Physics
	University of California, Los Angeles

Publications

P. Yu, X. Xu, A. Tableman, V. Decyk, F. Tsung, F. Fiuza, A. Davidson, J. Vieira, R. Fonseca, W. Lu, L. Silva, W. B. Mori, "Mitigation of Numerical Cerenkov Radiation and Instability Using a Hybrid Finite Difference-FFT Maxwell Solver and a Local Charge Conserving Current Deposit", Comput. Phys. Comm., vol. 197, 144-152 (2015).

B. B. Pollock, F. S. Tsung, F. Albert, J. L. Shaw, C. E. Clayton, A. Davidson, N. Lemos, K. A. Marsh, A. Pak, J. E. Ralph, W. B. Mori, C. Joshi "Formation of Ultrarelativistic Electron Rings from a Laser-Wakefield Accelerator", Phys. Rev. Lett., vol. 115, 055004 (2015).

A. Davidson, A. Tableman, W. An, F. S. Tsung, R. A. Fonseca, L. O. Silva, W. B. Mori, "Implementation of a hybrid particle code with a PIC description in r-z and a gridless description in ϕ into OSIRIS", J. Comp. Phys., vol. 281, 1063-1077 (2015).

P. Yu, A. Davidson, X. Xu, A. Tableman, V. K. Decyk, F. S. Tsung, J. Vieira, R. A. Fonseca, W. Lu, L. O. Silva, W. B. Mori, "Modeling of Laser Wakefield Acceleration in Lorentz Boosted Frame Using a Quasi-3D OSIRIS Algorithm," Proceedings of the 16th Advanced Accelerator Concepts Workshop, San Jose, CA, July 13-18, 2014.

R. A. Fonseca, J. Vieira, F. Fiuza, A. Davidson, F. S. Tsung, W. B. Mori, and L. O. Silva , "Exploiting Multi-Scale Parallelism for Large Scale Numerical Modelling of Laser Wakefield Accelerators," Plasma Phys. Control. Fusion, vol. 55, 124011 (2013).

A. W. Davidson, W. Lu, M. Zheng, C. Joshi, L.O. Silva, J. Martins, R. A. Fonseca, W. B. Mori, "Self and ionization-injection in LFWA for near-term lasers," Proceedings of the North American Particle Accelerator Conference (NA-PAC), Pasadena, CA, Sept. 30-Oct. 4, 2013.

A. W. Davidson, W. Lu, C. Joshi, L.O. Silva, J. Martins, R.A. Fonseca, W.B. Mori, "Numerical Study Of Self And Controlled Injection In 3-Dimensional Laser-Driven Wakefields," Proceedings of the Particle Accelerator Conference (PAC), New York, NY, Mar. 28-Apr. 1, 2011.

B. B. Pollock, C. E. Clayton, J. E. Ralph, F. Albert, A. Davidson, L. Divol, C. Filip, S. H. Glenzer, K. Herpoldt, W. Lu, K. A. Marsh, J. Meinecke, W. B. Mori, A. Pak, T. C. Rensink, J. S. Ross, J. Shaw, G. R. Tynan, C. Joshi, and D. H. Froula, "Demonstration of a Narrow Energy Spread, ~ 0.5 GeV Electron Beam from a Two-Stage Laser Wakefield Accelerator," Phys. Rev. Lett., vol. 107, 045001 (2011).

CHAPTER 1

Introduction

1.1 Introduction

A persistent and challenging problem in high energy physics is increasing the energy of beams used in lepton collision experiments, and to do so in the most efficient and cost effective manner possible. Tajima and Dawson proposed using intense short-pulse laser beams to drive plasma waves with phase velocities near the speed of light and then accelerate electrons in these eaves early as 1979[5, 6]. The Tajima and Dawson work relied on one-dimensional particle-in-cell (PIC) simulations. Since then, a tremendous amount of progress has been made in the development of a laser based plasma accelerator experimentally, computationally, and in theoretical understanding. Due to the analogy of a motor boat exciting a wake as it moves on water, the plasma waves are referred to as wakefields and this concept is now referred to as the laser wakefield accelerator (LWFA). IN 1985, Chen et al.[7] proposed using a relativistic electron beam to create the plasma wave wakefield that could then accelerate electrons or positrons. This scheme is referred to as the plasma wakefield accelerator (PWFA).

These two ideas constitute what is now referred to as Plasma-based acceleration (PBA), which is actively being pursued particularly because of the high acceleration gradients that can be sustained in a plasma. High acceleration gradients have the potential to lead to a generation of more compact and cheaper accelerators[8]. The accelerating gradient in conventional linear accelerators is limited to approximately 100 MeV/m, due to the breakdown voltage of the metallic walls of the structure. Plasmas, already being "broken down" by their very definition, do not have the same limitation. They can sustain plasma wave wakes

with electric field strengths given by the nonrelativistic wavebreaking formula [6, 9, 10], $E_0 = cm_e\omega_p/e$, or

$$E_0[V/cm] \simeq 0.96\sqrt{n_p}[cm^{-3}], \tag{1.1}$$

where $\omega_p \equiv (4\pi n_p e^2/m_e)$ is the electron plasma frequency, and n_p is the electron density. For example, a plasma with $n_p = 1.0 \times 10^{18} cm^{-3}$ will have an accelerating field of approximately $E_0 \simeq 100GV/m$ - a thousand times greater than a conventional linear accelerator. The relativistic extension is given in [10], but values beyond the nonrelativistic formula are not that common. The ability of a plasma to sustain large acceleration gradient over meter distances was confirmed in a PWFA experiment in which a part of a 42 GeV electron beam was doubled in energy to more than 84 GeV[11].

In the energy doubling PWFA experiment and many recent LWFA experiments, the wakefield is excited in what is now referred to as the blowout or bubble regime. This regime was first described based on observations from PIC simulations of PWFA [12]. It was subsequently, studied in 2D slab PIC simulations of LWFA one year later [13, 14]. Nearly a decade later, 3D PIC simulations of LWFA in this nonlinear regime started to be carried out[15, 16, 17, 18, 19, 20, 4].

If the wake is sustained over centimeter to meter distances it can generate multi-GeV electron beams [21, 4, 22, 23, 24, 25]. In order for such schemes to be successful, the laser must travel stably over many Rayleigh lengths in an very underdense plasma while the accelerating bubble structure also remains stable during the particle acceleration process. In order to improve our understanding of the manner with which the laser and the wake evolve over many Rayleigh lengths, we have conducted numerous particle-in-cell (PIC) simulations using the OSIRIS Simulation Framework[1, 26]. New simulation methods, such as the quasi-3D algorithm [3, 27], which is a focus of this dissertation, allow us to use fully nonlinear OSIRIS simulations to explore parameters in which the laser is self-guided over an even greater number of Rayleigh lengths. The quasi-3D algorithm enables us to revisit existing phenomenological scaling laws[4] and refine our understanding the nonlinear, self-guided regime of LWFA, as well as allow us to recast and reinterpret such theoretical models so they can be better optimized.

In the next section (Section 1.2) of this chapter we will first introduce basic concepts related to LWFAs, with an eye towards illucidating the challenges and the opportunities for this exciting technology. Section 1.3 will discuss the role of PIC simulations in the development and understanding of LWFAs, as well as a new development in simulation methods that is inevitably linked to our improved understanding of nonlinear self-guided LWFA in regimes that were not hitherto studied because the required simulations that were too computationally expensive. We will conclude in Section 1.4 with an overview explaining the structure of the dissertation as it relates to the intertwining development of simulation methods and our developing physical understanding of LWFAs.

1.2 LWFA Concepts

In a laser driven plasma based accelerator, the ponderomotive force or radiation pressure of a laser pulse displaces the plasma electrons away from a background of neutralizing ions. The space charge force of the ions pull the electrons back, forming a wake. It should be noted that there are multiple plasma based accelerator schemes that rely on lasers to create the plasma wave wakefield, including the LWFA[5] (Laser Wakefield Accelerator, first mentioned in Section 1.1), PBWA[28] (Plasma Beat Wave Accelerator) and SMLWFA[29, 30] (Self-Modulated Laser Wake Field Accelerator), and the Forced LWFA [15]. However, all of the additional schemes were created because laser technology did not provide the lasers required for the true LWFA concept. However, these laser systems now exist and for applications that require excellent beam quality the pure LWFA concept is preferred. Therefore, in this dissertation we restrict our attention to the pure LWFA, where the driver is an intense, ultra-short, laser pulse with a pulse length of about half the plasma wavelength. Although simple in concept, this regime has only been studied recently compared to the other regimes due to the technological requirement of generating extremely short pulse with high peak power. We note that it is also possible to use a relativistic electron (positron, proton, or antiproton) beam as the driver instead of a laser, in what is called a PWFA [31] (Plasma Wakefield Accelerator). Although not the focus of this dissertation, we will comment on

common physics between the LWFA and PWFA when appropriate.

In the LWFA (and in fact for PWFAs as well) the driver is tightly focused in order to achieve an intensity large enough to excite a large amplitude plasma wake wake. It cannot be focused too tightly because the ponderomotive force of the laser is exerted by the gradient of the laser intensity and therefore only exists where the laser is intense. As we discuss shortly, this is not the case when exciting a wake by an electron beam. Hence the spot size needs to be comparable to the wavelength of the wake in order for the wake to efficiently generated. The use if an intense laser with a spot size comparable to the wake's wavelength leads to a significantly multi-dimensional structure of the wake, that has a bubble-like structure with a sheath of electrons surrounding a of a pure ion column region. Operating a plasma-based accelerator in this regime, called the blowout or bubble regime[12, 16, 4], has many advantages for accelerating electrons including perfectly linear focusing forces, accelerating forces that are independent of the transverse coordinates, and focusing forces that do not vary in the axial direction [4]. This regime is also quite stable and self-guiding can occur which has several advantages over using an plasma channel. Most of the simulations presented in this dissertation have been conducted in this LWFA parameter regime.

In 1987 Sun et al.[32] studied relativistic self-focusing and showed theoretically that for a laser with a power larger than the critical power for relativistic self-focusing, P_c, that when it is focused to a spot size comparable to the plasma skin depth, c/ω_p a solution exists where all of the plasma electrons are evacuated. Essentially, when a laser with sufficient power is focused to a small enough spot size the ponderomotive force on electrons at the edge of the depleted region is large enough to balance the space charge force on them from the unshielded ions. They called this electron cavitation. It is worth noting that these authors used incorrect boundary conditions between the evacuated region and the electron sheath and they ignored the fact that the electrons in the sheath would be moving backwards. However, they were the first to discuss the basic concept of electron cavitation (or blowout). Essentially, for a laser with a sufficient power, i.e, $P \simeq P_c$ but with a spot size larger than some equilibrium spot size, the laser will self-focus to a spot size and intensity where cavitation occurs. Although this phenomenon was not originally proposed for its relevance to the LWFA, it was later used

to formulate the idea of a "matched" spot size for a given laser power, for which the spot size of the laser will remain relatively constant[4]. In order for particles to be accelerated in a controlled manner over many Rayleigh lengths, and thereby reach very high energies while maintaining excellent beam quality, it is important to understand how a laser remains self-guided in the plasma while forming a stable wake.

In 1991 Rosenzweig et al.[12], using 2D azimuthally symmetric r-z fluid and PIC simulations, discovered a regime for electron beam driven PWFAs for which the plasma electrons are completely evacuated and form a pure ion column. Most previous work for the PWFA had focused on the one dimensional or wide beam limit. However, unlike for a laser where the radiation pressure only exists at the laser, one can make the particle beam very narrow and still make a large wake since plasma electrons far from the beam feel the space charge force. It was found that when an intense short-pulse electron beam is focused with a spot size much less then the wake's wavelength, that the wake is formed by the space charge force from the electron beam predominantly radially expelling all of the plasma electrons. These electrons then stream backwards within a narrow sheath. They were the first to point out that in such nonlinear wakes the acceleration and focusing fields had ideal properties (discussed earlier) for accelerating electrons. No predictive or first principles theory was offered to explain the structure of these wakes.

Very soon thereafter, researchers realized that the ponderomotive force (radiation pressure) from an intense laser could also create similar wakes [13, 14]. These early nonlinear LWFA simulations were carried out in 2D slab geometry and were not run for long propagation distances. A linearly polarized laser cannot be modeled in 2D r-z simulations. Almost a decade later in 2002, Malka et al., [15] using CALDER and Pukhov and Meyer-ter-Vehn [16] using VLPL performed the first 3D PIC simulations of LWFAs. In [16], simulations of a 12J/30fs/400 TW/.8μm laser propagating in a $2 \times 10^{19} cm^{-3}$ plasma were presented. For these parameters, the wake amplitude is very large and the laser and wake evolve rapidly. It was observed that in this very nonlinear regime some of the electrons from the plasma became trapped and accelerated in the wake structure in a process they called wave breaking. In fact the trapping process occurred continuously throughout the entire propagation

distance. What was new was that although the trapping process was continuous was that the accelerated electrons eventually formed a quasi- monoenergetic beam. The formation of this beam occurred after electrons dephased and began to lose energy in a process later called phase space rotation. For these very nonlinear regime, the shape of the sheath is almost spherical in the shape of a "bubble". For this reason it is now referred to as the bubble regime.

These authors and others believed that self-injection only happened for high laser powers and plasma densities, but Tsung et al.[17] showed that self-injected mono-energetic beams could also be produced at lower laser powers and intensities, and plasma densities. Tsung et al. simulated a 50fs laser whose power was as low as 13 TW propagating in a $3 \times 10^{18} cm^{-3}$ plasma. In this case, the trapping was not continuous. The work of Tsung et al., also provided a qualitative description of beam loading as well as the observation that as a self-trapped electron bunch dephased it enhanced the wake leading to the self-trapping of additional bunches. In 2004, three experimental groups subsequently confirmed that moderate power lasers could indeed produce quasi-monoenergetic electron bunches when propagated through mm scale gas jets or density channels[18, 19, 20]. Subsequently, the production of quasi-monoenergetic beams has become commonplace and energies exceeding 1 GeV have now been obtained[33, 34, 23, 35].

Although, there had been much interest in the blowout (and bubble) regime since the work of Rosenzweig et al., [12], it was not until 2006 in which a predictive theory for it was developed. In 2006, Lu et al. [36], showed that the wake structure could be predicted by developing an equation for the trajectory of the electrons at the edge of the ion column (the blowout radius). They showed that the results were insensitive to the details of the structure of the sheath and presented a phenomenological model for the sheath. They then showed that with this parameterized sheath and trajectory of the blowout radius could be self consistently calculated because the field structure inside the blowout radius could also be determined. This theory held for small and large blowout radius and it showed that for large blowout radius (as compared to the skin depth) that the trajectory of the sheath was nearly a circle so the structure looked like a sphere or bubble.

In 2007 Lu et al, [4] combined many of these ideas into a phenomenological theory for LWFA in a nonlinear self-guided regime. Using their theory for the wake structure, concepts of local pump depletion, dephasing, and spot size matching they described how most of the physics scaled with the time and distances to the matched spot size and blowout radius. They also described how to scale the laser intensity as the density is lowered such that self-guiding would scale properly. They generated scaling laws for the energy gain of an electron and the amount of charge that could be loaded into the wake. The results were supported by a limited number of full scale 3D OSIRIS simulations. These simulations were for parameters that gave $\sim 1.5GeV$ energy gain. However, computational limits prevented simulating the lower densities and longer propagation distances that were needed to get even higher electron energies. Around the same time, Gordienko and Puhkov [37] also provided a self-similar theory for how the"bubble" regime could be scaled. However, this work makes clear that the bubble regime is used to describe a "highly nonlinear wakebroken" regime in which the wake is so loaded that no coherent wake structure is visible. In [4], parameters and a theory are presented in which the wake structure is useful for a generating high quality electron beams. They referred to their regime as the blowout regime. The work of [4] also clearly points out differences between their work and that of [37]. However, the community currently uses the terms blowout and bubble regimes synonymously.

In addition to the self-injection of pre-ionized plasmas, other methods of particle injection in LWFAs have been investigated, such as ionization-injection[38, 39, 40], colliding pulses[41], and down ramp injection[42, 43, 44, 45, 46]. Beams may also be injected from an external source. Each of these injection methods presents entirely new avenues for producing low emittance, high charge, high current electron beams, but the majority of this dissertation will be concerned with self-injection, which is the simplest of these methods to investigate when simulating new parameter regimes.

To summarize, laser self-focusing, bubble wake structure, and particle self-injection are all attractive qualities of a LWFA, which may be studied and fine-tuned to create an ideal particle accelerator. The goal is to guide the laser over longer distances, to produce a stable transfer of energy from the laser to the wake, to produce a coherent accelerating structure

with ideal accelerating and focusing properties, and to inject a larger amount of charge with as low a beam emittance as possible into this accelerating structure.

1.3 Particle-In-Cell Simulations

Analytical theory and controlled experiments have a complimentary relationship in the study of physics. The goal is to develop a theoretical understanding of the problem at hand through analytical equations derived from our understanding of fundamental physics, whose implications and predictions may later be verified by experimental results. Consistency and deviancy of the measured results from the derived theory give us guidance to further develop or change our theoretical understanding, thereby completing the circle that is the scientific method. In some fields, such as plasma physics, the equations that dictate the physics or the number of degrees of freedom is so large that processes are highly nonlinear and thereby difficult to break down into a concise, practically usable set of analytic equations. Simplified expressions may be derived for plasmas under very specific parameter regimes (cold fluid equations, MHD, etc.), but the assumptions of these equations may break down under special circumstances, and the results that they give are often approximated. In these instances, computational simulations are a crucial bridge between theoretical understanding and real experiments. The LWFA is an example of a physical problem for which few useful analytical equations may be derived for a realistic, fully 3-dimensional problem, but whose behavior and potential improvements may be studied in great detail through computational simulations or numerical experiments.

Simulations may be based on very fundamental equations of fluid and particle motions without resorting to nearly as many approximations as are necessary in many analytically derived equations. One family of plasma simulations, called PIC simulations[47, 48], are particularly fundamental and therefore straight forward to desribe. In PIC simulations, the electromagnetic fields are represented by a grid, and the particles move within the grid with a finite size comparable to the grid size. In each time step, the motion of particles are calculated via the equations of motion (such as the Lorentz force law), from fields that are interpolated

from the grid positions to the position of the particle. The charge and current density for a single particle is calculated from the particle motion and then interpolated onto the grid. The total charge and current density are summed to get the total values. Finally, the fields are advanced according to Maxwell's equations and the current source. Since the full set of Maxwell's equations and the relativistic equations of motion are self-consistently evolved, PIC simulations of plasmas give a very detailed and accurate description on the processes within the plasma. Within the validity of classical physics and numerical accuracy, they may even be considered numerical experiments. Because of the brute-force nature of these types of simulations, however, they are known to be very computationally expensive unless the compute time is reduced by a specific geometry or a special numerical technique. As computers become more robust and computer clusters more prominent, PIC-style simulations are becoming even more relevant.

One powerful and versatile framework for massively parallelized PIC simulations is OSIRIS[1, 26]. This framework is generalized to work in multiple geometries, such as 1D, 2D, and 3D Cartesian geometries, and a 2D cylindrical geometry. In this dissertation, we describe the details of how a new, 'quasi-3D' algorithm[3], is implemented into OSIRS[27]. We describe how the field equations, expressed in cylindrical coordinates, are solved as a truncated Fourier expansion of the Maxwell's equations in ϕ[27]. The particle motion, however, is solved in full 3D Cartesian space. The field equations may be truncated at any specified integer number of modes, however, any linearly or circularly polarized laser with an azimuthally symmetric spot size may be expressed by electromagnetic fields in the $m = 1$ part of the expansion. In a typical LWFA simulation, the plasma motion may be captured by the lowest, 0th mode, and the laser may be captured by the $m = 1$ mode. Since these two fields can be described using only a couple of 2D grids, these simulations capture 3D-like effects at a speed comparable to a 2D r-z simulation; which is much faster than a typical 3D Cartesian simulation. Therefore, this algorithm is ideal for the parameters scans of LWFAs.

When simulations have become so deeply instrumental for studying nonlinear physics of problems like LWFAs, the developments of newer, more efficient algorithms mark important milestones. Faster simulations allow for numerical experiments in parameter regimes that

were previously deemed too computationally expensive, and the newly enabled observations contribute to a more accurate theoretical understanding of the physics. This dissertation is therefore twofold: two of the chapters describe and explore the quasi-3D simulation algorithm, and the subsequent two chapters explore fine-tunings of the analytic theory of LWFAs that were made possible through these simulations. We thereby hope to convey this complex and multi-faceted nature of the evolution of nonlinear plasma physics.

1.4 Overview

In Chapter 1 we have offered some background and motivation behind the research that is presented in this dissertation. Chapter 2 will review the basic physical theories pertaining to LWFAs, including but not limited to the conditions for self-guiding, an estimate of trapped particle energies, and the basic conditions for trapping. Chapter 3 will present an in-depth description of how the quasi-3D geometry was implemented into the OSIRIS simulation framework, including the derivation of a new rigorously charge conserving current deposition scheme we developed in order to make simulations with this geometry more numerically accurate. Chapter 4 will present a variety of both LWFA and PWFA simulations with this quasi-3D algorithm as a way of presenting the full range of potential this new algorithm presents. Although this dissertation is concerned mainly with LWFA, we believe that this broad exposition will prove useful for future researchers who will implement this algorithm. Chapter 5 will revisit much of the theory presented in Chapter 2, and re-examine them under simulations in the parameter regimes that hitherto were not accessible but are now possible with the new geometry discussed in Chapter 3. Chapter 6 will re-cast the phenomenological laws of scaling in Chapter 2 in order to design simulations aimed at optimizing a LWFA whose parameters are constrained by a laser with fixed energy. Chapter 7 will summarize the important results that were obtained during the wide range of simulations that were conducted during the writing of this dissertation, as well as outlines possible future developments to the LWFA that were brought to light from our newfound knowledge base.

CHAPTER 2

Review of Trapping and Acceleration Processes

2.1 Introduction

In this chapter, we will review and discuss relevant theories concerning the self-guided, nonlinear blowout regime of LWFA. Until recently, most analytical theories on wakefield excitation have either been restricted to linear fluid theory[31, 49] or one dimensional nonlinear fluid theory[10]. However, in recent LWFA and PWFA experiments the wakes have been excited in the nonlinear blowout regime where neither fluid not one-dimensional theory applies. As an alternative to the purely analytical method, Gordienko and Puhkov[37] approached the problem by noting that for $a_0 \gg 1$, all quantities should scale with a single similarity parameter $S \equiv \frac{n_p}{n_c a_0}$. The coefficients of the scalings are determined from simulations, and predictions may be made for trapped particle evolution given that the laser's transverse and longitudinal profile, and aspect ratio, are kept the same. However, this approach has limited usefulness because in all experiments to date and for most applications it is not the case that $a_0 \gg 1$. Therefore, Lu et al.[4], developed a phenomenological description of the LWFA in the blowout regime which can be applied for $a_0 \gtrsim 1$. They identified the key physics as wake excitation, pump depletion, dephasing, and beam loading. They used these concepts to develop an expression for the accelerated particle energy, as well as the ideal laser spot size for self guiding. The ideas of Lu et al. overlap with those of Gordienko and Puhkov, but differ significantly in that the former apply for laser amplitudes of $a_0 \gtrsim 2$, which is far too low for the analysis of the latter which Lu et al. argued might be appropriate when $a_0 \gtrsim 2\sqrt{n_c/n_p}$. In addition, Lu et al., pointed out that, while other phenomenon can be "scaled" to lower densities (and higher output energies), it is not clear if self-guiding will

"scale".

Most of the concepts and derivations presented in this chapter are from Lu et al.[4], providing phenomenological scaling laws for LWFA in a self-guided, blowout regime. Such scaling laws help us provide us with estimates as to the expected accelerated particle energies for existing LWFA parameters, as well as design parameters for future LWFA experiments and simulations as we push for trapped particles with tens of GeV of energy. It is also important to consider what possible physical effects may not scale according to the existing model, and in what manner to adjust the LWFA parameters such that the model scales accordingly despite the newly considered effects. In addition, the condition for which particles are self-trapped in the 3D LWFA is discussed in order provide a better understanding of how self-trapping occurs. However, the scaling laws should also apply for externally injected electron beams.

The intent of this chapter is to introduce important theory and concepts pertaining to LWFAs operating in the blowout regime, so that these equations and concepts may be revisited later in this dissertation. Section 2.2 will introduce the basic field equations and approximations which are used to describe the behavior of LWFAs. Section 2.3 will discuss properties of the accelerating and focusing fields inside the ion column of the LWFA, which make it ideal for the acceleration of electrons. Section 2.4 will examine the conditions under which an LWFA operating in the blowout regime may self-guide. Section 2.5 will re-derive the estimate for the trapped particle energy of a LWFA presented by Lu et al.. Section 2.6 re-derives an expression Lu et al. presents for the possible scaling of the normalized laser amplitude to ensure that the laser is self-guided over a greater number of Rayleigh lengths which is needed for lower densities and higher electron energies. Section 2.7 derives a constant of motion given the quasistatic approximation, which is very useful in understanding the behavior of trapped particles in a LWFA. Section 2.8 derives a trapping condition for plasma particles in a LWFA that is applicable in three dimensions.

2.2 Basic Equations and the Quasistatic Approximation

In this section we discuss various equations for the electromagnetic fields and particle motion, and how they may be simplified and approximated given what we know about the important time scales in a LWFA problem. As we engage in this discussion, important coordinates and field quantities will arise which we will repeatedly return to over the course of this dissertation. We start from Maxwell's equations in the Lorentz gauge and the equation of motion for laminar fluids,

$$\left(\frac{1}{c^2}\frac{\partial^2}{\partial t^2} - \nabla^2\right)\begin{bmatrix}\mathbf{A}\\ \rho\end{bmatrix} = 4\pi\begin{bmatrix}\mathbf{J}/c\\ \rho\end{bmatrix}, \tag{2.1}$$

$$\frac{1}{c}\frac{\partial\phi}{\partial t} + \nabla\cdot\mathbf{A} = 0, \tag{2.2}$$

$$\left(\frac{\partial}{\partial t} + \mathbf{v}_i\cdot\nabla\right)\mathbf{p}_i = q_i\left[\mathbf{E} + \frac{\mathbf{v}_i}{c}\times\mathbf{B}\right], \tag{2.3}$$

where $\rho = \sum_i q_i n_i$ and $\mathbf{J} = \sum_i q_i n_i \mathbf{v}_i$, and they satisfy the conservation equation,

$$\frac{\partial\rho}{\partial t} + \nabla\cdot\mathbf{J} = 0. \tag{2.4}$$

There are three distinct time scales to the LWFA problem. The high-frequency laser oscillation scales as ω_0^{-1}, the plasma wave wake oscillation scales as ω_p^{-1}, and the laser envelope evolves on the scale of the Rayleigh length $Z_R \equiv \pi W_0^2/\lambda_0$, which, because the spot size W_0 is on the order of the plasma skin depth $k_p \equiv c/\omega_p$, actually scales as $(\omega_0/\omega_p)\omega_p^{-1}$. In order to describe the wakefield excitation, it is possible to average out the lowest scale, ω_0^{-1} and describe the equation of motion as a function of the smoothed fields $\mathbf{E}_s$ and $\mathbf{B}_s$ produced by the plasma charge density, and the ponderomotive force, $\mathbf{F}_p$ [50] :

$$\frac{d}{dt}\mathbf{p}_{i,s} = \left(\frac{\partial}{\partial t} + \mathbf{v}_{i,s}\cdot\nabla\right)\mathbf{p}_{i,s} = q_i\left[\mathbf{E}_s + \frac{\mathbf{v_{i,s}}}{c}\times\mathbf{B}_s\right] + \mathbf{F}_p, \text{ and} \tag{2.5}$$

$$\mathbf{F}_p = -\frac{q_i^2}{\overline{\gamma}_i m_i c^2}\nabla\left|\frac{\widehat{A}_L}{2}\right|^2, \tag{2.6}$$

where the laser field is described by $A_{\text{laser}} = \frac{\widehat{A}_L}{2}e^{-i\omega_0\xi/c} + \text{c.c.}$, $\frac{e\widehat{A}_L}{mc^2} \equiv a$, and $\overline{\gamma}_i = \sqrt{1 + \frac{p_i^2}{m_i^2c^2} + \frac{|a|^2}{2}}$. The subscripts "$i$" and "$s$" were added for clarity and will be omitted from henceforth. The

full derivation of the ponderomotive force expression is given by Mora and Antonsen Ref. [50].

There is another level of simplification to the field equations we can adopt by utilizing the separation between the wake oscillation time scale (ω_p^{-1}) and the laser envelope evolution time scale $(\omega_0/\omega_p)\omega_p^{-1}$. That is to say, on the scale of plasma particle motion, the near-stationary wake structure depends on the variable $\xi \equiv v_\phi t - z$, where the phase velocity v_ϕ is assumed to be very close to the speed of light. Mathematically, this is described by transforming from (x, y, z, t) variables to $(x, y, \xi \equiv v_\phi t - z, s \equiv z)$, letting $v_\phi \to c$, and approximating that $\partial_s \ll \partial_\xi$. Under this transformation, $\partial_z = \partial_s - \partial_\xi$, and $\partial_t = v_\phi \partial_\xi$. This was called the "quasistatic approximation" by Sprangle et al.[51] and the "frozen field approximation" by Whittum et al.[52]. For a laser driver, the quasistatic approximation is valid as long as $\frac{\omega_0}{\omega_p} \gg 1$. Under this approximation, Equations 2.1 and 2.2 simplify to

$$-\nabla_\perp^2 \begin{bmatrix} \mathbf{A} \\ \phi \end{bmatrix} = 4\pi \begin{bmatrix} \mathbf{J}/c \\ \rho \end{bmatrix}, \tag{2.7}$$

$$\nabla_\perp \cdot \mathbf{A}_\perp = -\frac{\partial \Psi}{\partial \xi}, \tag{2.8}$$

where $\Psi \equiv \phi - \frac{v_\phi}{c} A_z \to \phi - A_z$, $\nabla_\perp \equiv \hat{x}\partial_x + \hat{y}\partial_y$, and $\mathbf{A}_\perp = \hat{x}A_x + \hat{y}A_y$. This new scalar potential "Ψ" is sometimes called the "pseudo potential", or the "trapping potential".

Ref. [50] shows that the perpendicular motion of the plasma electrons evolve as

$$\frac{d}{d\xi}\mathbf{p}_\perp = \frac{\bar{\gamma}}{c\left(1 - \frac{q\Psi}{mc^2}\right)} \left\{ q\left[\mathbf{E} + \left(\frac{\mathbf{v}}{c} \times \mathbf{B}\right)\right]_\perp - \frac{q^2}{\overline{\gamma} mc^2} \nabla_\perp \left| \frac{\widehat{A}_L}{2} \right|^2 \right\}. \tag{2.9}$$

Equation 2.7, rearranged into an expression of Ψ, shows that the pseudo potential obeys a Poisson equation,

$$-\nabla_\perp^2 \Psi = 4\pi \left(\rho - \frac{1}{c} J_z \right). \tag{2.10}$$

Charge conservation (Equation 2.4) is re-expressed as

$$c\frac{\partial}{\partial \xi}\left(\rho - \frac{1}{c} J_z \right) + \nabla_\perp \cdot \mathbf{J}_\perp = 0, \tag{2.11}$$

which shows that if ξ is a time like variable then $\rho - \frac{1}{c} J_z$, rather than ρ, is conserved inside a transverse slice as it evolves in ξ. The perpendicular and longitudinal fields can be calculated

as

$$E_z = \frac{\partial \Psi}{\partial \xi}, \tag{2.12}$$

$$B_z = (\nabla_\perp \times \mathbf{A}_\perp) \cdot \hat{z}, \tag{2.13}$$

$$\mathbf{E}_\perp = -\nabla_\perp \phi - \frac{\partial \mathbf{A}_\perp}{\partial \xi}, \tag{2.14}$$

$$\mathbf{B}_\perp = \nabla_\perp \times (A_z \hat{z}) + (\partial_z \hat{z}) \times \mathbf{A}_\perp. \tag{2.15}$$

The accelerating field E_z is therefore the derivative of one scalar potential Ψ alone, and this convenient pseudo potential may be calculated by its sources ρ and J_z through Equation 2.10. Ψ is also important because it forms a part of a constant of motion given the quasistatic approximation (discussed in Section 2.7) and the condition for particle trapping in 3D (discussed in Section 2.8).

2.3 Properties of Accelerating and Focusing Fields Inside the Ion Column

When an intense enough short pulse laser propagates through a plasma, a pure ion column may form when the ponderomotive force of the laser blows all the plasma electrons aside while the heavier ions remain stationary during the times scales of interest. It is safe to assume, in this situation, that within a "blowout radius", $r < r_b$, the longitudinal current within the bubble is zero, or $J_z = 0$, since the electrons are vacant and the ions have zero velocity. The structure itself "moves" at a phase velocity very close to the speed of light, or $v_\phi \approx c$. It is useful at this point to extrapolate from the equations given in section 2.2 what properties the accelerating and focusing fields have for a charge moving near the speed of light within this structure, in order to ascertain its usefulness for accelerating electrons.

We will begin with the Lorentz force law for the focusing field,

$$\mathbf{F}_\perp = q\left[\mathbf{E}_\perp + \left(\frac{\mathbf{v}}{c} \times \mathbf{B}\right)_\perp\right],$$

in terms of the potentials with the help of Equation 2.14, which says that

$$\begin{aligned}\mathbf{E}_\perp &= -\nabla_\perp \phi - \partial_\xi \mathbf{A}_\perp, \text{ or} \\ &= \left[-\frac{\partial \phi}{\partial r} - \partial_\xi A_r\right] \hat{r},\end{aligned}$$

in cylindrical (r, θ, z) coordinates [1], and knowing that $E_\theta = 0$ assuming cylindrical symmetry. Now we turn to the magnetic field, given by

$$\begin{aligned}\mathbf{B} = \nabla \times \mathbf{A} &= \left[\partial_z A_r - \partial_r A_z\right] \hat{\theta} \\ &\quad + \frac{1}{r}\left[\partial_\theta A_z - r\partial_z A_\theta\right] \hat{r} \\ &\quad + \frac{1}{r}\left[\partial_r r A_\theta - \partial_\theta A_r\right] \hat{z}, \\ &= \left[-\partial_\xi A_r - \partial_r A_z\right] \hat{\theta}.\end{aligned}$$

Due to the azimuthal symmetry of the problem and to the fact that there is no current in θ, we have assumed that A_θ and $\partial_\theta = 0$. We may finally write the total transverse force on a charge q in the $\hat{r}$ direction as

$$\begin{aligned}\mathbf{F}_\perp = F_r \hat{r} &= q\left(E_r - \frac{v_z}{c} B_\theta\right) \hat{r}, \\ &= q\left(-\frac{\partial \phi}{\partial r} - \partial_\xi A_r + \frac{v_z}{c}\partial_\xi A_r + \frac{v_z}{c}\partial_r A_z\right) \hat{r}, \\ &= q\left[-\frac{\partial \phi}{\partial r} - \left(1 - \frac{v_z}{c}\right)\partial_\xi A_r + \frac{v_z}{c}\partial_r A_z\right] \hat{r}. \end{aligned} \tag{2.16}$$

For azimuthally symmetric situations, we could assume $\partial_r A_z = 0$, due to an extrapolation from the 2D Poisson-like equation 2.7 and the fact that $J_z = 0$ for $r < r_b$. However, to a bit more general we keep this term. If the charge is moving in the $\hat{z}$ direction with $v_z \to c$, then

$$\mathbf{F}_\perp = -q\frac{\partial\left(\phi - A_z\right)}{\partial r}\hat{r}. \tag{2.17}$$

If we compare equation 2.17 to the form of the accelerating electric field in Equation 2.12, we find that the focusing field and accelerating fields arise from a single potential, i.e., the

[1] Note that θ here is used for the angle in order not to confuse it with the scalar potential, ϕ. Elsewhere we use ϕ to refer to the azimuthal coordinate.

wake potential, namely that

$$\begin{aligned} F_\perp &= -q\partial_r \Psi, \text{ and} \\ F_\parallel &= qE_z = q\partial_\xi \Psi, \text{ or} \\ \partial_\parallel F_\perp &= \partial_\perp F_\parallel, \end{aligned} \tag{2.18}$$

where we note that $\partial_\parallel \simeq -\partial_\xi$ is the longitudinal gradient and $\partial_\perp = \partial_r$ is the transverse gradient. This relationship between the transverse and longitudinal fields is also referred to as the Panofsky Wenzel Theorem[53]. In this quick review we have assumed azimuthal symmetry. However, the fact that the focusing force on a relativistic electron is the transverse gradient of ψ still holds for each transverse direction even without azimuthal symmetry. The Panofsky Wenzel Theorem still holds in each transverse direction.

In Ref. [36] the Poisson-like equation given here as equation 2.10 was used to solve for an expression of Ψ given a source term, $\rho - J_z/c$, that is approximated by a step function of width Δ, at a distance r_b from the axis. The resulting expression from this simple model was

$$\begin{aligned} \Psi &= \Psi_0(\xi) - \frac{r^2}{4} = \frac{r_b^2(\xi)}{4}(1+\beta) - \frac{r^2}{4}, \text{ with} \\ \beta &\equiv \frac{(1+\alpha)^2 \ln(1+\alpha)^2}{(1+\alpha)^2 - 1}, \text{ and} \\ \alpha &\equiv \frac{\Delta}{r_b}. \end{aligned} \tag{2.19}$$

It is clear from this expression that the transverse force $F_\perp = -q\partial_r \Psi = -q\frac{1}{2}r$, is a perfectly linear focusing force for electrons[2]. The focusing force is also flat along the longitudinal direction, and the accelerating force, $\partial_\xi \Psi$, is flat along the transverse, r, direction. These are ideal properties for accelerating a beam of electrons while preserving its emittance along the entire beam (projected as well as slice emittance) and limiting the energy spread. It is also important to note that these properties remain when the wake is beam loaded [54].

[2]It is, however, a linear de-focusing force for positrons.

2.4 Conditions for Self-Guiding

In order to illustrate how and to what extent self-guiding is possible, it is informative to compare it with the effect of an external guiding channel. A laser can be guided with a stable spot size by a plasma channel with a parabolic density profile with its minimum on the laser's axis. The index of refraction of such a plasma may be expanded as [6, 55]

$$\eta = \frac{ck}{\omega} \simeq 1 - \frac{1}{2}\left(\frac{\omega_p}{\omega_0}\right)^2 \left(1 + \frac{\Delta n_c}{n_p}\frac{r^2}{W_0^2} + \frac{\Delta n}{n_p} - \frac{a_0^2}{8}\right), \tag{2.20}$$

where Δn_c is the depth of an external density channel, Δn is a density depletion from the transverse ponderomotive force, and $a_0^2/8$ is from a relativistic mass correction. If you were to externally guide the laser, you would set $\Delta n_c = mc^2/(\pi e^2 W_0^2)$, or $\Delta n_c/n_p = 4/(k_p W_0)^2$. Even without an external channel, however, relativistic mass corrections may potentially give the same effect on the index of refraction if

$$\frac{a_0^2}{8} \gtrsim \frac{4}{(k_p W_0)^2}, \text{ or} \qquad\qquad P \gtrsim P_c, \tag{2.21}$$

where

$$P_c = 17\left(\frac{\omega_0}{\omega_p}\right)^2 [GW], \tag{2.22}$$

is the critical power for relativistic self focusing [32]. At the front of the laser, however, the density compression from the ponderomotive force of the laser cancels out the increase in the index of refraction from relativistic mass effects, leading some to believe that a short pulse laser with $\tau \lesssim 1/\omega_p$ cannot be self guided [6]. On the contrary, Ref. [56] shows that for a high enough power self-focusing may be possible because the leading edge of the laser is continuously locally pump depleted before it diffracts, while the back of the pulse, located behind the density compression and inside an ion column, is still guided.

In order for the transverse profile of the self-guided laser to remain stable over the course of the particle acceleration process, an ideal spot size and amplitude must be chosen. Refs. [32, 57, 36] notes that the requirements for a matched profile may be estimated by balancing

$$\text{the transverse ponderomotive force} \quad : \quad k_p \nabla a_0^2/\gamma \sim \frac{a_0}{k_p R}, \text{ and}$$

$$\text{the force of the ion channel} \quad : \quad E_r \sim k_p R.$$

Equating these two gives $k_p R \sim \sqrt{a_0}$. Noting that the blowout radius scales with the laser spot size, and that the proportionality may be determined empirically through simulations, we have found that

$$k_p R \simeq k_p W_0 = 2\sqrt{a_0}. \tag{2.23}$$

Using what we extrapolated with Equation 2.21, it is possible to reformulate the above matching condition in terms of the laser power,

$$\frac{P}{P_c} \simeq \frac{a_0^2/8}{4/(k_p W_0)^2} = \frac{1}{32} a_0^2 (k_p W_0)^2 = \frac{a_0^3}{8}, \tag{2.24}$$

which implies

$$a_0 \simeq 2 \left(\frac{P}{P_c} \right)^{1/3}. \tag{2.25}$$

As the plasma density is decreased while laser frequency is kept the same, P_c necessarily increases. This means that if you want to scale to lower densities (which will later be shown is necessary in order to scale to higher trapped particle energies), you would need to equivalently increase the laser power in order to maintain comparable self-guiding with the same initial laser amplitude, a_0. Ref. [36] shows that, in order to remain in the nonlinear blowout regime, $a_0 \gtrsim 4.0$, implying a lower limit for the laser power given a specified plasma density.

2.5 Scaling of Trapped Particle Energy

In order to have an estimate on how much energy particles (self or externally injected) will acquire in an LWFA stage, it is important to determine the length scale over which the particles will experience an accelerating force, and to determine the time average of the acceleration gradient. Assuming that the laser is properly guided and diffraction is not an issue over the course of the process, the laser will traverse into the plasma until all of its energy is depleted from forming the plasma wake. Ref. [56] estimates the etching rate based on nonlinear 1D effects, giving $v_{\text{etch}} \simeq c\omega_p^2/\omega_0^2$, giving

$$L_{\text{etch}} \simeq \frac{c}{v_{\text{etch}}} c\tau_{\text{FWHM}} \simeq \left(\frac{\omega_0}{\omega_p} \right)^2 c\tau_{\text{FWHM}}. \tag{2.26}$$

There is another length scale that may dominate the acceleration process. The phase velocity of the wake is approximately $v_\phi \simeq v_g - v_{\rm etch}$, where v_g is the linear group velocity of a laser in an underdense plasma ($\omega_p^2 \ll \omega_0^2$). This results in the expression $v_\phi \simeq c[1 - \frac{3}{2}(\omega_p/\omega_0)^2]$. This is discussed in detail by Decker et al. [58, 59]. The wake slowly falls back to the trapped particles, which are traveling at a velocity very close to c. If the laser does not pump deplete beforehand, after the laser traverses an estimated dephasing length L_d, the zero of the wake outruns the location of the particles. The particles will then begin to decelerate. Given this understanding, L_d is estimated as

$$L_d \simeq \frac{c}{c - v_\phi} R \simeq \frac{2}{3}\left(\frac{\omega_0}{\omega_p}\right)^2 R, \tag{2.27}$$

where R is the radius of the bubble and is also the length of wake over which the longitudinal field is accelerating the particle. Thus, given that the trapped particles accelerate over some known distance, we may estimate the total change in the particle energy as

$$\Delta E = q E_{\rm LW} L_{\rm acc} = \epsilon_{\rm LW} l_{\rm acc} mc^2, \tag{2.28}$$

where E_{LW} is the average accelerating field of the wake, $L_{\rm acc}$ the acceleration length, $\epsilon_{LW} \equiv eE_{LW}/(mc\omega_p)$, and $l_{\rm acc} \equiv k_p L_{\rm acc}$. Comparing Equations 2.26 and 2.27, it becomes clear that you may match the pump depletion length to the dephasing length by simply adjusting the pulse length of the laser (Specifically, if we let $\tau_{\rm FWHM} = (2/3)R$). Assuming that this condition is met, we may simply set $L_{\rm acc} = L_d$, or, given the matched spot size condition,

$$l_{\rm acc} \simeq k_p \frac{2}{3}\left(\frac{\omega_0}{\omega_p}\right)^2 W_0 \simeq \frac{2}{3}\left(\frac{\omega_0}{\omega_p}\right)^2 2\sqrt{a_0}. \tag{2.29}$$

Ref. [36] shows that for $a_0 \gtrsim 4$ the ion column formed a sphere and that the accelerating field, apart from deviations at the edge of the sphere, depends linearly on the distance from the middle of the sphere. Specifically,

$$\frac{eE_z}{mc\omega_p} \simeq \frac{1}{2} k_p(\xi_0 - \xi), \text{ and} \qquad \frac{eE_{z,\max}}{mc\omega_p} \simeq \frac{1}{2} k_p R_b. \tag{2.30}$$

Because the wake is roughly a sphere, and the particles are self-trapped at the rear, it traverses a distance R in the moving window of the wake before it dephases at the center of the bubble. Because the accelerating field along the axis is roughly linear, the average

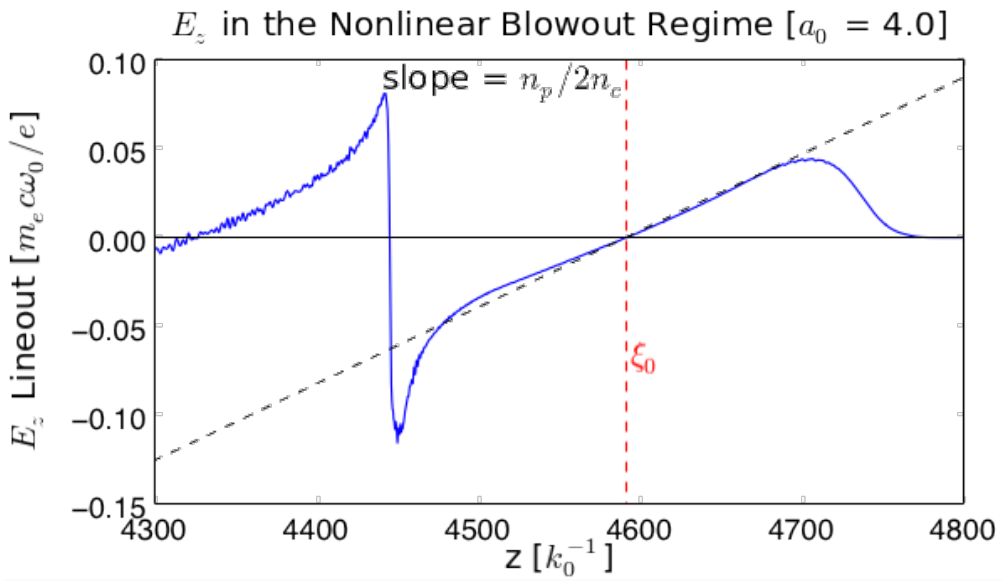

Figure 2.1: The basic structure of the accelerating field of a wake in the nonlinear blowout regime is approximated closely by Equation 2.30. Notable deviations are a nonlinear spike in the very back of the bubble, and a small bump around the location of trapped particles caused by beam loading.

electric field they experience is roughly a half of this, or $E_{LW} \approx \frac{1}{4} k_p R_b$. Under the matched spot size condition, this gives

$$\epsilon_{LW} \simeq \frac{k_p R_b}{4} \simeq \frac{\sqrt{a_0}}{2}, \tag{2.31}$$

which, combined with Equations 2.29 and 2.28 gives an estimate for energy gain of the trapped in terms of the plasma density and normalized laser amplitude,

$$\Delta E = \frac{2}{3} mc^2 \left(\frac{\omega_0}{\omega_p}\right)^2 a_0. \tag{2.32}$$

Using Equations 2.22 and 2.25, you can express the above equation in terms of the plasma density and laser power,

$$\Delta E[GeV] \simeq 1.7 \left(\frac{P[\mathrm{TW}]}{100}\right)^{1/3} \left(\frac{10^{18}}{n_p[cm^{-3}]}\right)^{2/3} \left(\frac{0.8}{\lambda_0[\mu m]}\right)^{4/3}. \tag{2.33}$$

The above representation illustrates the much stronger dependence that the output beam energy, i.e., energy gain, has on the plasma density than on the input laser power. However, Equations 2.22 and 2.25 indicate that a higher laser power will be necessary to ensure self

guiding for lower plasma densities. It is an important research question to consider how low of a plasma density, and how long a dephasing length, can it be appropriate to guide a laser with limited power. In addition, if a plasma channel is used, guiding can be maintained over a longer dephasing length for a lower input laser energy. However, channels present their own unique challenges such as misalignment wave front curvature, laser coupling, non-ideal focusing and acceleration fields.

2.6 Matching of Localized Pump Depletion with Diffraction

As we scale the LWFA to lower plasma densities, it necessitates the consolidation of physical effects that scale differently in spatial distances. Section 2.4 provides a spot size matching condition to ensure a stable laser evolution, as well as a general theory as to how self-guiding is possible in the nonlinear blowout regime. Even within this regime, the front of the pulse diffracts because the density compression from the ponderomotive force cancels out the increase in the index of refraction from relativistic mass effects. This means that a certain quantity of the laser is lost every Rayleigh length, $Z_R \equiv \pi W_0^2/\lambda$. Section 2.5 provides an estimate for the trapped particle energies assuming that the laser was self-guided during the particle acceleration process, which occurs over the course of the dephasing length, L_d. Using the spot size matching condition we may write these spatial scales as a function of a_0 and n_p,

$$L_d = \frac{4c\omega_0^2}{3}\left(\frac{m_e}{4\pi e^2}\right)^{3/2}\frac{\sqrt{a_0}}{n_p^{3/2}}, \text{ and} \qquad Z_R = \frac{4\pi c^2}{\lambda}\left(\frac{me}{4\pi e^2}\right)\frac{a_0}{n_p}. \tag{2.34}$$

The pump depletion length, L_{etch}, scales with the dephasing length if the pulse length is set at a fixed fraction of the spot size, so the only incongruity in scaling is between the dephasing length and the Rayleigh length. If you keep P/P_c, and therefore a_0, fixed, the number of Rayleigh lengths traversed by the laser over the course of particle acceleration therefore scales as $L_d/Z_R \sim 1/\sqrt{n_p}$. Specifically, if $a_0 = 4.0$, the laser must traverse 14 Z_R for a $n_p = 1.0 \times 10^{18} cm^{-3}$ plasma, 20 Z_R for a $n_p = 5.0 \times 10^{17} cm^{-3}$ plasma, and 44 Z_R for a $n_p = 1.0 \times 10^{17} cm^{-3}$ plasma, for full particle dephasing.

In order to estimate how much of the laser is lost due to diffraction each Rayleigh length, we resort to the quasi-static theory for the index of refraction [4, 51]

$$\eta \simeq 1 - \frac{1}{2}\left(\frac{\omega_p}{\omega_0}\right)^2 \left[\frac{1}{1+\psi}\right], \text{ and} \qquad \frac{\partial^2 \psi}{\partial \xi^2} - \frac{k_p^2}{2}\left[\frac{1+a^2}{(1+\psi)^2} - 1\right] = 0. \tag{2.35}$$

Comparing these expressions with Equation 2.20 and its subsequent discussion on the conditions for self-guiding, we see that self guiding occurs when the square-bracketed term on the left equals $1 - 4/(k_p W_0)^2$, or assuming $|\psi| \ll 1$,

$$1 - \frac{1}{1+\psi} \simeq \psi = \frac{4}{(k_p W_0)^2}, \tag{2.36}$$

where the right ride of Equation 2.35 reduces to

$$\frac{\partial^2 \psi}{\partial \xi^2} \simeq \frac{k_p^2}{2} a^2.$$

At the very front of the laser pulse where ψ is still assumed to be very small, it grows as $\psi \sim \frac{k_p^2}{4} a^2 \xi^2$, giving

$$\frac{k_p^2}{4} a_0^2 \left(\Delta\xi\right)^2 = \frac{4}{\left(k_p W_0\right)^2}$$

where $\Delta\xi$ is the distance over which it takes ψ to grow to the necessary value for self-guiding,

$$\Delta\xi \simeq \frac{4}{k_p^2 a_0 W_0} = \frac{2}{k_p^2 a_0^{3/2}} \tag{2.37}$$

This is the length of the laser that is susceptible to diffraction at a point in time, and is therefore the length of the laser that is lost over the course of a Rayleigh length. The laser is said to be self-guided as long as the pump depletion overtakes the diffraction process, meaning that the diffraction does not significantly alter the wake formation and particle acceleration. This means that

$$\frac{v_{\text{etch}}}{c} \simeq \frac{3}{2}\frac{n_p}{n_c} \sim \frac{\Delta\xi}{Z_R}, \tag{2.38}$$

which reduces to a scaling for the normalized laser amplitude,

$$a_0 \sim \left(\frac{n_c}{n_p}\right)^{1/5}, \tag{2.39}$$

which was suggested by Lu et al.[4] as a way to ensure proper scaling to lower plasma densities and longer acceleration distances.

2.7 Constant of Motion given a Quasi-static Approximation

In this section we will show that under the quasi-static approximation

$$D_t\left(\gamma mc^2 - v_\phi p_z - q\Psi\right) = 0 \tag{2.40}$$

where D_t is d_t for a particle and $\partial_t + \vec{v}\cdot\nabla$ for a field quantity, and $\Psi \equiv \phi - \frac{v_\phi}{c}A_z$. This constant of motion will prove useful in determining the conditions for the trapping of plasma particles in a 3D nonlinear wakefield excited by either a laser (LWFA) or a particle beam (PWFA).

Conservation of energy and momentum for a single particle in prescribed fields are

$$D_t\gamma mc^2 = q\mathbf{v}\cdot\mathbf{E} \qquad D_t\mathbf{p} = q[\mathbf{E} + \frac{\mathbf{v}}{c}\times\mathbf{B}]. \tag{2.41}$$

Henceforth, we consider electrons and for simplicity we let $m = 1$, $q = 1$, and $c = 1$. In normalized units and if we explicitly write out the terms in the dot and cross products we get

$$D_t\gamma = -\left[v_xE_x + v_yE_y + v_zE_z\right], \tag{2.42}$$

$$D_tp_z = -\left[E_z + v_xB_y - v_yB_x\right]. \tag{2.43}$$

These two expressions can be combined to obtain

$$D_t(\gamma - v_\phi p_z) = (v_\phi - v_z)E_z - v_x(E_x - v_\phi B_y) - v_y(E_y + v_\phi B_x), \tag{2.44}$$

where the electric and magnetic fields may be expressed in terms of their potentials,

$$\mathbf{E} = -\nabla\phi - \partial_t\mathbf{A}, \text{ and} \qquad \mathbf{B} = \nabla\times\mathbf{A}. \tag{2.45}$$

This gives us

$$\begin{aligned} D_t(\gamma - v_\phi p_z) = (v_\phi - v_z)[-\partial_z\phi - \partial_tA_z] \\ - v_x[-\partial_x\phi - \partial_tA_x + v_\phi\partial_xA_z - v_\phi\partial_zA_x] \\ - v_y[-\partial_y\phi - \partial_tA_y + v_\phi\partial_yA_z - v_\phi\partial_zA_y], \end{aligned} \tag{2.46}$$

where the first line can be conveniently rearranged by adding and subtracting $\partial_t\phi$, and $v_\phi v_z \partial_z A_z$, to form

$$\begin{aligned}(v_\phi - v_z)[-\partial_z\phi - \partial_t A_z] &= \partial_t(\phi - v_\phi A_z) - \partial_t\phi \\ &\quad + v_z\partial_z(\phi - v_\phi A_z) + v_\phi v_z \partial_z A_z - v_\phi \partial_z\phi + v_z\partial_t A_z \\ &= \partial_t(\phi - v_\phi A_z) + v_z\partial_z(\phi - v_\phi A_z) \\ &\quad + (\partial t + v_\phi\partial_z)\phi + v_z(\partial_t + v_\phi\partial_z)A_z.\end{aligned}$$

The terms of the equations can be organized as derivatives of $\phi - v_\phi A_z$, with the remaining terms are all operated on by $\partial_t + v_\phi\partial_z$. Following the same organization for the x and y components of Equation 2.46 gives a revealing representation,

$$\begin{aligned}D_t(\gamma - v_\phi p_z) &= \partial_t(\phi - v_\phi A_z) \\ &\quad + v_x\partial_x(\phi - v_\phi A_z) + v_y\partial_y(\phi - v_\phi A_z) + v_z\partial_z(\phi - v_\phi A_z) \\ &\quad - (\partial_t + v_\phi\partial_z)\phi \\ &\quad + v_x(\partial_t + v_\phi\partial_z)A_x + v_y(\partial_t + v_\phi\partial_z)A_y + v_z(\partial_t + v_\phi\partial_z)A_z.\end{aligned} \tag{2.47}$$

The partial derivatives of $\phi - v_\phi A_z$ can be rewritten singularly as a total derivative in time. The remaining derivatives are in fact negligible in the quasi-static approximation because $\partial_t + v_\phi\partial_z = v_\phi\partial_s = \ll \partial_\xi$. Written in another way,

$$D_t\left[\gamma - v_\phi p_z - (\phi - v_\phi A_z)\right] = -v_\phi\partial_s\phi + \mathbf{v}\cdot(v_\phi\partial_s\mathbf{A}) \simeq 0. \tag{2.48}$$

Therefore, under the quasi-static approximation, the quantity '$\gamma - v_\phi p_z - (\phi - v_\phi A_z)$' is a constant. We later show that the field quantity $\phi - v_\phi A_z$ predominantly determine the condition in which a particle may trap in the wake, and thereby define a 'trapping potential', Ψ. In non-normalized units, Equation 2.48 takes the form of Equation 2.40.

This constant of motion allows us to derive a particle's axial momentum from the perpendicular momentum. If we allow $v_\phi \to c$, and assume that the particle had an initial $\Psi_i = 0$, the constant of motion in normalized units becomes

$$\gamma - p_z = 1 + \Psi, \tag{2.49}$$

where $\gamma = \sqrt{1 + p_\perp^2 + p_z^2}$. If we square the two sides of the equation we get,

$$\begin{aligned}(\gamma - p_z)^2 &= (1+\Psi)^2, \\ \gamma^2 - 2\gamma p_z + p_z^2 &= 1 + p_\perp^2 + 2p_z^2 - 2\gamma p_z = (1+\Psi)^2, \\ 2p_z(\gamma - p_z) &= 2p_z(1+\Psi) = 1 + p_\perp^2 - (1-\Psi)^2,\end{aligned}$$

from which it becomes trivial to solve for p_z in terms of $p_\perp$ and Ψ,

$$p_z = \frac{1 + p_\perp^2 - (1+\Psi^2)}{2(1+\Psi)}, \tag{2.50}$$

$$\tag{2.51}$$

It is trivial to derive a couple more relationships for the particle quantities and ψ, namely,

$$\gamma = 1 + \Psi + p_z = \frac{1 + p_\perp^2 + (1+\Psi)^2}{2(1+\Psi)}, \tag{2.52}$$

$$1 - v_z = \frac{1+\Psi}{\gamma} = \frac{2(1+\Psi)^2}{1 + p_\perp^2 + (1+\Psi)^2}. \tag{2.53}$$

In addition to being a convenient scalar field that completely describes the accelerating field E_z (as was shown in Section 2.2), the pseudo potential Ψ is also pertinent in understanding particle motion in the quasistatic approximation.

2.8 Generalized Trapping Condition

In order to become trapped, a plasma electron beginning at rest ($v_z = 0$) at some initial trapping potential ($\Psi = \Psi_i$), must accelerate up the phase velocity of the wake ($v_z = v_\phi$) at a final trapping potential ($\Psi = \Psi_f$). Once it is in phase with the wake, it will continue to accelerate until it dephases with the accelerating structure of the wake. To obtain a precise condition, we can no longer let $v_\phi \to c$. From Equation 2.48 we know that we can relate the beginning and final states,

$$\gamma - v_\phi(\gamma v_z) - \Psi_f = 1 - \Psi_i, \tag{2.54}$$

where it is assumed that $v_{zi} = 0$ and $\gamma_i = 1$. An electron is trapped when $v_z = v_\phi$. To determine what change in the trapping potential ($\Delta\Psi \equiv \Psi_f - \Psi_i$) is necessary in order for

$v_z = v_\phi$ we rewrite Equation 2.54 (with $v_z = v_\phi$) as,

$$\gamma(1 - v_\phi^2) = 1 + \Delta\Psi, \text{ or} \tag{2.55}$$
$$\frac{\gamma}{\gamma_\phi^2} = 1 + \Delta\Psi,$$

where $\gamma_\phi \equiv 1/\sqrt{1 - v_\phi^2}$. To simplify this equation further we note from special relativity that for $v_z = v_\phi$,

$$\gamma^2 = 1 + p_\perp^2 + (\gamma v_\phi)^2, \tag{2.56}$$
$$\gamma = \sqrt{\frac{1 + p_\perp^2}{1 - v_\phi^2}} = \gamma_\phi \sqrt{1 + p_\perp^2}.$$

Plugging Equation 2.56 into Equation 2.55 gives us a generalized condition for the change in potential the particle must undergo in order to be trapped,

$$\Delta\Psi = \frac{\sqrt{1 + p_\perp^2}}{\gamma_\phi} - 1. \tag{2.57}$$

This condition holds in multi-dimensions and this form for the 3D trapping condition first appeared in the literature in Pak et al. [39]. We also stress that this condition assumes ψ is static which will not be the case for an evolving bubble (caused by an evolving driver) or in a density gradient. In practice, the trapping condition is $\Delta\Psi \approx -1$ for $\gamma_\phi \gg 1$, but for moderate γ_ϕ it is possible for a particle to be trapped at a smaller potential difference it the particle is trapped with a high perpendicular momentum. For a particle in a pre-ionized plasma, we expect $\Psi_i = 0$ so that $\Delta\Psi = \Psi_f$ to be the actual trapping potential difference at the spot in the wake where the particle is accelerated to the phase velocity of the wake. For the case where a particle is created inside the wake through ionization we expect Ψ_i to be the value of the potential at the spot where the particle was created and we assume it is still born at rest. Since the particles are injected near the peak of the laser and near the transverse axis, then the initial wake potential can be a nonzero positive value. This means that the particle may be trapped with a smaller minimum in the trapping potential meaning that is easier to self-inject through ionization than in a preionized plasma. See Figures 2.2 and 2.3 for a demonstration of this difference in the trapping condition.

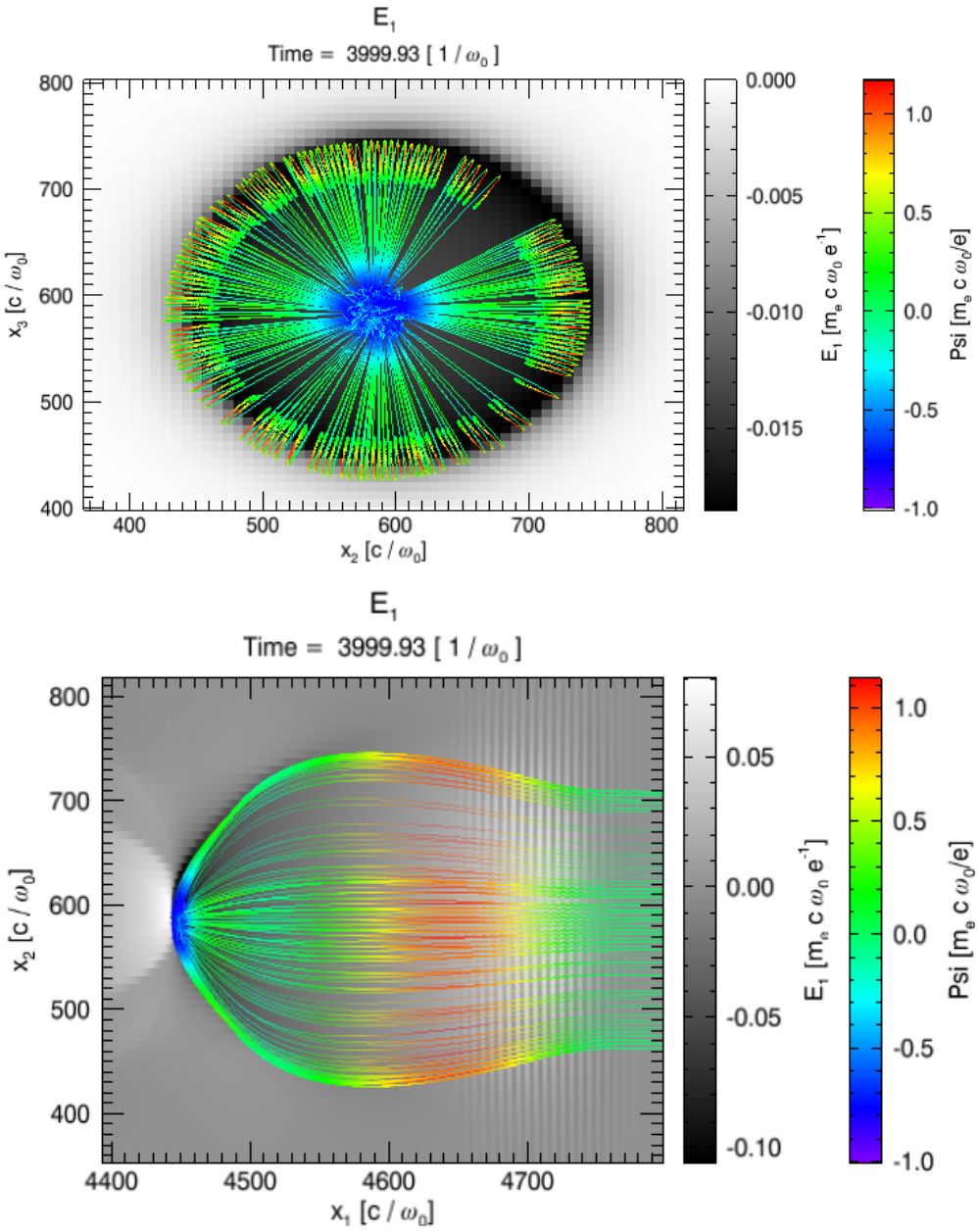

Figure 2.2: The 2D cross-section in x-y (top), and z-x (bottom), of the wake superimposed with the tracks of the particles in the pre-ionized plasma simulation, 0.5 mm into the plasma. The trapped particles undergo $\Delta\Psi \approx -1$.

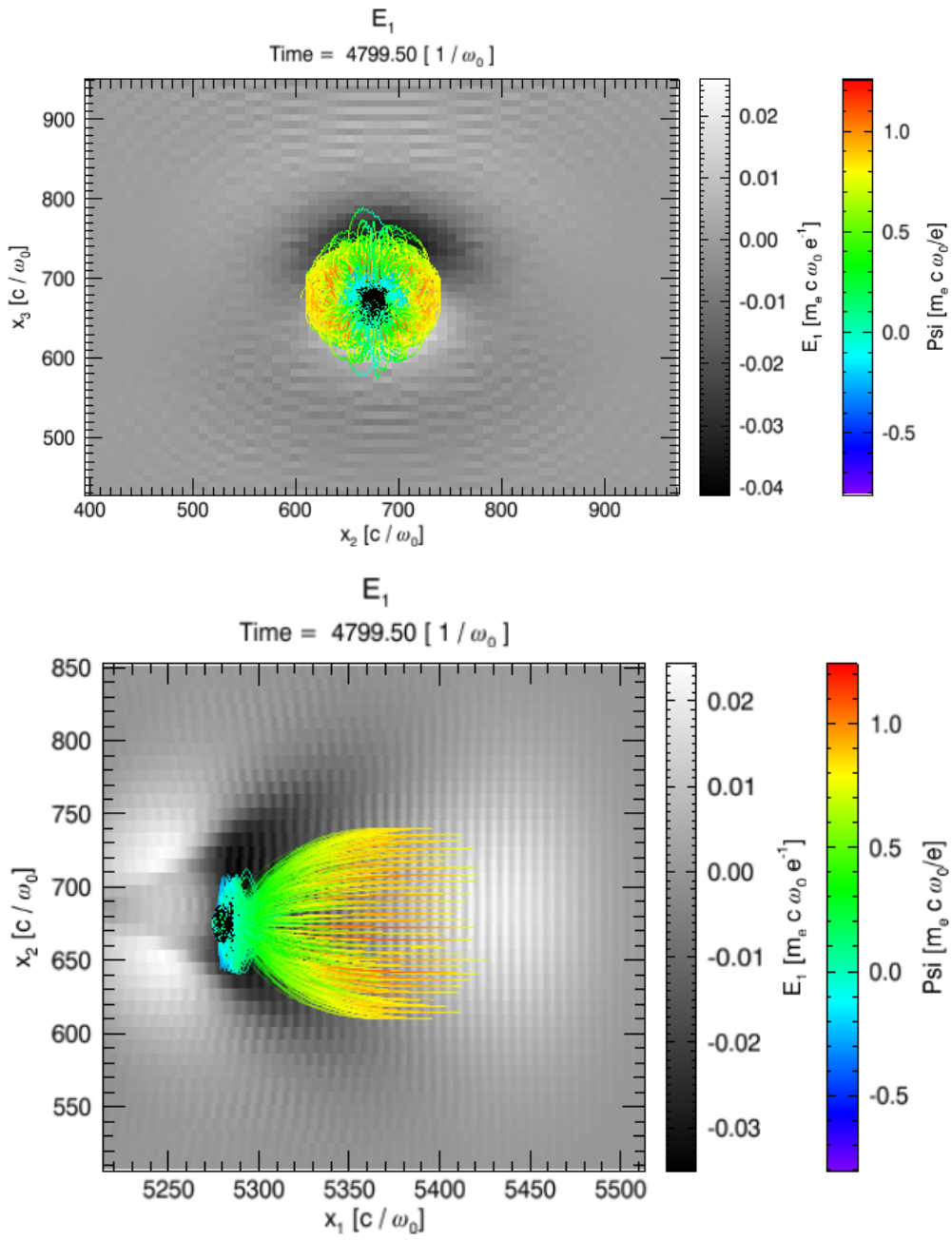

Figure 2.3: 2D cross-section of the wake superimposed with the tracks of the particles from the ionization-injection run. Although $|\Psi_f|$ is smaller, $\Delta\Psi \approx -1$.

CHAPTER 3

Implementation of a Quasi-3D Algorithm into the OSIRIS Simulation Framework

3.1 Introduction

Simulating laser wakefield acceleration (LWFA) in a nonlinear self-guided, self-injection regime is very challenging. The challenges arise because it is necessary to accurately model how a laser beam is self-guided and evolves (envelope and spectral content) as it creates a nonlinear plasma wave wakefield while propagating through long regions of tenuous plasmas , how the wakefield is formed and evolves, how electrons are self-injected into the wake, and how electrons are accelerated and focused as they get accelerated. These processes involve many nonlinear and relativistic processes which require fully kinetic (where the details and crossing of the trajectories of individual electrons matter) and relativistic. The simulation method of choice is therefore the particle-in-cell method. Particle-in-cell simulations are ubiquously used and well established for simulating not only plasma based acceleration but also in processes in fields ranging from magnetic fusion, inertial confinement fusion, and space and astrophysics. These simulations are conducted in one, two, and three dimensions. The two dimensional simulations are often conducted in cartesian "slab" geometry or r-z "cylindrical" geometry. While the two dimensional simulations can be very useful for carrying out parameter scans and illuminating physics, there are some physics problems in which three dimensional effects lead to both qualitative or quantitative differences. In addition, in some cases there can significant quantitative differences between 2D slab and 2D cylindrical simulations. This is the case when modeling LWFA or PWFA and the differences can be dramatic when studying the nonlinear wakefield regime.

In the nonlinear regime, the wake is excited by the space charge forces of an intense particle beam or the radiation pressure of an intense laser expelling all of the plasma electrons radially outward (as well as forward). The electrons are then pulled back by the space charge force from the resulting ion column. The amplitude of the space charge force of the ion column is different in 2D slab (the E field from a sheet of charge does not fall off with distance) as compared to 2D cylindrical geometries (the E field from a line of charge falls off as r^{-1}. Unlike a 2D slab code, a 2D r-z code can therefore provide an accurate representation of the geometric scaling factors for the wake excitation in the nonlinear blowout regime when there is azimuthal symmetry. It also has the correct the space charge force from a drive particle beam (PWFA) or a trailing (externally or self injected) beam so long as they are round. The self-injection process is also modeled more accurately in 2D r-z because the wake amplitude and geometrical convergence of particles to the axis is correct. The use of a 2D r-z code has been used very successfully when modeling PWFA. However, the use of an r-z code precludes hosing and the effect of asymmetric spot sizes of both the drive and trailing particle beams.

Unfortunately, it is not possible to use a standard 2D r-z code to model LWFA. The reason is simple. A linearly (or any linear combination of linear polarized lasers such as circularly or elliptically polarized) laser is not azimuthally symmetric in cylindrical geometry. A laser field (with an azimuthally symmetric spot size) that points in the $\hat{x}$ (or $\hat{y}$) direction is proportional to Re $\hat{r}e^{i\phi} + i\hat{\phi}e^{i\phi}$ (or Re $-i\hat{r}e^{i\phi} + \hat{\phi}e^{i\phi}$). Therefore, a linearly polarized laser is an m=1 mode in ϕ when decomposed into cylindrical coordinates. Therefore, only a radially polarized laser can be represented in a pure 2D r-z code.

Due to the computational resources needed to carry out three-dimensional simulations of beam or laser driven plasma based acceleration, numerous techniques and methods have been developed over the past 25 years for more efficiently modeling plasma-based acceleration. These include the moving window method [60], quasi-static methods [50, 61, 62], the ponderomotive guiding center (PGC) method for modeling laser propagation [50, 63], and the use of simulating the physics in Lorentz boosted frames [64, 65, 25, 66]. In some cases these methods are combined. For example, a combination of quasi-static field equations and

the ponderomotive guiding center approximation are used in QuickPIC[62, 61] to model laser wakefield acceleration.

In addition, each of these methods have advantages and disadvantages when compared to full PIC methods in the rest frame of the plasma. The quasi-static methods cannot accurately model self-injection, and the ponderomotive guiding center model can have difficulty modeling nonlinear laser-plasma interactions over pump-depletion distances (a method to avoid some of these difficulties was discussed in [67]). Despite the recent progress on understanding the numerical Cherenkov instability, there is still research left on the use of Lorentz boosted frames to model nonlinear regimes of laser wakefield acceleration [68, 69, 70]. In addition, parameter scans over plasma length are easier in the lab frame. Work continues on each of these methods.

Very recently [3], an algorithm was proposed that would allow modeling laser propagation with similar computational costs to an r-z code. In this algorithm the fields and currents are expanded into azimuthal harmonics (modes) where the amplitudes of each harmonic are complex and functions of r and z. This expansion is substituted into Maxwell's equations to generate a series of equations for the evolution of the complex amplitudes for each harmonic. In [3] the expansion was truncated at a maximum of $m = 3$. Recently, simulations with modes up to $m = 6$ were presented by Corde et al. [71]. The particles are pushed in 3D cartesian geometry and are then used to obtain the complex amplitudes for each harmonic of the current. In [3] the current deposition method did not conserve charge so a Marder's method [72] was used to maintain the accuracy of Gauss's law. The Marder's method is an approximation to the Boris correction [73, 74] in which a correction, $\mathbf{E_c}$ is added to an uncorrected field, $\mathbf{E}^{'}$ such that $\nabla \cdot (\mathbf{E}^{'} + \mathbf{E}_c) = \rho$. The correction to the field is defined as $\mathbf{E_c} = -\nabla\phi_c$ where $\nabla^2\phi_c = \nabla \cdot (\mathbf{E}) - \rho$. They also showed results for laser wakefield acceleration and found agreement with a full PIC code.

In this Chapter, we describe the implementation of such a truncated azimuthal Fourier decomposition (i.e., harmonic expansion) into the OSIRIS simulation framework. OSIRIS is a fully parallelized PIC finite-difference code that has been used in 1D, 2D, 3D geometries[2]. For 2D simulations a cartesian slab (xz) or a cylindrical (rz) geometry can be used. We have

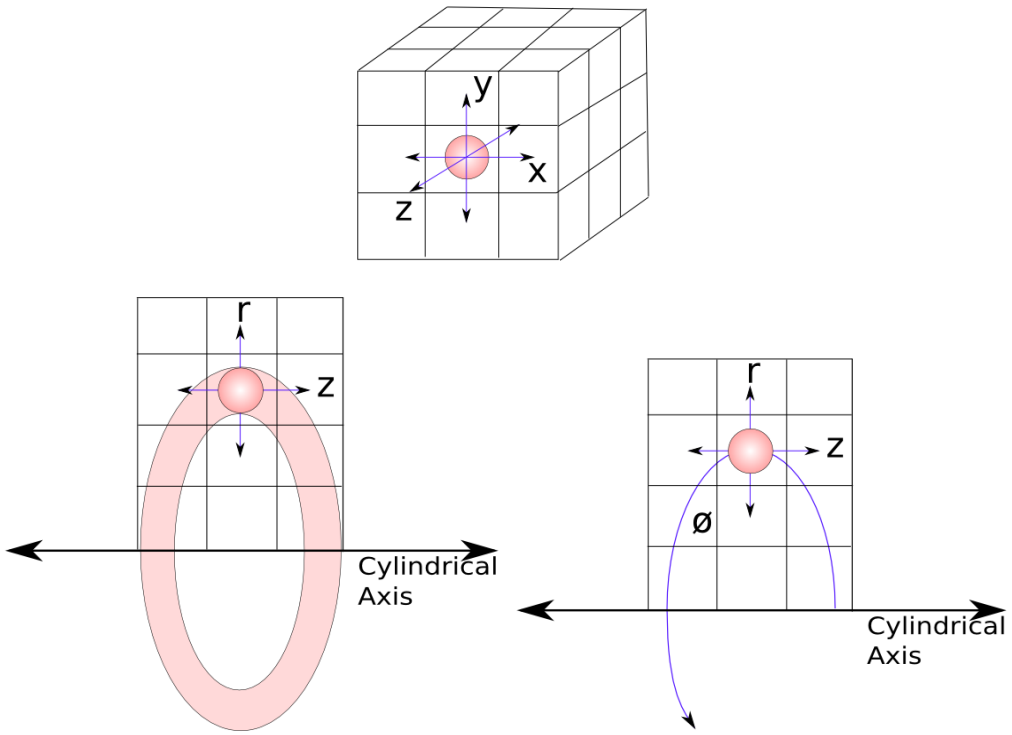

Figure 3.1: A traditional 3D Cartesian PIC simulation is depicted (top), where a particle moves about a electromagnetic field that is gridded in every direction of motion. A 2D Cylindrical PIC simulation (bottom left), is not gridded in ϕ, but the particles do not move in ϕ because they are rings. In a quasi-3D simulation (bottom right), the electromagnetic fields (whose azimuthal expansions are truncated) are gridless in ϕ, a direction about which a particle is free to move.

reused as much of the existing 2D r-z structure as possible. We view this algorithm as a hybrid between a traditional PIC method where quantities are defined on an r-z grid and a gridless method[75] in ϕ where quantities are expanded in global basis functions (e.g., Fourier modes) defined at all locations and the expansion is truncated (see Figure 3.1). This strategy of combining gridded and gridless algorithms is actually not new. For example, in the early 1980s Godfrey and collaborators developed IPROP[76, 77], which was capable of following an arbitrary number of azimuthal modes to study filamentation as well as hosing of high current electron beams propagating in the atmosphere.

In the implementation for OSIRIS an arbitrary number of harmonics can be kept. In

addition, OSIRIS uses a rigorous charge conserving current deposition for the PIC part. Therefore, we have used this as a starting point to develop a new current deposition scheme which conserves charge for each harmonic particle by particle. OSIRIS can also use higher order particle shapes so we have implemented this into the PIC part of the algorithm. For the gridless part we have used point particle shapes but have described how to extend this to higher order particle shapes. In addition, OSIRIS can model plasma wakefield acceleration and beam loading. This will illustrated through a few examples of such simulations in Chapter 4 using the new algorithm. We also note that this algorithm can be combined with the PGC as well as Lorentz boosted frame ideas for even more dramatic speed ups over full 3D simulations. Details for how to combine the azimuthal mode expansion and the Lorentz boosted frame have recently been described by P. Yu et al.[78].

In section 3.2 we will discuss the fundamentals of describing Maxwell's equations as a truncated expansion of equations for each azimuthal mode, the field equations that it follow from such a truncated expansion, and the boundary conditions of the fields on the cylindrical axis. In section 3.3 we describe the actual algorithm for the field solver, for the particle pusher, and the current deposit. A detailed derivation for the new rigorously charge conserving current deposition scheme that uses much of the existing current deposit in OSIRIS is included. The new current deposit appears to provide better simulation results than had been previously published.

3.2 Theory

3.2.1 Electromagnetic fields expressed in azimuthal harmonics

We begin by expanding the electromagnetic fields and the charge (ρ) and current densities ($\mathbf{J}$), expressed in cylindrical coordinates, into a Fourier series in ϕ,

$$\mathbf{F}(r,z,\phi) = \Re\left\{\sum_{m=0} \mathbf{F}^m(r,z)e^{im\phi}\right\} \tag{3.1}$$

$$= \mathbf{F}^0(r,z) + \Re\{\mathbf{F}^1\}\cos(\phi) - \Im\{\mathbf{F}^1\}\sin(\phi) \tag{3.2}$$
$$+ \Re\{\mathbf{F}^2\}\cos(2\phi) - \Im\{\mathbf{F}^2\}\sin(2\phi)$$
$$+ \cdots.$$

Note that the amplitudes of each Fourier harmonic (for all fields) $\mathbf{F}^m$ are complex, whereas the physical fields they are describing, $\mathbf{F}$, are real. As shown in [3] a major advantage of this expansion is that it allows modeling a linearly polarized laser with only the first harmonic. Consider a laser with a polarization angle ϕ_0 and amplitude E_0,

$$\mathbf{E}(r,z,\phi) = E_0\cos(k_z z - \omega t)\cos(\phi_0)\hat{x} + E_0\cos(k_z z - \omega_0)\sin(\phi_0)\hat{y} \tag{3.3}$$

$$\mathbf{B}(r,z,\phi) = -E_0\cos(k_z z - \omega t)\sin(\phi_0)\hat{x} + E_0\cos(k_z z - \omega_0)\cos(\phi_0)\hat{y}, \tag{3.4}$$

and let $a(r,z) = E_0\cos(k_z z - \omega t)$. Decomposing the cartesian unit vectors into cylindrical coordinates unit vectors then gives the radial and azimuthal field components which will have $\sin(\phi)$ and $\cos(\phi)$ terms. By equating these fields to the expansion in Equation 3.1, it can be easily shown that these fields are represented by the $m = 1$ terms

$$E_r^1 = a(r,z)[\cos(\phi_0) - i\sin(\phi_0)] \tag{3.5}$$

$$E_\phi^1 = a(r,z)[\sin(\phi_0) + i\cos(\phi_0)] \tag{3.6}$$

$$B_r^1 = a(r,z)[-\sin(\phi_0) - i\cos(\phi_0)] \tag{3.7}$$

$$B_\phi^1 = a(r,z)[\cos(\phi_0) - i\sin(\phi_0)]. \tag{3.8}$$

Circularly and elliptically polarized lasers can obtained by adding two linearly polarized lasers with equal or non equal amplitudes and phase and polarization offset by $\pi/2$.

The time-evolution of electromagnetic fields are described by Faraday's and Ampere's equations (effectively written in normalized units),

$$\frac{\partial \mathbf{B}}{\partial t} = -\nabla \times \mathbf{E}, \tag{3.9}$$

$$\frac{\partial \mathbf{E}}{\partial t} = \nabla \times \mathbf{B} - \mathbf{J}. \tag{3.10}$$

Substituting the expansions for each field into these equations, we obtain the following equations for each mode, m,

$$\frac{\partial B_r^m}{\partial t} = -\frac{im}{r} E_z^m + \frac{\partial E_\phi^m}{\partial z} \tag{3.11}$$

$$\frac{\partial B_\phi^m}{\partial t} = -\frac{\partial E_r^m}{\partial z} + \frac{\partial E_z^m}{\partial r} \tag{3.12}$$

$$\frac{\partial B_z^m}{\partial t} = -\frac{1}{r}\frac{\partial}{\partial r}(r E_\phi^m) + \frac{im}{r} E_r^m \tag{3.13}$$

$$\frac{\partial E_r^m}{\partial t} = \frac{im}{r} B_z^m - \frac{\partial B_\phi^m}{\partial z} - J_r^m \tag{3.14}$$

$$\frac{\partial E_\phi^m}{\partial t} = \frac{\partial B_r^m}{\partial z} - \frac{\partial B_z^m}{\partial r} - J_\phi^m \tag{3.15}$$

$$\frac{\partial E_z^m}{\partial t} = \frac{1}{r}\frac{\partial}{\partial r}(r B_\phi^m) - \frac{im}{r} B_r^m - J_z^m \tag{3.16}$$

We use different conventions for the coordinate system than that used in reference, [3], but the idea is identical. In vacuum, each mode evolves independently of every other mode. In addition, for a linear plasma response there is also no coupling between modes because under this limit each harmonic for the current is only driven by the same harmonic for the fields. However, there is coupling between harmonics due to the macroparticle motion, i.e., nonlinear currents. The finite difference expression of these equations and associated complications near the r=0 axis will be discussed in Section 3.3.

3.2.2 Symmetry properties of the axis

When implementing the field equations expressed in cylindrical coordinates one inevitably comes across singularities at the $r = 0$ axis. The exact location of the singularities will depend on the layout of the grid values, but you can resolve issues from the singularities using symmetry-based arguments. As pointed out in ref [3], G.S. Constantinescu and S.

K. Lele [79] discuss in detail how the field values behave at the cylindrical, $r = 0$, axis. To summarize, for any scalar and cartesian fields (E_z, B_z) only the $m = 0$ mode is non-vanishing on the r=0 axis (this was already used in OSIRIS). On the other hand, for cylindrical field components $(E_r, B_r, E_\phi, B_\phi)$, only the $m = 1$ mode is non-vanishing on the r=0 axis. These symmetry properties can also be inferred from rather simple arguments. Away from the origin, each azimuthal harmonic for the components of the cylindrical fields is determined by the value of the fields at all angles (it is global). However, at the origin, each harmonic is determined only from the fields at the origin (local). It is then easier to visualize the fields at the origin in cartesian coordinates. At the origin any field (e.g., $\vec{E}$) can be written in cartesian coordinates as $\hat{x}E_x + \hat{y}E_y + \hat{z}E_z$ where the components of the field do not depend on ϕ. Therefore, to determine dependence of this vector in cylindrical coordinates, one only has to decompose the unit vectors. The unit vector, $\hat{z}$, has no ϕ dependence. Therefore only the m=0 mode for E_z is non zero at the origin. On the other hand, the unit vectors $\hat{r}$ and ϕ do depend on ϕ, and when decomposed into $\hat{r}$ and $\hat{\phi}$ it is straightforward to show that they only have m=1 components. Therefore, only the m=1 mode for E_r and E_{phi} are non zero at the origin. The same argument holds for $\vec{B}$ and $\vec{J}$.

3.2.3 Boundary conditions for fields and particles

Currently, we use conducting boundary conditions for the fields, and an absorbing boundary condition for the particle at $r = r^{\max}$. We also use a moving window in the z direction. In the future, more boundary conditions will be added in both r and z, including the ability to launch a laser from a wall or a moving antenna. Recently, PML boundary conditions at r=r_{max} have been implemented into OSIRIS [80].

3.3 Algorithm

The truncated azimuthal mode expansion has been incorporated into the OSIRIS simulation framework. The electromagnetic fields are calculated on $2m + 1$ separate 2D grids; one grid is used to represent the cylindrically symmetric (and real) 0^{th} order mode, while the

rest represent the real and imaginary components of the higher order modes. Each field mode is advanced in accordance to Maxwell Equations 3.11-3.16, whose implementation will be discussed in more detail in Section 3.3.1. The macroparticle values (x, y, z, p_x, p_y, p_z) are stored in 3D coordinates. When the fields were interpolated onto the particles, the mode contributions from each grid are added together as per Equation 3.1, and converted into Cartesian coordinates. The particles were then advanced according to the relativistic equations of motion,

$$\frac{d}{dt}\mathbf{P} = q(\mathbf{E} + (\mathbf{v}/c) \times \mathbf{B}), \tag{3.17}$$

$$\frac{d}{dt}\mathbf{x} = (1/m\gamma)\mathbf{P}, \tag{3.18}$$

where q and m are the macroparticle charge and mass, respectively. Using the motion of the particles, the current can be deposited onto each of the $2m + 1$ 2D grids particle by particle using a charge-conserving deposition scheme described in detail in Section 3.3.2.

3.3.1 Field solver

The equations for each harmonic that follow directly from Maxwell's Equations 3.11-3.16 are discretized over a uniform grid defined on the Yee Lattice [81]. Due to the staggering required for second order accuracy, the fields with the same index lie at different positions with respect to the axis, as is shown in Figure 3.2. Some field values reside exactly on the cylindrical $r = 0$ axis, which in this case will cause a singularity when solving Equations 3.13 and 3.14. It is important to note here that the location of the axis in our simulation is different from that of Lifschitz [3], where the equations for B_r and E_z present a singularity. Although the singularities occur for different field components, the logic with which we resolve these issues are effectively the same.

As discussed in Section 3.2.2, the axial fields are usually zero. The only axial fields we need to solve for are B_z^0, E_r^1, and B_ϕ^1; the last of which does not pose a singularity. We use the integral form of Faraday's Law to find B_z^0 on the axis by integrating $\oint \mathbf{E} \cdot d\mathbf{l}$ in a loop of

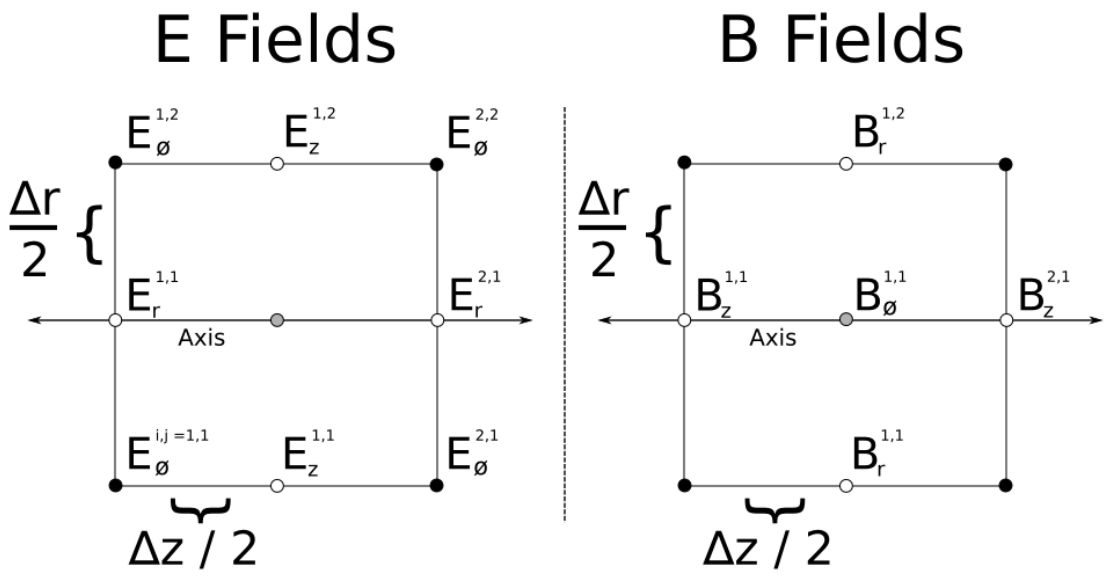

Figure 3.2: The layout of the grid for the field components in relation to the cylindrical axis. The grid indices associated with the field point is indicated on the superscript. The E_r, B_z and B_ϕ lie on the cylindrical axis for the axial cell.

radius $\Delta r/2$ around the axis, resulting in

$$\begin{aligned} \frac{\partial B}{\partial t} &= \oint d\mathbf{l} \cdot \mathbf{E}, \\ \pi \left(\frac{\Delta r}{2}\right)^2 \frac{B^{0,i,1}_{z,\text{new}} - B^{0,i,1}_{z,\text{old}}}{\Delta t/2} &= 2\pi \left(\frac{\Delta r}{2}\right) E^{0,i,2}_{\phi,,\text{old}}, \\ B^{0,i,1}_z &= B^{0,i,1}_z - 4\frac{\Delta t}{2} \times \frac{E^{0,i,2}_\phi}{\Delta r}, \end{aligned} \tag{3.19}$$

where it is assumed that the terms on the right hand side of the equations refer to old field quantities, and the terms on the right hand side refer to the new, solvable field quantities. The time step is divided in half to get $\Delta t/2$ because in OSIRIS, due to the leap frog scheme, **B** fields are updated each half time step. This is the same method that was used in the 2D Cylindrical simulation that was already implemented in OSIRIS in some parts of the code. As for the $m = 1$ mode, we use the fact that

$$\lim_{r\to 0} \frac{im}{r} B^m_z = im \frac{\partial B^m_z}{\partial r},$$

to define

$$\frac{im}{r}B_z^{m,i,1} = im\left.\frac{\partial B_z}{\partial r}\right|^{r=0} = im\frac{B_z^{m,i,2}}{\Delta r},$$

where the fact that $B_z^{m,i,1} = 0$ was used. We then obtain a nonsingular expression for $\frac{\partial E_r^1}{\partial t}$ at the axis,

$$\frac{\partial E_r^{m=1,i,j=1}}{\partial t} = i\frac{1}{\Delta r}B_z^{1,i,2} - \frac{1}{\Delta z}\left(B_\phi^{1,i,1} - B_\phi^{1,i-1,1}\right) - J_r^1, \tag{3.20}$$

where $j = 1$ is the radial index of the cell that sits on the axis.

3.3.2 Charge conserving current deposition algorithm

In OSIRIS Gauss's law is maintained by using a rigorously charge conserving deposit. For example, in 3D Cartesian geometry the particles have a shape

$$S_x(x - x_p(t))S_y(y - y_p(t))S_z(z - z_p(t)),$$

and the cell corners (where the charge density is defined) are defined at x_g, y_g, z_g. The charge density at a time t at the grid locations is therefore,

$$\rho = S_x(x_g - x_p(t))S_y(y_g - y_p(t))S_z(z_g - z_p(t)).$$

The current is defined at different locations (the cell faces) and is defined such that

$$\frac{\overline{\partial}}{\partial t}\rho + \overline{\nabla}\cdot\mathbf{J} = 0,$$

where $\bar{}$ indicates a finite difference representation of the derivative, e.g.,

$$\left.\frac{\overline{\partial}}{\partial t}\rho\right|^{t+\Delta t/2} = \frac{1}{\Delta t}\left[S_x(x_g - x_p(t+\Delta t))S_y(y_g - y_p(t+\Delta t))S_z(z_g - z_p(t+\Delta t))\right.$$
$$\left. - S_x(x_g - x_p(t))S_y(y_g - y_p(t))S_z(z_g - z_p(t))\right]. \tag{3.21}$$

There is not a unique solution for a $\mathbf{J}$ such that $\frac{\overline{\partial}}{\partial t}\rho + \overline{\nabla}\cdot\mathbf{J} = 0$ as one can always add the curl of a vector to one solution. To determine $\mathbf{J}$, OSIRIS implements a version of the Density Decomposition method described by Esirkepov [82], which is the generalization of the method developed by Villasenor and Buneman [83] for arbitrary particle shapes. In

the method of Villasenor and Buneman, linear particle shapes are assumed. If the particle motion stays within a cell and moves from x_i, y_i to x_f, y_f in one time step, this method can be viewed as averaging the current contribution over all paths that are decomposed into segments that include motion orthogonal to a cell face. If the particle motion crosses cell boundaries, then the motion is split into segments lying entirely inside individual cells, and the method is applied to each individual segment.

Extending the charge conserving current deposit to 2D r-z is relatively straight forward because the cells are still rectangular. In this case, one needs to recognize that $S_r(r - r_p(t))$ includes a $1/r_g$ term. Viewed another way each simulation particle represents a fixed amount of charge so as it moves closer to the $r = 0$ axis the charge density must increase. The J_ϕ component is simple to define in such a code as it is simply $\rho v_{\phi,p}$, where $v_{\phi,p}$ is the velocity of the particle in the ϕ direction.

On the other hand, it is not straightforward to define J_ϕ in the new algorithm. In particular, for the $m = 0$ harmonic the standard method works but for the $m \neq 0$ harmonics more thought is needed. However, as we show next, J_ϕ^m can be determined using the $J_\perp$ from existing charge conserving deposition scheme for the m=0 mode. We begin from the definition of the particle shape in cylindrical coordinates.

$$S \equiv S_r(r - r_p(t))S_\phi(\phi - \phi_p(t))S_z(z - z_p(t))$$

so the charge density is QS, where Q is the charge of a simulation particle. We also note that S_r has a $1/r_g$ factor so that

$$\int drrd\phi dzS = 1.$$

It should be noted here that in the simulation grid the charge is defined on discrete grid points. For b-splines, if the integral over the charge density is unity, then the discrete sum of the charge over the grid points is also unity. The particle positions are known at full integer values of time, $t + \Delta tn$, and the particle momentum (and velocity) are known at half integer values of time, $t + \Delta t(n + \frac{1}{2})$. In addition, the currents are only defined on the r-z grid, i.e., there is no grid in ϕ.

Next, we look for solutions for $\mathbf{J}$ that satisfy the finite difference operator version of the continuity equation

$$\begin{aligned}\frac{\overline{\partial}}{\partial t}\rho\bigg|^{n+\frac{1}{2}} &= \sum_p Q_p \left[S_r(r-r_p^{n+1})S_\phi(\phi-\phi_p^{n+1})S_z(z-z_p^{n+1})\right.\\ &\qquad\qquad \left. - S_r(r-r_p^{n})S_\phi(\phi-\phi_p^{n})S_z(z-z_p^{n})\right]\\ &= -\overline{\nabla}\cdot\mathbf{J}^{n+\frac{1}{2}}. \end{aligned} \tag{3.22}$$

where Q_p is the charge associated with the particle p. For simplicity $Q_p = 1$ for the rest of this derivation. The next step is to expand S_ϕ in global basis functions (azimuthal harmonics),

$$S_\phi(\phi-\phi_p) = \sum_m S_{\phi,m}(\phi_p)e^{im\phi}, \tag{3.23}$$

where

$$S_{\phi,m} \equiv \int_0^{2\pi} \frac{d\phi'}{2\pi} e^{-im\phi} S_\phi(\phi'-\phi_p).$$

If $S_\phi \equiv \delta(\phi-\phi_p)$ then $S_{\phi,m} = \frac{1}{2\pi}e^{-im\phi_p}$. In addition, ρ and $\mathbf{J}$ defined on the r-z grid are expanded in azimuthal harmonics

$$\begin{pmatrix}\rho\\ \mathbf{J}\end{pmatrix} = \sum_m \begin{pmatrix}\overline{\rho}_m(r_g,z_g,t)\\ \overline{\mathbf{J}}_m(r_g,z_g,t)\end{pmatrix} e^{im\phi}, \tag{3.24}$$

where the $_g$ refers to a quantity defined only on the grid. The continuity equation can be written as

$$\frac{\overline{\partial}}{\partial t}\rho + \overline{\nabla}_\perp\cdot\mathbf{J}_\perp + \frac{1}{r}\frac{\partial}{\partial\phi}J_\phi = 0, \tag{3.25}$$

where $\perp$ refers to the r-z plane. Substituting Equations 3.23 and 3.24 into Equation 3.25 gives

$$\begin{aligned}\sum_m e^{im\phi}\Bigg\{ &\sum_p \frac{1}{\Delta t}\left[S_r(r_g-r_p^{n+1})S_{\phi,m}(\phi_p^{n+1})S_z(z-z_p^{n+1})\right.\\ &\qquad\qquad \left. - S_r(r_g-r_p^{n})S_{\phi,m}(\phi_p^{n})S_z(z-z_p^{n})\right]\\ &+ \overline{\nabla}_\perp\cdot\overline{\mathbf{J}}_{\perp,m}^{n+\frac{1}{2}} + \frac{im}{r}\overline{J}_{\phi,m}^{n+\frac{1}{2}}\Bigg\} = 0 \end{aligned} \tag{3.26}$$

We next recognize that by definition, for each particle

$$\overline{\rho} = \sum_m \overline{\rho}_m e^{im\phi}, \quad \text{and} \qquad\qquad \overline{\rho}_m = \overline{\rho}_0 S_{\phi,m}, \tag{3.27}$$

where $\overline{\rho}_0$ is the charge for one particle on the r-z grid for the $m = 0$ mode (recall $S_{\phi,0} = 1$ by normalization). Likewise

$$\overline{\mathbf{J}}_\perp = \sum_m \overline{\mathbf{J}}_{\perp,m} e^{im\phi}, \quad \text{and} \qquad\qquad \overline{\mathbf{J}}_{\perp,m} = \overline{\mathbf{J}}_{\perp,0} S_{\phi,m} \tag{3.28}$$

in the continuous time limit. We next show that using these definitions and a $\overline{\mathbf{J}}_{\perp,0}$ defined to conserve charge for the m=0 mode (this is already calculated in the r-z version of OSIRIS) leads to an expression for $\overline{J}_\phi$. Substituting these expressions into Equation 3.26 gives for each m and p in the sum

$$\begin{aligned}\frac{1}{\Delta t}\left[S_r(r_g - r_p^{n+1}) S_{\phi,m}(\phi_p^{n+1}) S_z(z_g - z_p^{n+1}) - S_r(r_g - r_p^n) S_{\phi,m}(\phi_p^n) S_z(z_g - z_p^n)\right] \\ + S_{\phi,m}(\phi_p^{n+\frac{1}{2}}) \overline{\nabla}_\perp \cdot \overline{\mathbf{J}}_{\perp,0}^{n+\frac{1}{2}} + \frac{im}{r} \overline{\mathbf{J}}_{\phi,m}^{n+\frac{1}{2}} = 0.\end{aligned} \tag{3.29}$$

By definition $\frac{\overline{\partial}}{\partial t}\overline{\rho}_0 + \overline{\nabla}_\perp \cdot \overline{\mathbf{J}}_{\perp,0} = 0$, so we are left with

$$\begin{aligned}\overline{J}_{\phi,m}^{n+\frac{1}{2}} = i\frac{1}{\Delta t}\frac{r}{m}\Big\{S_r(r_g - r_p^{n+1}) S_z(z_g - z_p^{n+1}) \left[S_{\phi,m}(\phi_p^{n+1}) - S_{\phi,m}(\phi_p^{n+\frac{1}{2}})\right] \\ - S_r(r_g - r_p^n) S_z(z_g - z_p^n) \left[S_{\phi,m}(\phi_p^n) - S_{\phi,m}(\phi_p^{n+\frac{1}{2}})\right]\Big\},\end{aligned} \tag{3.30}$$

For $S_\phi = \delta(\phi - \phi_p)$ we have $S_{\phi,m} = \frac{1}{2\pi} e^{-im\phi_p}$. We then define $\overline{\phi}_p \equiv \frac{\phi_p^{n+1} + \phi_p^n}{2}$ and $\Delta\phi_p \equiv \phi_p^{n+1} - \phi_p^n$, to obtain the result we now use in the new algorithm OSIRIS uses for each particle,

$$\begin{aligned}\overline{J}_{\phi,m} = i\frac{r}{m}\frac{1}{\Delta t}\frac{e^{-im\overline{\phi}_p}}{2\pi}\Big[S_r(r_g - r_p^{n+1}) S_z(z_g - z_p^{n+1}) \left(e^{im\frac{\Delta\phi_p}{2}} - 1\right) \\ - S_r(r_g - r_p^n) S_z(z_g - z_p^n) \left(e^{-im\frac{\Delta\phi_p}{2}} - 1\right)\Big],\end{aligned} \tag{3.31}$$

where the particle shapes in r and z are still general. Currently, OSIRIS implements linear, and quadratic interpolation for the new algorithm. The treatment of the current at the boundary is a simple extension of what has already been implemented in the pure r-z version of the OSIRIS framework. Due to the finite size of the particles, some current is deposited in the guard cells located across the $r = 0$ axis[1]. Therefore, due to the symmetry of the

[1]Negative values of r have no physical meaning. The guard cells in r actually correspond to positive values at r but with ϕ rotated by π.

azimuthal modal geometry, we can merely 'fold' these values for the current into the physical cells with $r > 0$. At each time step ($J^{m,i,j=0,1,1}$ is added to $J^{0,1,2}$, $J^{0,1,0}$ is added to $J^{0,1,3}$, and so on).

3.3.3 Complex Exponentials

When evaluating expressions like Equation 3.1 and 3.31, you need to evaluate the complex exponential $e^{im\phi}$. The particle variables are stored in Cartesian coordinates, and nowhere in the simulation is ϕ directly stored or calculated. In addition, evaluating trigonometric functions will be computationally inefficient. Instead, we use double and triple angle formulas to obtain these values up to $m = 4$,

$$e^{i\phi} = (x + iy)/r \tag{3.32}$$

$$e^{i2\phi} = ((x^2 - y^2) + 2ixy)/r \tag{3.33}$$

$$e^{i3\phi} = (4x^3/r^3 - 3x/r) - i(y^3/r^3 - 3y/r) \tag{3.34}$$

$$e^{i4\phi} = ((x^2 - y^2)^2 - 4x^2y^2)/r^4 + 4ixy(x^2 - y^2)/r^4. \tag{3.35}$$

This same optimization is used by Lifschitz [3]. In order to calculate $e^{-im\phi}$ one only needs to swap the sign of the imaginary part. One may extend this method to an arbitrary number of modes using the exponential relation $e^{im\phi} = e^{i\phi} \times e^{i(m-1)\phi}$, which is what is done in OSIRIS to capture any number of modes specified by the user.

3.3.4 Virtual Particle Method

As mentioned in Section 3.3.2, if the particle motion crosses cell boundaries, then the motion is split into segments lying entirely inside individual cells, and the rigorous charge conserving current deposition scheme is applied to each individual segment. This method, called the virtual particle method [83], is more accurate than a method which does not break up the path of the particles, since it approximates the path more closely. An advantage of the current deposition method described in Section 3.3.2 is that the current deposited in the higher modes is the current deposited in the $m = 0$ mode times a phase factor, which

happens to be $e^{-im\bar{\phi}_p}$ for the current in the r and z directions, with an additional function of $e^{-im\Delta\phi/2}$ for the z direction. Because of the way we calculate the phase factors in OSIRIS (See Section 3.3.3) we never calculate ϕ directly but rather calculate the phases from position values in x and y. Therefore we must find out the final and initial (x, y) positions for each virtual particle, which which we can extrapolate the values for $e^{-im\bar{\phi}_p}$ and $e^{-im\Delta\phi/2}$ for each mode (in fact, in the current implementation of OSIRIS, we calculate $J_{\phi,m}$ by multiplying out the exponentials in $e^{im\bar{\phi}_p}$ and $e^{im\Delta\phi/2}$ so that we merely calculate the exponentials $e^{im\phi_p^{n+1}}$ and $e^{im\phi_p^n}$ in the manner described in Section 3.3.3).

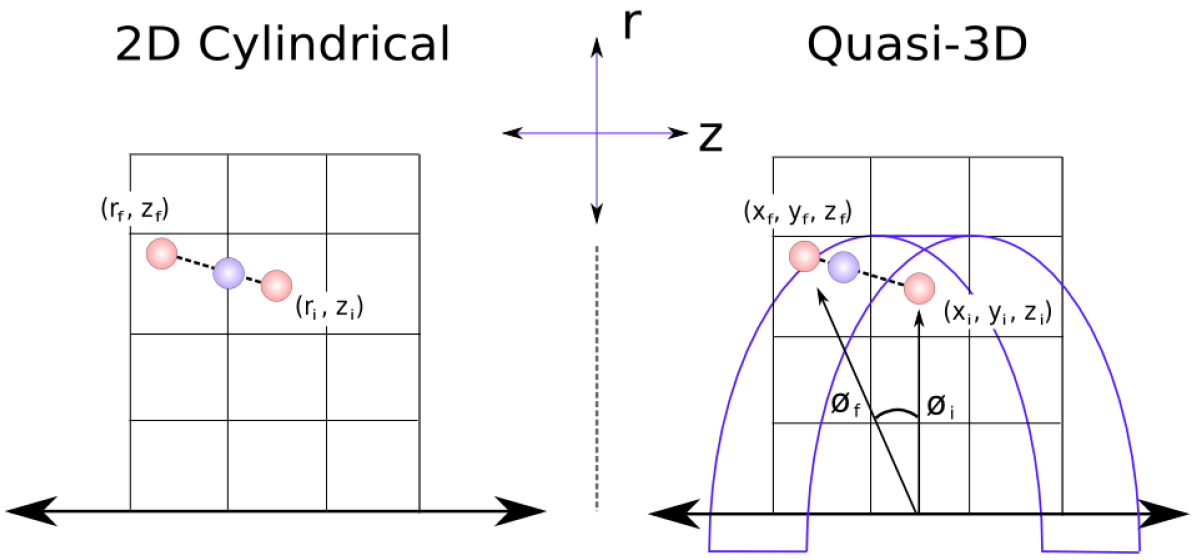

Figure 3.3: An illustration of the differences in virtual particle splitting in 2D cylindrical (left) and quasi-3D (right) geometries. In 2D cylindrical geometry, one must simply calculate the point where the particle crosses a specific value in r or z. In the quasi-3D geometry, one effectively has to calculate the location where the particle crosses the rectilinear toroidal boundary, given that a point particle travels in a straight line in Cartesian space.

The cell boundaries are located at regular fixed intervals. Calculating the position of the boundary that the cell crosses is therefore trivial, and one must then use that knowledge to calculate which point along the boundary the particle has crossed. For example, if a particle crosses a vertical boundary along a fixed value of z, one solves for the r position of the virtual particle given its known value. In the 2D Cylindrical geometry, where the particle positions

are stored in cylindrical coordinates (z, r), it is only necessary to solve, given initial positions (z_i, r_i) and final positions (z_f, r_f), the algebraic line equation,

$$\frac{z - z_i}{z_f - z_i} = \frac{r - r_i}{r_f - r_i}, \tag{3.36}$$

where the particle crosses each cell boundary. Given a known position in z where the boundary has been crossed, one may solve for the position in r, and vice versa.

In the quasi-3D geometry this becomes more complicated, as the cells are gridded in r-z but the particle positions are stored in (x, y, z) (See Figure 3.3). Naturally, since the initial and final r positions are easily calculable (due to boundaries being located at fixed intervals in r), it is possible to calculate the intermediate virtual particle z positions of each virtual particle in the same manner as a 2D Cylindrical code. After solving the line equation $r = \text{slope} \times z + \text{Const.}$ for where the particle's z position where it crosses a boundary in r, we can find the initial and final x-y positions of the virtual particles as well. After having calculated the z positions of each virtual particle with Equation 3.36 , one may solve another line equation,

$$\frac{z - z_i}{z_f - z_i} = \frac{x - x_i}{x_f - x_i} = \frac{y - y_i}{y_f - y_i}, \tag{3.37}$$

to find the initial and final (x, y) positions of the virtual particles.

Equation 3.37 has no singular solution where $z_f - z_i = 0$, which poses a problem when a particle crosses the cell boundary in r while it remains motionless in z, therefore a different set of equations must be solved for this specific case. Specifically, we must solve, given a position in r, the equations

$$r^2 = x^2 + y^2, \text{ and}$$
$$\frac{x - x_i}{x_f - x_i} = \frac{y - y_i}{y_f - y_i}.$$

We may solve for the value of x given the line equation, and solve for its square, giving

$$x = \alpha(y - y_i) + x_i,$$
$$x^2 = \alpha^2(y - y_i)^2 + 2\alpha(y - y_i)x_i + x_i^2,$$

where $\alpha \equiv (x_f - x_i)/(y_f - y_i)$. We can plug this expression into $x^2 + y^2 = r^2$ in order to solve for a quadratic expression of y in terms of r,

$$
\begin{aligned}
0 &= Ay^2 + By + C, \text{ where} \\
A &\equiv \alpha^2 + 1, \\
B &\equiv 2\alpha x_i - 2\alpha^2 y_i, \\
C &\equiv \alpha^2 y_1^2 - 2\alpha x_i y_i + x_i^2 - r^2.
\end{aligned}
\tag{3.38}
$$

After solving for y we may easily solve for x via $x = \sqrt{r^2 - y^2}$. If $y_f - y_i = 0$ (resulting in a singularity in the above method), we may re-derive Equation 3.38 as an quadratic expression of x, and subsequently solve for y. In our implementation in OSIRIS, the solution that is closest to the initial particle position is automatically picked after solving the quadratic equation $y = (-B \pm \sqrt{B^2 - 4AC})/2A$ (or the equivalent equation for x). Since a boundary has been crossed in r, there is either a nonzero difference in x or in y, and all possibilities of singular equations have been eliminated. Fortunately, this specific case of particle motion rarely happens, and so these extra calculations do not slow down the simulation significantly. With the initial and final positions of each virtual particle known in 3D Cartesian coordinates, it is possible to calculate the current deposited by each virtual particle.

CHAPTER 4

Validity of the Quasi-3D OSIRIS Algorithm

4.1 Introduction

In this chapter we present examples from simulations using the new quasi-3D PIC algorithm. We henceforth refer to it as a quasi 3D algorithm. We present simulation results for a laser wakefield accelerator (LWFA), a plasma wakefield accelerator (PWFA), and a beam loading case with a LWFA driver (combining the laser and beam propagation capabilities) respectively. In [3] only an LWFA example was given. We also demonstrate the degree to which Gauss' law is conserved with the new current deposit algorithm. The new algorithm has many more potential applications than LWFA/PWFA and we will discuss some in the conclusions and directions for future work section. For the quasi-3D r-z simulations, we typically use 2 particles per cell in the r-z directions, and 8 or 16 particles distributed evenly over $0 \leq \phi < 2\pi$ (The particles are distributed along spokes at each z). The former can be considered as 16 particles per cell when comparing to the speed up from the full 3D simulation. The effect of the particle resolution in ϕ will be discussed for some of the examples, but for these simulations 8 particles over 2π radians appeared to be enough to capture the physics. We note that different methods for initiating the particles can be considered and we leave this for future work.

For the LWFA simulations, we model the example given in Lu et al., [4]. In this example a circularly polarized $200TW$, $30fs$, $0.8\mu m$ laser pulse with a spot size of $19.5\mu m$ propagates through a fully ionized plasma of density $n = 1.5 \times 10^{18} cm^{-3}$. The laser has a normalized vector potential of magnitude $a_0 = 4$. In ref. [4], it was found using full 3D OSIRIS simulations that such a laser could generate an ultrashort ($10fs$) self-injected mono-energetic

bunch with an energy centered at $1.5GeV$. We have reproduced the 3D simulation for this chapter using quadratic splines (linear splines were used in [4]).

In section 4.2 we present data from quantitative tests on how well charge is conserved and equivalently how well Gauss's Law is satisfied. We showed that charge is conserved to the roundoff error of the double precision floating point number - the precision to which OSIRIS operates in these examples. In section 4.3 we will further bench mark the quasi-3D algorithm by comparing LWFA simulation results with a full 3D Cartesian simulation with comparable simulation parameters. In section 4.4 additional example simulations are presented in which externally injected trailing beam of electrons are placed in the nonlinear wake excited by a laser. In section 4.5 PWFA simulation results are presented which demonstrate that particle beam hosing can be studied, thereby showing that higher mode asymmetrical effects can be studied in the quasi-3D geometry.

4.2 Charge Conservation Tests

We start by checking the degree to which charge, i.e., Gauss' law is conserved. To test the effectiveness of the deposition scheme in Equation 3.31, we need to carefully examine Gauss' law for the new algorithm. We begin by expanding Gauss' law as per Equation 3.1,

$$\nabla \cdot \mathbf{E} - \rho = \Re \left\{ \sum_m \nabla \cdot \left[\mathbf{E}^m(r,z) e^{im\phi} \right] - \sum_m \rho^m(r,z) e^{im\phi} \right\} = 0, \tag{4.1}$$

$$\implies \nabla_\perp \cdot \mathbf{E}^m + i\frac{m}{r} E_\phi - \rho^m = \frac{1}{r}\frac{\partial}{\partial r}(rE_r) + \frac{\partial E_z}{\partial z} + i\frac{m}{r}E_\phi - \rho^m = 0. \tag{4.2}$$

This means that the charge of each mode must be conserved independently from each other mode, and that the $\nabla \cdot \mathbf{E}$ is simultaneously affected by both the real and imaginary parts of the fields. If Equation 4.2 is not satisfied, as would be the case is the current deposit did not conserve charge, we would have to add a correction to the longitudinal part of the electric field (This was done in [3]). We used the LWFA case described above as the test case. For these tests we used a smaller computational window of dimensions $76.4\mu m \times 127\mu m$, and 3000×256 grid points. We let the laser pulse propagate $0.1mm$ into the plasma, so that a well defined wake is formed as shown in Figure 4.1. We used 2 particles per cell in the

$r - z$ plane and 8 particles in the ϕ direction, giving a total of 16 particles per cell. We ran simulations keeping up to the 2nd harmonic ($m = 0, 1$, and 2) and the charge conservation of each mode was tested rigorously. Both linear and quadratic interpolations were tested (the particle shape in the ϕ direction was a delta function). The output of the charge conservation diagnostic for the real part of mode 1 (for which the numerical noise was the greatest) is shown in Figure 4.2. In these simulations we used double precision floating point numbers, which have 15 numerical orders of accuracy in decimal units. When subtracting two nearly identical numbers, a roundoff error 10^{-15} below the working order of magnitude, which in this case is 2.83 shall be observed. In Figure 4.2 charge is seen to indeed be conserved to within the roundoff error of the double precision arithmetic at each grid point of the simulation. The noise is slightly larger as r approaches zero, since the field values are scaled to $1/r$ when calculating the divergence.

The lineout along the axis of the charge conservation for each mode is presented in Figure 4.3. The numerical noise was slightly higher for quadratic interpolation than for linear interpolation, but in each case the charge conservation was satisfied to roundoff error for every mode. In addition, the largest residual error is in the m=1 harmonic which includes the laser field. The error in Gauss's law can accumulate over time if charge is not conserved since it is an integral over time of the continuity equation. However, the sign of the errors are random so the accumulation of the errors will be less then the accumulation of the magnitude of the errors. In the future we may include a Marder's correction to clean up any accumulated errors to the longitudinal part of the electric field if necessary. These tests validate the use of Equation 3.31 and the existing current deposition algorithm for the m=0 harmonic in the r-z grid. We have also tested the charge conservation for many more cases.

4.3 Comparison of LWFA Results with 3D Simulations

We next present results from the LWFA simulation described earlier keeping only up to the $m = 1$ harmonic. The LWFA simulation discussed at the beginning of this section was run to about $0.1cm$. For the full 3D simulation, a $4000 \times 300 \times 300$ grid with dimensions

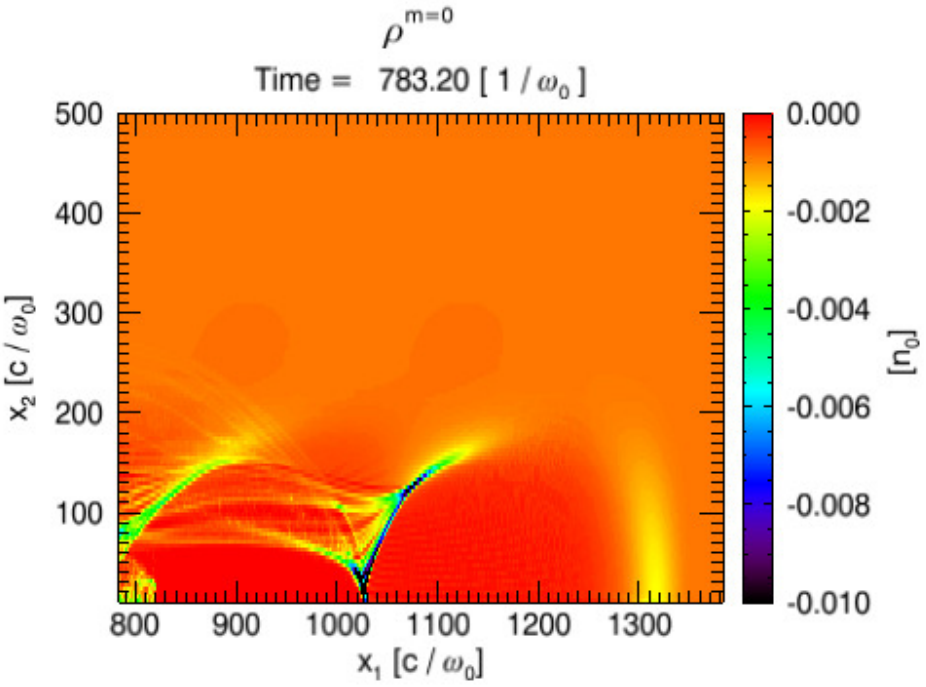

Figure 4.1: A wake formed by a circularly polarized laser penetrating $0.1mm$ into the plasma, presented here in the $m = 0$ azimuthal mode of the charge density. The charge conservation tests presented in Figure 4.3 correspond to this result of this simulation. If you take the divergence of the electric fields in mode 0, it will correspond to this plot exactly.

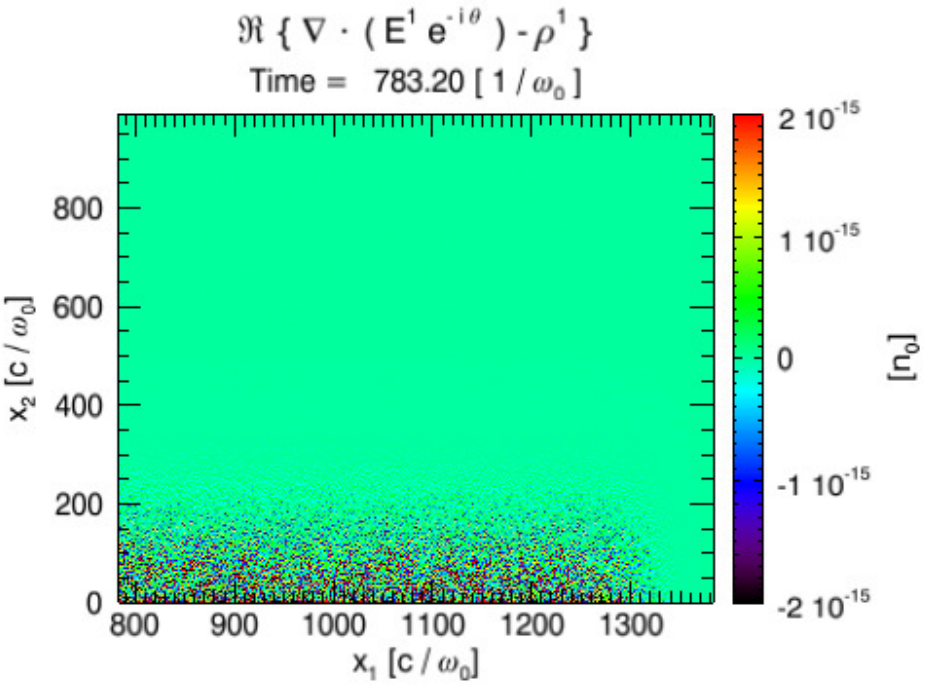

Figure 4.2: The deviation of the charge conservation (Gauss' law) of the real part of mode $m = 1$, for a simulation utilizing quadratic particle interpolation. The deviation in the Gauss' law is maintained to within the accuracy of double precision arithmetic.

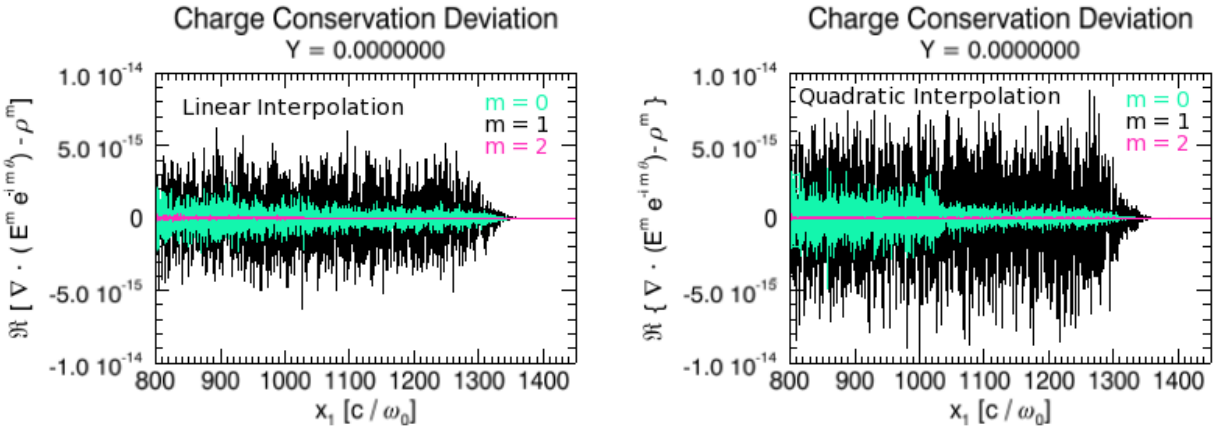

Figure 4.3: The deviation of charge conservation (Gauss' law), along $r = 0$, for modes 0, 1, and 2. Quadratic interpolation (right) shows a slightly larger roundoff error then the linear interpolation result (left). The error in $m = 1$ (the component with the laser) is the largest in both cases.

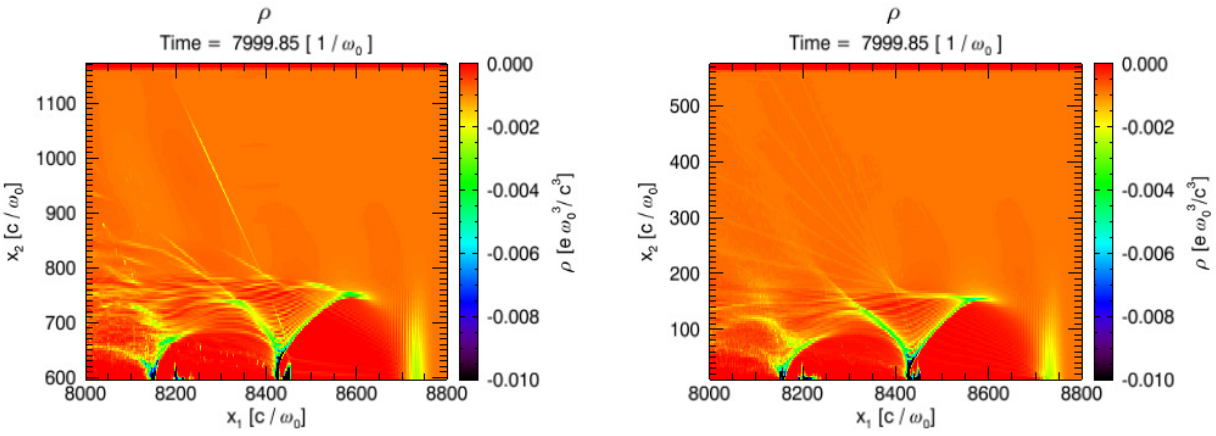

Figure 4.4: These are the electron charge density distributions for the full 3D simulation at 0.1cm (left) and the cylindrical mode simulation at 0.1cm (right). The cylindrical mode density cross-sections are taken at $\phi = 0$, which corresponds to the top half of the cross section of the 3D simulation at $y = 0.0$. Both simulations used quadratic interpolation, and both simulations used the same cell sizes.

$101.9\mu m \times 149.2\mu m \times 149.2\mu m$ was used with 2 particles per cell . The time step was chosen as close as possible to the Courant limit. The quasi-3D simulation used a computational window of dimensions $101.9\mu m \times 74.6\mu m$ and 4000×150 grid points for the r-z grid. The simulation was conducted with 2 particles per cell in the r-z directions and 16 particles in the ϕ direction. For typical LWFA simulations, keeping only the $m = 1$ mode essentially models a laser with a symmetric spot size and it precludes hosing and asymmetric spot size effects[1]. In future publications and work we will describe the additional physics that can be studied by including more harmonics. Note that the wake excited by a linearly or circularly polarized cylindrically symmetric laser is itself cylindrically symmetric. For the quasi-3D simulations we use a time step as close to the stability limit as possible. It can be argued heuristically and confirmed empirically that the time step is limited by a 3D Courant limit where an "effective" cell size in the ϕ direction is given by $\Delta r\pi/m_{max}$ where m_{max} is the highest harmonic kept. In addition, we found that only 8 particles across $0 \leq \phi < 2\pi$ were needed to avoid substantial noise in the first bubble. The signal-to-noise ratio scales as $\sqrt{m_{max}}$, so more particles per 2π are needed as more harmonics are included[3]. This impacts the effective speed up as it will be roughly proportional to the number of simulation particles. In a 3D simulation $n_p^{3D} = N_x N_y N_z N_{pc}$ particles are used, where N_x, N_y, and N_z are the number of cells in each Cartesian directions, and N_{pc} is the number of particles per cell. In the quasi-3D simulation the number of particles is $n_p^{\text{quasi-3D}} = N_z \frac{N_x}{2} N_{p,r\text{-}z} N_{p,\phi}$, where $N_{p,r\text{-}z}$ is the number of particles in the r-z plane and $N_{p,\phi}$ is the number of particles distributed over $0 \leq \phi < 2\pi$.

In Figures 4.4 - 4.7, we show results after the laser was propagated through the plasma over a distance of $0.1cm$. Two-dimensional density plots corresponding to an axial cut across the data of the 3D simulation is compared against the $\phi = 0$ plane for the quasi-3D in Figure 4.4. The 2D density contours for the wake were identical throughout most of the simulation, until a small number of particles are trapped late in the full 3D simulation. However, this did not significantly affect the acceleration process of the mono-energetic

[1]However, it does include hosing of the self-injected (or externally injected) particle beam which loads the wake.

bunch. Lineouts of the accelerating electric field of the 3D and the quasi-3D simulations are shown on the left hand side, and lineouts of the laser field ($m = 1$ mode) are shown on the right hand side of Figure 4.5, respectively. The spectrum of the trapped particles from the two cases are shown in Figure 4.6 and the longitudinal momentum distribution are shown in 4.7. There is excellent agreement between the quasi-3D simulation with only mode 1 and the 3D simulation, both quantitatively and qualitatively. This illustrates that even in full 3D simulations the physics remains nearly azimuthally symmetric.

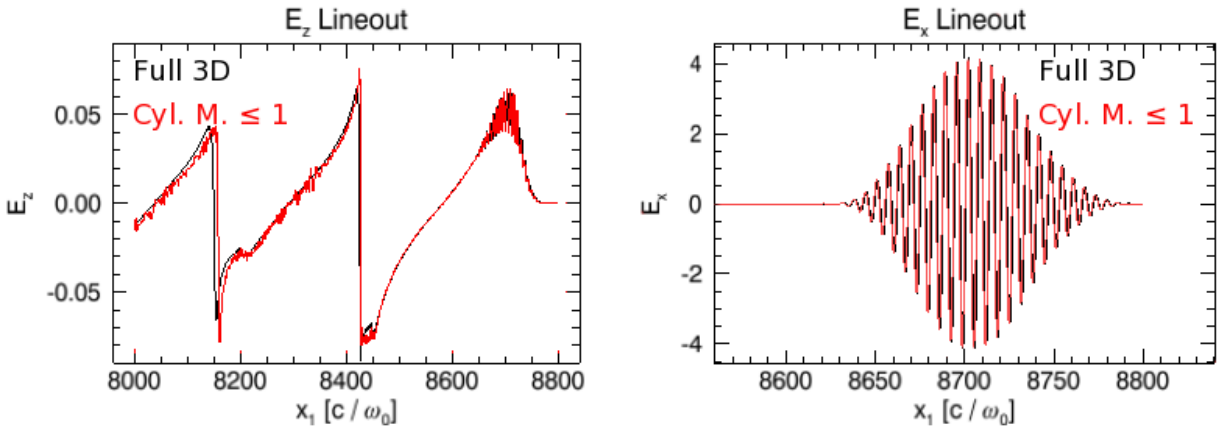

Figure 4.5: Lineouts along the laser for the E_z and E_x fields for the 3D (black) and quasi-3D (red) simulations. The lineout of E_x is zoomed in to more easily see the matching of the phase of the laser.

4.4 Beam Loading in LWFA

Implementing the new algorithm into OSIRIS immediately provides the capability of modeling beam driven plasma based acceleration concepts, beam loading of laser produced wakes, as well as particle beam driven wakes and modeling beam loading over pump depletion distances. Beam loading in particle beam driven wakes has been studied extensively using r-z PIC simulations as well as 3D quasi-static PIC simulations. On the other hand, beam loading studies for laser driven wakes has had to rely on a limited number of full 3D simulations or ponderomotive guiding center simulations (3D, r-z, or quasi-static). However, the pon-

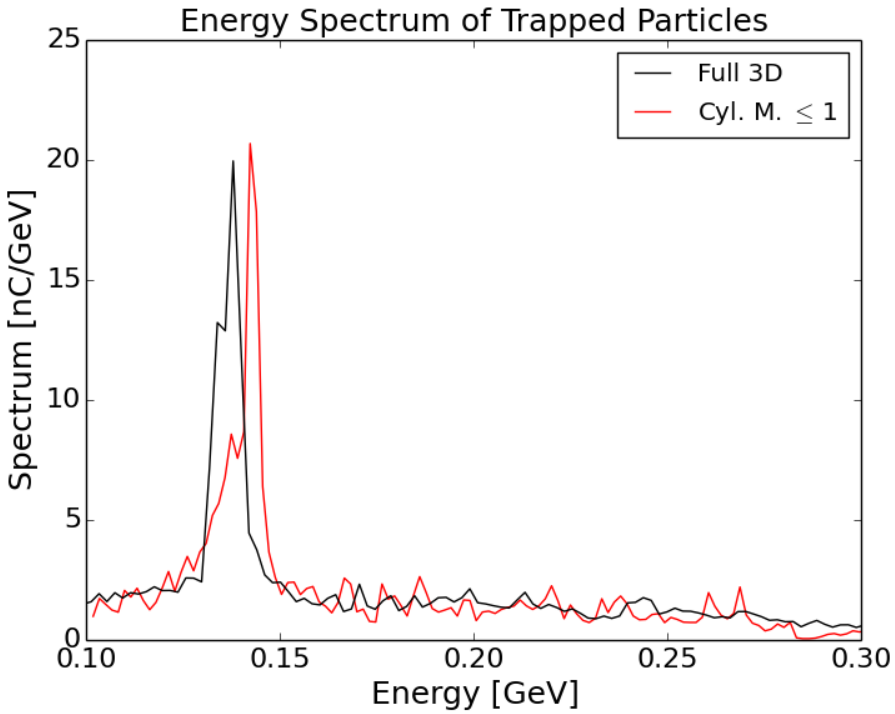

Figure 4.6: The spectrum of the trapped particles from the 3D (black) and quasi-3D (red) simulations. The laser has propagated $0.1cm$ into the plasma.

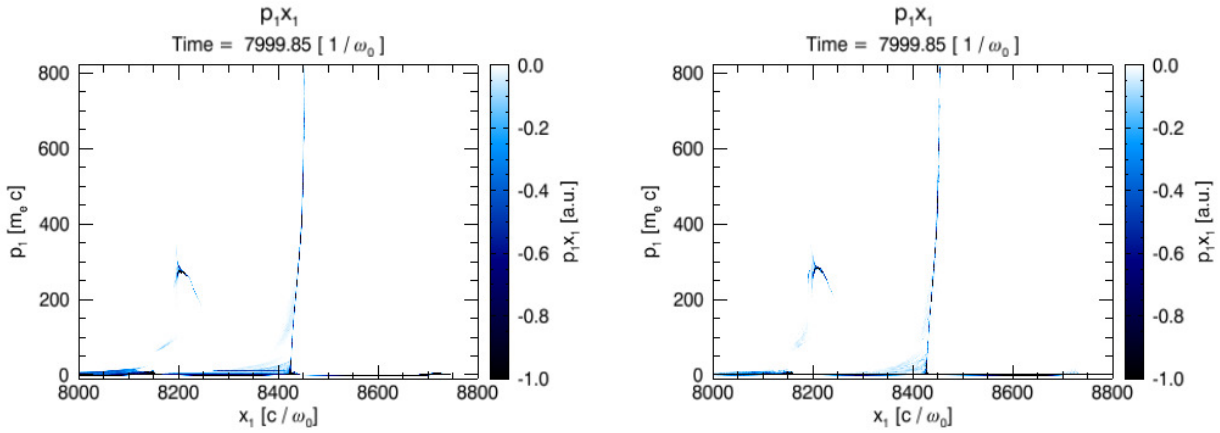

Figure 4.7: The p_1x_1 phase-space plot for the 3D (left) and quasi-3D (right) simulations, after the laser had propagated $0.1cm$ into the plasma.

deromotive guiding center has limitations for high laser intensities. Therefore, combining the ability for studying laser propagation with only the $m = 1$ mode together with the ability to launch a particle beam will permit rapid parameter scans for LWFA beam loading scenarios. We next show preliminary results where we beam load the wake in the LWFA simulations by Lu et al. described earlier. Recently, Tzoufras et al.[54] described how to analyze beam loading in nonlinear wakes, but there has been very little computational studies of beam loading in nonlinear wakes created by lasers due to the inability to routinely study this in three dimensions[2]. Here we show that the quasi-3D scheme could be a very useful tool for such studies. We loaded a Gaussian electron beam with $k_p\sigma_z = 0.5$ and $k_p\sigma_r = 0.2$, and a peak density such that $(n_b/n_p)k_p^2\sigma_r^2 \equiv \Lambda \approx 2$ into the wake. Here $1/k_p$ is the plasma skin depth, amd σ_z and σ_r are the standard deviation of the gaussian profile in the z and r dimensions, respectively. n_b is the peak density of the beam profile, and n_p is the density of the plasma. The normalized charge per unit length, Λ, is the critical normalized parameter which describes the degree of nonlinearity in the wakefield driven by the beam [4, 36]. For $n_p = 1.5 \times 10^{18} cm^{-3}$, this corresponds to a bunch with $\sigma_z = 2.2\mu m$, $\sigma_r = 0.87\mu m$, and $N \approx 1.9 \times 10^9$ ($\approx 300pC$). The spacing between the laser and the particle beam was varied. The trailing beam was initialized with an energy of 2 GeV, i.e., with a proper velocity of $\gamma v_z = 40000.0c$. The beam loading of the wake is shown in Figure 4.8. This figure shows how the wake is loaded differently depending on the spacing between the laser and the trailing beam. In the future, the quasi-3D scheme will enable routine studies of how the qualities of the trailing bunch and the overall efficiency depend on the location, shape, and current profile of the bunch. It will provide detailed parameter scans including the lowest order three dimensional effects and point towards parameters for full 3D simulations.

[2]Some physics of beam loading from an externally injected trailing beam can be studied using quasi-static algorithms together with the ponderomotive guiding center method. However, such studies cannot be carried out over pump depletion distances because the PGC uses the envelope approximation.

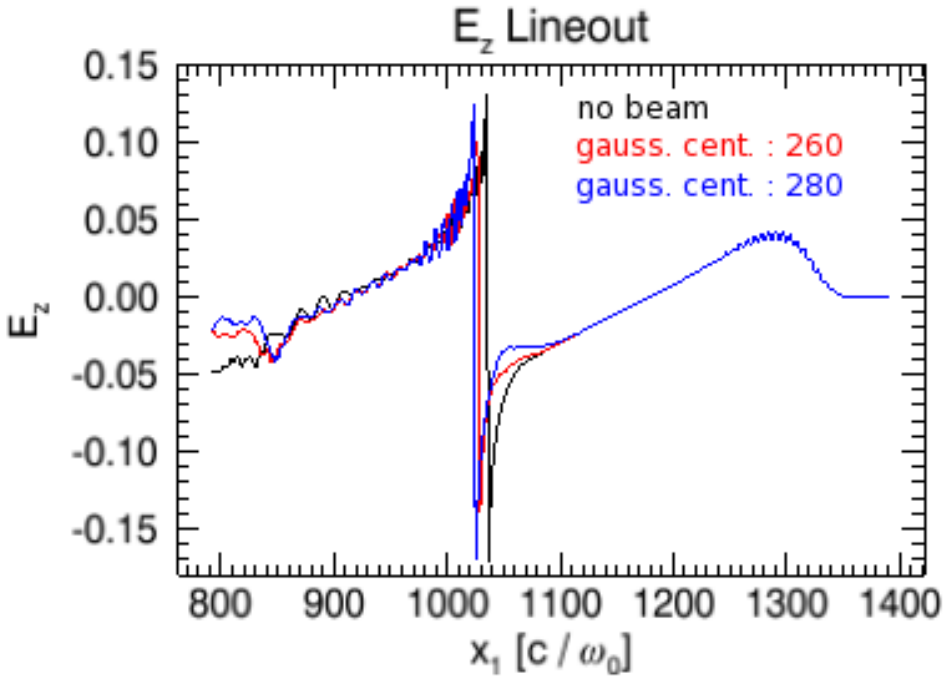

Figure 4.8: Lineouts of E_z along the laser for LWFA simulations including beam loading. The black is the wake without beam loading. The red and blue lines show the wake as it is loaded with a gaussian beam with its center at $z_0 = 260c/\omega_0$, and $z_0 = 280c/\omega_0$, respectively. The center of the laser is initially at $503c/\omega_0$, and the laser has propagated $0.1mm$ into the plasma.

4.5 Hosing of Particle Beam Driver

In this section we present an example of using the quasi-3D version of OSIRIS to study a particle beam driven wakefield accelerator, ie., PWFA. Axisymmetric r-z simulations have been effectively utilized to study PWFA. However, such simulations cannot investigate asymmetric effects such as hosing and asymmetric spot-size effects. Here we present a sample result for a PWFA simulation including $m \leq 2$ harmonics. The parameters are $n_b/n_p = 10.0$, with $k_p\sigma_z = 1$, and $k_p\sigma_r = 0.2$, $\Lambda = 0.4$. The simulation box size was $600c/\omega_p \times 120c/\omega_p$ in the z and r directions, respectively. The initial beam proper velocity was $\gamma v_z = 40000.0c$. The plasma was simulated with 16 particles across ϕ, while the beam was simulated with 32 particles across ϕ. There were 4 particles per r-z cell both species. The beam was initialized as an azimuthally symmetric beam and any higher order harmonics grow from the noise.

For this simulation we kept up to the 2^{nd} harmonic. Initially, as expected, the beam produces an azimuthally symmetric wake (and the beam remains symmetric). For short propagation distances the $m = 1$ and $m = 2$ modes are not important and the 2D r-z and quasi-3D results look the same, as seen in Figure 4.9. The 2D r-z plot was generated by mirroring the result from positive r to "negative" r. We also note that the 2D r-z code and full 3D results have been compared for round beams with no tilt and excellent agreement was found[1]. For longer propagation distances hosing occurs. Hosing theory [84, 85] is based on coupling the $m = 1$ modes for the centroid of the beam to that of the wake. In this simulation hosing grows from random noise in the beam density and it can clearly be seen in Figure 4.10. The upper plot is from a 2D r-z simulation where hosing is precluded. The lower plot is from a quasi-3D simulation. We emphasize that the result from a quasi-3D and full 3D simulation will not quantitatively agree if physics which grows from a random noise source is important. However, if the dominant source for growth is an initial beam tilt agreement should exist and the growth rates should agree well. After a longer period of time the spot size begins to deviate due to a higher modal ($m = 2$) effect. This is shown in Figure 4.11. If the $m = 2$ was not present then hosing would only occur in a single plane. The fact that it is occurring in both planes shows that $m = 2$ is present. In principle, the

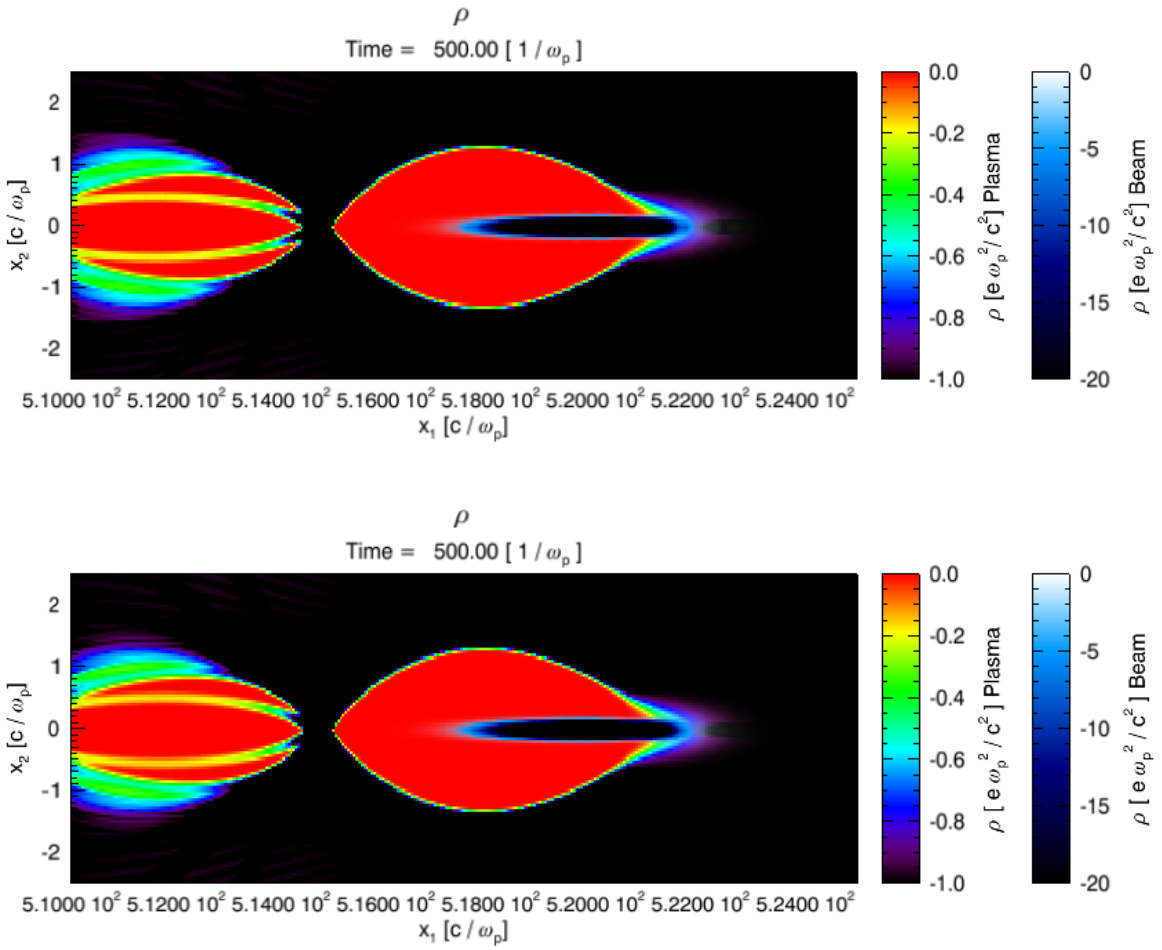

Figure 4.9: The density from PWFA simulations with a 2D cylindrical geometry simulation (top) and an $m \leq 2$ quasi-3D simulation (bottom). The beam has only moved $500c/\omega_p$ into the plasma. The bottom plot was created by summing the modes at $\phi = 0$ on the top half of the grid, and at $\phi = \pi$ on the bottom, which gives us the $y = 0$ cross-section of the three-dimensional beam. The 2D cylindrical simulation plot simply mirrors the bottom half from the top. For short distances the two simulations agree very well.

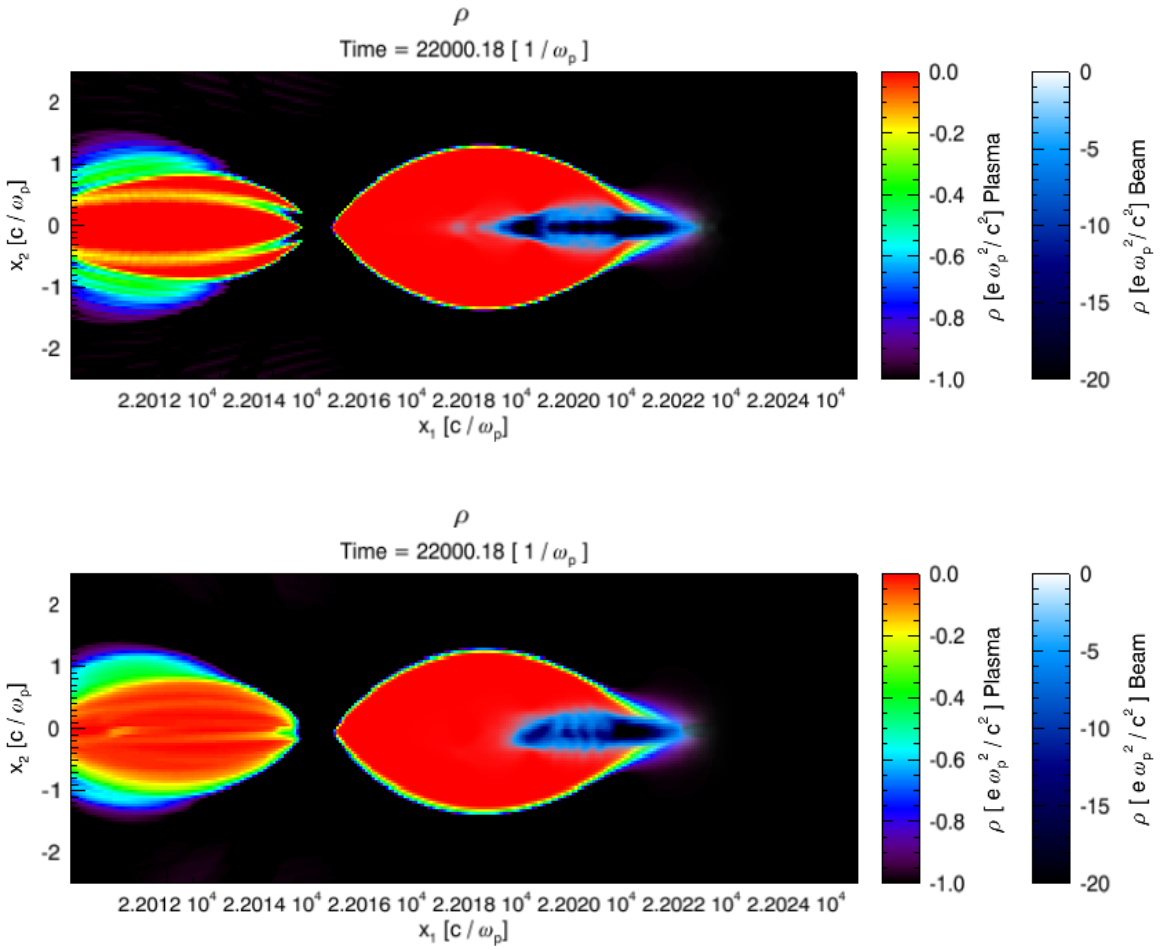

Figure 4.10: The density plots after the beam has propagated $22000.18c/\omega_p$ into the plasma. Hosing is observed $m \leq 2$ quasi-3D simulation (bottom). A result from an equivalent 2D cylindrical simulation is shown for comparison (top). The bottom plot was created by summing the modes at $\phi = 0$ on the top half of the grid, and at $\phi = \pi$ on the bottom, which gives us the $y = 0$ cross-section of the three-dimensional beam. The 2D cylindrical simulation plot was generated by simply mirroring the bottom half from the top.

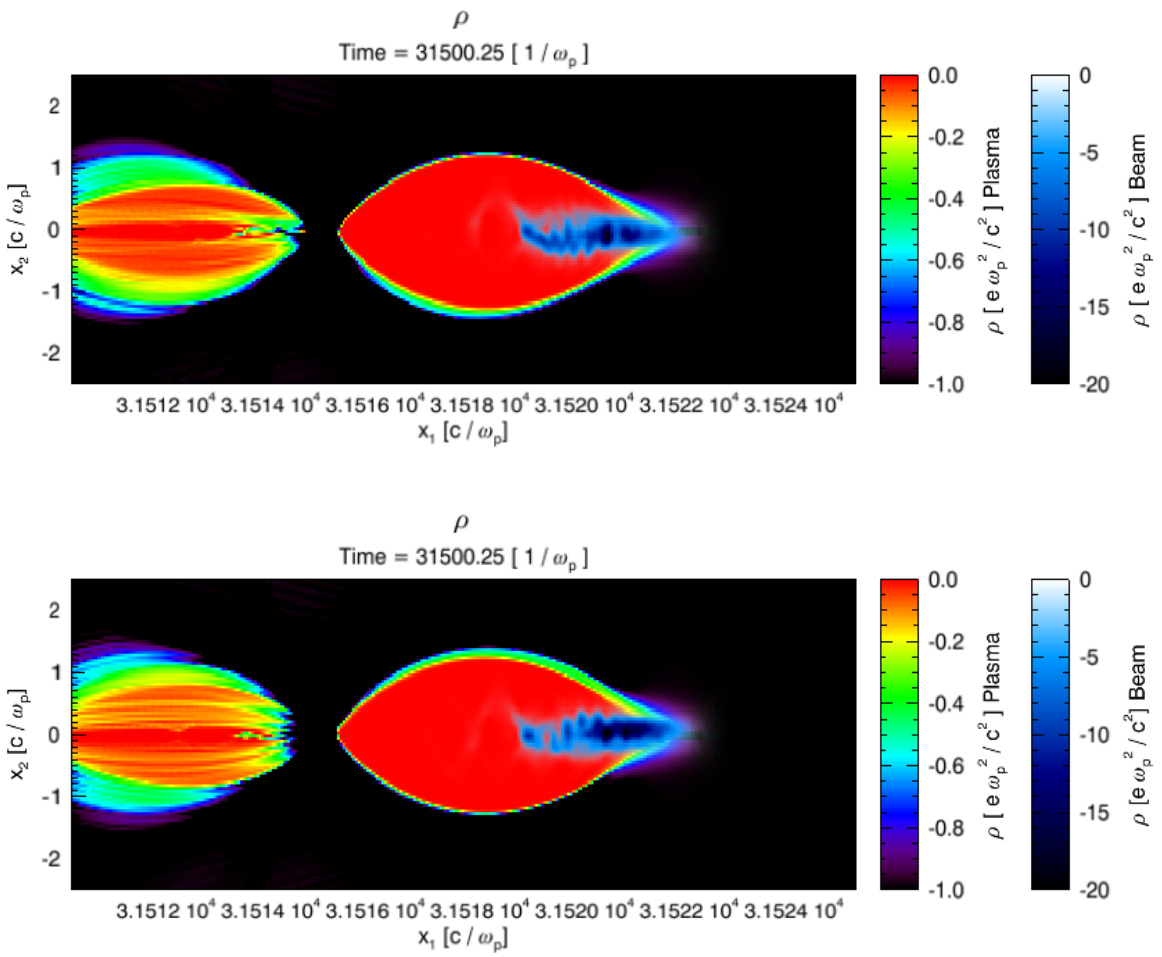

Figure 4.11: Cross section of the beam and plasma density for the x-z (top) and y-z (bottom) planes.

more the physics is azimuthally asymmetric, the more modes we would want to retain, and this is an area for future work. For example, if an initial tilt was provided for the beam, the greater the tilt, the greater number of modes we would need in order to converge to the full 3D results. Future work will include modeling beams with tilts and studying how the results change as the harmonic number increases.

CHAPTER 5

Validity of the Phenomenological Scaling Laws of the Self-Guided Nonlinear Blowout Regime of LWFA Beyond a Few GeV

5.1 Introduction

In this chapter we use the new quasi-3D version of OSIRIS to examine the self-guided nonlinear blowout regime of LWFA for existing and future lasers and compare the results against the predictions of the scaling laws in Lu et al.[4]. We consider laser and plasma conditions which cannot be currently studied using full 3D PIC simulations because of their high computational cost. In sections 2.4 and 2.5, matching conditions for the laser spot size and pulse length were presented as well as scaling laws of accelerated electron energy in terms of laser and plasma parameters. In the nonlinear blowout regime, the laser can be self-guided due to the laser energy in the leading edge being locally depleted before it diffracts. Lu et al. compared the scaling laws against the results for a fully nonlinear 3D PIC simulation for a 200TW (6 Joule) laser. The advent of the quasi-3D algorithm presented in chapters 3 and 4 now make it possible to study these scaling laws for higher laser intensities and/or higher laser energies.

An extensive and detailed understanding of the phenomenological model is crucial to its further development as an accurate model of LWFAs for greater acceleration lengths. As discussed in section 2, the phenomenological model description of the LWFA in the blowout regime identifies the key physics as self-guiding, wake excitation, pump depletion, particle dephasing, and beam loading. As we scale to higher trapped particle energies, we may

discover that we need to address new physical effects into the model. One reason for concern is that, as we reduce the plasma density and lengthen the particle dephasing length, L_d, the laser must theoretically traverse a greater distance in Rayleigh lengths, Z_r, before it is completely dephased. In order to maintain a consistent accelerating structure over the acceleration length, the laser must remain self guided over the entire accelerating distance. In section 2.6 we revisit a suggestion made in Lu et al. that the normalized amplitude of the laser may be scaled to match the length of the laser lost due to pump depletion and localized diffraction at every Rayleigh length by scaling a_0 as $(1/n_p)^{1/5}$. If the rate at which the laser is lost due to diffraction over the dephasing length can indeed be adjusted to be the same as we increase the dephasing length, we would have successfully added self-guiding over a scaled number of Rayleigh lengths into the list of key physics incorporated into the model.

This issue of self-guiding or balancing diffraction with local pump depletion brings forth two important questions that must be considered when testing the scaling laws to higher electron energies. First, we want to know how well the laser remains self-guided for longer dephasing lengths in units of Rayleigh lengths if the normalized laser amplitude is scaled as $(1/n_p)^{1/5}$. Secondly, we want to know how well the model scales if we adjust the laser amplitude, and whether a noticeable improvement in self-guiding of the laser is observed as was intended; and if the electron energy is higher. As a result, we present two different sets of simulations: one set in which a_0 is kept constant as we scale to lower densities and longer dephasing lengths, and another in which we scale $a_0 \sim (1/n_p)^{1/5}$ as we explore results for lower densities.

Performing successive simulations with parameters scaled to longer dephasing lengths and higher beam energies quickly become computationally infeasible if one were conducting fully 3D Cartesian simulations. Estimates for the cpu hours of a sequence of such simulations are presented in Table 5.1. The estimates were calculated by assuming a basic resolution of $\Delta z = 0.2k_0$, $\Delta r = 0.1k_p$, and a box size of about $5.2W_0$ in the longitudinal direction (width comparable to the original Lu et al. run), and a transverse box size equal to the initial spot size times the total number of Rayleigh lengths over the dephasing lengths $(L_d W_0/Z_R)$ [1].

[1]We found that for our simulations we needed large box sizes to accurately simulate laser evolution over

We also assumed two particles were initialized per cell. When we use a quasi-3D algorithm, however, we can expect a speedup on the order of the number of cells in the transverse dimension (which is a dimension we no longer have to resolve). This can mean more than a hundred times the speedup, and the parameters presented in Table 5.1 were proven to be feasible using this geometry.

Est. CPU hours -3D-	Power (TW)	n_p (cm^{-3})	W_0 (μm)	L_d (cm)	a_0	ΔE (GeV)
100,000	200	1.5e18	19.5	1.5[2]	4.0	1.58
430,000	324	1.0e18	22.0	2.62	4.44	2.52
3,200,000	649	5.0e17	31.7	7.37	4.44	5.28
26,000,000	1298	2.5e17	44.8	20.8	4.44	10.57
⋮	⋮	⋮	⋮	⋮	⋮	⋮

Table 5.1: Here we list roughly estimated CPU hours for a simulation with parameters based on a Lu et al. simulation[4], and successive simulations that scale the same parameters to lower plasma densities, longer dephasing lengths, and higher beam energies. There are effects not taken into consideration in this estimate, such as the imbalance of computational load across multiple nodes.

In section 5.2 we will discuss how well the phenomenological model for LWFA in the self-guided blowout regime and a matched laser scales as we keep a_0 fixed. We will also discuss the detailed extent to which the electron energies and wake evolution scale over the estimated dephasing length, L_d. We also discuss how a simplification implicit in the Lu et al. energy estimate leads to predictions that are generally less than what is found in the simulations. We also discuss how the strengths of the scaling laws lies in their capturing the important physics. This permits refinement in their accuracy as each phenomenon is better understood. In section 5.2 we show that if a_0 and the laser transverse and longitudinal profiles remain fixed in normalized units, that the results "scale" remarkably well even when self-guiding is

many Rayleigh lengths.

[2]Lu et al. conducted this simulation over $0.75cm$, and not the entire dephasing length, L_d.

required over tens of Rayleigh lengths. In section 5.3 we will conduct simulations with the same density parameters as section 5.2, but with the normalized laser amplitude increased as we go to lower densities in the manner suggested by Lu et al to maintain self-guiding. We will discuss how the laser evolution, the wake evolution, and the electron dephasing process did not exactly scale when we increased the normalized laser amplitude, even though as predicted higher electron energies and self-guiding are achieved. We will also address how these added complications in the scaling of the LWFA problem may potentially be addressed in the future. We will summarize our findings in section 5.4.

5.2 Scaling to Lower Densities With a Fixed a_0

5.2.1 Near-identical scaling of particle energies and wake evolution

Calculated								Simulated	
a0	P (TW)	τ (fs)	n_p (cm^{-3})	Z_R (cm)	W_0 (μm)	L_d (cm)	Est. E (GeV)	Q_{mono} (pC)	Max E (GeV)
4.44	324	50	1.00e18	0.19	22.0	2.62	2.52	306	3.46
4.44	649	72.0	5.0e17	0.394	31.7	7.37	5.28	255	6.63
4.44	1298	102.5	2.5e17	0.788	44.8	20.8	10.57	146	13.6

Table 5.2: Quasi-3D simulations were conducted with the laser profile and matched spot size scaled exactly for lower plasma densities and longer dephasing lengths. a_0 here was kept at the same value for all of the runs.

A series of quasi-3D PIC simulations were conducted with OSIRIS in order compare how the wake evolution and trapped particle acceleration scales to lower density, as we keep the pulse shape and normalized laser amplitude the same. The details of the axial laser profile are given in the next chapter in section 6.2. The laser is defined by a polynomial function with a well defined beginning and end. In Table 5.2 τ is the FWHM of the laser intensity. Simulations were conducted with $a_0 = 4.44$, $n_p = 10.0,\ 5.0$, and $2.5 \times 10^{17} cm^{-3}$

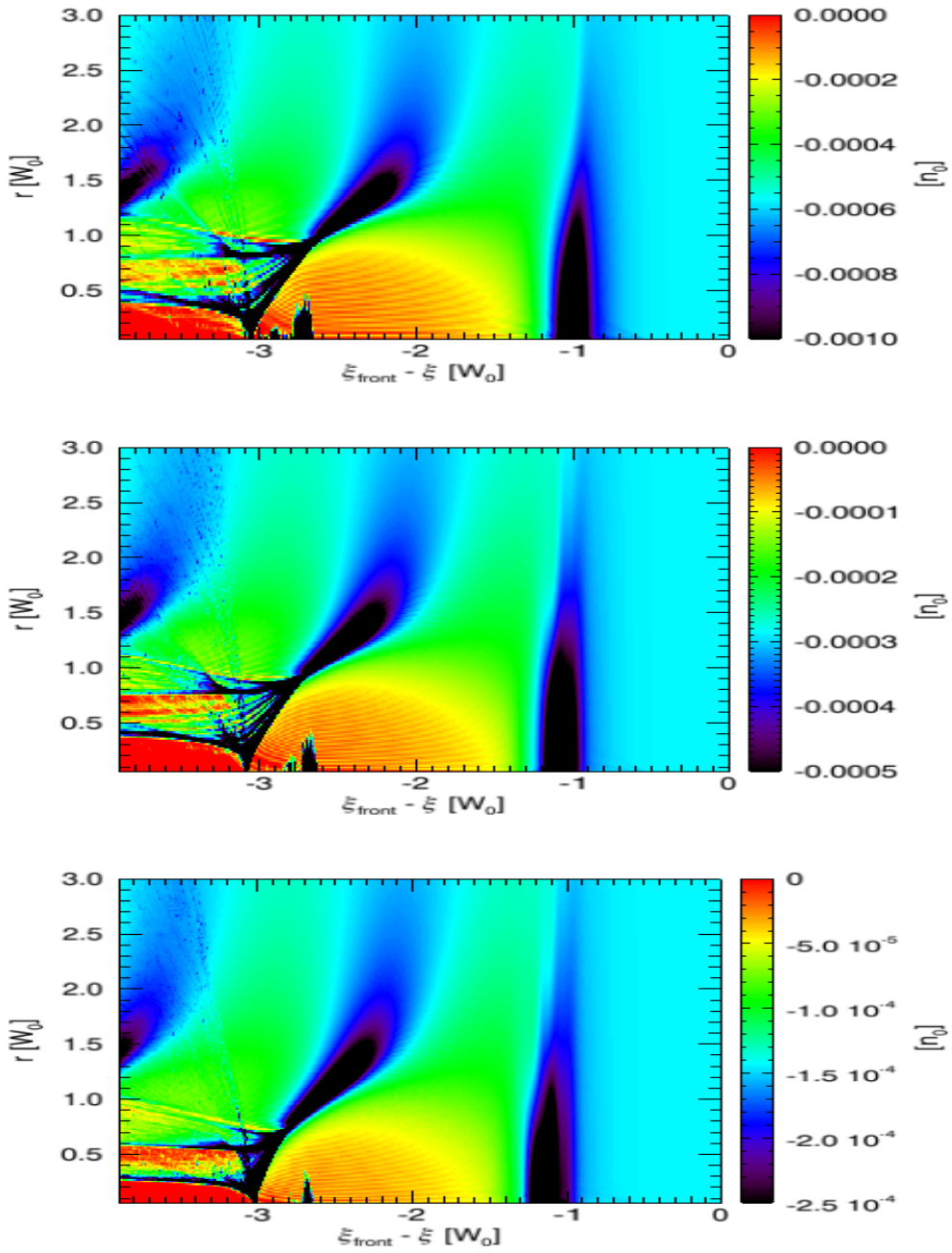

Figure 5.1: The 0^{th} azimuthal mode of the density of the $n_p = 1.0 \times 10^{18}$ (top), $n_p = 5.0 \times 10^{17}$ (middle), and $n_p = 2.5 \times 10^{17}$ (bottom) LWFA simulations. $a_0 = 4.44$ for all of these simulations, and the laser has traversed $0.5L_d$ into the plasma. The horizontal axis is measured as the distance ξ, as a fraction of the initial spot sizes, W_0, from the front of the initial laser profile, ξ_{front}.

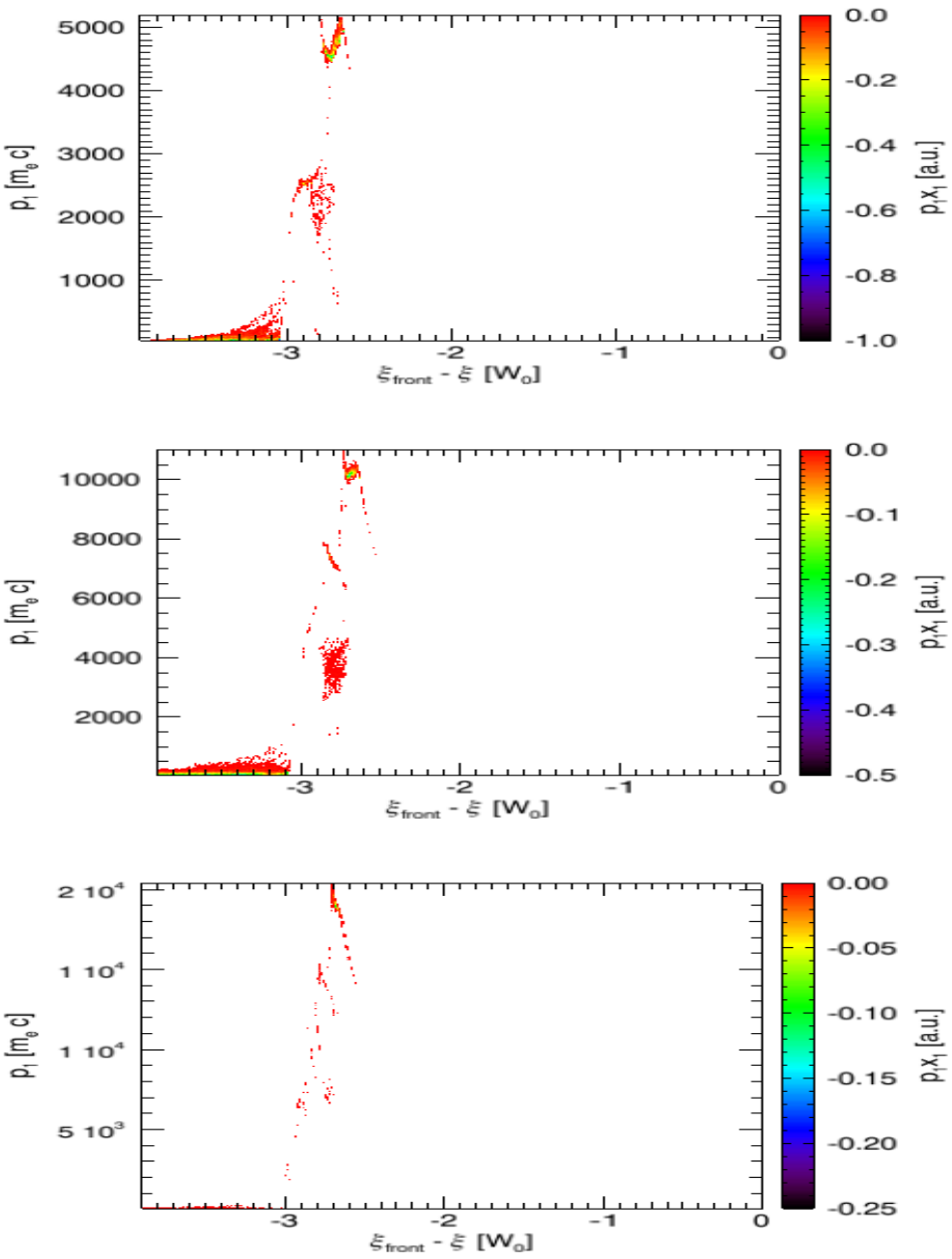

Figure 5.2: The $p1x1$ of the trapped particles in the $n_p = 1.0 \times 10^{18}$ (top), $n_p = 5.0 \times 10^{17}$ (middle), and $n_p = 2.5 \times 10^{17}$ (bottom) LWFA simulations. $a_0 = 4.44$ for all of these simulations, and the laser has traversed $0.5L_d$ into the plasma. The horizontal axis is measured as the distance ξ, as a fraction of the initial spot sizes, W_0, from the front of the initial laser profile, ξ_{front}.

(for $\lambda_0 = 0.8\mu m$), with a matched spot size and the same longitudinal profile, with a FWHM of the pulse length for the laser intensity of $\frac{2}{3}W_0$. The simulations were run out beyond the distance of the estimated dephasing length, L_d. A cell resolution of $\Delta z k_0 = 0.2$ was used for all three simulations, and $\Delta r k_p \approx 0.096$, 0.068, and 0.057 were used, respectively. The (r,z) box sizes ranged from $(7.6W_0, 6.4W_0)$ for the first simulation, $(16.8W_0, 7.0W_0)$, for the second, and $(16.8W_0, 4.5W_0)$ for the third and longest simulation. The box size in the r direction was expanded to ensure boundary effects did not affect the results as the plasma lengths become an increasingly large number of Rayleigh lengths. We initialized particles at two locations in the r-z cell and for each z location. 8 particles were initialized in ϕ. The basic physical parameters of these simulations are presented in Table 5.2.

In Figure 5.1 we plot the plasma density for the wake ($m = 0$ mode) for the three cases of Table 5.2 at the same normalized distance, $0.5L_d$. The plot sizes are the same in terms of normalized units ($3W_0$ in r and $3.9W_0$ in z). Note the simulation box was larger. We also plot this with the horizontal axis being the distance from the front of the laser, ξ_{front}, normalized to the spot size of the laser for each of the scaled simulations. The results scale very well but not perfectly. The $p1x1$ plots in Figure 5.2 indicate that the details in the momentum space of the trapped particles scale similarly, with the exception of low momentum particles in the second bucket which appear to dephase with the bubble over longer distances. When the energy spectrums of the trapped particles are plotted with the momentum normalized to the energy scaling law, they overlap very well, as shown in Figure 5.3.

As a further illustration of the usefulness of the scaling laws, we show the evolution of the maximum trapped particle energy, and the evolution of the maximum decelerating field in Figure 5.4. The plots overlap remarkably well when distance is scaled to the estimated dephasing length and the particle energies and maximum decelerating fields are scaled by the corresponding estimated quantities in Lu et al.'s phenomenological model ($\Delta E \simeq (2/3)mc^2(\omega_0/\omega_p)^2 a_0$, and $eE_{z.\max}/(2mc\omega_p) \simeq \sqrt{a_0}/2$). This model accurately captures the manner with which the wake and the particles evolve when simulations are scaled properly, despite the complexity of the evolution process. However, note that neither the final electron energy nor the maximum decelerating field are exactly equal to the estimate.

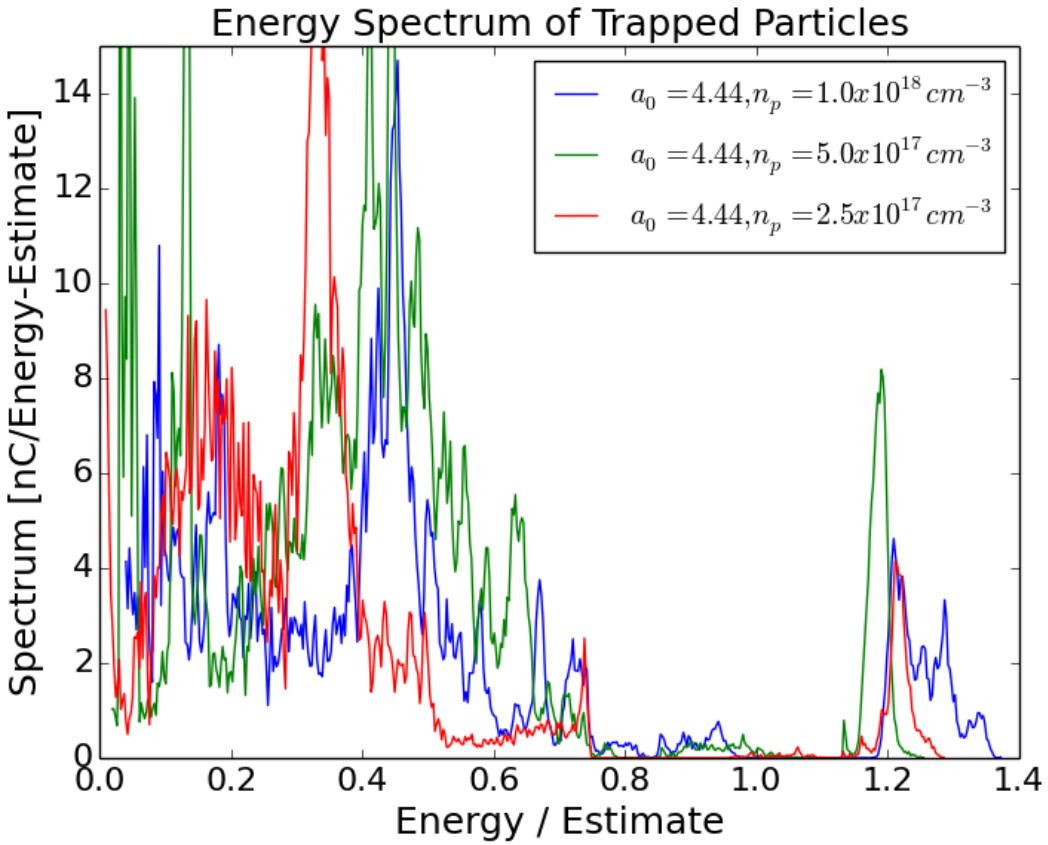

Figure 5.3: The total trapped particle spectrums for three scaled LWFA simulations with a fixed a_0 - each after the laser has traversed a distance of L_d.

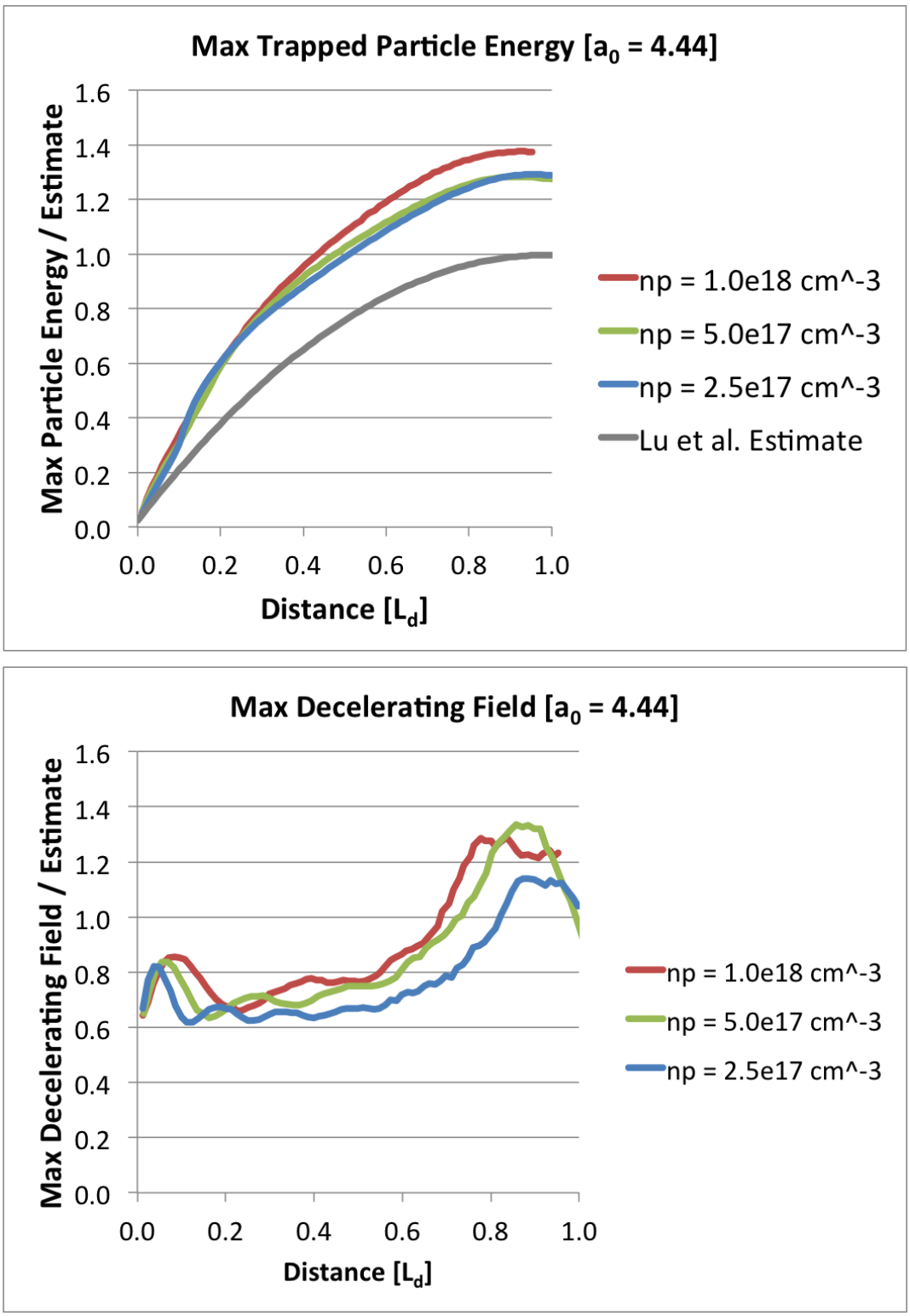

Figure 5.4: Scaling of trapped particle energy evolution (top), and the evolution of the maximum decelerating field, which scales with the maximum accelerating field (bottom).

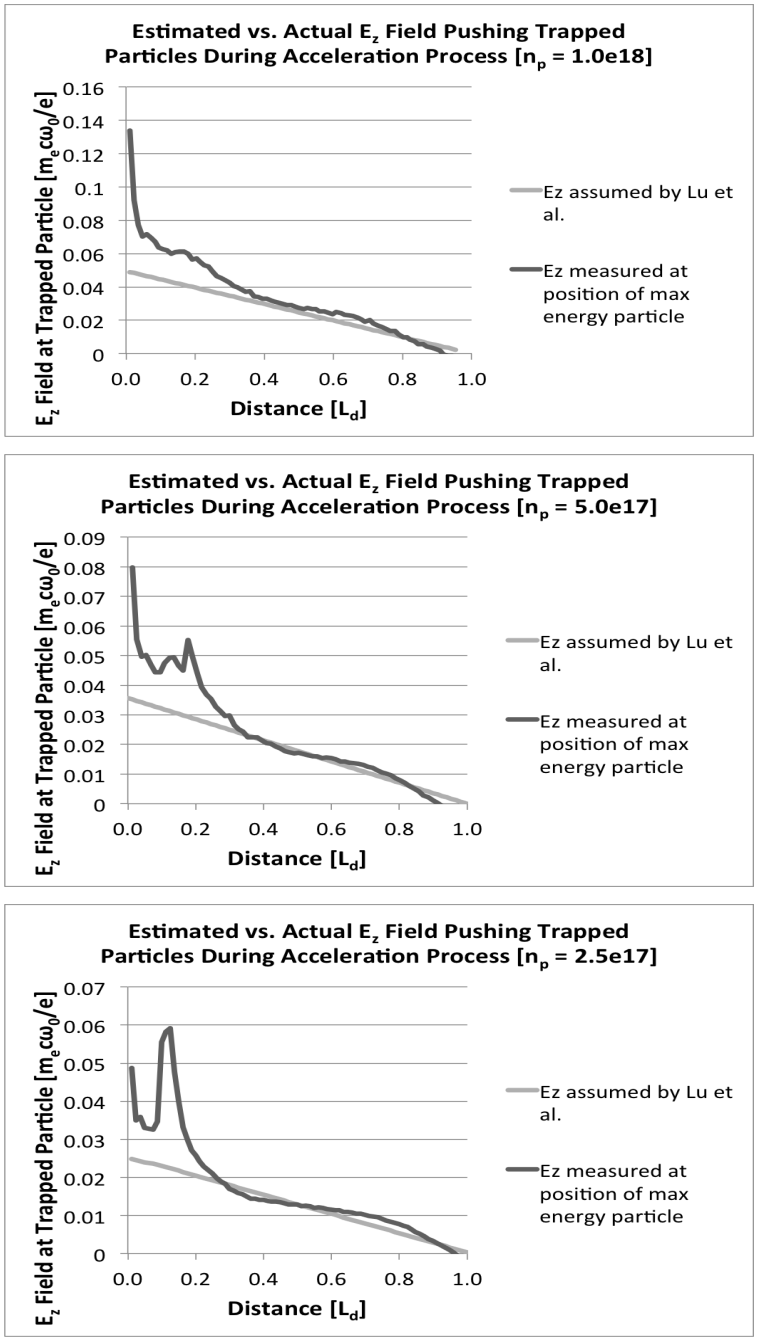

Figure 5.5: The accelerating field experienced by the trapped particle with maximum energy is plotted over the course of the acceleration process. This is compared with the perfectly linear ramp in the accelerating field assumed by the Lu et al. estimate.

Note that the vertical axis are normalized to the predictions from the scaling laws. This illustrates that the phenomenological theory does an excellent job of describing the proper scaling but does not provide the exact coefficients.

5.2.2 Deviation of energy from estimate

Lu et al.'s estimates are approximated from the geometry of the accelerating structure, based on the fact that for $a_0 \gtrsim 4.0$ the ion column forms a sphere and the accelerating field, for the most part, depends linearly on the distance from the middle of the sphere[36]. An exception to this rule is the spike in the accelerating field at the back end of the bubble, where the particles are initially injected. The result of this is that, early in the acceleration process, the particles undergo a greater acceleration and energy gain than is accounted for in the model. A comparison of the evolution of the accelerating field experienced by the highest-energy electron, and the corresponding value assumed by model, is shown in Figure 5.5. It could be seen that the model is in fact tremendously accurate after the early stages of the acceleration process. Although the spike is not considered in the estimate, its structure and size scale with the bubble radius and a_0, and therefore it's contribution to the scaling of the trapped particle energy is fully accounted for in the phenomenological model. We need to refine the coefficients.

5.2.3 Why does self-guiding work?

When designing the simulations with the parameters described in Table 5.2, a remaining question was whether self-guiding would continue to be effective if we maintained a_0 at a constant value while scaling to higher particle energies and longer dephasing lengths, i.e., when moving to lower densities. To maintain self-guiding, Lu et al. argued that a_0, i.e., P/P_c would need to be scaled. Using quasi-3D OSIRIS, we have actually found that even if a_0 is kept constant the laser remained sufficiently self-guided even up to the $10GeV$ range of electron energies. In this section we will revisit investigating the reasons for why self guiding is very effective for LWFA in the blowout regime, and discuss the extent to which self-guiding

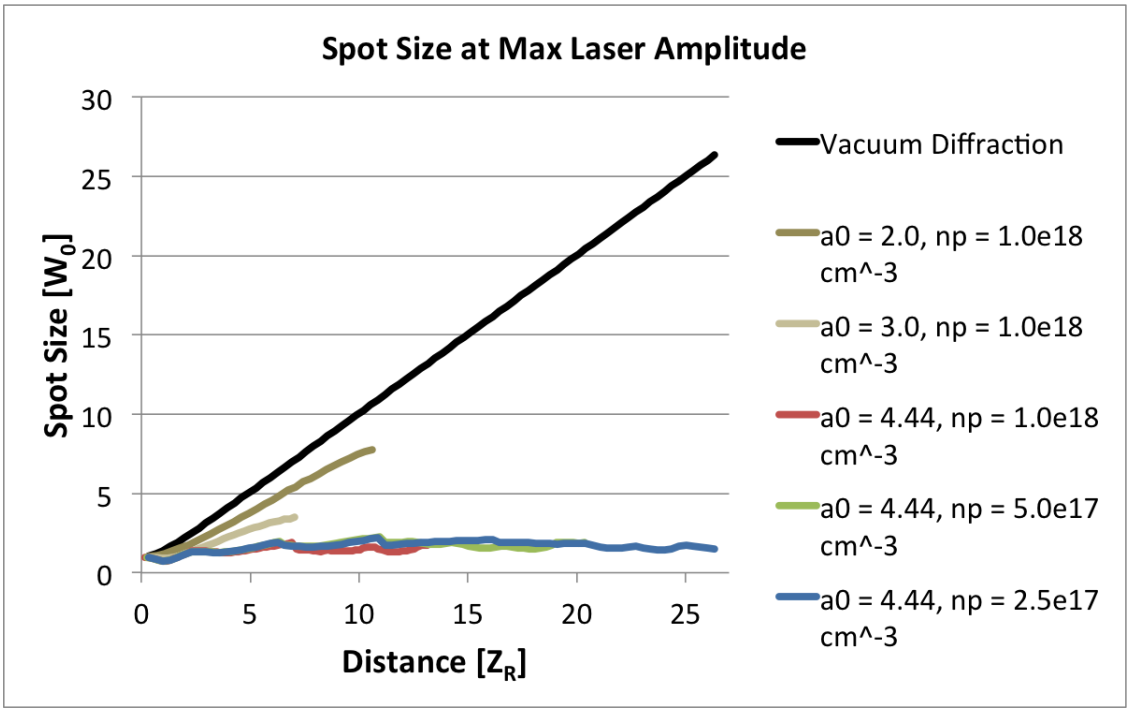

Figure 5.6: The evolution of the spot sizes at the location of the maximum laser amplitude is plotted over distance in Rayleigh lengths is presented, demonstrating the effectiveness of laser self-guiding at many Rayleigh lengths. The plot for Vacuum diffraction is shown for comparison, and two simulations with $a_0 < 4.0$ are also presented to show that at low normalized laser amplitudes self-guiding is not effective.

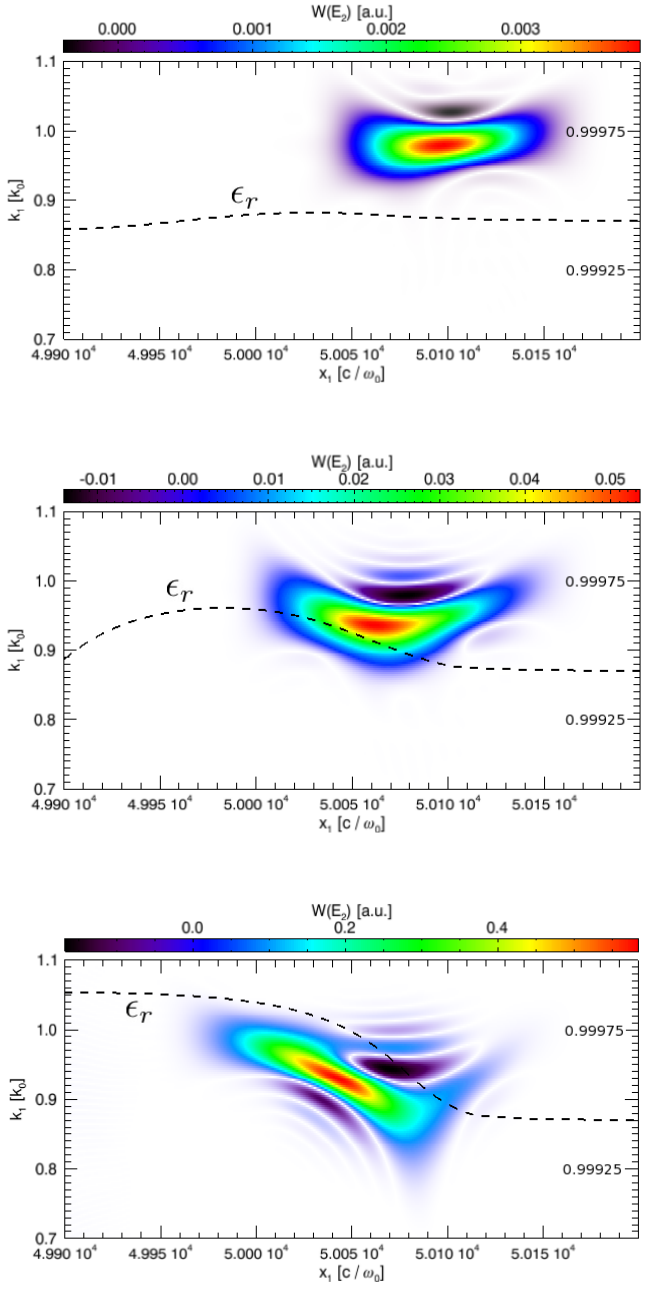

Figure 5.7: The Wigner transforms of the x component of the laser electric field along the axis along with the relative permittivity, after a propagation distance of $6.5mm$. The three plots correspond to simulations conducted with a plasma density of $n_p = 1.0 \times 10^{18} cm^{-3}$, and with a normalized laser amplitude of $a_0 = 2.0$ (top), $a_0 = 3.0$ (middle), and $a_0 = 4.44$ (bottom).

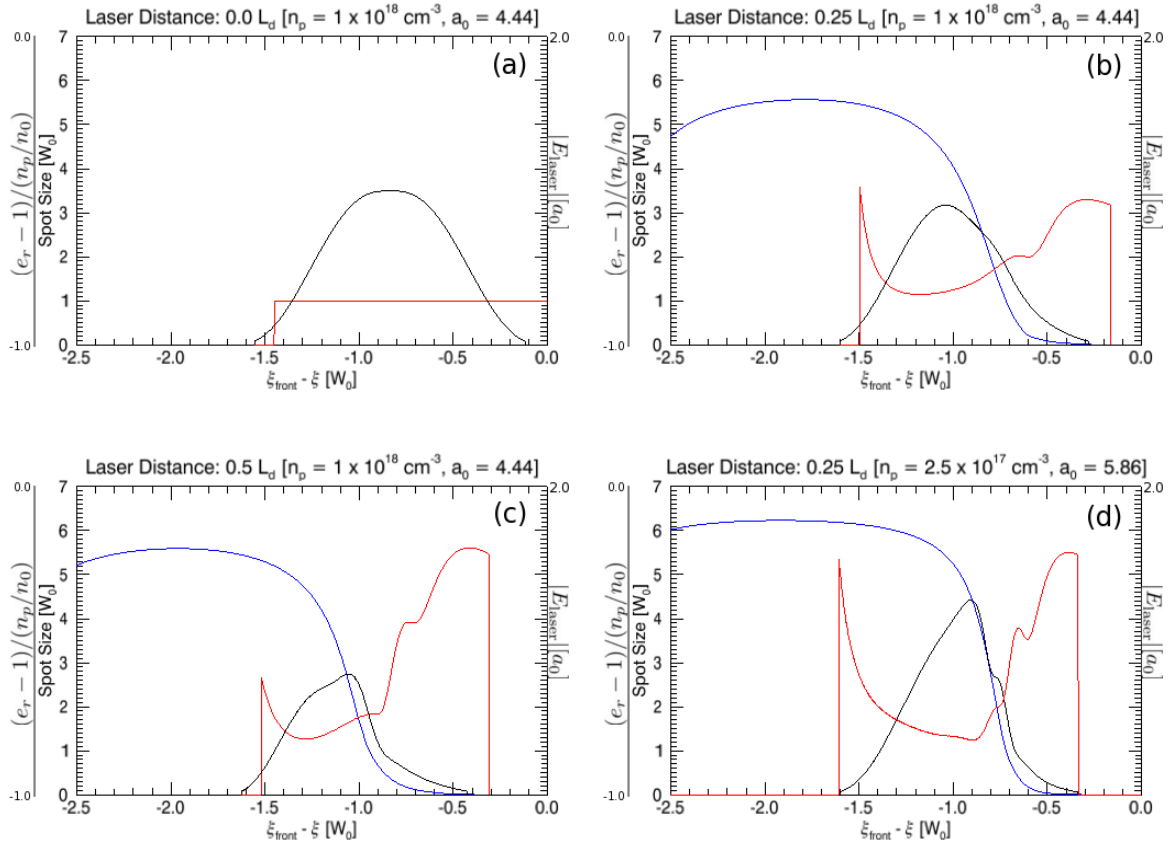

Figure 5.8: The laser field amplitude lineouts (black) along with the cross-sectional spot size (red) and the relative permittivity (blue) along the z-axis of the laser, where the axis are scaled to the initial spot size, W_0. Three of the plots correspond to a plasma density of $n_p = 1.0 \times 10^{18} cm^{-3}$, $a_0 = 4.44$, and a laser traversal distance of 0.0 L_d (a), 0.25 L_d (b), and 0.5 L_d (c). We also present this plot for $n_p = 2.5 \times 10^{17} cm^{-3}$, and $a_0 = 5.86$, at a laser traversal distance of 0.25 L_d (d).

is affected by the scaling to a larger distances in Rayleigh lengths.

In order to fully illustrate how well self guiding has been effective throughout these simulations, we plot the evolution of the spot size at the maximum laser amplitude versus the laser propagation distance in Rayleigh lengths. We define the spot size as $\sqrt{\int drrE^2r^2/\int drrE^2}$ at the z position where E^2 is maximum. The evolution of the spot size is compared with the characteristic vacuum diffraction. We also include results from other simulations for which self guiding is not effective in maintaining the spot size of the laser. These additional simulations were conducted with a plasma density of $n_p = 1.0 \times 10^{18} cm^{-3}$, and with one with $a_0 = 2.0$ and the other with $a_0 = 3.0$. The spot sizes were matched in each of these cases, and the pulse length (FWHM of intensity) was set to $(2/3)W_0$, which is consistent with the rest of the simulations presented in this chapter. The box sizes and cell resolution for these runs are identical to the $2.52GeV$ simulation. As can be seen in Figure 5.6, for these two simulations with smaller a_0 the laser spot size continually expands although it does so at a rate slower than vacuum diffraction. These results are consistent with Lu et al.[4], which found that $a_0 \gtrsim 4.0$ is necessary in order for a short pulse laser to self guide. For example in Figure 5.6, with an $a_0 = 4.44$, the laser spot size remains stable up to even $26Z_R$.

In section 2.4 we explained in detail how a laser with a matched spot size and sufficient power can self guide over many Rayleigh lengths in a plasma, even though when $P \gtrsim P_c$, the front of the laser is not guided (the index of refraction requires a time $\sim \omega_p^{-1}$ to build up[51]). This is because the leading edge of the laser pump depletes before it is diffracted, while the rest of the pulse remains guided [56]. Figure 5.7 depicts the Wigner transforms[3] of the x component of the laser field along the axis, together with the relative permittivity[4] along the axis as a function of z. The Wigner transform illuminates how localized pump depletion is occurring and the relationship between local pump depletion and photon deceleration, which is described in ref. [55]. The process of pump depletion can be viewed as the gradient of the index of refraction leading to a decrease in laser frequency, which is a photon deceleration. Since the number of photons are invariant, this results in the depletion of the laser energy[55].

[3]The Wigner transform[86] of a function $\varphi(z)$ is defined as $W_\varphi(z,k) \equiv \int_{-\infty}^{\infty} e^{-ikz'} \varphi(z + \frac{z'}{2}) \varphi^*(z - \frac{z'}{2}) dz'$.

[4]The relative permittivity is calculated with the quasistatic approximation, $\epsilon_r = \eta^2 \simeq 1 - \frac{n_p}{n_c} \frac{1}{1+\Psi}$.

As can be seen in Figure 5.7, when $a_0 = 4.44$, the relative permittivity has a relatively sharp gradient localized at the front of the pulse, which means the energy is being absorbed in a localized region. This is characteristic of the blowout regime ($a_0 > 4$). Because of this, in the region at the front of the pulse the index of refraction of the plasma is not yet high enough to guide the laser, the pulse is already being depleted. In contrast, in the region at the back of the pulse the index of fraction is high enough to guide the laser, it has no gradient so there is no pump depletion. When a_0 is not sufficiently high (as in the cases of $a_0 = 2$ and $a_0 = 3$), the rise in permittivity is gradual, and pump depletion is not localized to the front of the pulse. In the Wigner transform, it can be seen that the frequency content at the very front of the laser remain unchanged.

In Figure 5.8 we plot the laser amplitude and the relative permittivity along the $r = 0$ axis as well as the laser spot size versus $\xi_{\text{front}} - \xi$ where ξ_{front} is defined at the position of the box where the front of the longitudinal laser profile was located at its initialization. In Figure 5.8:(a), we show the initial lineouts for the $a_0 = 4.44$ and $n_p = 1.0 \times 10^{18} cm^{-3}$ case. In Figure 5.8:(b), the laser has propagated $0.25 L_d$ into the plasma. The spot size of the laser is seen to be expanding as in vacuum. However, a large part of the leading edge of the laser is expanding more slowly. After 0.5 L_d of propagation (Figure 5.8:(c)) the laser has steepened. In Figure 5.8:(d) we show results for a larger a_0 case after $0.25 L_d$ of laser propagation. This case shows steepening occurs closer to the front and more of the pulse is guided. The steepening is partly due to the local pump depletion in the front. We note that the increase in spot size at the rear of the pulse is an artifact of the diagnostic. Laser energy is reflected near the plasma edge at large r from the front of the laser and contribute to the spot size diagnostic.

In section 2.6 we addressed the question of whether self guiding will scale as needed as we scale to lower densities to achieve higher energies. We investigated the width in ξ at the front of the laser that is required before ψ grows to the necessary value for self-guiding. This resulted in the estimate given in equation 2.37 (From the quasistatic approximation we know that the permittivity along the axis of the plasma is a function of ψ). We may compare the normalized distance from the front of the laser that it takes for the permittivity to rise to

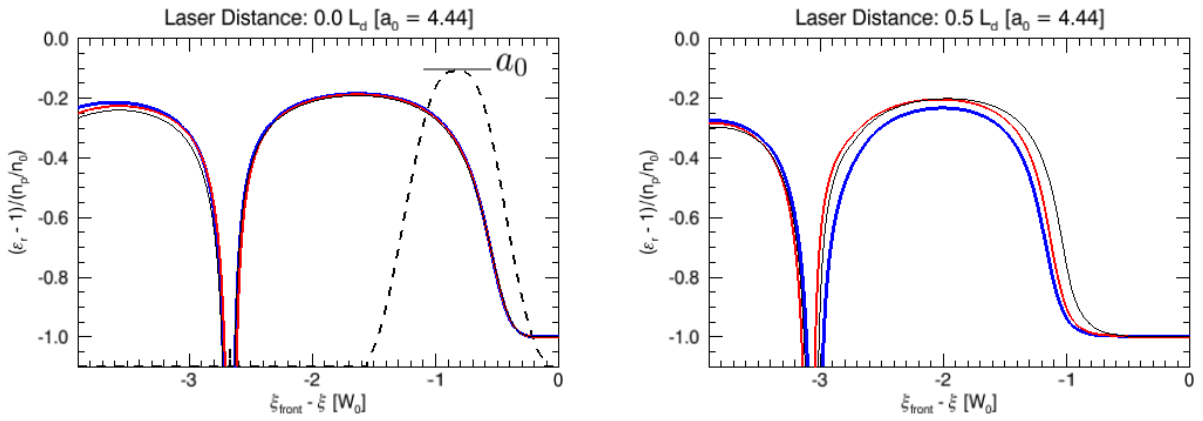

Figure 5.9: The relative permittivities along the axis of the three scaled LWFA simulations with $a_0 = 4.44$, and a plasma density of $n_p = 1.0 \times 10^{18} cm^{-}3$ (black), $5.0 \times 10^{17} cm^{-}3$ (red), and $2.5 \times 10^{17} cm^{-}3$ (blue), for a laser propagation distance of $\approx 0.0 L_d$ (left), and $0.5 L_d$ (right). The horizontal axis is measured as the distance ξ, as a fraction of the initial spot sizes, W_0, from the front of the initial laser profile, ξ_{front}.

a significant value, and thus allow the rest of the laser to self-guide[5]. In order to compare the growth of the relative permittivity along the laser as we scale to lower plasma densities, we plotted the related value $(\epsilon_r - 1)/(n_p/n_c)$ in Figure 5.9. The relative permittivity is zero at the front of the laser. When each simulation has a matched spot size, and the FWHM of the intensity profile used in the OSIRIS simulations is matched to $\frac{2}{3}W_0$, the first half max of the intensity occurs at $\xi_{\text{front}} - \xi_{\text{Half Max Rise}} = -0.53W_0$, and the second half max is at $\xi_{\text{Half Max Fall}} - \xi_{\text{front}} = -1.20W_0$. Therefore, when the rise in permittivity slips back on the right side of Figure 5.9 for a lower plasma density, it means that a slightly greater portion of the laser will diffract as compared to a higher density case.

We know from Figure 5.6 that the laser remained self-guided for all of the simulations presented in Table 5.2. However, it may prove illuminating to compare the evolution of the permittivity rise for each of these simulations to see in detail how well the self-guiding scaled in each run. We can see from Figure 5.9 that as we scaled the parameters to lower plasma

[5]Note that once blowout occurs then the meaning of Ψ with respect to self-guiding and photon deceleration changes.

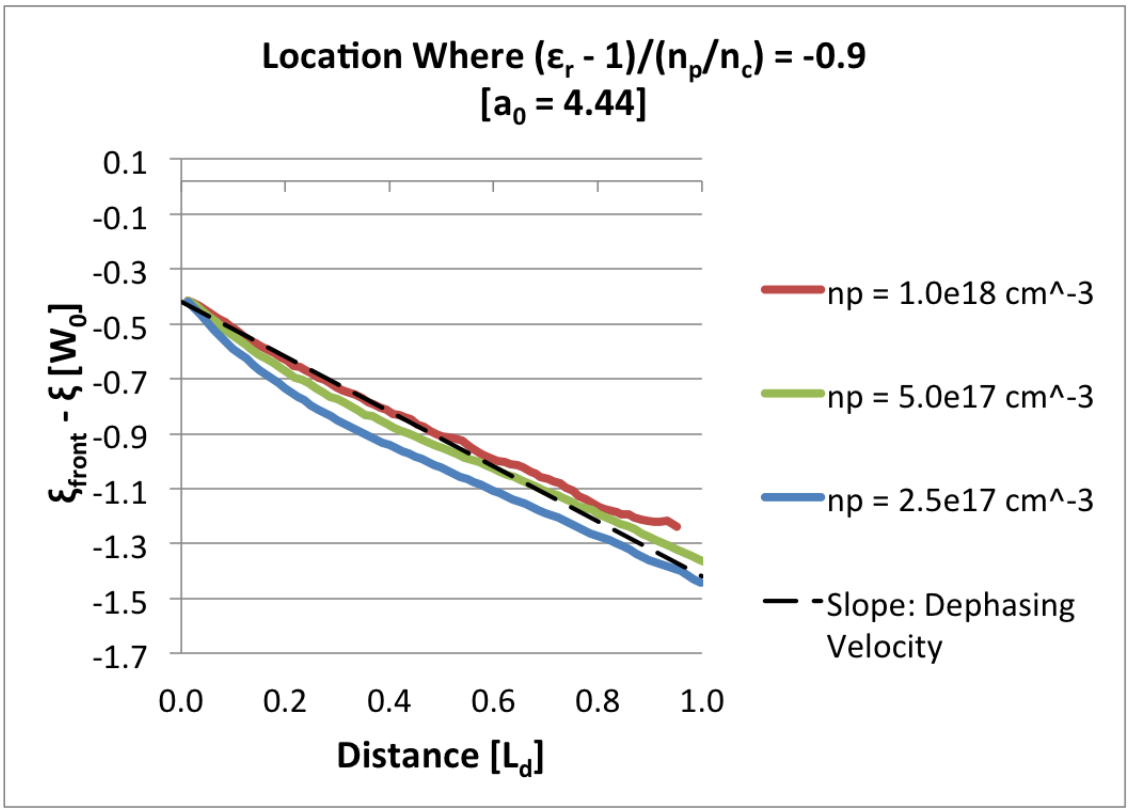

Figure 5.10: The approximate location of the first significant increase in permittivity, which we have declared as the point along the axis where $(\epsilon_r - 1)/(n_p/n_c) = -0.9$. This threshold is somewhat arbitrary, but is sensible as you can see from Figure 5.9 that $\epsilon_r - 1$ rises rapidly upwards from -1. You can extrapolate that within the region above the lines presented in this plot, a laser cannot be self-guided, whereas in the region below the lines a laser would be partially to fully self guided.

densities with a fixed a_0, there was some increase in the slippage of the permittivity rise over the course of the dephasing length. We can quantify this difference in slippage by tracking the location at which $(\epsilon_r - 1)/(n_p/n_c) = -0.9$, as a representation of the first significant rise in the permittivity of the plasma along the axis, as we have in Figure 5.10. The choice of 0.9 is somewhat arbitrary, but is sensible as can be seen from Figure 5.9 where $\epsilon_r - 1$ rises upwards from -1. We can extrapolate that within the region above the lines presented in this plot, a laser cannot be self-guided, whereas in the region below the lines a laser would be partially to fully self guided. Although there is a slippage of the permittivity rise between the $n_p = 1.0 \times 10^{18} cm^{-3}$ simulation and the $n_p = 2.5 \times 10^{17} cm^{-3}$ simulation, it is fairly small considering the fact that the laser has propagated, in one L_d, nearly twice as many Rayleigh lengths as in the latter case. The greatest significant difference is early in the simulation, below $L_d = 0.2$. After this propagation distance the slopes of each line remain more or less the same - indicating that a steady state of laser evolution has been reached.

5.3 Scaling to Lower Densities While Varying a_0

5.3.1 Non-Scaling of Particle Energy Evolution and Dephasing

	Calculated							Simulated	
a0	P (TW)	τ (fs)	n_p (cm^{-3})	Z_R (cm)	W_0 (μm)	L_d (cm)	Est. E (GeV)	Q_{mono} (pC)	Max E (GeV)
4.44†	324	50	1.00e18	0.19	22.0	2.62	2.52	306	3.46
5.1	1000	80.0	5.0e17	0.48	35.0	8.40	5.8	N/A	6.76
5.86	2984	117.7	2.5e17	1.04	51.5	24.0	13.9	N/A	13.6

Table 5.3: † This is the same simulation as is presented in the first line of Table 5.2. In these quasi-3D simulations a_0 was scaled as $\sim (1/n_p)^{1/5}$, which is the suggested scaling by Lu et al. to match localized laser diffraction with the laser lost due to pump depletion.

A separate, related series of quasi-3D PIC simulations were conducted with OSIRIS in

order to compare how the wake evolution and trapped particle acceleration scales to lower density, as we scale the normalized laser amplitude upwards. The simulations in section 5.2 were all performed with $a_0 = 4.44$ as we scaled to lower densities, but if we followed the suggestion of section 2.6 we would increase the laser amplitude to $a_0 = 5.1$ for a plasma density of $n_p = 5.0 \times 10^{17} cm^{-3}$, and to $a_0 = 5.86$ for $n_p = 2.5 \times 10^{17} cm^{-3}$. Scaling a_0 in this way is intended to lower the ratio of the length of the laser lost due to localized diffraction to the amount of laser lost due to pump depletion over each Rayleigh length, as compared to the $a_0 = 4.44$ and $n_p = 1 \times 10^{18} cm^{-3}$ case.

Two new simulations were conducted with $a_0 = 5.1$, $n_p = 5.0 \times 10^{17} cm^{-3}$, and $a_0 = 5.86$, $n_p = 2.5 \times 10^{17} cm^{-3}$, over the normalized dephasing length, L_d. Each simulation was conducted with a laser with a matched spot size, the same normalized pulse length and the same transverse and longitudinal profile shapes. In both cases $\Delta z k_0 = 0.2$, and $\Delta r k_p \approx 0.068$, and 0.057 were used, respectively. The (r,z) box sizes were $(15.2W_0, 6.4W_0)$, and $(14.6W_0, 3.9W_0)$, respectively, and were chosen to be wide enough that no boundary effects were visible. As before particles were initialized at two locations in each r-z cell and at each location 8 particles were initialized along ϕ. The basic physical parameters of these simulations are presented in Table 5.3.

These simulations show when scaled in this way the results are not "similar" when plotted in normalized (scaled) units. In Figure 5.11 we plot the density profiles of each of these LWFAs with the axis scaled to the spot size of each simulation. Comparison with similar plots for the fixed a_0 cases presented in Figure 5.1 clearly indicates that the features of the plasma blowout no longer scale equivalently for these runs where we have increased the value of a_0. One may similarly compare Figures 5.12 and 5.2 to see that the phase space density profile of the trapped particles have also scaled differently in each of these runs. Namely, for the two lower density, higher a_0 instances, the spectrum of the self-trapped particles are no longer quasi-monoenergetic, and there now exists a long tail of trapped particles with lower energy. A much greater number of particles are being trapped in general leading to the significant increase in beam loading, which explains in part the differences in wake structure visible in Figure 5.11 at the back of the bubble.

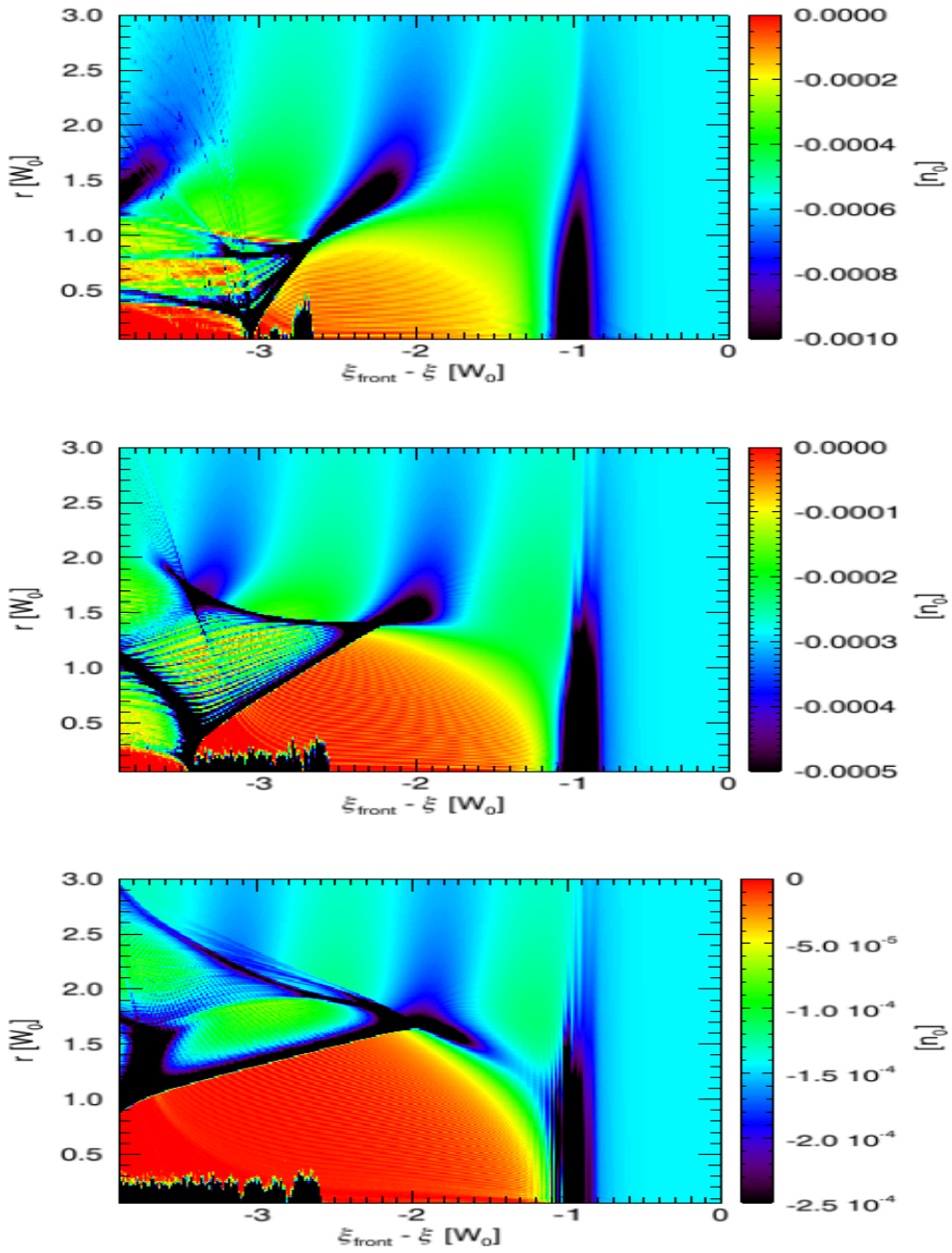

Figure 5.11: The 0^{th} azimuthal mode of the density of the $n_p = 1.0 \times 10^{18}$, $a_0 = 4.44$ (top), $n_p = 5.0 \times 10^{17}$, $a_0 = 5.1$ (middle), and $n_p = 2.5 \times 10^{17}$, $a_0 = 5.86$ (bottom) LWFA simulations. The laser has traversed $0.5L_d$ into the plasma. The horizontal axis is measured as the distance ξ, as a fraction of the initial spot sizes, W_0, from the front of the initial laser profile, ξ_{front}.

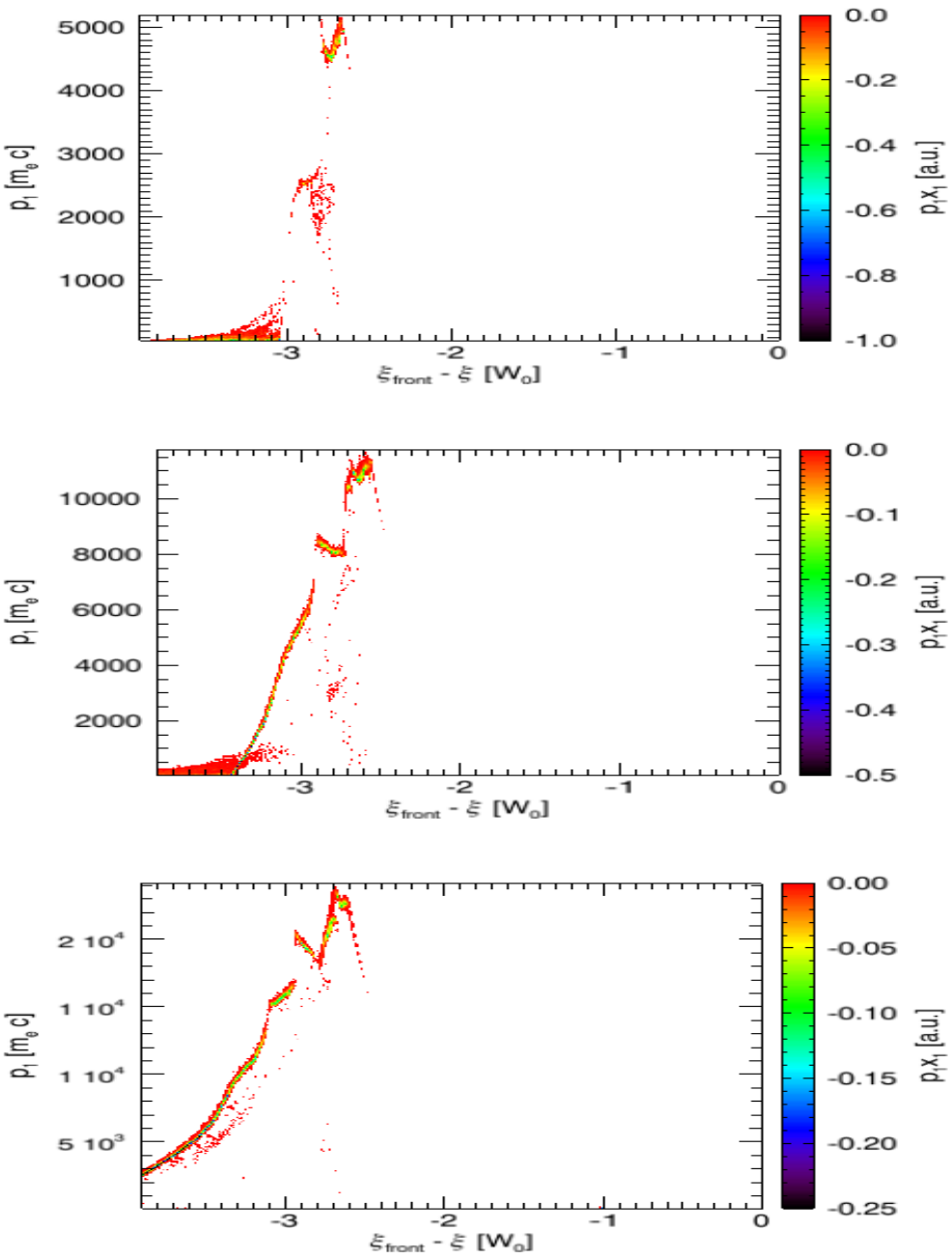

Figure 5.12: The $p1x1$ of the trapped particles in the $n_p = 1.0 \times 10^{18}$, $a_0 = 4.44$ (top), $n_p = 5.0 \times 10^{17}$, $a_0 = 5.1$ (middle), and $n_p = 2.5 \times 10^{17}$, $a_0 = 5.86$ (bottom) LWFA simulations. The laser has traversed $0.5L_d$ into the plasma. The horizontal axis is measured as the distance ξ, as a fraction of the initial spot sizes, W_0, from the front of the initial laser profile, ξ_{front}.

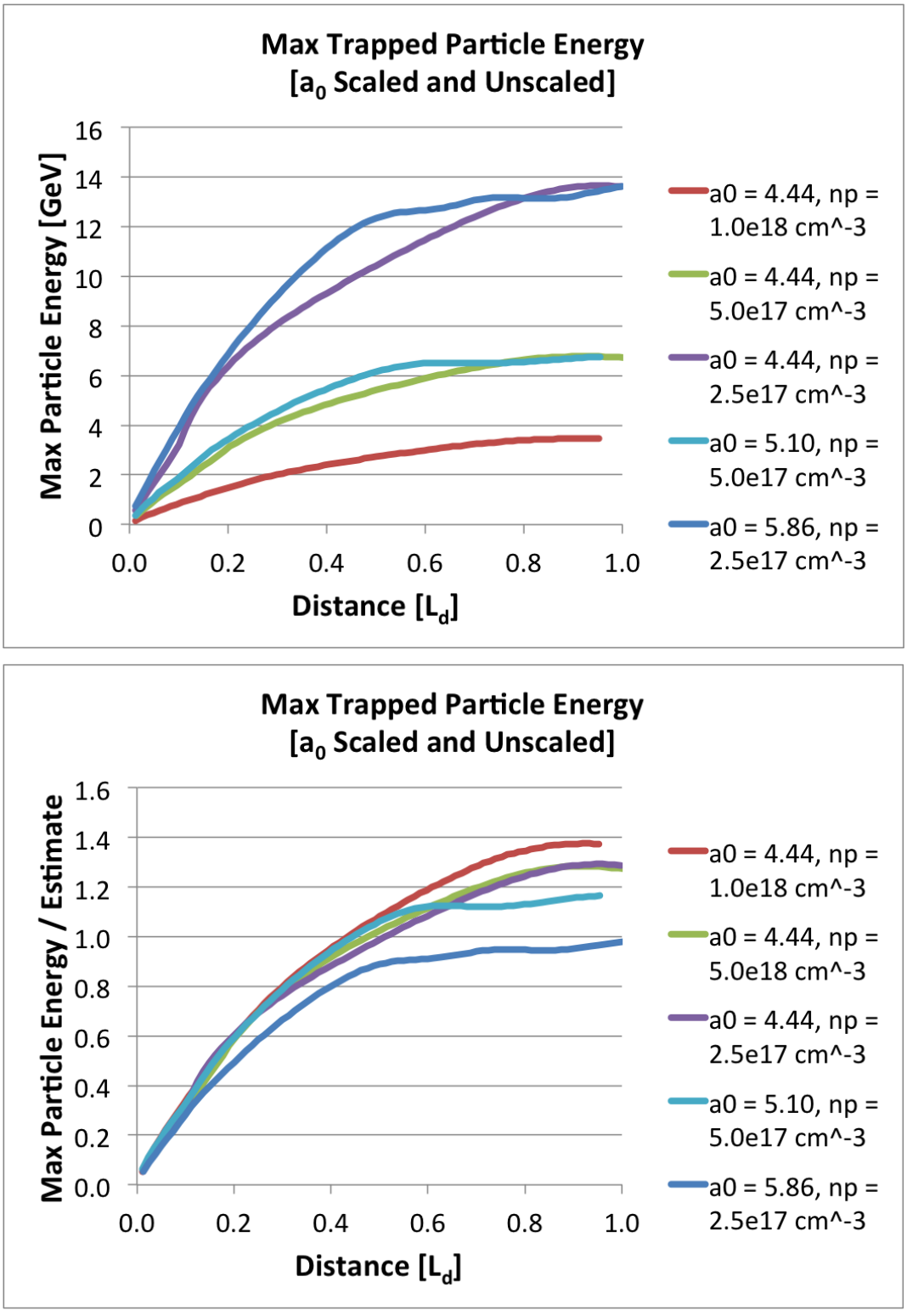

Figure 5.13: The evolution of the maximum trapped particle energies in GeV (top) and as a fraction of the estimate (bottom) for each scaled simulation.

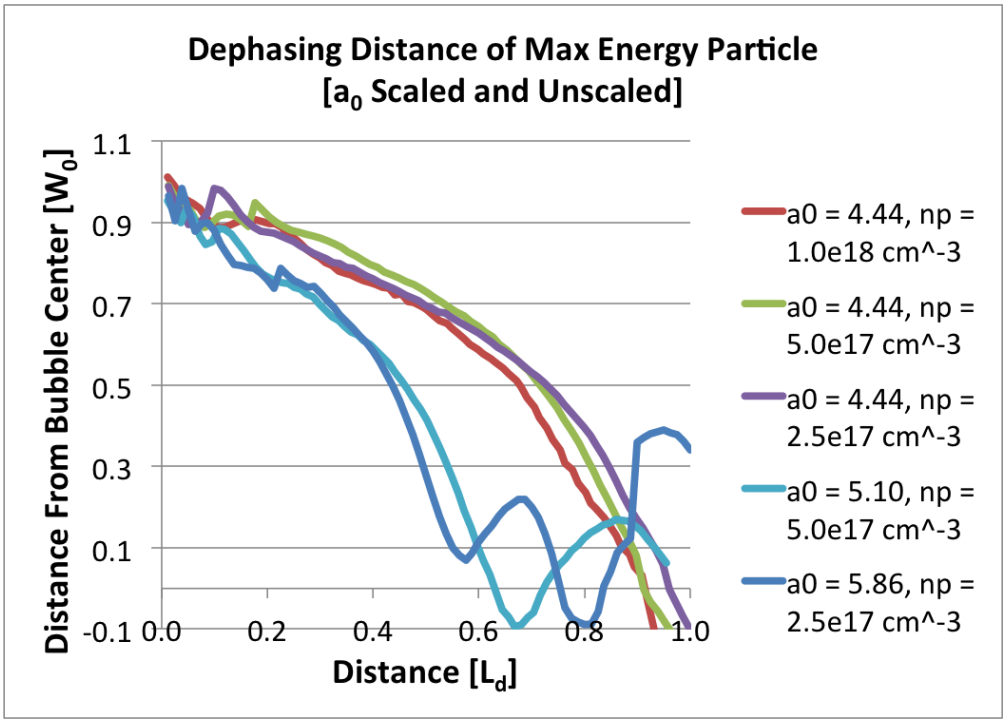

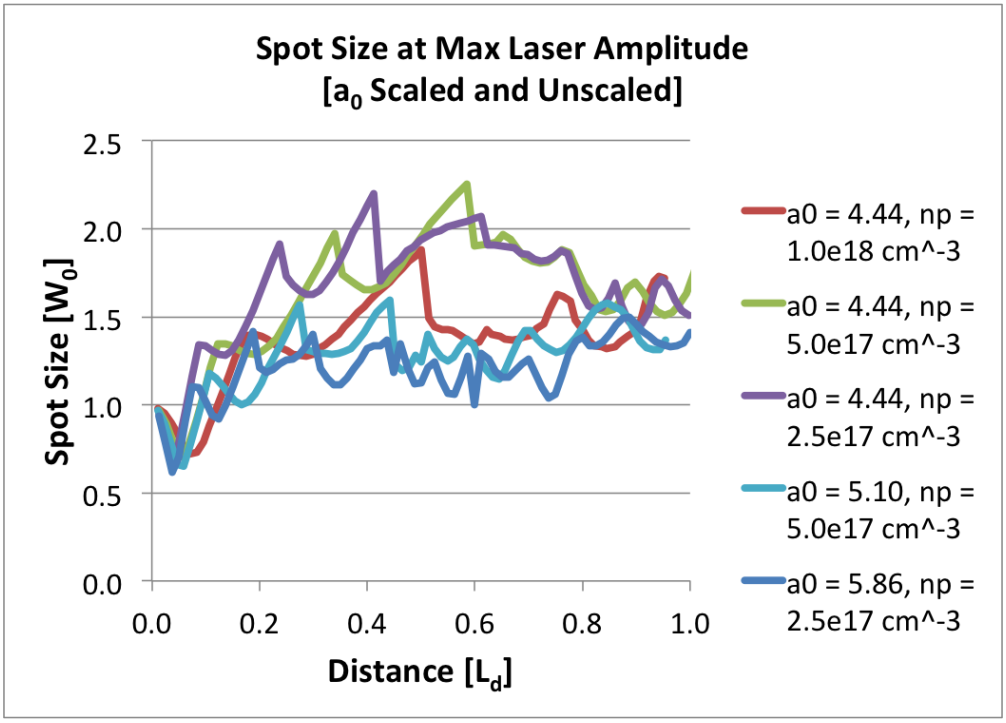

Figure 5.14: Top: The scaling of the evolution of the distance between the position of the trapped particle with maximum energy, and the zero of the accelerating field structure - also described as the distance remaining for the particles to dephase with the wake. Bottom: The evolution of the spot sizes at the position of the max laser field.

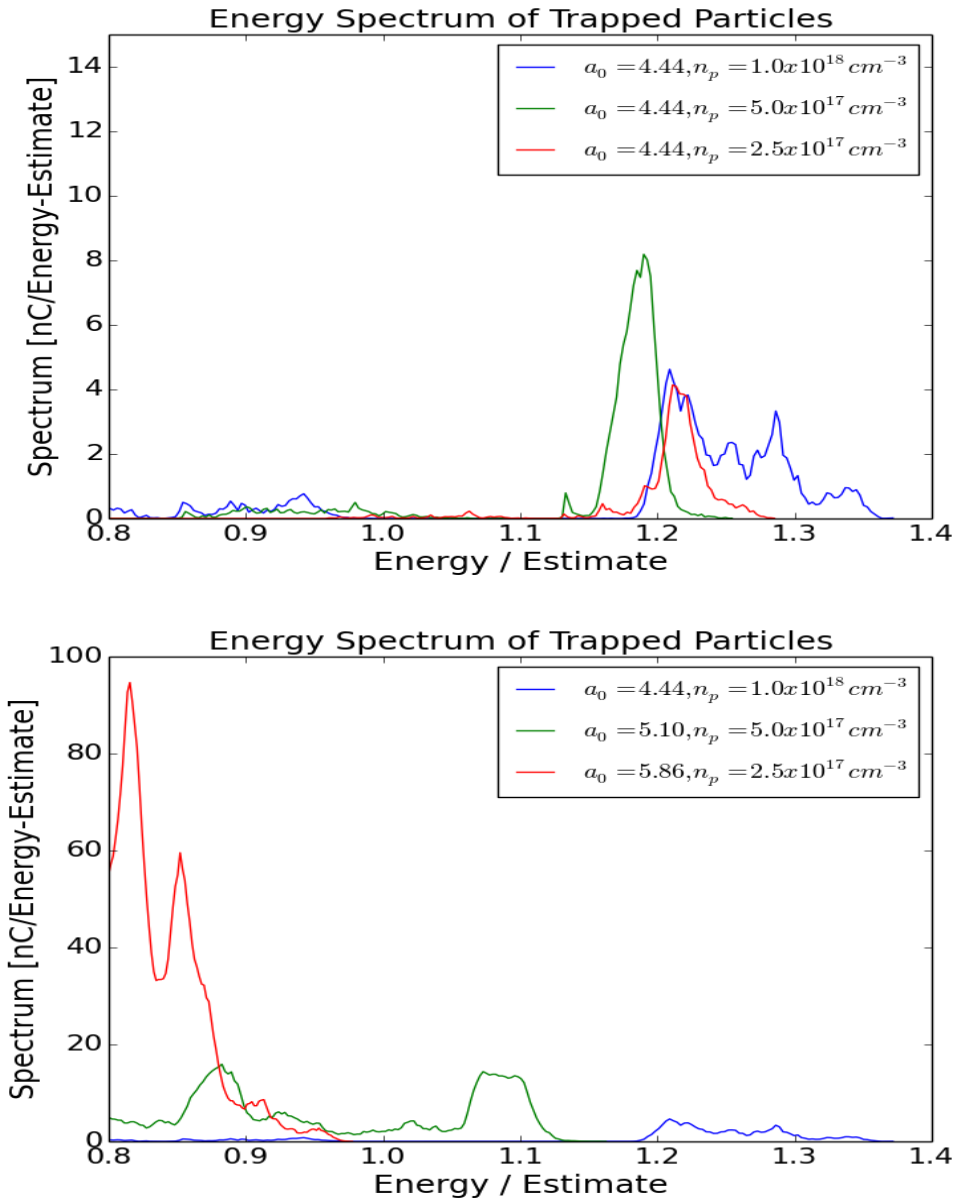

Figure 5.15: The overlapped trapped particle spectrums for scaled simulations with a fixed a_0 (top), and an a_0 scaled as $(1/n_p)^{1/5}$ (bottom) - the quantities plotted as a fraction of the energy estimate. They are all plotted after the laser has traversed a distance of L_d, given their respective plasma parameters.

Quantitatively, we can observe the differences by plotting the evolution of the trapped particle energies for these simulations in comparison to the fixed a_0 cases in Figure 5.13. We see that there is a comparative drop in trapped particle energies as compared to simulations with equivalent plasma densities but lower a_0. This is in contrast to the scaling law estimate which predicts a higher trapped particle energy for fixed density and an increased a_0. It is also apparent from these plots, that, although the evolution of the energies scale well for fixed a_0 simulations, this is not so for simulations with increased a_0. For the cases in which $a_0 = 5.1$ and $a_0 = 5.86$, the particles cease to accelerate long before the estimated dephasing length, L_d. The unexpectedly quick dephasing of the particles with the wake results in a lower overall energy gain in normalized units. The difference is most remarkable for the latter simulation, with $n_p = 2.5 \times 10^{17} cm^{-3}$, for which the trapped particle energy actually plateaued below the scaling law estimate. This is an indication that processes which are not considered in the phenomenological scaling laws are taking effect when a_0 is increased above the parameters presented in the previous section. When we compare the trapped particle spectrums of these simulations at the point of particle dephasing as we do in Figure 5.15, we can also confirm the loss of the mono-energetic feature.

In the top of Figure 5.14, we plot the evolution of the distance between the max energy particle and the zero of the longitudinal wake field structure. As we scale to lower densities while keeping $a_0 = 4.44$ constant, we found that the distance at which the maximum energy particle reached its maximum value remained roughly the same. Namely, it dephased once the laser propagated $0.91L_d$, $0.90L_d$, and $0.95L_d$, for $n_p = 10.0$, 5.0, and $2.5 \times 10^{17} cm^{-3}$, respectively [6]. When a_0 was increased to 5.1 for the plasma density of $5.0 \times 10^{17} cm^{-3}$, however, the particles dephased prematurely at $0.62L_d$. For the highest amplitude run with $a_0 = 5.86$ it dephased slightly later at $0.75L_d$, after appearing to oscillate once. The trapped particles, which are traveling at a velocity very close to c, sit at a relatively fixed point in the simulation box, which is a window moving along the plasma at a velocity of c. Therefore, the evolution of the laser and the bubble structure is primarily responsible for the premature

[6] This is also a verification that the given estimate for the dephasing length, L_d, is highly accurate for this value of the normalized laser amplitude ($a_0 = 4.44$).

dephasing of the particles.

Further examination of the simulation results indicate how the increase of a_0 has altered the evolution of the wake. The most visible differences in Figure 5.11, as we increase in a_0, are the increased presence of trapped particles, and the increase in the bubble radius in comparison to the initial spot size. These two observations are related. If and when the bubble expands during the evolution of the LWFA, the effective phase velocity of the wake will drop, leading to a relaxed trapping condition for the plasma particles and a greater overall number of trapped particles. The bubble itself is expanding in a manner that mirrors a significant bump in the maximum laser field shown in Figure 5.16, which indicates that subtleties in the laser evolution processes in the LWFA are responsible for this difference in the wake evolution. In the next section we will discuss in greater detail the manner in which the laser evolution did or did not scale in accordance to our understanding of the phenomenological scaling laws.

5.3.2 Scaling of Laser Evolution

The reason for adjusting a_0 as $(1/n_p)^{1/5}$ was to improve self-guiding over an increased distances in Rayleigh lengths, and thereby to improve the stability of the wake over the course of the particle acceleration process. In contrast, we are observing a less stable wake structure due to the fact that there is an increase in the laser amplitude as shown in Figure 5.16. Interestingly, the spot size evolution is more stable for the scaled a_0 runs as seen in the bottom plot of Figure 5.14. A closer examination will be presented in order to form a clearer picture of how the adjustment in a_0 has affected the self-guiding of the laser and its evolution as a whole.

In order to understand why the laser field amplitude increases for these runs, it is helpful to examine the Wigner transforms of the x component of the laser field along the axis. The Wigner transforms for the $n_p = 5.0\times10^{17} cm^{-3}$ cases with $a_0 = 4.44$ and 5.1 are superimposed with their relative permittivity lineouts[7] in Figure 5.17. Similar to Figure 5.7, this figure

[7]The relative permittivity is calculated with the quasistatic approximation, $\epsilon_r = \eta^2 \simeq 1 - \frac{n_p}{n_c}\frac{1}{1+\Psi}$.

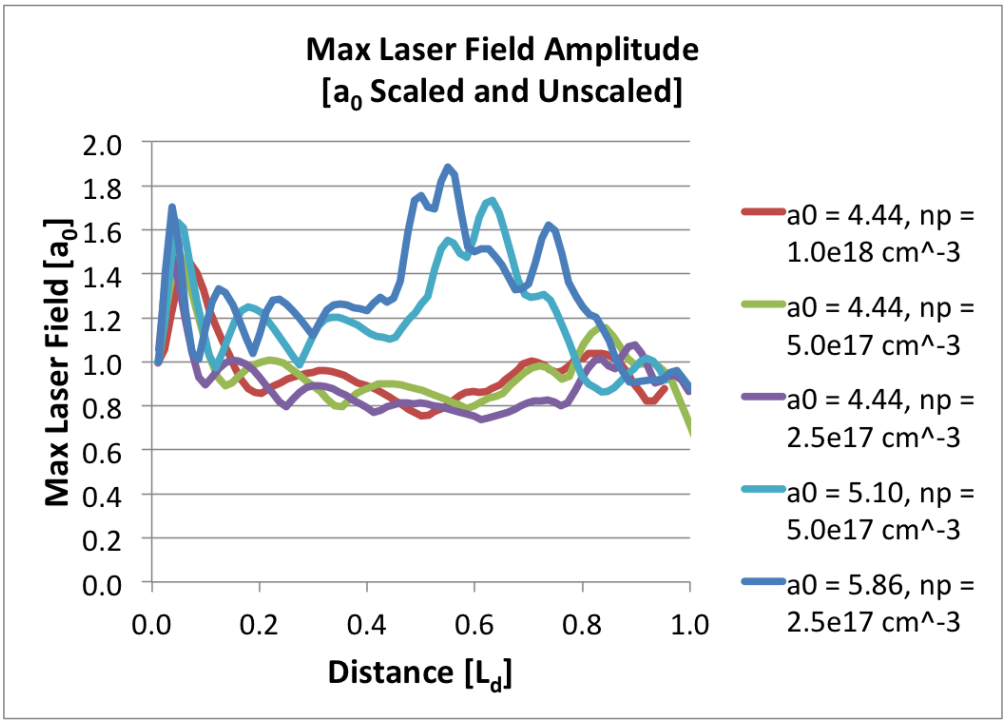

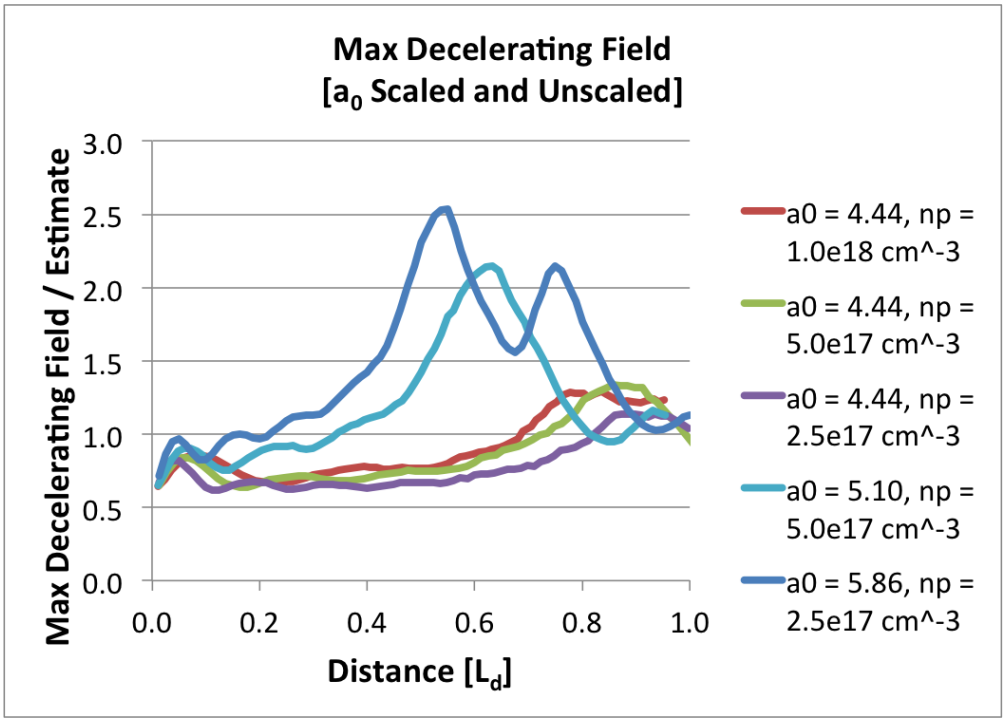

Figure 5.16: Top: The maximum laser field as the laser traverses L_d for various scaled simulation parameters. Bottom: The evolution of the maximum decelerating field, which is proportional to the maximum accelerating field and the bubble radius.

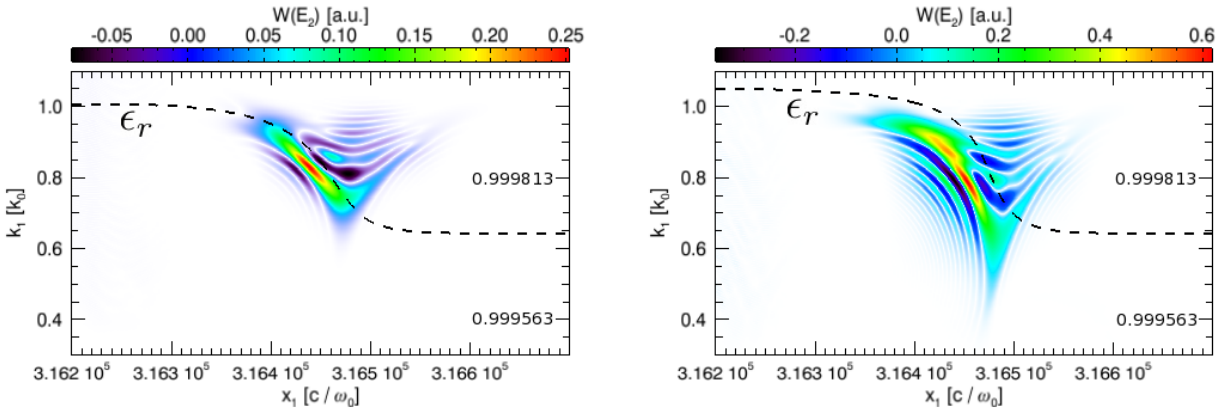

Figure 5.17: The Wigner transforms of the x component of the laser electric field along the axis with the relative permittivity, after a propagation distance of $0.5L_d$. Both plots correspond to a plasma density of $n_p = 5.0 \times 10^{17} cm^{-3}$, with a non-adjusted $a_0 = 4.44$ (left), and adjusted $a_0 = 5.10$ (right), normalized laser amplitudes.

shows how pump depletion, shown as decelerated photons with lowering k values, matches the gradient of the rise in the relative permittivity. For these two equal densities you can see that a higher a_0 results in a sharper gradient in the permittivity, and a more localized region of pump depletion. As is visible for the $a_0 = 5.1$ case, a rapid decrease in the wave number can lead to pulse compression since the faster photons in the tail catch the slower photons in the head of the beam[87, 88, 89]. A narrower, more rapid pump depletion at the head has resulted in a substantial compression at the head of the pulse analogous to how a show plow compresses the snow at the head of its path. Far enough into the plasma ($\approx 0.7L_d$) the compression leads to a maximal point, and the electric field amplitude begins to uniformly deplete resulting in the gradual drop visible in Figure 5.16.

As we scale to lower plasma densities while adjusting a_0, we can see that the initial rise of the relative permittivity becomes comparatively sharper in Figure 5.18. Interestingly, this same plot shows how, over the course of the dephasing length, the front of the permittivity curves remain nearly perfectly overlapped, especially in comparison to the gradual slippage that is seen in Figure 5.9 where a_0 is not scaled but kept fixed. The key point of the argument presented in section 2.6 is that a_0 must be adjusted in order to keep the ratio of the length

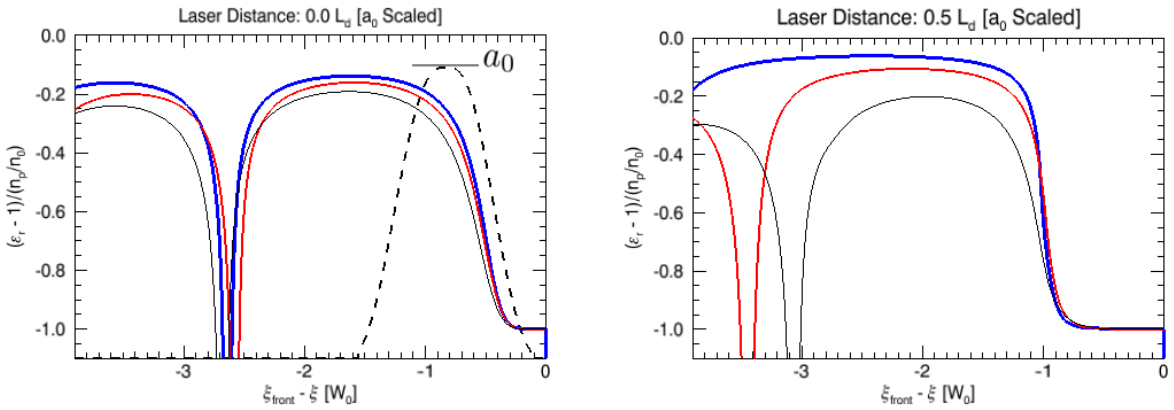

Figure 5.18: The relative permittivities along the axis of the three scaled LWFA simulations with scaled a_0, with $n_p = 1.0 \times 10^{18} cm^{-}3$ and $a_0 = 4.44$ (black), $5.0 \times 10^{17} cm^{-}3$ (red) and $a_0 = 5.10$, and $2.5 \times 10^{17} cm^{-}3$ and $a_0 = 5.86$ (blue). The laser has propagated a distance of $\approx 0.0 L_d$ (left), and $0.5 L_d$ (right). The x-axis is measured as the distance ξ, as a fraction of the initial spot sizes, W_0, from the front of the laser profile, ξ_{front}.

of the plasma susceptible to diffraction over each Rayleigh length to that lost to local pump depletion. The portion of the laser to which is not self-guided is estimated by finding the position where ψ becomes sufficiently large enough guide the laser. The results shown in Figure 5.18 show that indeed if we scale a_0 accordingly we find that after a fixed amount in dephasing lengths the relative permittivity, and therefore ψ, becomes big enough to begin self guiding at the same position relative to the laser profile. Essentially, by scaling a_0 we have sharpened the gradient of the permittivity to compensate for the greater number of Rayleigh lengths that need to be traversed by the laser.

We plot the location of the first significant rise in permittivity along the axis of the laser in 5.19, in the same manner as we did for the fixed amplitude cases in Figure 5.10. We find that by tracking the location where $(\epsilon_r - 1)/(n_p/n_c) = -0.9$ is a crude but useful way of tracking the evolution of the rise in the permittivity. The vertical axis is the distance from the initial front of the laser pulse where the relative permittivity = .09, as a fraction of the initial spot size. This provides an estimate of the ratio of the portion of the laser is not self-guided to the normalized pulse length. When a_0 is scaled as $(1/n_p)^{1/5}$, these lines

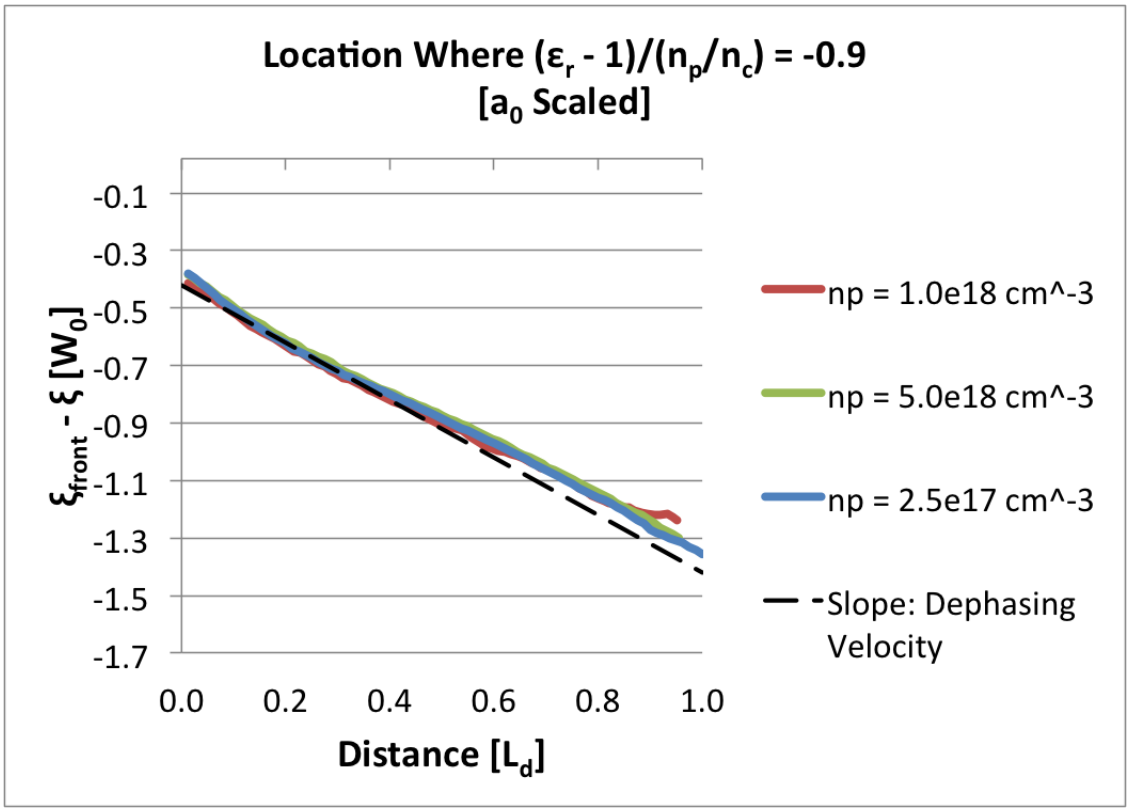

Figure 5.19: The approximate location of the first significant increase in permittivity, which we have declared as the point along the axis where $(\epsilon_r - 1)/(n_p/n_c) = -0.9$. This threshold is somewhat arbitrary, but is sensible as you can see from Figure 5.18 that $\epsilon_r - 1$ rises upwards from -1. You can extrapolate that within the region above the lines presented in this plot, a laser cannot be self-guided, whereas in the region below the lines a laser would be partially to fully self guided.

representing the diffraction front follow extremely with the dephasing velocity, especially in comparison to the unscaled cases presented in Figure 5.10. These results when taken together show that the original concept of increasing a_0 in order to match the evolution of the diffraction front with the rate at which the laser is proportionally lost due to pump depletion is confirmed.

Unfortunately, for the very reason that the gradient of the permittivity is becoming sharper with increased a_0, pump depletion is more severely localized, and the pulse compression at the head of the pulse becomes significant enough to alter the evolution of the maximum laser field amplitude. The increase in the field amplitude causes the bubble radius to expand midway through the dephasing length (inferred by Figure 5.16), which results in an overall shifting of the bubble center and a premature dephasing of the trapped particles (inferred by Figures 5.13 and 5.14). Considering that section 5.2 demonstrated that self guiding was effective to particle energies above $10GeV$, and that the particle acceleration and bubble evolution scaled remarkably with a fixed a_0, one may conclude that it is not necessarily advantageous to increase a_0 for what appears to be a marginal improvement for the guiding properties.

The results of this Chapter taken as a whole reveal that the phenomenological scaling laws of Lu et al. provide a very useful approach to understand LWFA in the self-guided blowout regime. In some cases, if a_0 and the shape of the laser in both the axial and transverse directions are kept fixed then within reason the results of one simulation can be scaled to higher energies. However, these simulations also show that for the parameters we considered it is not practical to attempt to develop a true "self-similar" theory where all details within a single simulation can be scaled to lower densities and higher laser energies. Furthermore, if one scales the results to higher a_0 (or changes the laser pulse shape or transverse profile), then the details of the physics makes it difficult to simply scale the results, rather one has to understand how the key phenomena that has been identified will be effected. A new simulation must be performed and then these results can then be "scaled" if a_0 and the axial and transverse profiles are all kept fixed.

5.4 Conclusion

In this Chapter, we were able to explore the extent to which our existing phenomenological scaling law for LWFAs operating in the blowout regime extended to particle energies above $10GeV$ because of a new computationally cost effective and robust simulation framework provided by the new, quasi-3D algorithm in OSIRIS. We find that although the phenomenological scaling laws of Lu et al. are very useful, that one must always consider the possibility that the relative importance of physical effects will come into play and that the understanding of the phenomenology can be refined. The simulations reveal that as one scales results for fixed a_0 that the details of the evolution of the wake and laser do not scale as well as the final energy of the electrons scale. The new computational capability allows us to better understand the extent to which diffraction effects modify the scaling as we extend the dephasing length to many Rayleigh lengths. Fortunately, our simulations show that effective self-guiding of the laser is possible over this range of parameters without even having to adjust the normalized laser amplitude in order to compensate for it. In fact, we found that many of the finer details of the physics scale if we keep a_0 fixed as we scale the parameters to lower densities and higher particle energies. In addition, it appears that for a fixed laser energy the the electrons energy scales better when the value of a_0 is kept fixed. The implications for the scaling laws for fixed laser energy are examined in great detail in the next Chapter.

The fine details and qualitative characteristics of the scaling laws are found to be reasonable. When the pulse length, spot size, and plasma densities are appropriately adjusted, and a_0 remains fixed, the temporal evolution of the wake and the trapped particles remain very similar. Even the shape of the trapped particle energy spectrums remain the same, retaining their characteristic mono-energetic features to higher and higher energies. We discovered that an exception to this rule can occur when a_0 is increased. When a_0 is increased, it appears that a sharper increase in the permittivity of the plasma occurs along the axis of the LWFA. This is ideal when intending to exactly match the evolution of the diffraction front over the dephasing length, but results in a significant alteration of the evolution of the

frequency profile of the laser. The overall effect, unless otherwise compensated, will be that a sharp rise in the laser amplitude may occur from a snowplowing of the rapidly decelerated photons at the front of the laser. The result of the laser amplitude rise is an expanding wake, the premature dephasing of the trapped particles, and a lower final particle energy compared to the scaling law prediction. It is possible that this effect may be compensated for by adjusting the longitudinal profile of the laser, and that is a potential area for future research.

A detailed and accurate understanding of the scaling of LWFA parameters to higher energies is crucial in the development and design of existing and future accelerators. Given a specific set of apparatus operating at an incorrectly scaled set of parameters, one may obtain sub-optimal results in particle acceleration.

CHAPTER 6

Optimization of Self-Guided LWFAs with Fixed Laser Energy

6.1 Motivation

The scaling laws as presented in section 2.5 provide a powerful tool for estimating the accelerated electron beam energy given a laser's power P and a plasma density n_p. Furthermore, it suggests that, given that the spot size, W_0, is matched according to Equation 2.23 and the laser axial profile is scaled proportionally to W_0, the acceleration and dephasing process of the laser should scale on the order of the dephasing length, L_d, defined in Equation 2.27. Given a specific set of parameters we find ideal for a LWFA with a shorter acceleration length, we may scale it to a longer dephasing length if the plasma density is lowered, and expect "similar" evolution of the laser, wake, and accelerated electrons if the quantities are scaled properly.

However, for many experimental applications, it is not practical to think in terms of successively reducing the plasma density while increasing the laser power and total laser energy. Experimental facilities have lasers with limited ability to change the total energy, but with possible control over its spot size and pulse length. In addition, the plasma profile provided by a gas jet or a pressure chamber is more easily adjusted to optimize the LWFA given a specified laser profile. Therefore it is useful to investigate the best laser profiles to optimize the output energy for a fixed laser energy.

It is also important to note that Lu et al.[4] suggests a laser profile that matches the estimated dephasing length to the estimated laser etching distance, giving a pulse length of

$\tau_{\mathrm{FWHM}} \cong (2/3)W_0$. This is a useful starting point to guarantee self-guiding over the course of the dephasing distance, but in practice it is possible to use a shorter pulse length without significant negative effects to the laser and wake evolution, while permitting using lower plasma density and hence higher particle energy. When optimizing a laser for a fixed energy, it would be beneficial to know exactly how much you may trim the pulse length in practice. This will be discussed in greater detail in section 6.5.

In this chapter we will reformulate the phenomenological scaling laws in order to determine the ideal plasma density n_p given a total laser energy E_L. Furthermore, we will explore the extent to which we may adjust the laser spot size, pulse length, and amplitude for a laser with fixed energy in such a way that we may optimize the desired qualities of a LWFA operating in the nonlinear, self-guided regime. The degree to which we will explore the possible laser profile characteristics will be discussed in section 6.2. In section 6.3, we will rewrite the scaling laws in a form that is useful for a fixed laser energy, while in sections 6.4 and 6.5 we will present and discuss numerous OSIRIS simulations in which we explore the various possible adjustments to the laser profiles discussed in section 6.2. Section 6.6 addresses the effect of longitudinally asymmetric, i.e., forwardly skewed pulse profiles for optimizing the electron energy. In section 6.7, we will present observations on how to choose ideal LWFA parameters for future simulations. We will summarize our results in section 6.8.

6.2 Details Concerning the Laser Profile Characteristics

If the laser energy is assumed fixed and the transverse profile is a symmetric Gaussian shape then there is are limited paths to adjusting the laser shape. You may,

- increase the amplitude a_0, which necessitates decreasing its overall volume (spot size and pulse length), and/or
- decrease the pulse length and increase the spot size to retain volume, or
- change the longitudinal profile, i.e., use asymmetric longitudinal profiles.

It is simple and general to use a Gaussian profile in the transverse directions as Gaussian beams remain close to Gaussian as they self-guide. Furthermore, we assume it is symmetric in the transverse plane. There is a lot of room for exploring various longitudinal laser profiles, as they would presumably alter the evolution of the laser profile over the course of the particle acceleration process - particularly if the laser is longitudinally asymmetric. However, in interest of simplicity, we will restrict our attention here to the default longitudinal profile for the electric field in the OSIRIS simulation framework, which is the polynomial

$$
\begin{aligned}
f_{\text{poly}}[\overline{z}(z)] &= 10\overline{z}^3 - 15\overline{z}^4 + 6\overline{z}^5 \\
\overline{z} &\equiv \frac{|\text{lon\_start} - z|}{\text{lon\_rise}} \qquad \text{, for } z > \text{lon\_start - lon\_rise} \\
\overline{z} &\equiv \frac{z - \text{lon\_start} + \text{lon\_rise} + \text{lon\_fall}}{\text{lon\_fall}} \qquad \text{, for } z < \text{lon\_start - lon\_rise,}
\end{aligned}
\tag{6.1}
$$

where 'lon_rise' is the length of the polynomial rise, 'lon_fall' is the length of the polynomial fall, and 'lon_start' is the location of the right edge of the longitudinal profile. In section 6.6 we will explore situations in which 'lon_rise' is smaller than 'lon_fall', designating a forwardly skewed pulse. Note also that this is the profile for the electric field (not intensity) of the laser pulse when it is initiated in the simulation grid. When we speak of the pulse length τ_{FWHM}, we are speaking of the FWHM of the intensity profile, which is roughly 1.295 times the FWHM of the above function for symmetric pulses.

In order to quantitatively understand how the laser parameters can be altered for a fixed laser energy we need to have a rigorous method to calculate the laser energy for the assumed transverse and longitudinal profiles. First, if we assume that the pulse is a symmetric Gaussian, $E \sim e^{-r^2/W_0^2}$, in the transverse directions with a spot size W_0, and integrate across the plane we obtain,

$$P_0(z) = \frac{\pi}{2} I_0(z) W_0^2, \tag{6.2}$$

where P_0 is the total power of that x-y cross-section , and

$$I_0(z) = \frac{c}{8\pi} E_0^2(z) = \frac{c}{8\pi} \left(\frac{m_e c \omega_0}{e} \right)^2 a_0^2 f^2(z) \tag{6.3}$$

is the max intensity on the axis along z, and $f(z)$ is an arbitrary longitudinal profile normalized such that the maximum value is 1. The total energy of the laser is given by

$$E_L = \frac{1}{c}\max(P_0)\int_{z_{\min}}^{z_{\max}} f^2(z)dz, \tag{6.4}$$

where $z_{\min}$, and $z_{\max}$ marks the axial span across which the laser exists.

6.3 Scaling Law for a Specified Laser Energy

The equations in section 2.5, taken from Lu et al.[4], are expressed in terms of the laser power P and the plasma density, n_p, or quantities that are directly calculated from the plasma density such as ω_p and k_p. The total laser energy E_L can be calculated by the laser power and pulse length as

$$E_L = \alpha P \tau, \tag{6.5}$$

where $\tau \equiv \tau_{\text{FWHM}}$ of the energy, and α is a constant that depends on the exact shape of the longitudinal profile (for a symmetric longitudinal profile of the functional form given in Equation 6.1, $\alpha \approx 1.04365$). Using Equations 2.25 and 2.22 the power of the laser for a matched spot size can be expressed as a function of n_p, a_0, and ω_0,

$$P = \mathcal{A}\omega_0^2\left(\frac{m_e}{4\pi e^2}\right)\left(\frac{a_0}{2}\right)^3\frac{1}{n_p}, \tag{6.6}$$

where $\mathcal{A}$ is the constant from Equation 2.22 that is equal to 17 GW in MKS units. The pulse length depends ultimately on the choice for the profile of the laser, but for our purposes here we will assume that it is some specified fraction $\mathcal{F}$ of the spot size W_0, or $\tau = \mathcal{F}W_0$. Lu et al.[4] matches the estimated pump depletion distance L_p and the dephasing length L_d (Equations 2.26 and 2.27) by setting $\mathcal{F} = 2/3$, but simulations may find empirically that there is a better choice for this value. In combination with the matched spot size condition presented in Equation 2.23, this gives us

$$\tau = 2\mathcal{F}\sqrt{a_0}\sqrt{\frac{m_e}{4\pi e^2}}\frac{1}{n_p^{1/2}}. \tag{6.7}$$

Substituting Equations 6.6 and 6.7 into Equation 6.5 we find E_L as a function of n_p, and then invert it to find the matched plasma density as a function of laser energy, amplitude,

and proportional pulse length, $\mathcal{F}$,

$$n_p = \alpha^{2/3} \left(\frac{m_e}{4\pi e^2}\right) \left[\frac{\mathcal{A}\omega_0^2}{4}\right]^{2/3} \frac{\mathcal{F}^{2/3} a_0^{7/3}}{E_L^{2/3}}. \tag{6.8}$$

When designing parameters for a LWFA, we may retroactively calculate W_0 from the above calculated density and a specified value for a_0 with the spot size matching condition. Assuming that the trapped particles accelerate over the entire dephasing length, one may estimate the output particle beam energy with Equation 2.32 ($\Delta E = (2/3)mc^2(\omega_0^2/\omega_p^2)a_0$), giving

$$\Delta E = \frac{2}{3}\frac{m_e c^2}{\alpha^{2/3}} \left[\frac{4\omega_0}{\mathcal{A}}\right]^{2/3} \frac{E_L^{2/3}}{\mathcal{F}^{2/3} a_0^{4/3}}. \tag{6.9}$$

There are a number of observations to be made from the above equations. If you keep E_L and $\mathcal{F}$ fixed and conduct LWFA experiments with varying laser amplitudes, the trapped particle energy will drop as a_0 is increased. Although Equation 2.32 suggests that the trapped particle energy increases with a_0, its indirect drop due to the increased density necessitated by Equation 6.8 outweigh this benefit. This means that, broadly speaking, you would want the lowest a_0 possible in order to reach higher particle energies given a laser with a fixed energy. Solutions of this equation for various a_0 given a fixed $\mathcal{F} = (2/3)$ are given in Figure 6.1, illustrating this fact. Optimization by reducing a_0 is limited by the fact that, in order to ensure a spherical ion column and effective self-guiding, $a_0 \gtrsim 4.0$ is required[4, 36].

Another observation from Equation 6.9 is that if you keep E_L and a_0 fixed and decrease $\mathcal{F}$, you will observe an increase in the trapped particle energy. This is due to the fact that, given a fixed energy, if you shorten the length of the pulse you would have to simultaneously increase the spot size, which, by the spot size matching condition, would permit the use of a lower density plasma. This will increase the dephasing length which increases the final energy. This can also be seen from Equation 2.32, which predicts that the trapped particle energy will be higher if a_0 is fixed and n_p is decreased. There is a lower limit to how far $\mathcal{F}$ can be decreased because the laser etches backwards due to local pump depletion and self-guiding may not be possible. This seems to suggest the acceleration distance that is shorter than the dephasing length, $L_p < L_d$, estimated by Equation 2.26. [56]. It is important to note that this estimate is taken by calculating how long the etching process takes to move back

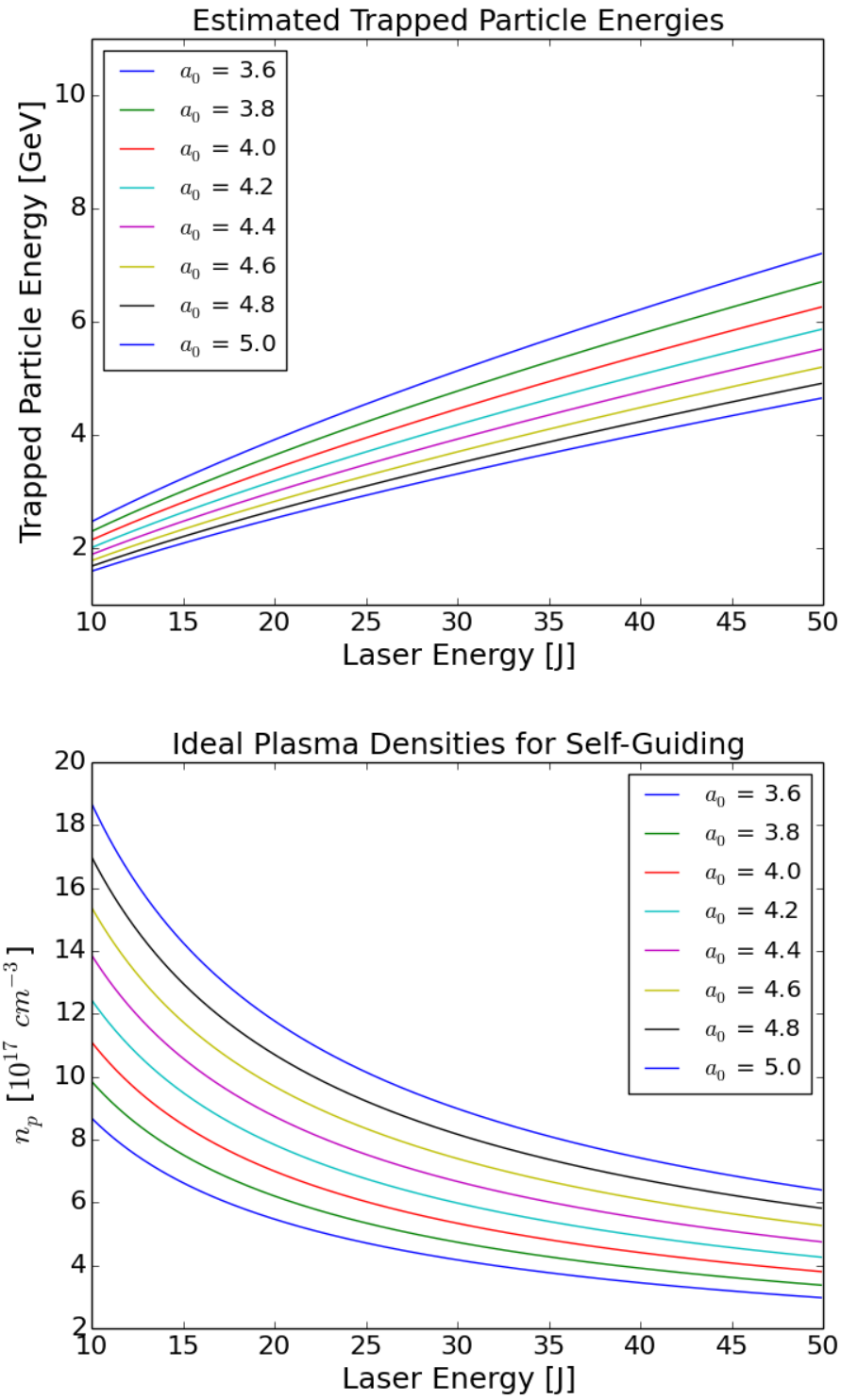

Figure 6.1: Here we show the ideal plasma densities for self-guiding given a specified laser energy and amplitude a_0 (bottom), and the estimated trapped particle energies (top). Here, $\mathcal{F} = 2/3$, with a symmetric longitudinal profile of the form described in Equation 6.1.

through the FWHM of the laser intensity, τ. The FWHM of the square of the longitudinal profile described in Equation 6.1 is in fact ≈ 0.3856 times the total length of the profile from the zero in the front to the zero in the back. In reality the etching can occur over a longer distance across the laser profile than the FWHM of the intensity, and therefore the optimal pulse length may be shorter. The exact extent to which we can afford to shorten the pulse may depend on the evolution of the longitudinal profile over the course of the acceleration process. As noted earlier simulations can be used to empirically determine $\mathcal{F}$. The results will also change if the longitudinal profile is also different.

6.4 Laser Amplitude Adjustment

Calculated								Simulated	
a0	P (TW)	τ (fs)	n_p ($10^{17} cm^{-3}$)	Z_R (cm)	W_0 (μm)	L_d (cm)	Est. E (GeV)	Q_{mono} (pC)	Max E (GeV)
3.80	271	53.1	7.52	0.224	23.9	3.70	3.01	231	3.97
4.00	280	51.3	8.48	0.210	23.1	3.17	2.81	176	3.97
4.20	289	49.7	9.50	0.196	22.4	2.74	2.63	265	3.64
4.40	298	48.1	10.6	0.185	21.7	2.38	2.47	337	3.22
4.60	307	46.8	11.7	0.174	21.0	2.08	2.33	402	2.91
4.80	316	45.5	13.0	0.164	20.5	2.08	2.20	477	2.66

Table 6.1: These are the parameters of LWFA simulations for a 15 J laser, given an optimal density calculated with Equation 6.8 and a spot size matched according to Equation 2.23. The ratio of pulse length to spot size is such that $\tau = \frac{2}{3} W_0$. The charge and the max energy of the mono-energetic particle beam are also shown.

Equation 6.9 seems to suggest that, in order to achieve higher accelerated particle energies, one should choose as low a laser amplitude as possible. Although this may be true, this quantity also affects the self-guiding of the laser, the stability of the wake, and the number of self-trapped particles, and therefore it may not be preferable to blindly choose the lowest

Calculated								Simulated	
a0	P (TW)	τ (fs)	n_p ($10^{17} cm^{-3}$)	Z_R (cm)	W_0 (μm)	L_d (cm)	Est. E (GeV)	Q_{mono} (pC)	Max E (GeV)
3.80	429	66.9	4.74	0.356	30.1	7.40	4.77	64.1	5.26
4.00	444	64.7	5.34	0.333	29.1	6.34	4.46	148	6.08
4.20	459	62.6	5.98	0.312	28.2	5.48	4.18	225	5.69
4.40	473	60.7	6.67	0.293	27.3	4.76	3.93	317	5.02
4.60	487	58.9	7.40	0.276	26.5	4.17	3.70	401	4.56
4.80	502	57.3	8.17	0.261	25.8	3.67	3.50	506	4.13

Table 6.2: These are the parameters of LWFA simulations for a 30 J laser, given an optimal density calculated with Equation 6.8 and a spot size matched according to Equation 2.23. The ratio of pulse length to spot size is such that $\tau = \frac{2}{3} W_0$. The charge and the max energy of the mono-energetic particle beam are also shown.

value possible. In order to better understand how the self-guided nonlinear regime for LWFA operates under different initial laser amplitudes given a fixed laser energy, we performed a variety of quasi-3D OSIRIS simulations for a 15 J and a 30 J laser, with $3.8 \leq a_0 \leq 4.8$. The azimuthal modes for each simulation was truncated at $m = 1$, and the lasers were circularly polarized. The plasma was simulated with 8 particles across ϕ and 2 particles per r-z cell. We used cell sizes of $\Delta r \approx 0.1 k_p$ and $\Delta z = 0.2 k_0$. The optimal density of the plasma was calculated with Equation 6.8 for each simulation, and the various parameters are presented in Tables 6.1 and 6.2. They also show the maximum energy and the total charge of the mono-energetic beam of the self-trapped particles in each simulation.

As you can see from the tables, the higher the initial a_0, the greater the charge of the trapped mono-energetic beam by the end of the simulation. However, the maximum trapped particle energy decreases, as was predicted by theory. The exact spectra of the trapped electrons are presented in Figure 6.2, superimposed upon each other for comparison. The evolution of the maximum energy over the course of the simulation is presented in Figure 6.3.

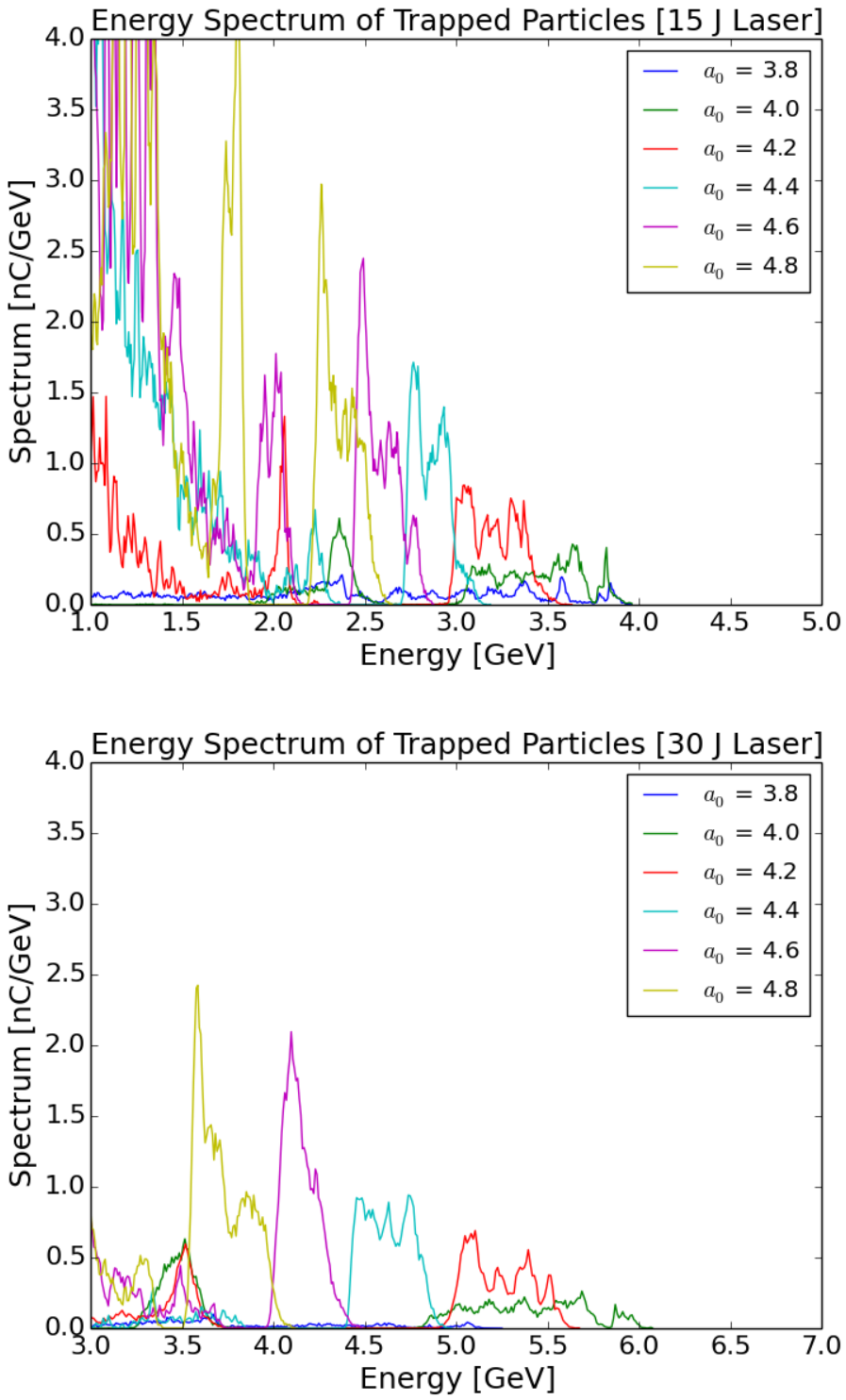

Figure 6.2: Energy spectrum for the 15 J and 30 J lasers. The trapped particle spectrums of LWFA simulations for different a_0 are superimposed for a 15 J laser (top), and a 30 J laser (bottom). The ratio of pulse length to spot size is such that $\tau = \frac{2}{3}W_0$.

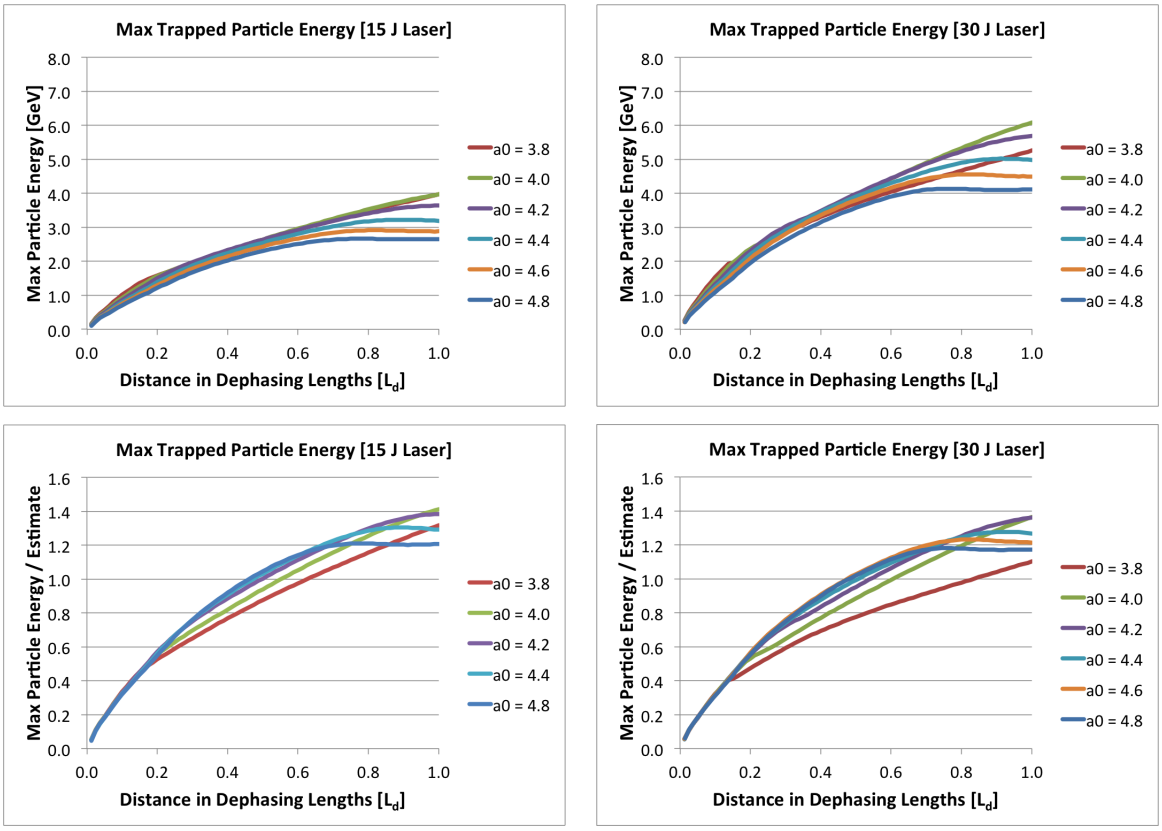

Figure 6.3: The evolution of the maximum energy for 15 J and 30 J laser. The evolution of the maximum trapped particle energies for different a_0 for the 15 J laser (left) and the 30 J laser (right), plotted in GeV (top) and as a ratio with respect to the scaling law estimate (bottom). One may extrapolate how the initial laser amplitude a_0 for a fixed laser may affect the particle acceleration process. The ratio of pulse length to spot size is such that $\tau = \frac{2}{3}W_0$.

The exact energy and spread of the beam, as well as the degree to which they agree with the scaling law estimate, depend on detailed aspects of the LWFA, such as the evolution of the spot size and the stability of the wake. The evolution of the spot size at the maximum laser amplitude is presented in Figure 6.4. This quantity effectively demonstrates localized nonlinear self-guiding, because it is this region of the laser that is most effectively self-guided while the front of the pulse is undergoing simultaneous diffraction and pump depletion.

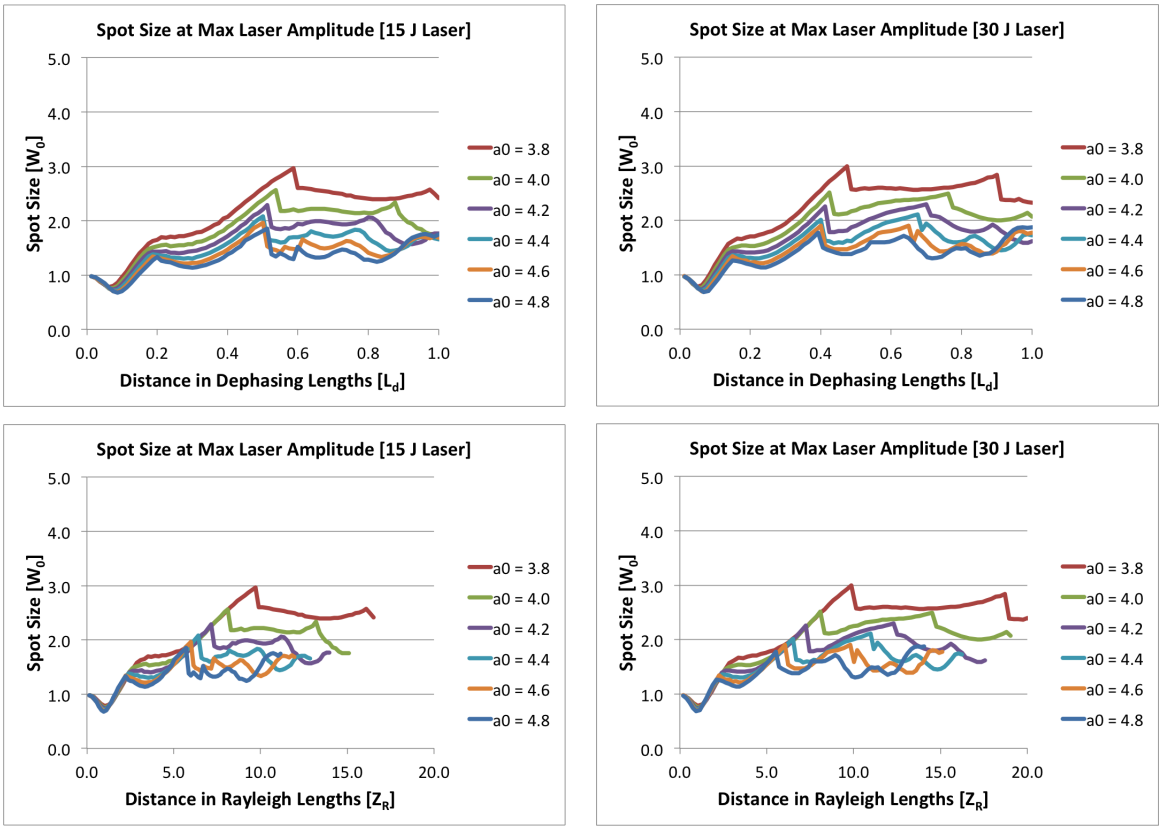

Figure 6.4: The evolution of the spot size at the maximum laser amplitude for the 15 J laser (left) and the 30 J laser (right), plotted over distance in L_d (top) and in Z_R (bottom). One may extrapolate how the initial laser amplitude a_0 may affect the nonlinear self-guiding of the laser. The ratio of pulse length to spot size is such that $\tau = \frac{2}{3}W_0$.

The plots in Figure 6.4 use either the dephasing lengths L_d or the Rayleigh lengths Z_R to normalize the laser propagation distance (horizontal axis). The plasma lengths in dephasing lengths is the same in each simulation but it is different in units of Rayleigh lengths due to the use of matched spot sizes. This figure reveals differences in the effectiveness of self-

guiding. Notably, the laser in the $a_0 = 3.8$ case propagated through the greatest number of Z_Rs, while simultaneously Equation 2.39 suggests that reducing a_0 will reduce the distance over which self-guiding will be effective.

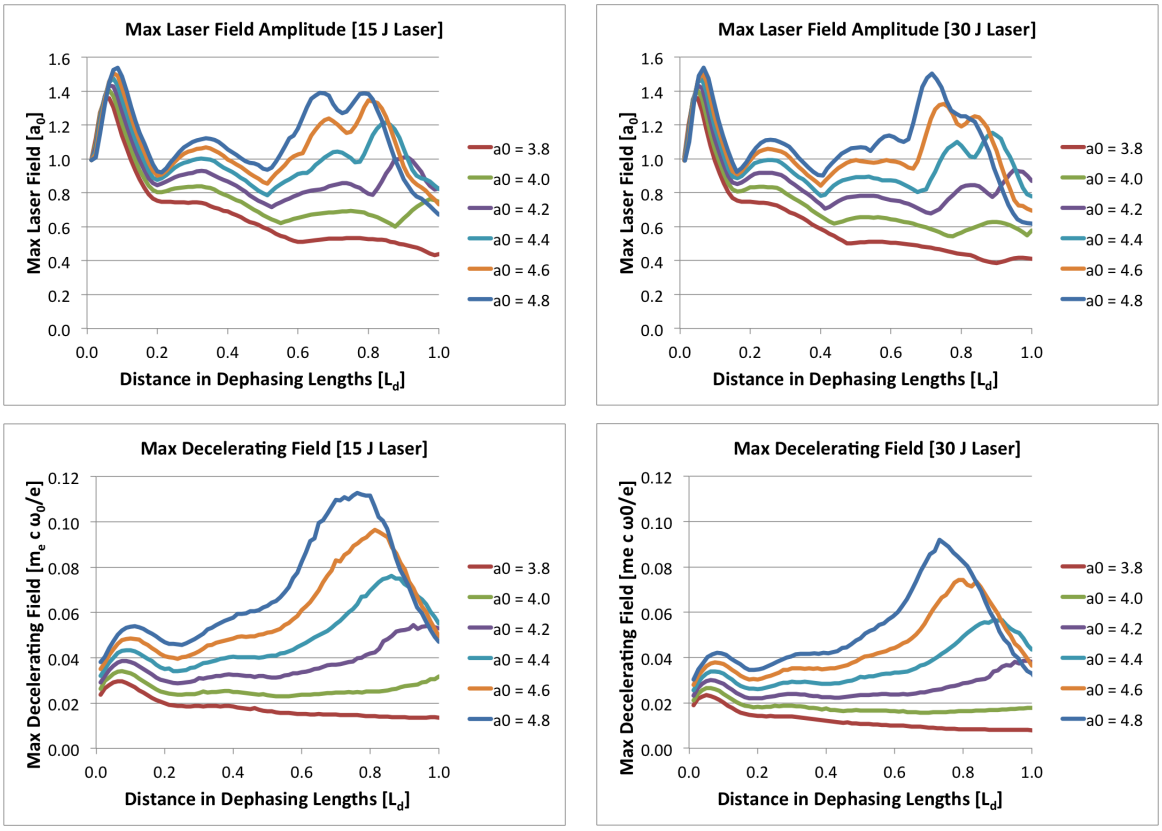

Figure 6.5: The evolution of max laser field amplitude (top) and the max decelerating field at the front of the wake (bottom). The max decelerating field scales with the maximum accelerating field, but is not subject to beam-loading, and so provides a representation of the stability of the wake. The ratio of pulse length to spot size is such that $\tau = \frac{2}{3}W_0$, and a_0 is varied.

The evolution of the spot size will indirectly affect the stability of the laser and the wake. The pump depletion process, which is not directly related to self-guiding, also affects the evolution of the laser and the wake. In order to demonstrate how these two things vary as we adjust a_0, the evolution of the maximum laser field amplitude as well as the evolution of the maximum decelerating field for the simulations are presented in Figure 6.5. The maximum decelerating field scales with the maximum accelerating field, but is not subject

to modifications brought upon by beam loading. The plots in Figure 6.5 indicate that both the laser and the wake are most stable for $a_0 \approx 4.2$ for the 15 J laser and, similarly, $a_0 \approx 4.4$ for the 30 J laser, as long as $\mathcal{F} = (2/3)$.

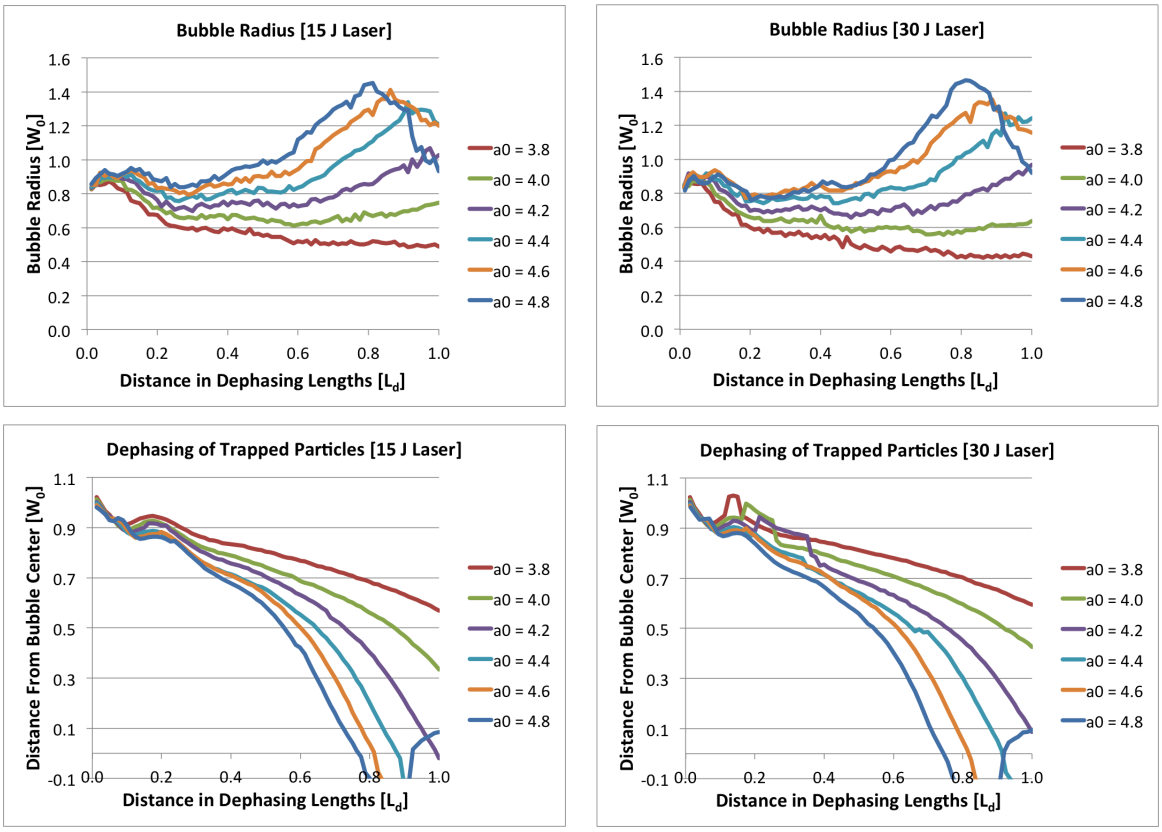

Figure 6.6: The evolution of the bubble radius (top) and the distance of the trapped particles from the bubble center (bottom). The bubble radius is estimated by taking the distance from the first zero of the wake from the position of the max decelerating field, and the distance of the trapped particles from the zero of the wake shine light on the particle dephasing process. The ratio of pulse length to spot size is such that $\tau = \frac{2}{3}W_0$, and a_0 is varied.

Another method to measure the stability of the wake is to measure the bubble radius as the distance from the zero of the wake to the position of the maximum decelerating field, which is presented in Figure 6.6. When the bubble radius expands dramatically over the course of the simulation, because of a resulting sharp rise in the maximum laser field amplitude, the zero of the accelerating field structure shifts further back in ξ. The trapped particles, which are traveling near the speed of light, can then prematurely dephase before

the estimated dephasing length, L_d. We plot the distance between the position of the particle with the maximum energy to the position of the zero of the wake in Figure 6.6. The trapped particles in the $a_0 = 3.8$ case hardly dephase by the end of L_d, whereas the trapped particles in the highest a_0 cases dephase much earlier due to the expansion of the bubble late in the simulation.

6.5 Optimization of Pulse Length

Based on the results in section 6.4, we next fix the laser amplitude at $a_0 = 4.44$ and attempt to optimize the pulse length. The previous results showed that for $a_0 \cong 4.44$ a mono-energetic particle beam with $\approx 300pC$ of charge is obtained with a pulse length of $\mathcal{F} = (2/3)$. Furthermore, the physics that is observed is consistent with the phenomenological scaling laws. We reduce $\mathcal{F}$ in hopes of reaching higher particle energies in accordance with Equation 6.9. Similarly to section 6.4, we performed a variety of simulations for a 15 J and 30 J laser, but we keep a_0 fixed and vary $0.45(2.3) \leq \mathcal{F} \leq 0.95(2/3)$. The number of azimuthal modes for each simulation is truncated at $m = 1$, and the lasers were circularly polarized. The plasma was simulated with 8 particles across ϕ and 2 particles per r-z cell, and $\Delta r \approx 0.1k_p$ and $\Delta z = 0.2k_0$. The optimal density of the plasma was calculated with Equation 6.8 for each simulation, and the various simulation parameters are presented in Tables 6.3 and 6.4. They also show the maximum energy and the total charge of the mono-energetic beam of the self-trapped particles in each simulation.

As we decrease $\mathcal{F}$, the charge of the self-trapped mono-energetic beam of the density-matched LWFA decreases. Although the wake can support more charge at lower densities[54], the amount of self-injected charge is less at lower densities for a fixed a_0. The maximum trapped particle energy, on the other hand, increases, as was estimated by theory, until $\mathcal{F}$ becomes too small. When $\mathcal{F} = 0.55(2/3)$ and $0.45(2/3)$ the trapped particles fail to continue to accelerate after an early point in the simulation. The exact spectra of these trapped particles are presented in Figure 6.7, superimposed upon each other for comparison. The evolution of the maximum energy over the course of the simulation is presented in

Calculated								Simulated	
$\mathcal{F}$	P	τ	n_p	Z_R	W_0	L_d	Est. E	Q_{mono}	Max E
% $\frac{2}{3}$	(TW)	(fs)	($10^{17} cm^{-3}$)	(cm)	(μm)	(cm)	(GeV)	(pC)	(GeV)
95	324	46.0	10.5	0.188	21.9	2.43	2.52	355	3.25
85	348	42.8	9.75	0.202	22.7	2.71	2.71	301	3.57
75	378	39.4	8.95	0.220	23.7	3.08	2.95	227	4.04
65	416	35.8	8.15	0.242	24.8	3.54	3.24	83.4	4.60
55	464	32.1	7.28	0.271	26.3	4.20	3.63	N/A	N/A
45	532	28.0	6.38	0.309	28.1	5.11	4.14	N/A	N/A

Table 6.3: The parameters of LWFA simulations for a 15 J laser, given an optimal density calculated with Equation 6.8 and a spot size matched according to Equation 2.23. The initial amplitude of the laser is kept constant at $a_0 = 4.44$. The charge and the max energy of the mono-energetic particle beam are also shown.

Calculated								Simulated	
$\mathcal{F}$	P	τ	n_p	Z_R	W_0	L_d	Est. E	Q_{mono}	Max E
% $\frac{2}{3}$	(TW)	(fs)	($10^{17} cm^{-3}$)	(cm)	(μm)	(cm)	(GeV)	(pC)	(GeV)
95	513	58.2	6.60	0.299	27.6	4.86	4.00	320	5.08
85	554	54.0	6.13	0.322	28.6	5.43	4.31	235	5.69
75	602	49.7	5.64	0.350	29.8	6.15	4.68	103	6.76
65	662	45.2	5.12	0.385	31.3	7.11	5.16	2.99	6.04
55	738	40.5	4.58	0.431	33.1	8.41	5.77	N/A	N/A
45	845	35.4	4.01	0.492	35.4	10.3	6.59	N/A	N/A

Table 6.4: The parameters of LWFA simulations for a 30 J laser, given an optimal density calculated with Equation 6.8 and a spot size matched according to Equation 2.23. The initial laser amplitude is kept constant at $a_0 = 4.44$. The charge and the max energy of the mono-energetic particle beam are also shown.

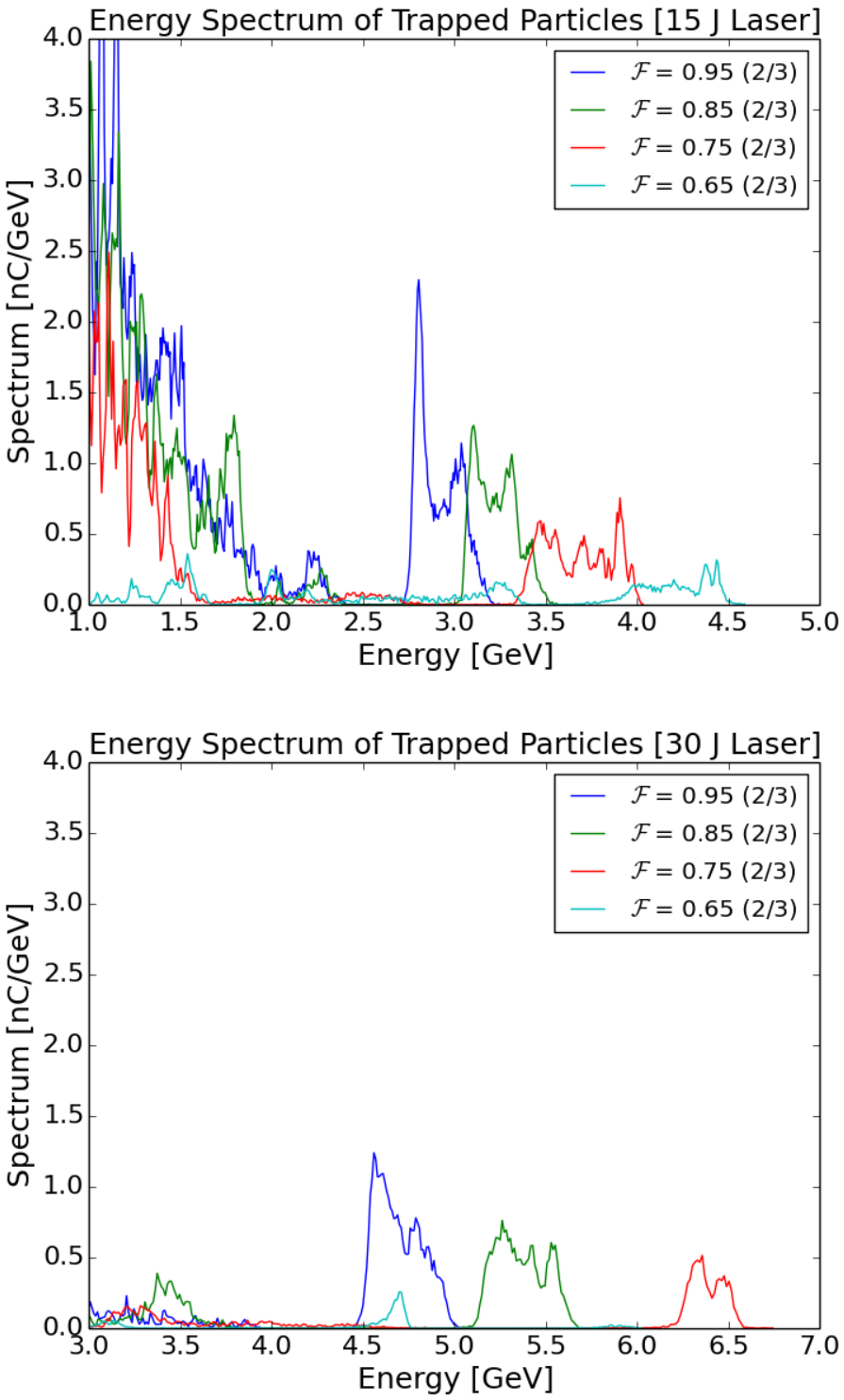

Figure 6.7: The superimposed trapped particle spectrums of LWFA simulations for a 15 J laser (top), and a 30 J laser (bottom), conducted with varying proportional pulse lengths. The initial laser amplitude is kept at $a_0 = 4.44$.

Figure 6.8.

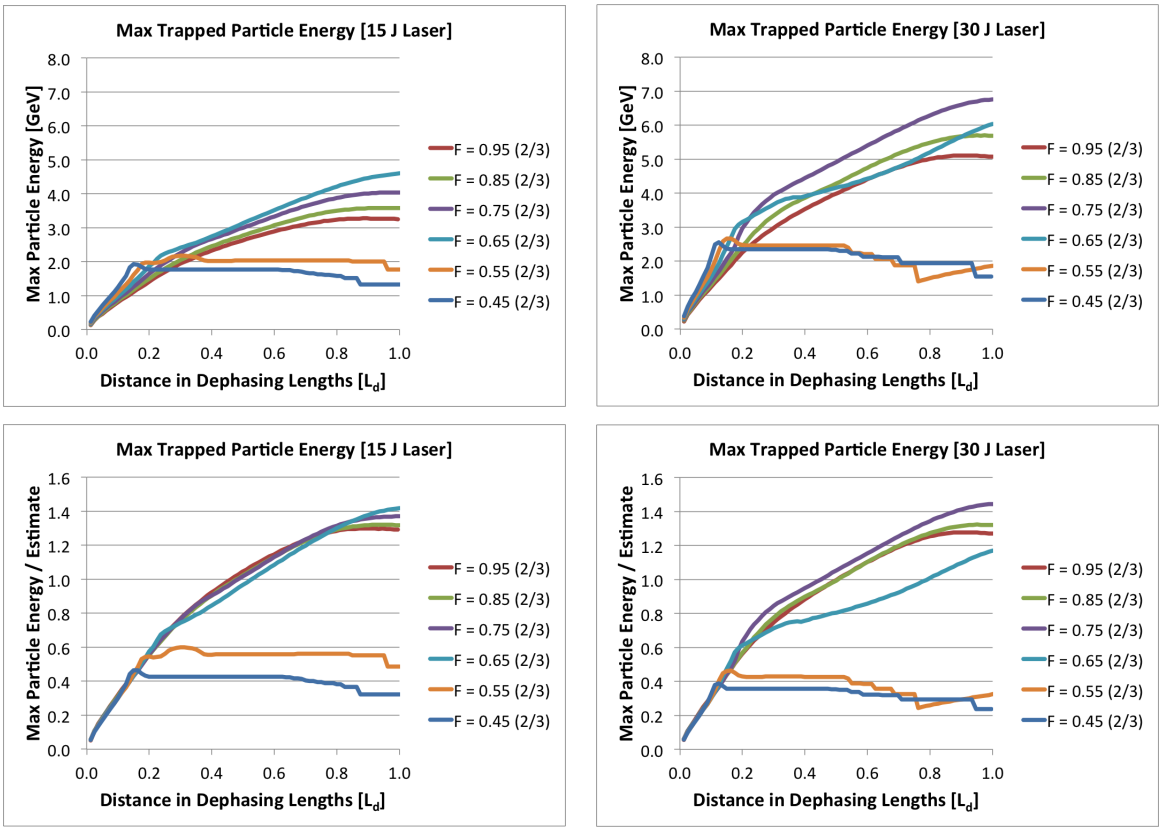

Figure 6.8: The superimposed evolution of maximum trapped particle energies for the 15 J laser (left) and the 30 J laser (right), plotted in GeV (top) and as a ratio with respect to the scaling law estimate (bottom). One may extrapolate how the proportional pulse length $\mathcal{F}$ for a fixed laser may affect the particle acceleration process. The initial laser amplitude is kept at $a_0 = 4.44$.

In order to gauge how the normalized pulse length affects the stability of the laser over the course of the acceleration process, we present the plots of the evolution of the spot size at maximum laser energy in Figure 6.9. As we decrease $\mathcal{F}$, Equations 6.8 and 2.27 indicate that L_d, the estimated distance over which the particles must be accelerated, increases. This means that the particles will be accelerated over a greater number of Rayleigh lengths. The region of the laser which may pump deplete and locally diffract decreases, and there is now a proportionally smaller region which is guided. Therefore, if the pulse gets too short the laser will pump deplete and diffract too quickly. In Figure 6.9 it can be seen that the self-guiding

of the laser does indeed become less effective as $\mathcal{F}$ is decreased, to the point where it ceases to occur at $\mathcal{F} = 0.45(2/3)$.

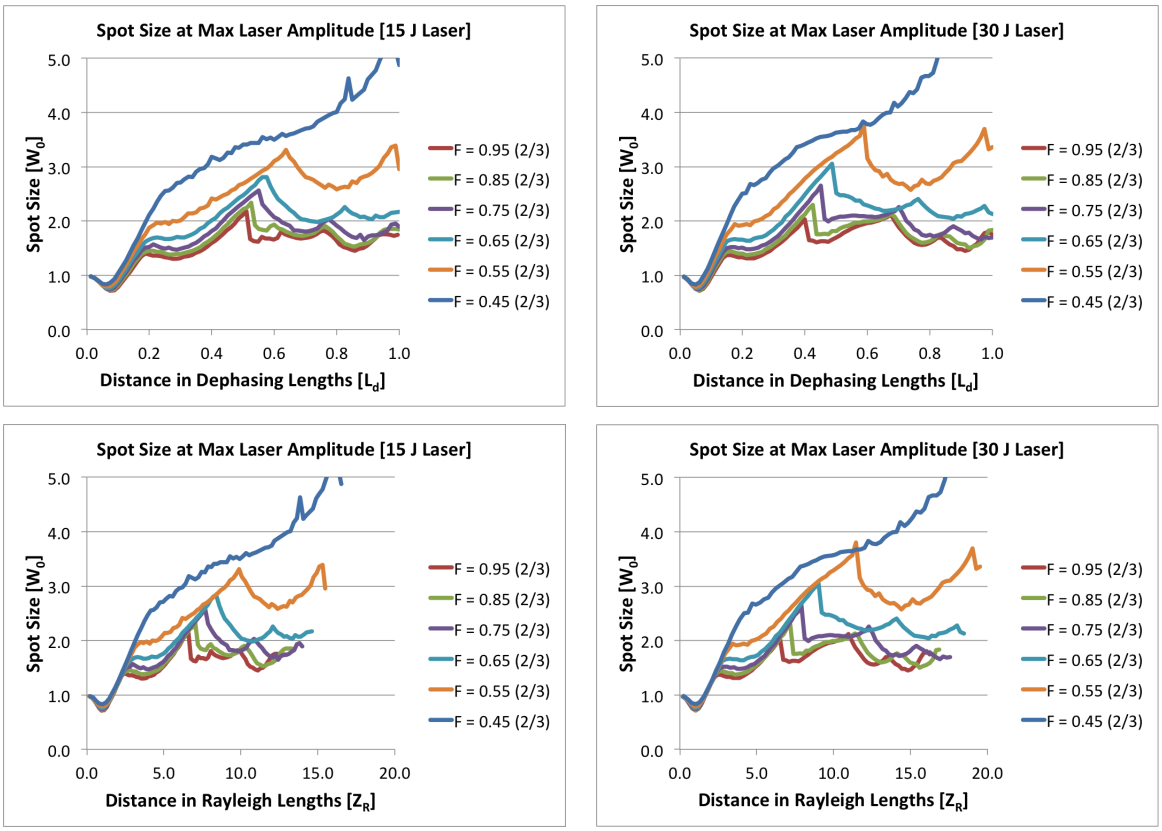

Figure 6.9: The evolution of the spot size at the maximum laser amplitude for the 15 J (left) laser and the 30 J laser (right), plotted over distance in L_d (top) and in Z_R (bottom). One may extrapolate how the proportional pulse length $\mathcal{F}$ may affect the nonlinear self-guiding of the laser. The initial laser amplitude is kept at $a_0 = 4.44$.

The self-guiding of the laser only indirectly affects the particle acceleration process by altering the evolution of the wake structure. In order to demonstrate how adjusting $\mathcal{F}$ affects the stability of the accelerating wake structure, in Figure 6.10 we show the evolution of the maximum laser field amplitude, as well as the evolution of the maximum decelerating field for both the 15 J and 30 J cases. These plots indicate that $\mathcal{F} \approx 0.75(2/3)$ provides the most stable evolution for the laser and the wake for both the 15 J and 30 J cases. For shorter pulses the laser evolves such that its maximum amplitude drops dramatically over the course of the simulation. This is related to the dramatic rise in the spot size due to diffraction, that

is seen in Figure 6.9.

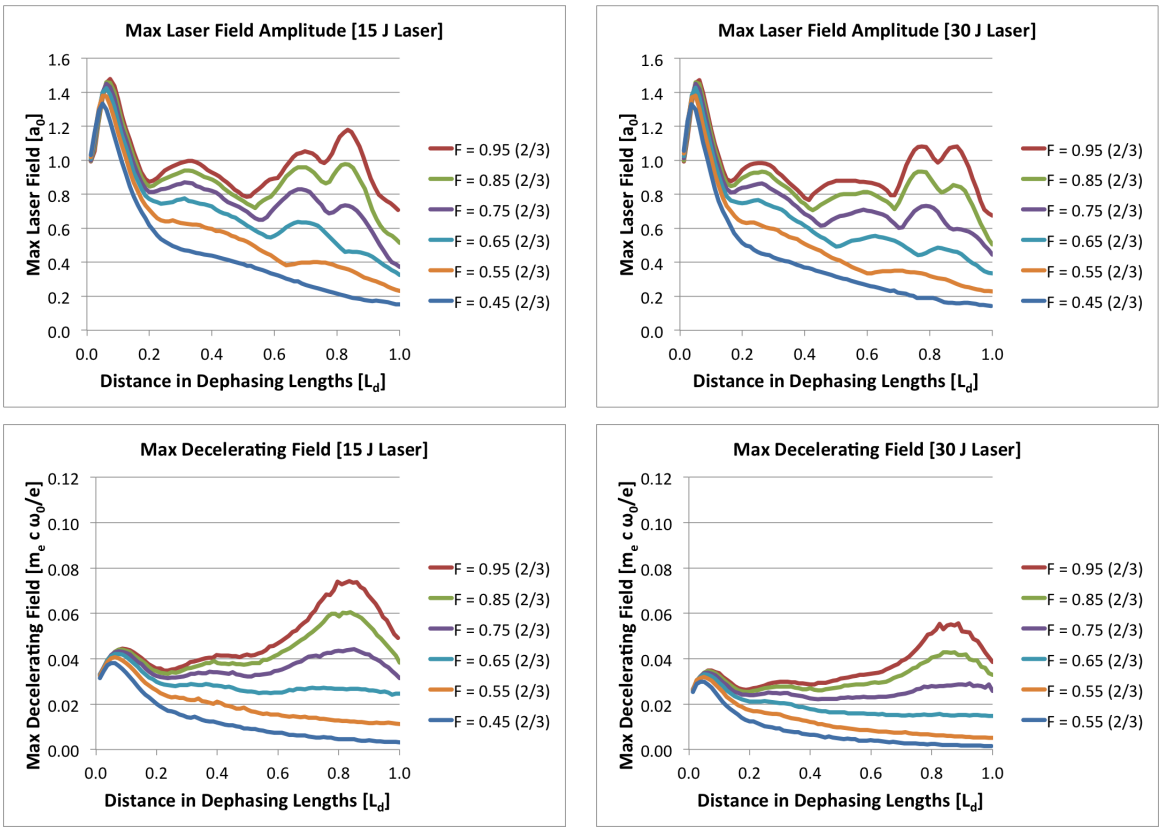

Figure 6.10: The evolution of the max laser field amplitude (top) and the max decelerating field at the front of the wake (bottom). The max decelerating field scales with the maximum accelerating field, but is not subject to beam-loading, and so provides a representation of the stability of the wake. The initial laser amplitude is always $a_0 = 4.44$, and the proportional pulse length $\mathcal{F}$ is varied.

The reduction in the peak laser intensity over the dephasing distance for the two shortest-pulse-lengths leads to a decrease in the wake amplitude, i.e., in the maximum decelerating field. It also leads to a decrease in the estimated bubble radius as shown in Figure 6.11. This decrease in the bubble size begins to occur after a distance of about 0.2 L_d, and is responsible for the trapped particles falling behind the wake. If the bubble size decreases too rapidly then the effective phase velocity of the wake rapidly increases so that electrons in the rear of the first bubble will fall backwards into the second bubble. At this point they will begin to possibly decelerate and may even be defocused. This is the reason for

the dramatic saturation[1] of the energy gain in Figure 6.8. If the bubble radius expands too rapidly then the phase velocity will speed up and also lead to premature dephasing. This is why the energy gain rolls over earlier (in units of L_d) for the two longest pulse length cases in Figure 6.8.

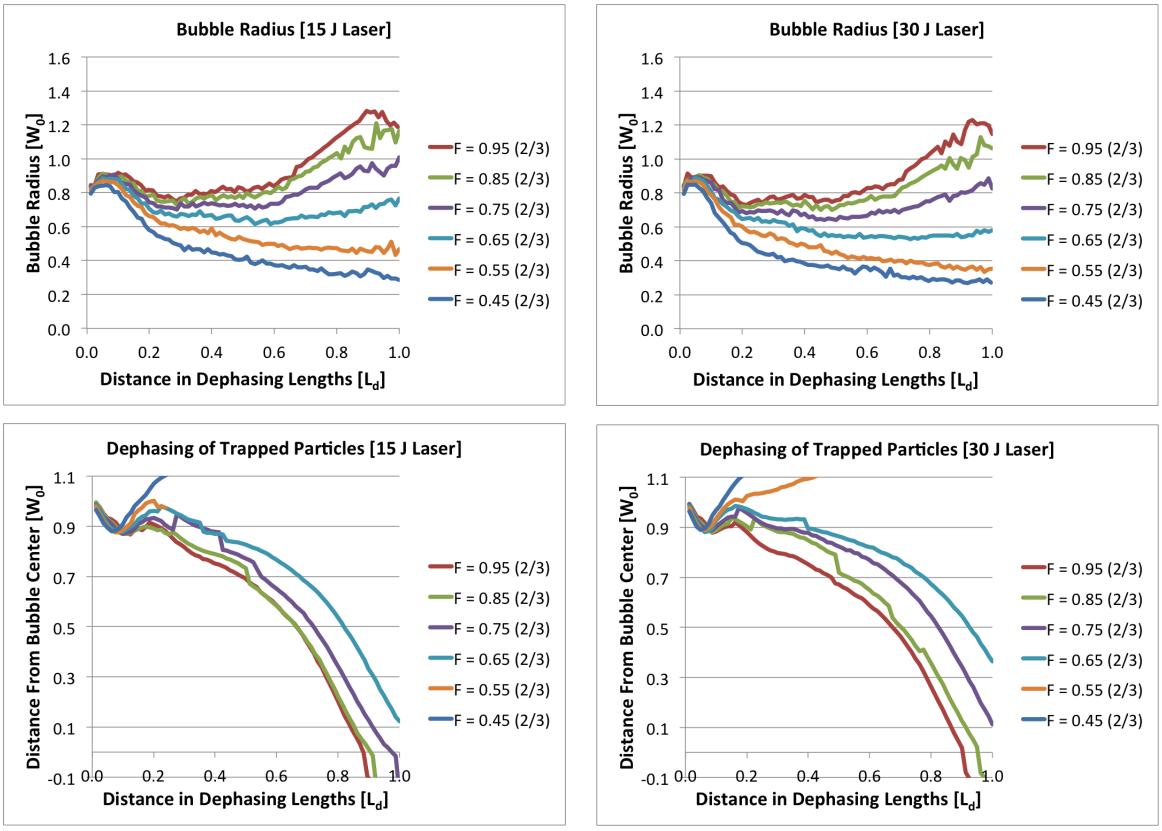

Figure 6.11: The evolution of the bubble radius (top) and the distance of the trapped particles from the bubble center (bottom). The bubble radius is estimated by taking the distance from the first zero of the wake from the position of the max decelerating field, and the distance of the trapped particles from the zero of the wake is shine light on the dephasing process. The initial laser amplitude is always $a_0 = 4.44$, and the proportional pulse length $\mathcal{F}$ is varied.

Overall, the conjecture that the proportional pulse length should be shortened to optimize a fixed-energy laser for higher trapped particle energies is successfully supported. We have

[1] after $\sim 0.2L_d$ for the shortest laser pulse cases.

also confirmed that there is a lower bound to the extent to which we may shorten the pulse length, due to limitations brought upon by self guiding and pump depletion. For both the 15 J and 30 J cases, it appears that $\mathcal{F} \approx 0.75(2/3)$ was the most optimal in terms of producing the highest output particle energy while maintaining the stability of the wake, as well as being the most successful in producing a mono-energetic feature with hundreds of pC of charge. Particles were still successfully trapped and accelerated for the $\mathcal{F} \approx 0.65(2/3)$ cases, but the instability of the wake causes visible oscillation in the acceleration of these particles, particularly for the 30 J case. This suggests the refinement in pulse shape may lead to further improvement in the energy gain for fixed laser energy.

6.6 Longitudinally Asymmetric Pulses

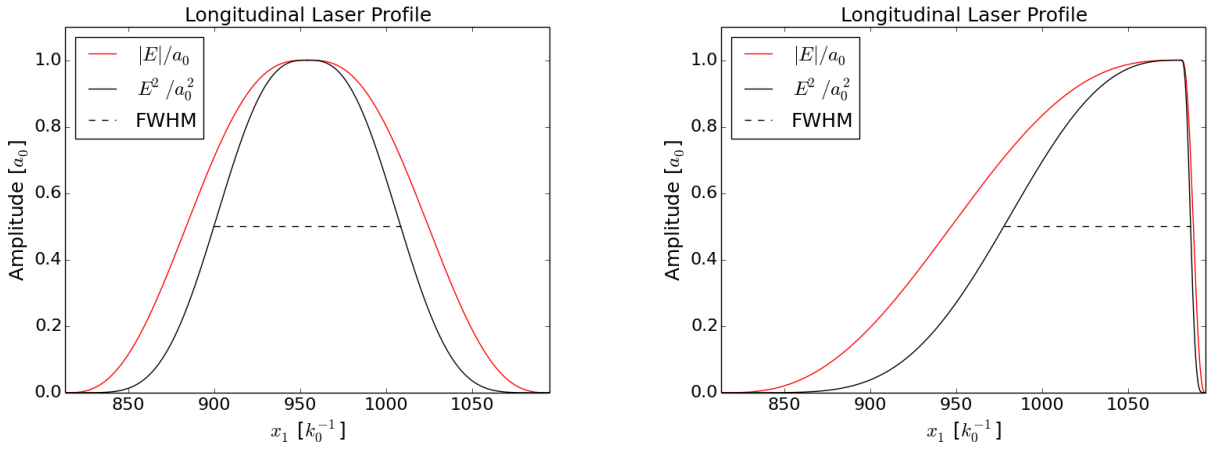

Figure 6.12: Illustration for symmetric and asymmetric axial laser profiles. On the right side is an example of a longitudinally asymmetric laser profile that we used for the 15 J, $\mathcal{F} = 0.95(2/3)$ simulation, with a 5% rise time as compared to the total rise and fall times. On the left is a symmetric profile with a 50% rise time for comparison.

The simulations presented in this chapter up to this point have been conducted with longitudinally symmetric pulses. There is much room for understanding the evolution of pulses with different profiles, and in this section we present a preliminary exploration of asymmetric profiles that are forwardly skewed. Such a parameter scan is only possible with

the new quasi-3D algorithm. An example of such a pulse and it's comparison to the symmetric pulse with the same energy and peak intensity is presented in Figure 6.12. Aside from the difference in the longitudinal profile of the laser, the simulation parameters are identical to those already presented for the 15 J and 30 J cases in section 6.5 with a proportional pulse length of $\mathcal{F} = 0.95(2/3)$ and $0.75(2/3)$. In the original, longitudinally symmetric, simulations the laser profile had a 50% rise time as compared to the duration/length of the entire laser pulse (See section 6.2 for a detailed description of the laser profile in a typical OSIRIS simulation). The maximum amplitude, a_0, is kept the same but there is a smaller specified rise time between 5% to 25%, designating a forwardly skewed pulse profile. Due to a new introduced degree of freedom in the amplitude profile, there is an ambiguity in the amplitude value along the longitudinal profile to which the spot size should be matched to. In the simulations presented here, they are all matched to the maximum amplitude, and we have empirically found that the evolution of the spot size at the maximum amplitude (a key diagnostic we used to verify laser self-guiding in the previous sections), remains nearly the same for the symmetric and asymmetric cases (See Figure 6.13).

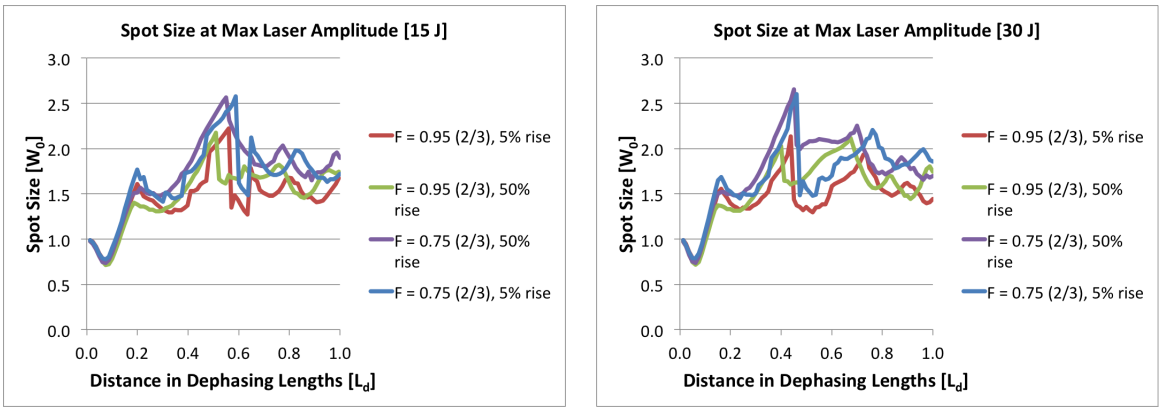

Figure 6.13: Here we present the evolution of the spot size at the maximum laser amplitude for the 15 J cases (left), and 30 J cases (right), of the two extremes (5% and 50%) in our simulations exploring the effects of the forward skewed-ness of the laser pulse. The spot size is matched to the maximum laser amplitude along the profile in all cases.

Upon examining identical simulations with such disparate longitudinal profiles, we find that in some cases the forwardly skewed pulses leads to a higher maximum trapped particle

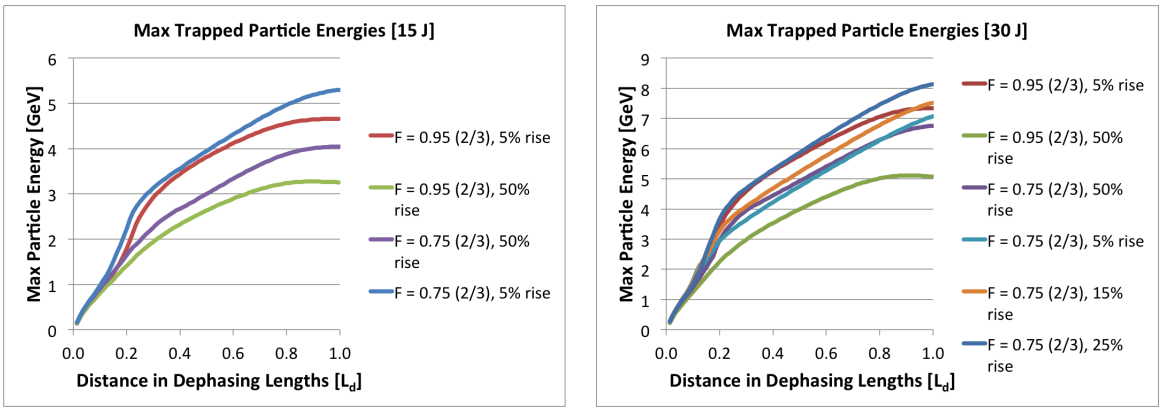

Figure 6.14: These are the evolutions of the max trapped particle energies for 15 J (left), and 30 J (right) for the proportional pulse length of $\mathcal{F} = 0.95(2/3)$ and $0.75(2/3)$, with varying proportional rise times for the longitudinal profile.

energy. Comparative plots of trapped particle energies conducted under various parameters and longitudinal rise times are presented in Figure 6.14. For example, if we constrain ourselves to a pulse length with $\mathcal{F} = 0.95(2/3)$ and reduce the rise time from 50% to 5% of the total pulse length, the particle energy of the 15 J simulation rises from 3.25 GeV to 4.66 GeV, which is about a 43% increase, while the particle energy of the 30 J simulation rises from 5.11 GeV to 7.34 GeV, which is about a 44% increase. These particle energy increases are substantial and suggest a new method of LWFA optimization of a laser with a fixed energy.

An important question is whether a skewed pulse will also significantly increase the energy when compared to a pulse which is already shortened to $\sim 0.75\frac{2}{3}W_0$. Plots of the evolution of the maximum trapped particle energy for a shortened symmetric and skewed pulse length of $\mathcal{F} = 0.75(2/3)$ for the 15 J and 30 J cases are also presented in Figure 6.14. With a 15 J laser, reducing the rise time from 50% to 5% increased the peak particle energy from 4.04 GeV to 5.30 GeV (31 % increase); however, with a 30 J laser this same modification to the laser profile only results in an increase from 6.76 GeV to 7.07 GeV (4.5% increase). A subsequent simulation where the rise time was increased to 25% for the 30 J, $\mathcal{F} = 0.75(2/3)$ showed that the output particle energy may be increased to 8.1 GeV (20 % increase), which is more substantial. These results indicate that it is possible to improve the particle energy

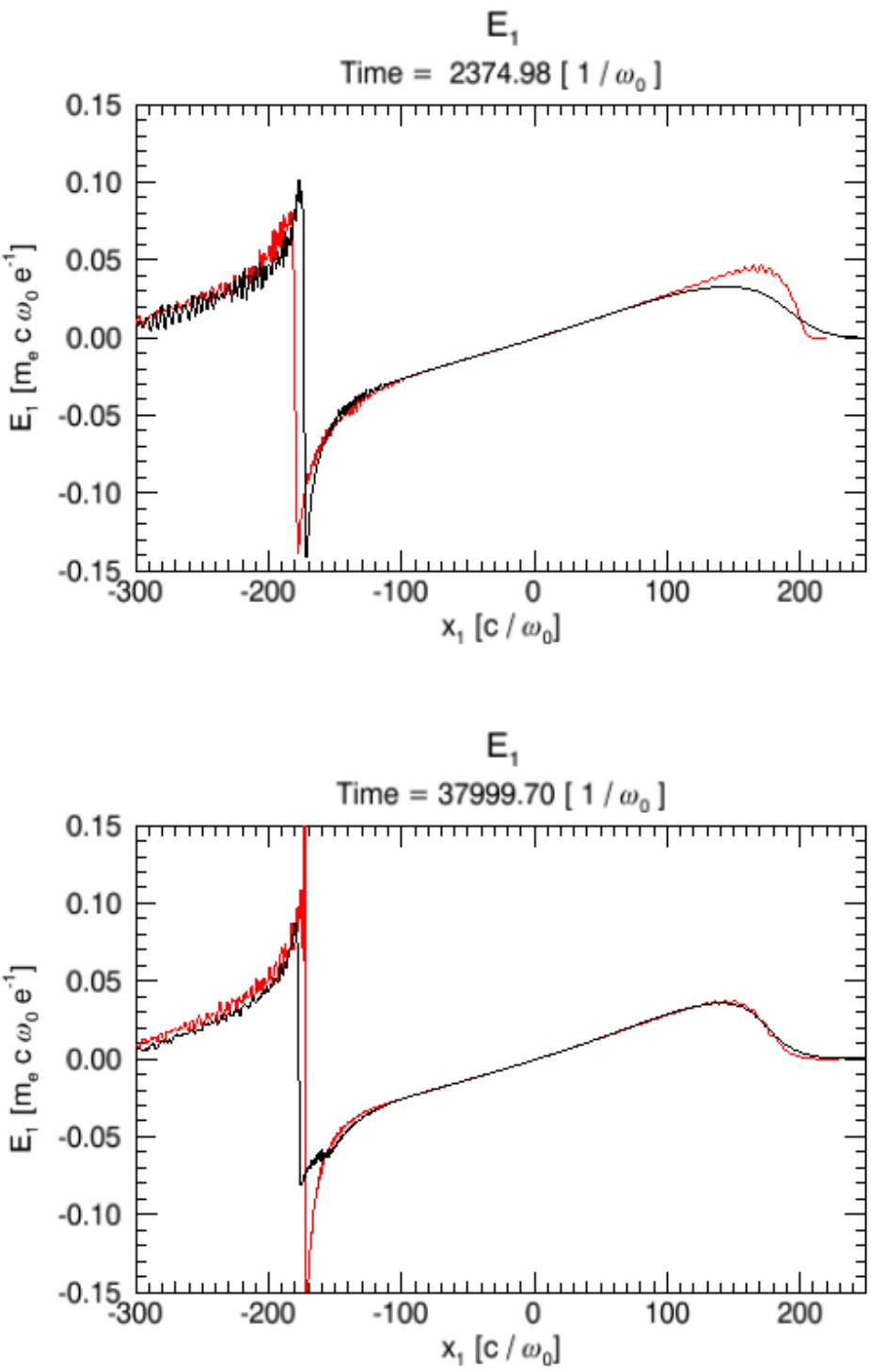

Figure 6.15: The accelerating field lineouts of the 15 J, $\mathcal{F} = 0.95(2/3)$ simulations with a 50% rise time (black) and 5% rise time (red) at approximately $z = 0$ (top) and $z = 0.2L_d$ (bottom). The x_1 axis is offset such that the first zeros of the E_1 lineouts overlap.

by scanning for the optimal rise time in the laser profile, which may depend on the total laser energy and normalized pulse length of the laser. So far we have shown that by optimizing the combination of the pulse length with a forwardly skewed pulse, the peak energy can be increased by 63% above that obtained for a normalized pulse length of $\frac{2}{3}W_0$ for the 15 J laser, and increased by 58% for a 30 J laser. A better result may possibly be obtained by better understanding the physical processes behind the optimization methods.

It is important to understand how the laser profile affects the accelerating field experienced by the trapped particles over the course of its acceleration process. If one recalls from Equation 2.30, the accelerating field in the blowout regime is a function of the plasma density and the distance from the bubble center, i.e.,

$$\frac{eE_z}{mc\omega_p} \simeq \frac{1}{2}k_p(\xi_0 - \xi),$$

where ξ_0 is the center of the blowout bubble. Assuming the particles are trapped at the back of the bubble, and they dephase with respect to the bubble at a constant velocity until reaching their highest energy at its center, one obtains the estimate for the final trapped particle energy given in Equation 2.32. Given the above expression, there is no reason to believe the normalized slope in the acceleration field will be affected by the plasma, regardless of the laser's longitudinal profile if it is sufficiently intense[2]. Examining Figure 6.15 shows us that the assertion that the linear slope of the accelerating field will be the same for simulations with different laser intensities. Therefore, the slope will not evolve in the laser propagation distance[3]. However, there are fluctuations in the bubble radius, namely, that the bubble size for the simulation with a 5% rise time shrinks dramatically at the point where the laser traverses $0.2L_d$ into the plasma, which is where we observe the greatest accelerating gradients in the trapped particles in Figure 6.14. This occurs because the shrinkage in the bubble radius causes a forward movement of the spike in the accelerating field - a spike which is characteristic of LWFAs in a cold plasma. The particle can then experience the spike and hence a larger accelerating field.

[2]The length (size) of the bubble increases for higher laser intensities.

[3]However, the peak acceleration field is larger than $2\sqrt{a_0}$ because of the spike seen at the rear of the bubble in Figure 6.15. The presence of this spike together with the evolution of the bubble can lead to variations in the acceleration gradient felt by a particle.

In most cold-fluid simulations this spike causes an unestimated boost in the acceleration of the trapped particle energy in the beginning of the simulation, which results in a final particle energy that is greater than the estimate (see section 5.2.2)). Ordinarily, the particles quickly accelerate to the linear portion of the accelerating field structure, but the decrease in bubble radius causes a second boost in the acceleration, which in this case occurs where the laser traverses $0.2L_d$ into the plasma.

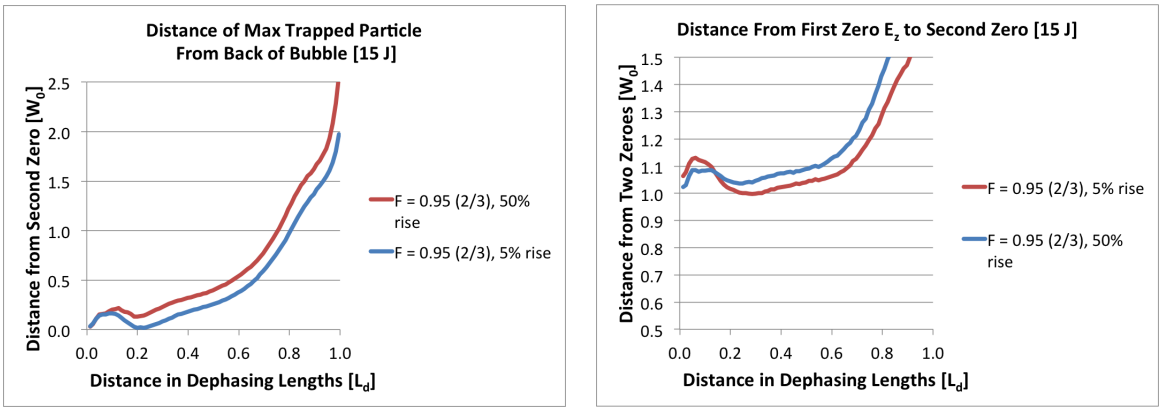

Figure 6.16: Left: The evolution of the distance between the trapped particles and the second zero of the E_1 lineout (also referred to as the back of the bubble), for the 15 J, $\mathcal{F} = 0.95(2/3)$ simulation with a 50% and 5% rise times in the profile of the laser. Right: The distance between the first two zeroes of the E_1 lineout, which is roughly the initial spot size until beam loading causes it to expand later in the simulation.

It appears that when the laser is forwardly skewed, the bubble will shrink partway into the simulation due to the diffraction and pump depletion of the head of the pulse. This shrinkage causes a re-phasing of the trapped particles with a nonlinear accelerating field at the back of the bubble. To illustrate the evolution of the bubble, and the evolution of the trapped particle's position to the back of the bubble, we present the plots in Figure 6.16. The E_z field is zero at multiple positions within the wake. Within the bubble the first zero for E_z occurs at the center of the bubble, and the second zero is at the rear of the bubble. In Figure 6.16 (left) we plot the distance of this second zero to the position of the trapped particles. It can be seen that at approximately $0.2L_d$ the trapped particles in the 5% rise case are once again at the very back of the bubble. This occurs because of the shrinkage

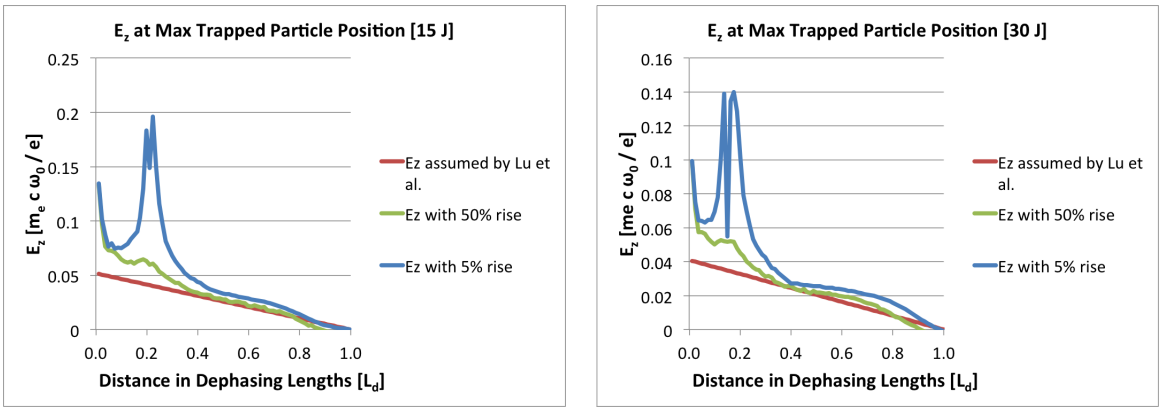

Figure 6.17: The E_1 at the position of the trapped particle with maximum energy for the 15 J (left) and 30 J (right) cases with $\mathcal{F} = 0.95(2/3)$ and 50% or 5% rise time in the longitudinal profile of the laser.

in the bubble size when it is measured from the center of the bubble to it's back (As time progresses the particles then move forward with respect to the second zero because of beam loading effects and the increase in laser amplitude). This same behavior is observed in the 50% rise time case as well but to a much lesser extent. In this case a significant part of the laser is being lost at the front of the pulse. The bubble shrinkage in the symmetric case is not enough to cause a significant boost in the trapped particle acceleration. As a more direct illustration of how the accelerating field of the trapped particles evolve over the course of the dephasing process, we present Figure 6.17. In the symmetric, 50% rise time simulations, we observe a larger-than-estimate accelerating field strength in the same manner as was discussed in section 5.2.2. In the forwardly skewed, 5% rise time simulations, however, we see a second, distinct spike in the accelerating field at the same moment that the accelerating bubble is shrinking in size. Late in the simulation the trapped particles have dephased to the portion of the accelerating field structure that has a linear slope, and the field experienced matches the linear slope estimate. The extra spike in the accelerating field explains the overall increase in the final trapped particle energies we observed in Figure 6.14.

6.7 Optimizing LWFA Parameters for Higher Laser Energies

It would be very useful to provide a procedure for designing optimal parameters for a LWFA given any laser with a fixed laser energy. One may, given a specified function for the longitudinal profile, calculate the proportionality, α, of the laser energy with it's associated power and pulse length (Equation 6.5) by integrating over the square of the longitudinal laser profile (Equation 6.4). It is then possible to estimate the output particle energy as a function of the maximum laser amplitude a_0 and the fraction for the pulse length $\mathcal{F}$ in normalized units with Equation 6.9. In principle, one would choose values of a_0 and $\mathcal{F}$ such that the laser will not pump deplete or diffract before the trapped particles are accelerated over the dephasing length L_d. We may then use Equation 6.8 to find the ideal matched density for such set of laser parameters. Other LWFA parameters, such as the spot size and the total length of the plasma, may be calculated from the relevant equations in section 2.5 given the calculated density.

Calculated								Simulated	
$\mathcal{F}$	P	τ	n_p	Z_R	W_0	L_d	Est. E	Q_{mono}	Max E
% $\frac{2}{3}$	(TW)	(fs)	$(10^{17} cm^{-3})$	(cm)	(μm)	(cm)	(GeV)	(pC)	(GeV)
100	1063	90.1	3.05	0.646	40.6	15.5	8.66	219	10.1
85	1185	80.9	2.74	0.721	42.8	18.2	9.65	107	11.9
80	1233	77.7	2.63	0.750	43.7	19.3	10.0	114	10.4
75	1288	74.4	2.52	0.783	44.6	20.6	10.5	52.9	8.70

Table 6.5: The parameters of LWFA simulations for a 100 J laser, given an optimal density calculated with Equation 6.8 and a spot size matched according to Equation 2.23. The initial amplitude of the laser is kept at $a_0 = 4.44$. The charge and the max energy of the mono-energetic particle beam are also shown.

After a quick parameter scan (potential values extrapolated from the parameter scans presented in section 6.4 and 6.5) the ideal a_0 and $\mathcal{F}$ for such a simulation can be found. To illustrate this, we conduct simulations of a 100 J laser with various spot sizes and pulse

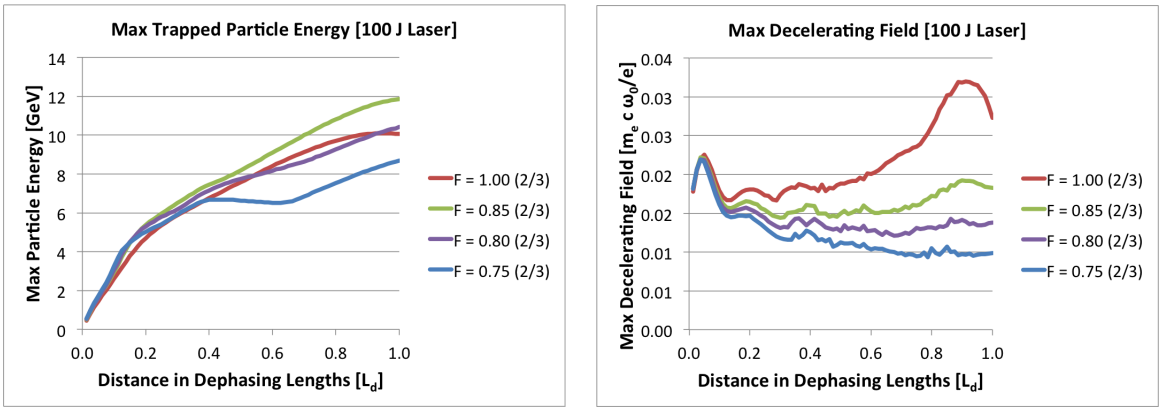

Figure 6.18: The evolution of the max trapped particle energies (left) and the max decelerating field (right), which scale with the max accelerating field, for varying proportional pulse lengths $\mathcal{F}$ for a matched 100 J laser.

lengths, and demonstrate that the output beam energy can be higher with respect to a similar simulation with non-optimized parameters. We started with an $\mathcal{F} = 0.75(2/3)$, which was optimal for the 30 J case, and then gradually reduced $\mathcal{F}$ until diffraction became an issue.

A table of the parameters and the resulting trapped particle energies are presented in Table 6.5, and the evolution of the corresponding maximum particle energy and maximum decelerating field are plotted in Figure 6.18. The optimal normalized pulse length is larger for the 100 J simulation than was found for the 15 J or 30 J cases. This is due to the fact that a greater number of Rayleigh lengths need to be traversed over the course of the simulation. A greater fraction of the laser is lost due to diffraction over a given fraction of the dephasing length, and the stability of the LWFA is affected. The right side of Figure 6.18 suggests that the normalized pulse length that gave the greatest energy gain also provided for the most stable accelerating field in much the same way that the ideal pulse length for the 15 J and 30 J cases did for their wakefield evolutions. Due to this restriction in how small the pulse-length can be made, only an 18% gain in the resulting energy was observed from the default parameters, which is less than 33% in the 30 J case and 42% in the 15 J case. The stability of the wake may be improved through the use of channel guiding, and in turn may improve the amount of gain in the trapped electron energy. The diffraction of the pulse can be limited through the presence of a prepulse which might improve optimization due to the

improvement of laser self-guiding[90]. Given a cold fluid plasma, one may potentially explore various longitudinal pulse rise times to further increase the trapped particle energy through an accordion effect in the manner described in section 6.6.

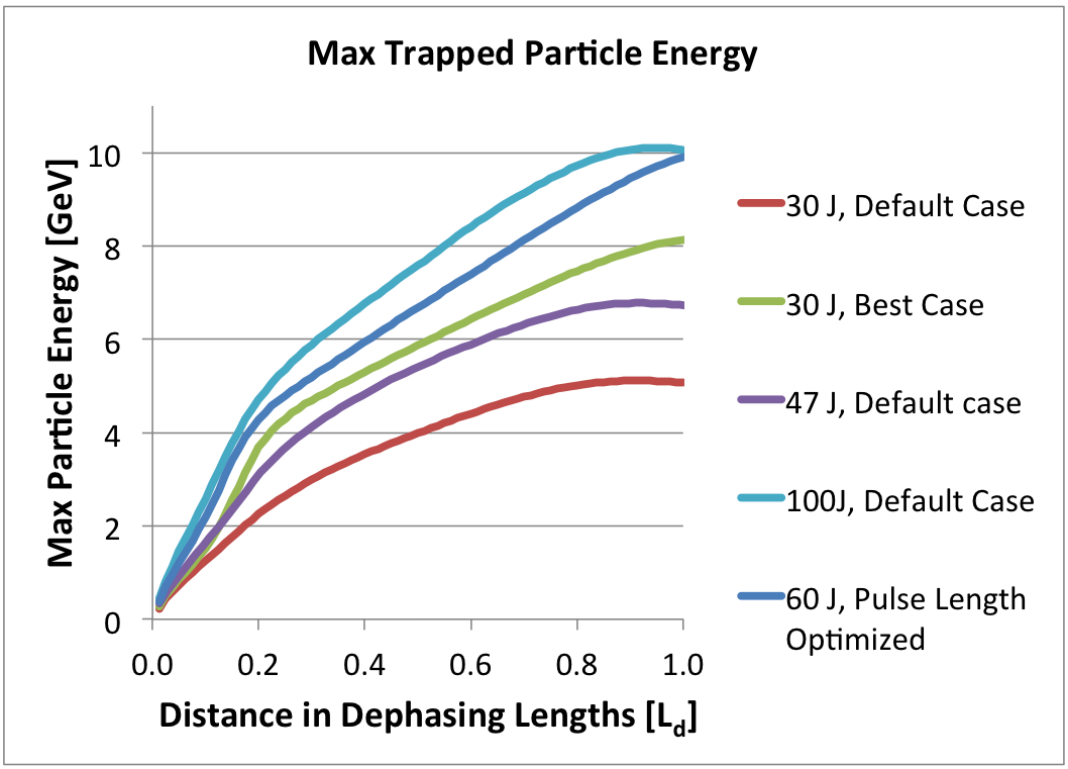

Figure 6.19: The evolution of trapped particle energies for various laser energies and optimization schemes in order to intuit whether a 10 GeV particle was possible with a 50-60 J laser. Given typically chosen parameters it is necessary to use a 100 J laser to reach this energy. However, the improvement in efficiency of the 30 J observed in last simulations and the known laser energy for a previously conducted, 47 J simulation suggest that this is not unreachable. In fact, we were able to quickly show that 60 J simulation with $a_0 = 4.3$ and proportional pulse length of $\mathcal{F} = 0.85(2/3)$ is able to reach this particle energy.

The use of a tool such as quasi-3D OSIRIS now makes it possible to carry out parameter scans to optimize the output beam energy and overall efficiency of LWFA in the self-guided nonlinear regime. However, the optimization procedure also requires improvements in the understanding of the physics that can also be obtained from the simulations. For example, we have already found at least a 58% increase was possible in the particle energy of a LWFA with

a 30 J laser, given a combination of a optimized proportional pulse length, and a forwardly skewed pulse. Knowing this, and given that a previously conducted 47 J simulation with default parameters found 6.64 GeV electrons, it is not unfeasible to believe that we can obtain 10 GeV electrons for a 50-60J laser given appropriate optimizations. In fact, we were able to demonstrate that for a 60 J laser with appropriately chosen laser amplitude and pulse length, such an electron beam energy was possible. For this simulation, we used a 824 TW, $69.7fs$ laser with a spot size of $36.9\mu m$ and $a_0 = 4.3$, and a plasma density of $n_p = 3.57 \times 10^{17} cm^{-3}$. Comparative plots of the trapped particle energies for all of these simulations are presented in Figure 6.19. An even greater trapped particle energy may be possible for a 60 J laser if we can assume that we are using a cold fluid plasma, and that we may optimize the laser using a forwardly skewed profile.

6.8 Conclusion

It is of great interest to achieve the greatest electron beam energy in a LWFA stage at a fixed laser energy. Thanks to the highly efficient hybrid-3D algorithm introduced into the OSIRIS simulation framework, numerous parameter scans were able to be conducted in order to study various methods of optimizing an LWFA given a fixed energy laser. In this chapter, we first discussed the laser characteristics that could be modified while keeping the total energy the same, and then we reformulated the phenomenological scaling laws in order to find an estimate for the accelerated particle energies. This estimate showed that by reducing the normalized amplitude, and reducing the pulse length to spot size ratio, we can improve the efficiency of the LWFA as long as the reduction is not so much that it affects the self-guiding of the laser. The degree to which these adjustments affect the features of the mono energetic bunch of self-trapped particles were also discussed. The features of the self-trapped particles are not as important as the actual energy gain, because it is also possible to inject particles externally.

By conducting a parameter scan we observed that for 15 J and 30 J lasers, the energy gain was improved by about 24% and 33% by reducing the proportional pulse length to $\mathcal{F} =$

$0.75(2/3)$. For the 15 J case the gain was improved by 42% by reducing it to $\mathcal{F} = 0.65(2/3)$, although the evolution of the bubble seemed significantly less stable. The stability of the bubble becomes more difficult for larger laser energies, for which the scaling laws dictate a longer acceleration distance in Rayleigh lengths. For this reason the same parameter scan for a 100 J laser showed that the proportional pulse length could only be reduced to $\mathcal{F} = 0.85(2/3)$, with an 18% improvement in output beam energy. In later simulations and experiments we could explore to what extent the laser may be optimized if guiding is improved through other mechanisms, such as with a low amplitude pre-pulse.

There is still much room to explore in terms of improving the longitudinal profile of a laser pulse with a fixed total energy. For the purposes of this chapter, we restricted our attention to pulses what are symmetric along its center in the z-axis, and pulses with the same functional form but with a smaller rise time compared to the total rise plus fall time, which gives them a forward skew. We found that in some cases giving the pulses a forward skew may improve the energy of the outgoing electron beam. The mechanism by which the acceleration of electrons is improved is dependent on a downward spike at the rear of the bubble in the accelerating field which is characteristic of LWFAs operating in the bubble regime in a cold fluid plasma. The improvement in energy gain is improved though an accordion-like effect, in which the field spike is re-phased with respect to the trapped particles at later in propagation distances after the pulse head has been diffracted or pump depleted, resulting in a slight reduction of the bubble radius. The re-phasing of the spike with the trapped particles results in a spike in the acceleration gradient of the particles over that region. Combining the optimization pulse-length with a forwardly skewed laser pulse, we were able to demonstrate 63% increase in the outgoing particle energies given a 15 J laser, and 58% increase for the 30 J laser. These values are not meant to form an upper limit, as quantities can be improved upon through a better understanding of the physics and an adjustment of the optimization processes.

The optimization of LWFAs given restricted experimental capacities is an art as much as it is a science. The scaling laws and phenomenological theories with which we are provided give us a great starting point in understanding the acceleration processes and estimating

possible particle energies. A great illustration of this is how we were able to demonstrate that 10 GeV particles are possible with a 60 J laser, when simple estimates appear to indicate that, with $a_0 = 4.3$ and a pulse length set to two-thirds of the spot size, only an energy of 6.4 GeV is estimated. With better optimizations this energy may possibly be reached with even smaller laser energies.

CHAPTER 7

Summary

7.1 Important Results

Plasma-based acceleration (PBA) in which electrons or positrons surf to high energies at ultra-high acceleration gradients in plasma wave wakefields has matured from a simple concept based on one-dimensional simulations and linear analysis to technology that is being seriously considered as the basis for the next generation atom smasher or light source. This maturation has occurred due to close synergy between theory, simulation, and experiment. Plasma based acceleration falls under two basic categories, laser wakefield acceleration (LWFA) and plasma wakefield acceleration (PWFA) depending on if the wakefield is driven by a laser or a particle beam respectively. The simulation method of choice has been particle-in-cell (PIC) simulations. PIC simulations have become crucial for developing an accurate theoretical understanding of LWFAs (and PWFAs), for designing of experiments, for the subsequent interpretation of experiments, and for extrapolating to parameter regimes beyond current experiment capabilities.

While there has been tremendous progress in PBA research, there has also been tremendous progress in the capabilities of PIC tools. This progress includes ensuring that the three-dimensional PIC codes can scale to the largest and fastest computers and hardware but also includes developing efficient and/or reduced models that maintain high fidelity.

In the spirit of this progress, in Chapter 3 of this dissertation we presented a new reduced model into the OSIRIS simulation Framework. This idea was inspired by a 2009 paper by Lifschitz et al.[3]. In this model the fields and current are decomposed into azimuthal harmonics (in ϕ) with amplitudes being functions of r and z. The expansion can be truncated

at an arbitrary number. This decomposition is substituted into Maxwell's equations and a set of equations for each harmonic is obtained. The harmonics are summed onto each r-z grid point and the fields are then interpolated to the location of the particle within the grid. No interpolation in ϕ is needed so we call this gridless in ϕ. The fields are then transformed to Cartestian coordinates to push the momentum and position of the particles. This motion is then transformed back to r, ϕ, z space to deposit the current. We developed a new charge conserving current deposit for this algorithm. The current is then projected onto the harmonics space and these projections are then used in harmonic expansion of Maxwell's equation. This cycle is then repeated. This algorithm can model low mode azimuthal asymmetries with a computational cost that is similar to a 2D r-z code.

A pure 2D r-z PIC has been a powerful tool for parameters scans of PWFA. However, simulating a linearly polarized laser that has a perfectly symmetric spot size requires an m=1 mode. Therefore, this algorithm is a powerful tool for studying LWFA for laser spots with near azimuthal symmetry. In later Chapters of this dissertation we have used this new tool to carry out extensive parameter scans of the self-guided, nonlinear blowout regime of LWFA. We find that the phenomenological theory of Lu et al. is very useful with a wide range of applicability. Specifically, when we carry out PIC simulations of the self-guided, nonlinear blowout regime of LWFA to lower plasma densities and higher electron energies we find that indeed self-guiding continues to occur and that if the normalized vector potential is kept constant, the laser "shape" remains unchanged and the results scale well. We then use the theory of Lu et al., to develop scaling laws for this regime in terms of the laser energy (rather than power) to show that with existing lasers in the 30 Joule range that 5-8 GeV energies are possible in this self-guided regime. The simulation study also includes examining the optimum laser pulse length and shape.

A partial list of the major results in this dissertation include:

1. A new rigorous charge conserving current deposition scheme for the quasi-3D geometry is presented. In this geometry, the electromagnetic fields are advanced by Maxwell's equations expressed in truncated azimuthal modes. The particles are initialized and

pushed in a fully 3D Cartesian geometry. This geometry is ideal for a nearly cylindrically symmetric plasma problem such as the LWFA, and the new algorithm gives nearly identical results to fully 3D Cartesian geometry simulations with a speed up of more than a factor of one hundred. We present a derivation of the the current deposition scheme and we demonstrate that charge is conserved (and hence Gauss's Law is maintained) for each of the higher order modes. The new scheme explicitly uses the existing current deposition scheme in the r-z plane which ensures that the fundamental, i.e., 0th mode, is already charge conserving (which it is in the traditional 2D Cylindrical geometry in the OSIRIS framework).

2. Numerical tests were performed to insure that the proposed quasi-3D algorithm is in fact rigorously charge conserving. It was indeed shown to be charge conserving to the numerical roundoff of the double precision floating point number, which is the numerical precision with which OSIRIS operates.

3. Comparisons were made between the quasi-3D simulation results and the fully 3D Cartesian results in order to insure that they are consistent. For LWFA problems the results were shown to agree with high accuracy even when the azimuthal modes expansion was truncated at a mode number as low as $m = 1$. Higher order modes may be included in LWFA and PWFA problems in which higher-modal effects such as hosing and asymmetric spot size self-modulation become significant.

4. The phenomenological scaling laws presented by Lu et al.[4] were re-examined with the results of LWFA simulations conducted in the quasi-3D geometry over distances as long as tens of centimeters. We discovered that the exact numerical estimates are merely approximated, but the results scale qualitatively and quantitatively to lower densities if the longitudinal profile and the normalized laser amplitude stays the same. This refines our interpretation of the scaling laws as a way of predicting simulation results for lower plasma density, longer acceleration distance runs from high plasma density, short acceleration distance runs with appropriately scaled laser profile parameters.

5. We found that the scaling laws for energy gain presented by Lu et al. does not accu-

rately apply if the normalized amplitude of the laser is changed as we reduce the plasma density. This is an important consideration when designing LWFAs which accelerate particles over many Rayleigh lengths, as it might be found desirable to increase the normalized laser amplitude in order to match the rate at which the laser is lost due to diffraction with the rate that it is lost due to pump depletion. One important aspect in which these simulations do not scale is that the trapped particles may prematurely dephase due to an expansion of the plasma blowout bubble resulting from a snowplowing of the laser profile. However, we have not had the necessity to increase the normalized amplitude of the laser for most of our simulations due to the fact that the laser appears to be self-guided over couples of tens of Rayleigh lengths with an amplitude as low as $a_0 = 4.44$. However, we find that the phenomenology of Lu et al. is actually quite accurate, that is that the wake amplitude, pump depletion, dephasing, and matching work as predicted. However, if the normalized vector potential is changed then the evolution of the wake spot size has small variations that lead to changes to the final electron energy.

6. Our refined understanding of the scaling laws highlight that it is possible to optimize a given LWFA by adjusting the laser parameters, such as the proportional pulse length and the longitudinal amplitude profile. We recast the scaling laws as an expression of the energy of the laser in order optimize the resultant trapped particle energy given a fixed laser energy. We showed that by reducing the proportional pulse length and by adjusting the longitudinal profile we may significantly improve the trapped particle energy of an LWFA given a fixed laser energy. This result is highly relevant to the design of future LWFAs, which are more limited by their laser apparatus than the plasma density and profile parameters.

7. The proportional pulse length with which the LWFA operates optimally does not scale in the same manner as the other parameters in the phenomenological scaling laws. This is largely because the laser will not self-guide over longer Rayleigh lengths if the pulse length is too short. This means that in order to better optimize LWFAs over

longer distances and and higher laser energies one must find a way to more efficiently guide the laser over many Rayleigh lengths. There are a number of ways this may be done, such using a laser with a axially dependent spot size or with a low-amplitude pre-pulse laser, each of which opens new avenues for future research.

7.2 Future Potential

Despite the significant progress in the development of the simulations and the theoretical understanding of LWFAs, much work is left to be done in both of these inter-dependent branches of study. The development of a new, rigorously charge conserving current deposition algorithm in a quasi-3D geometry opens doorways to studying physical problems that are not investigated in this dissertation. In addition, this geometry may be used in conjunction with other simulation methods for greater speed improvement and more accurate results concerning the optimization of LWFAs.

Directions for future work involving the quasi-3D algorithm include optimizing the algorithm to reduce the overhead of keeping m copies of the mesh and interpolating the forces on the particles, including ionization, binary collision, and the PGC approximation, as well as additional field solvers with improved dispersion properties, and boundary conditions such as perfectly matched layers. We are interested in using the new quasi-3D code to study asymmetric spot size self-modulation and self focusing and other self-modulation processes [55, 91, 92, and references therein] for the laser and also how these couple to related instabilities for the trailing particles under different beam loading scenarios. The new code can also be used to study the tolerances of LWFA or PWFA in hollow or near hollow channels with small azimuthal mode asymmetries. We are also interested in using the new quasi-3D code to study laser solid interactions involved in fast ignition[93, 94, 95] and proton acceleration[96], as well as stimulated Raman scattering [97, 98] and the high frequency hybrid instability of a single speckle[99]. In addition to all of this, the effects of mobile ion motion may be considered in future LWFA simulations in the blowout regime[100].

We have focused on demonstrating that the self-guided, nonlinear blowout regime for

LWFA an be extended towards energy beyond 10 GeV in a single stage using existing laser technology. However, our simulations used standard self-injection in a uniform preformed plasma as the source of the electrons. For many applications, the beam quality of these electrons is critical. A direction for future work is to use the quasi-3D code to study how to use this regime to generate high quality 5-10 GeV class electron beams. Therefore, future work will involve externally injected high quality beams and seeing how their beam quality is maintained or studying self-injection using ionization injection and downramp injection.

Faster simulation algorithms entail the ability to study an even greater range of parameter regimes. We are currently pursuing using this new quasi-3D scheme in a Lorentz boosted frame using a hybrid finite difference-FFT Maxwell solver to obtain even more dramatic speed ups[101]. Openmp support has also been integrated into this simulation algorithm for more efficient parallel computing within each node. Efforts are being made to integrate GPU support in all the geometries in the OSIRIS simulation framework, which will provide another level of boost in simulation speeds. Ensuring an effective integration of multiple different simulation algorithms and optimization methods is a ongoing effort in the massive multi purpose, multi-author code such as OSIRIS. This is being improved in part by having better object orientation and branch integration in newer, developing version (4.0) of OSIRIS. We are also developing the ability to properly unit-test the code in Git to ensure new developments do not break previously existing lines of code. All of these efforts converge in creating a powerful and versatile framework for PIC simulations in general.

In addition to developments in simulation software, there is much work to be done in developing the theoretical understanding of the scaling of LWFA parameters. Our simulations of self-guided LWFAs operating in the blowout regime shows that self-guiding appears to be effective in the $\sim 10GeV$ range without adjusting the normalized laser amplitude. There was, however, a quantifiable increase in the evolution of the length of the laser susceptible to diffraction over the dephasing length, which brings to question exactly how high of a particle energy can you reach in the self-guided regime while keeping a_0 fixed. It appears that increasing a_0 appropriately can counteract this mismatch of the scaling of diffraction and dephasing effects, but an increased a_0 may lead to complications in a unstable wake

evolution resulting from the compression of the photons at the front of the pulse. This complication may in fact be remediable by adjusting the longitudinal profile of the laser, which is something that may be investigated in future simulations. Similarly, the effectiveness of using a pre-pulse to stabilize the evolution of the laser and the wake in this regime may also be investigated.

We were able to determine that the efficiency of a LWFA may be improved given a laser with a fixed energy if we narrow the proportional pulse length and match the spot size to a lower plasma density, but we have yet to determine the degree to which the laser may be optimized in this manner for any given energy. By performing parameter scans for symmetric, Gaussian pulses of $15J$, $30J$, and $100J$ cases we were able to determine that for higher laser energies, the cutoff value of the proportional pulse length at which the wake is no longer stable becomes greater. This means that, proportionally, the amount of energy gain we may obtain through this optimization technique will drop as we go to higher energies for symmetric, Gaussian pulses. Given that we may improve the stability of the wake through other means such as the use of a laser pre-pulse or a guiding plasma channel, it may be possible to shorten the pulse length further and increase the particle energy gain further without losing the stability of the wake. Lastly, we were also able to further increase the trapped particle energy by decreasing the rise time of the laser as compared to the fall time, in other words, by making the pulses forwardly skewed while maintaining its maximum amplitude and spot size. A more thorough parameter scan in which a greater variety of longitudinal profiles are studied are in order.

Finally, we created a new window into the understanding of LWFAs through the incorporation of the quasi-3D geometry into the OSIRIS simulation framework. There is much to anticipate in the degree to which a new perspective will open new avenues into the exploration of the physical processes that are involved as we reach for higher and higher energies.

Appendix A

Two Stage Ionization-Injection

A.1 Introduction

Although this dissertation has been primarily concerned with the self-injection of LWFAs in pre-ionized plasmas driven by high amplitude lasers, over the course of this study we have also performed illuminating simulations of a two-staged ionization injected LWFA schemes. In a ionization-injected LWFA, the wakefield is excited in a plasma created from a gas or a gas mixture that has multiple ionization states[38, 39, 40]. In [38] a Li plasma confined by a He has was discussed, while in [39] experiments were carried out in a mixture of He with trace amounts of N gas. The desirable choice of trace ions with multiple ionization states depends on the plasma density and laser condition used.

In the example of a He and N mixture, the leading edge of the laser pulse is intense enough to fully ionize the He atoms and the outer five electrons of the N gas. For these electrons the ponderomotive force of the laser is strong enough to push them off its axis, forming a wake. There is a large difference between the ionization potential of the L shell (consisting of the N^{5+} electron) and the K-shell electrons (N^{6+} and N^{7+}), and this difference may be matched to the laser intensity and plasma density in such a way that the K-shell electrons are tunnel ionized at rest and slip backwards into the wake. If the accelerating field of the wake is great enough, these electrons are trapped within the wake and are accelerated until they reach their dephasing length.

One advantage of the ionization-injection scheme is its characteristically low trapping potential. A revisitation of the derivation of Equation 2.57 shows that a more general trapping potential is the change in Ψ, i.e., $\Delta\Psi$, from the particle's initial to trapped position.

In a simple self-injection scheme, the initial potential of the electrons is zero, and $\Delta\Psi = \Psi_f$, but when an ionized-injected electron is born at the peak of the wake potential it can experience a larger $|\Delta\Psi|$ than one starting where $\Psi = 0$. (For a more detailed illustration of this, refer to Figures 2.2 and 2.3). The lower trapping potential requirement in turn means that particles may be trapped with a lower laser intensity and at a lower plasma density. Numerical simulations in the blowout regime have indicated that $a_0 \gtrsim 4$[17] is necessary for self-injection (some experiments have indicated $a_0 \sim 3.8$ is required for self-trapping[102]), while both simulations and experiments demonstrated ionization-injected electrons for $a_0 \approx 1.6$[39]. Thus ionization injection is a useful mechanism for injecting electrons into laser produced wakefields.

An inherent drawback to both self and ionization injection is that the charge is usually continuously injected into the wake, forming an accelerated beam with a large energy spread. Pollock et al.[103] performed experiments with a two-stage ionization injection scheme using the Callisto laser system at the Laurence Livermore National Laboratory. The LWFA constructed in this experiment consisted of an injection regime, filled with a mixture of 99.5% He and 0.5% N gas, and an acceleration regime containing pure He. For these gas mixtures injection will only occur at the first stage, while the acceleration may occur over the entire dephasing length within the second stage. This results in the acceleration of a mono energetic beam that maintains its approximate energy spread while being accelerated to higher energies. In confirmation of the principle behind the method, the experiment has produced a 460MeV electron beam with $< 5\%$ energy spread.

The simulations presented in this appendix are modeled after the scheme used in the Callisto experiment. In section A.2 we will discuss the parameters, results, and implications of these simulations. In section A.3 we will summarize the findings of these simulations.

A.2 Simulations

Figure A.1 portrays the density profile of the two-stage scheme simulated by full 3D OSIRIS. The peak plasma density of the profile is $n_p = 1 \times 10^{18} cm^{-3}$. Three distinct cases of laser

parameters were simulated, corresponding to a laser power of 90 TW, 100 TW, and 500 TW, with spot sizes of 20.0μm for the first two cases and 26.2μm in the last case. Unlike many of the simulations presented in this dissertation, the first two cases presented here have slightly mismatched spot sizes, with the 90 TW case having 20% mismatch and the 100 TW case having 12% mismatch. The 500 TW simulation, in contrast, has a matched spot size. In all three of these cases the FWHM of the laser is a 60fs.

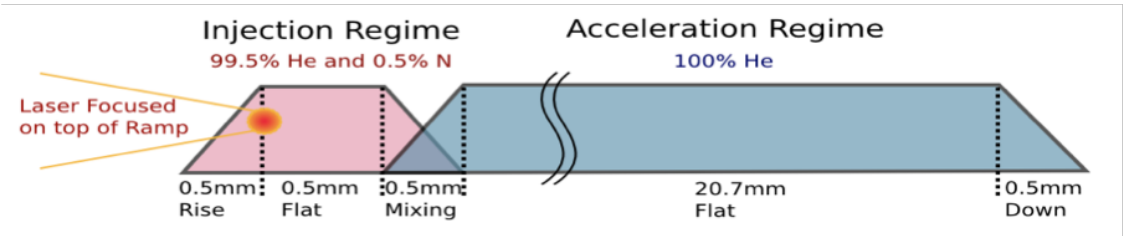

Figure A.1: A pictorial representation of the density profile of the two-stage LWFA scheme. The pure injection regime ramps up for about 0.5mm and flattens for another 0.5mm until it gradually down ramps into the acceleration regime in a 0.5mm mixing region. The much longer acceleration regime continues for another 20.7mm until it ramps down to zero density over another 0.5mm.

These simulations were conducted with OSIRIS in 2 and 3 dimensions in Cartesian coordinates, using the ADK model[104] to simulate the ionization of neutral gases. In the 3D, 90 TW simulation, $4000 \times 300 \times 300$ cells were used (4000×300 for 2D), and it was run for 315621 time steps. The 3D, 100 TW simulation also used $4000 \times 300 \times 300$ cells (4000×300 for 2D), but used 904802 time steps. The 3D, 500 TW simulation used $4000 \times 360 \times 360$ cells (4000×360 for 2D), and 505008 time steps. In all of these simulations 2 particles were initialized per cell for each gas. The 2D simulations were conducted over the full length of the plasma, whereas two of the 3D simulations were stopped at a point within the acceleration stage due to limitations in computational resources. Quadratic particle shapes were used, along with current smoothing and compensation.

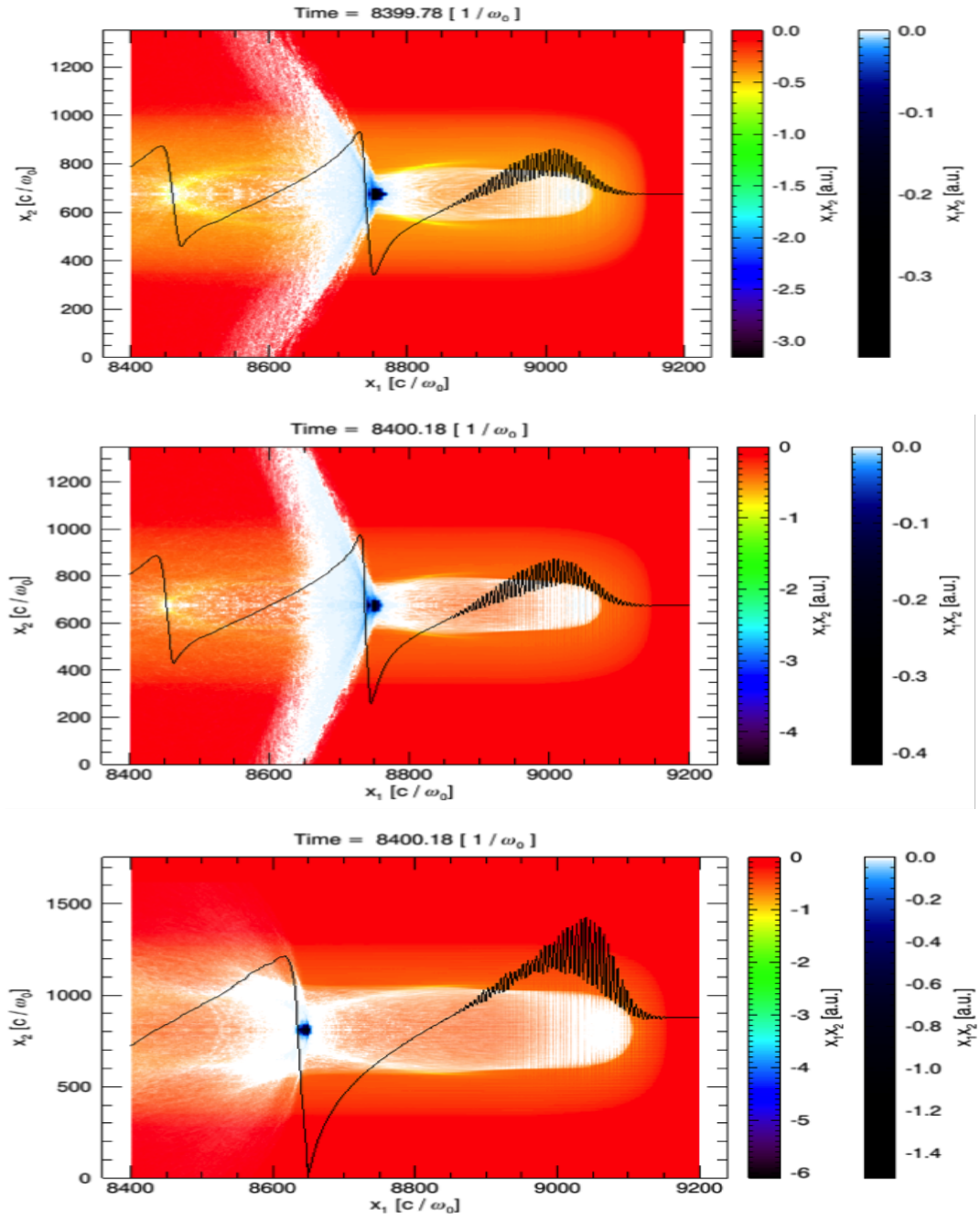

Figure A.2: The density cross sections and the E_z lineouts of the 3D, two-stage LWFA simulation 0.1cm into the plasma, which is near the end of the injection regime. Results for the 90 TW (top), 100 TW (middle), and 500 TW (bottom) cases are presented. The density of the He electrons are represented by rainbow colors whereas the density of the injected N^6 and N^7 electrons are presented on a blue-white spectrum.

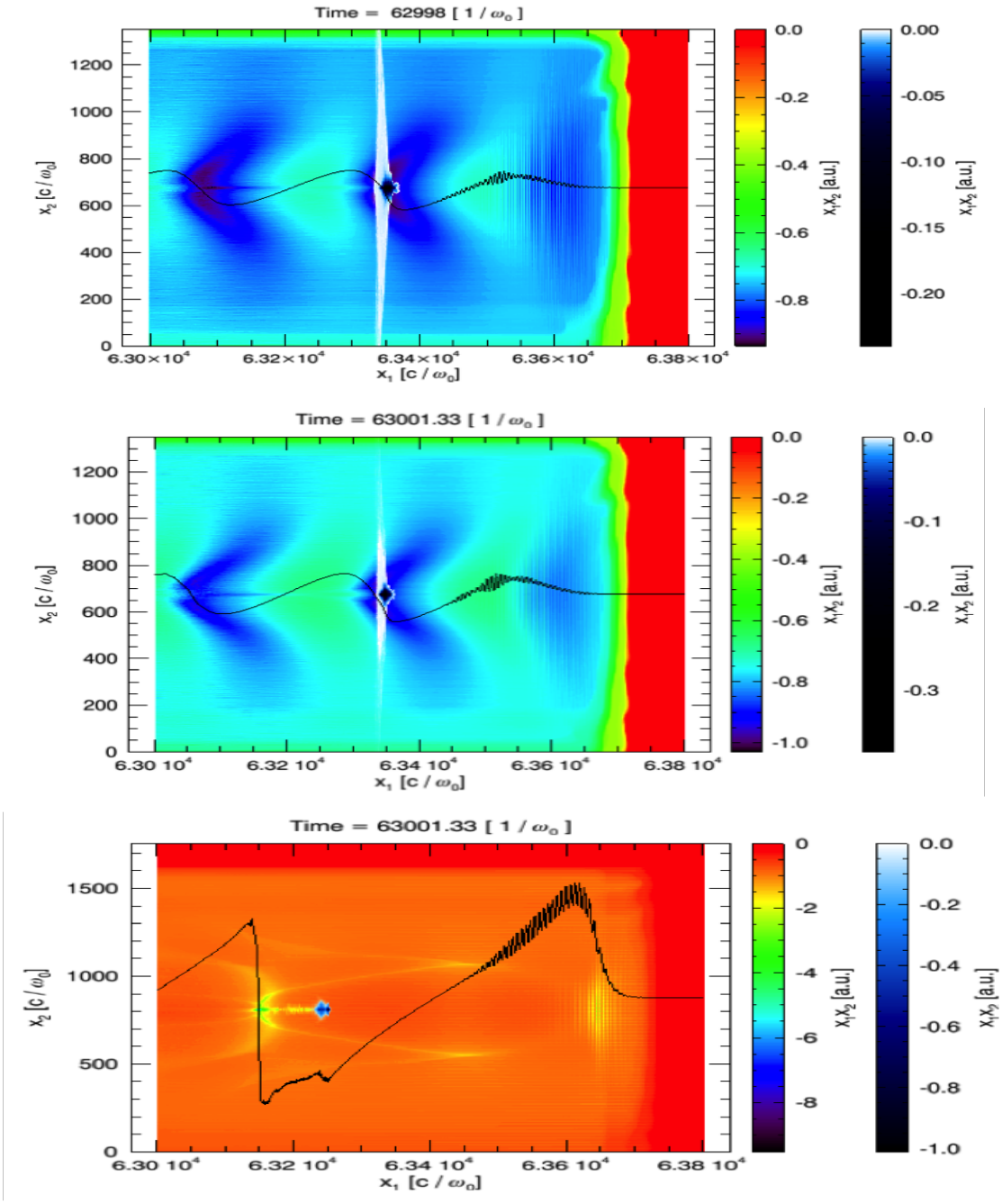

Figure A.3: The density cross sections and the E_z lineouts of the 3D, two-stage LWFA simulation 0.8cm into the plasma, which is well into the acceleration regime. Results for the 90 TW (top), 100 TW (middle), and 500 TW (bottom) cases are presented. The density of the He electrons are represented by rainbow colors whereas the density of the injected N^6 and N^7 electrons are presented on a blue-white spectrum.

A.2.1 The Effectiveness of the Two-Stage Scheme

Figure A.2 presents the density cross sections and the E_1 lineneouts of each LWFA simulations before the down ramp of the injection regime, and Figure A.3 presents the same for a position within the acceleration regime. The He electrons, which form the wake, may be distinguished from the injected N^6 and N^7 electrons by their differing color schemes. The white ellipses in Figure A.2 extending from the location of the laser the back of the first bubble indicate that the N^6 and N^7 are indeed being ionized at the laser and then falling behind, many to be captured by the high acceleration field before falling behind the back of the bubble. In Figure A.3 there are no longer any trails of white particles being ionized at the front of the bubble, but there is a concentrated blue mass within the bubble, which are the continually accelerated particles (not yet dephased) that were injected during the laser's passage through the injection regime. These plots indicate that the injection mechanism is indeed being modeled by the two-stage mechanism as it was originally intended.

The purpose of separating the injection stage from the acceleration stage is to produce low energy spread beams by continuing to accelerate the trapped electrons after switching off the injection mechanism early in the simulation. As a detailed illustration of this principle, the energy spectrums of the trapped particles for each 3D simulation is shown in Figure A.4 immediately after the injection regime ($0.15cm$ into the plasma) and some distance into the acceleration stage ($0.8cm$ into the plasma). After the injection stage there are trapped particles with energies continuously ranging from zero to the maximum trapped particle energy. Inside the acceleration stage this same bunch continues to accelerate, with a widening gap between the lowest trapped particle energy and zero GeV. The result is a decreasing relative energy spread - with the lowest energy spread occurring for the 500 TW, where the highest energy peak of the trapped electrons have a relative energy spread as low as 10% at $0.8cm$.

In their experiment, Pollock et al.[103] used a 3mm long injection stage and a 5mm long acceleration stage. Upon designing and running our simulations we have determined that the ideal length of the acceleration regime is much longer than that of the injection stage - as

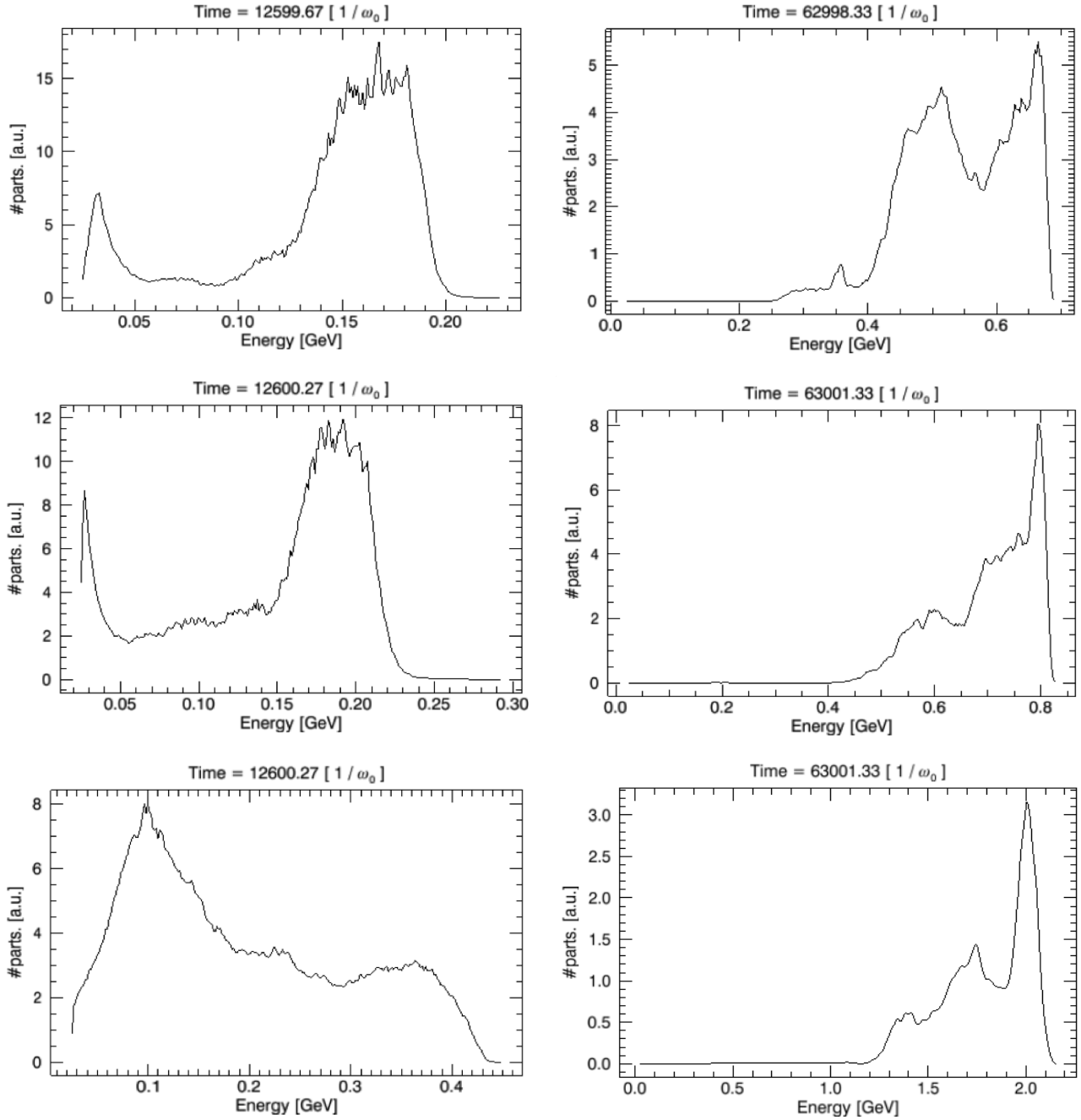

Figure A.4: The energy spectrums of the trapped particles at $1.5cm$ into the plasma (left) and $0.8cm$ into the plasma (right). The spectrums are shown for the 3D, 90 TW (top), 100 TW (middle), and 500 TW (bottom) simulations.

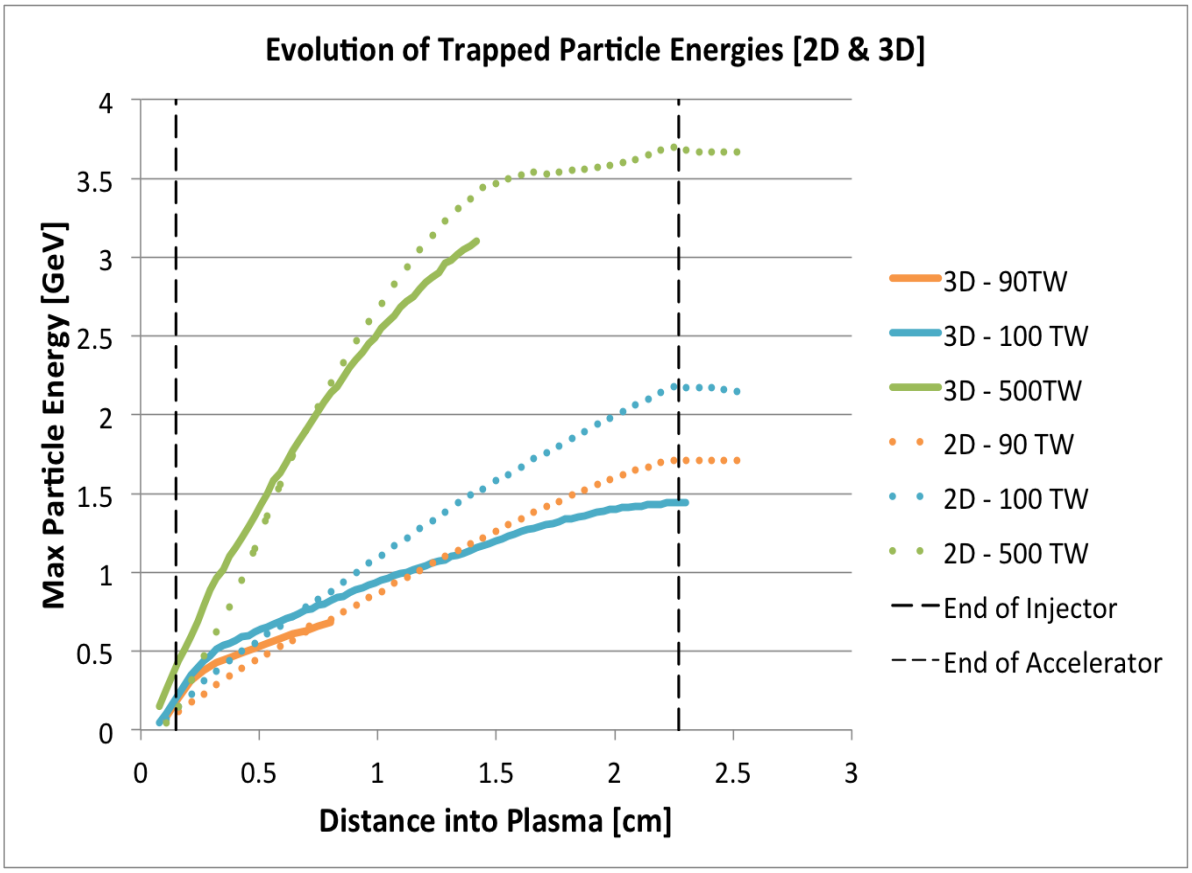

Figure A.5: The maximum particle energy of the trapped particles over the course of each two-staged ionization injection simulation (in both 2D and 3D). The 2D simulations, being much cheaper computationally, were conducted to longer distances than a couple of the corresponding 3D simulations. The difference in the trapped energy evolution highlights the importance of performing a fully 3D simulation to obtain accurate results.

was inferred by the slow rate at which the particles dephased with respect to the wake in our simulations. Our simulations were extended to tens of mm to determine the approximate maximum energy the particles could be accelerated to, given the laser parameters and a specified injection stage profile. The resulting evolution of the trapped particle energies are plotted (for both 2D and 3D simulations) in Figure A.5. This seems to indicate that in future experiments it might be more effective to have an even longer acceleration regime. The two-stage ionization injection scheme is an effective and powerful method to inject a monoenergetic beam to high energies, and there is great potential for future simulations and experiments that may be conducted to improve upon this method.

A.2.2 Comparisons Between 2D and 3D Simulations

As was highlighted by Figure A.5, there were some remarkable differences between 2D and 3D simulations of the two-stage ionization injected LWFA simulations. Early in the simulation (less than 2cm into the plasma) the acceleration gradient appears to be steeper for the 3D cases than the 2D cases. Later on and for a longer period in these simulations, the acceleration gradient is higher for the 2D cases than the 3D cases. The overall effect, in terms of the maximum particle energy evolution, was that the 2D simulations predicted higher energies compared to the 3D cases. Since we know that 3D simulations capture the geometry effects of how the laser and wake evolve it is important to understand how to properly interpret 2D slab simulations. The importance of geometrical effects between 3D and 2D slab is the major motivation for the development of the quasi-3D algorithm about which much of this dissertation is focused on. In this subsection we will denote and summarize some of the major differences we've observed in the 2D and 3D results.

The difference in steepness of the maximum particle energy gradient is explained by the difference in the spike in the accelerating field in the 2D and 3D cases (Shown in Figure A.6). This spike is a feature of the bubble regime when the wake is formed in a cold plasma, and only affects the acceleration of the particles early in the dephasing process - before it reaches the linear portion of the lineout (for a detailed discussion of how this spike affects the particle

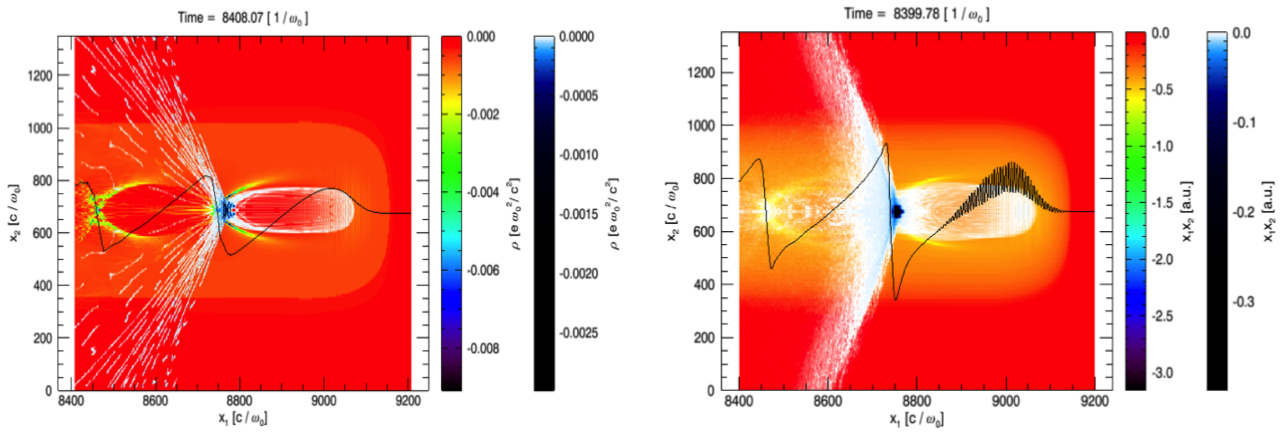

Figure A.6: The charge density and E_1 lineouts for the 90 TW simulations in the 2D case (left) and the 3D case (right) are shown at 1mm into the plasma in order to emphasize the difference in the spike in the acceleration field.

acceleration process, refer to Section 5.2.2). The drop in the acceleration gradient in late in the 3D simulations compared to the 2D simulations may be accounted for by the difference in the influence of diffraction on the laser amplitude in the two geometries. If you were to solve the paraxial equation for a laser with a vector potential amplitude $A(z)$ and spot size $W(z)$ a distance z into the plasma, you would find that in the 2D case $A(z)\sqrt{(W_0/W(z))}$ is constant, while in the 3D case $A(z)(W_0/W(z))$ is constant. That is to say that, as the laser diffracts and the spot size increases, the laser will experience a more dramatic drop in amplitude in the $3D$ case than in the $2D$ case, resulting in a quicker deterioration of the wake structure. The laser evolution for these problems is more complicated than simple diffraction, given issues of spot size matching and localized pump depletion, but the difference in physics between 2D and 3D simulations is important to stress.

The difference in the evolution of the emittances of the trapped particles is presented in Figure A.7. In general, smaller emittances have been observed in the 2D simulations of each case than in their 3D counterparts. In addition, there is a significant amount of oscillation observed in the 3D case of the 100 TW simulation which is not visible in the 2D counterpart. When simulating to find parameters for optimal emittance beams, differences like these will be crucial.

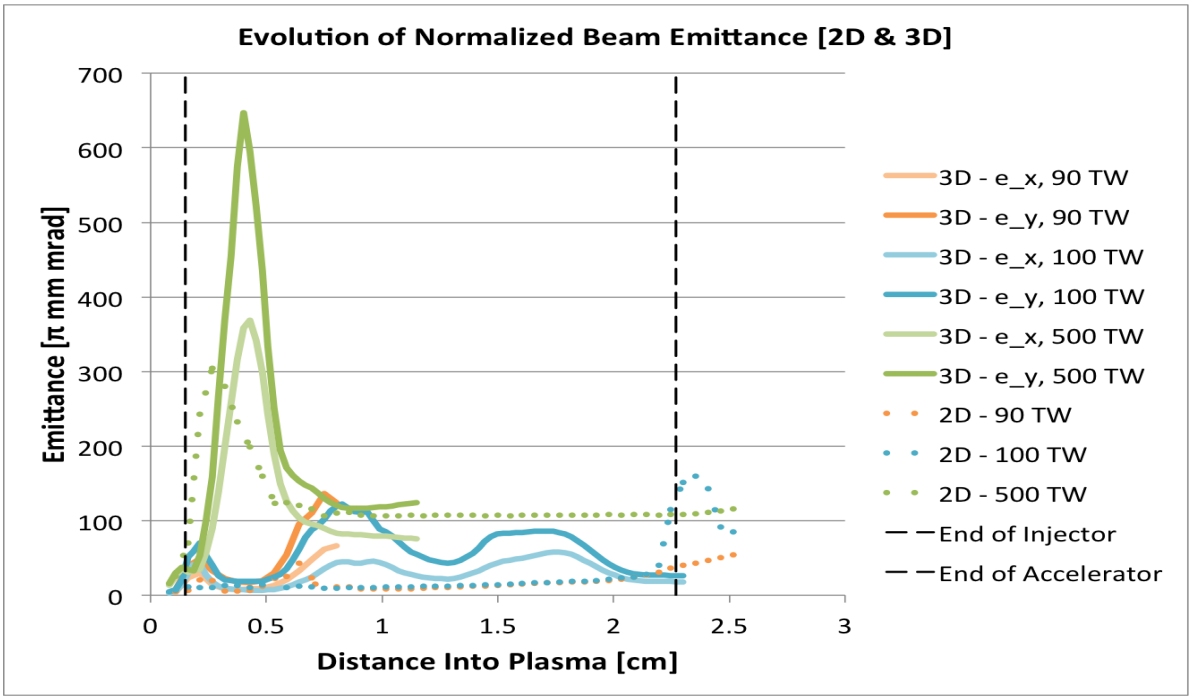

Figure A.7: The emittances of the trapped particles in the 2D and 3D simulations of the two-staged ionization injection simulations. The 3D simulations each have two emittances (e_x and e_y) for the two directions transverse to the laser, one of which has a higher value due to the polarization of the laser in the y direction. The 2D simulations only have one emittance due to there being only one dimension transverse to the laser.

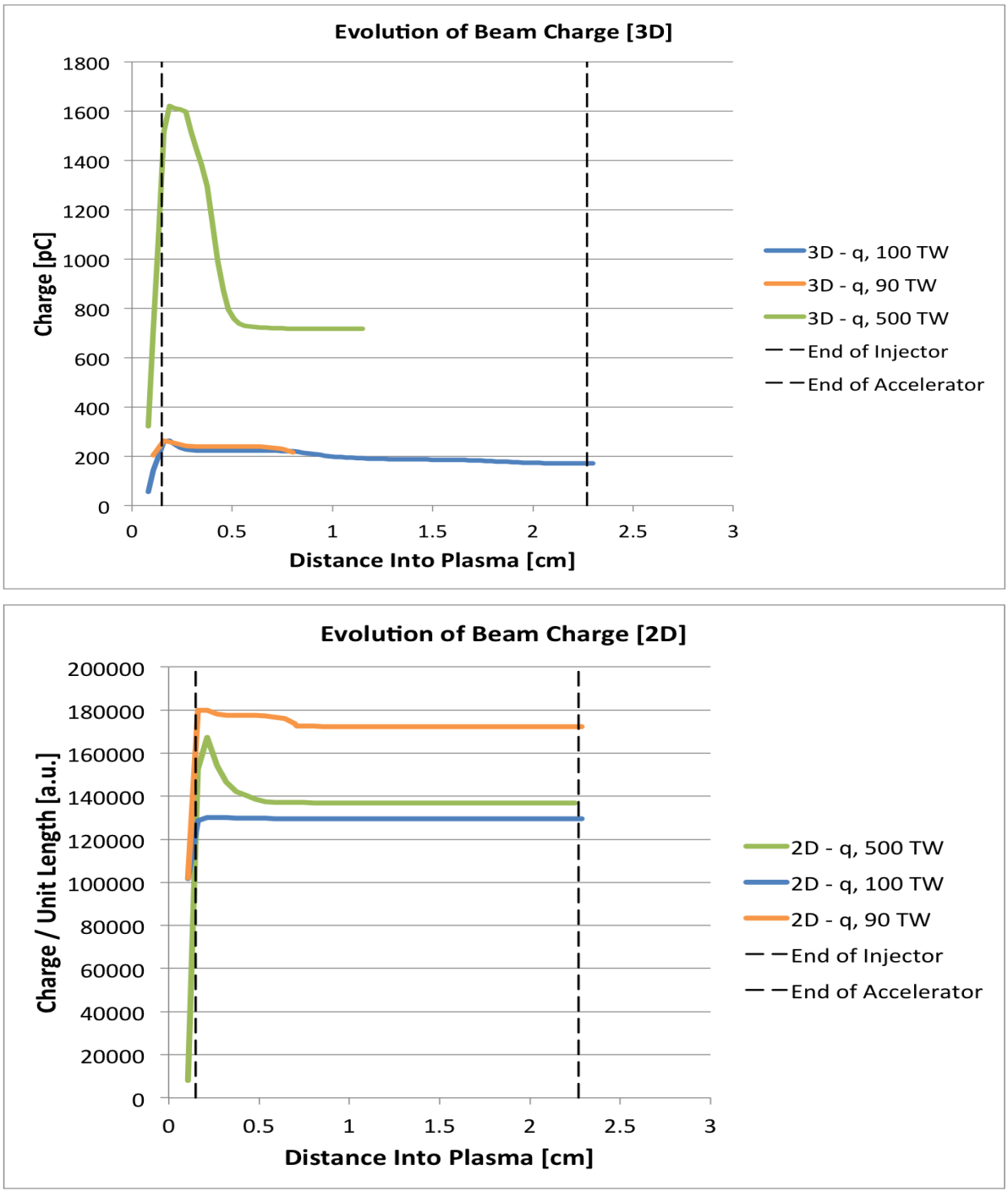

Figure A.8: The total trapped particle charge (for 3D simulations) and charge-per-unit-length (for 2D simulations) for the two staged ionization injection scheme. After approximately 0.6cm the 'trapped' charge of the 3D simulation drops due to many of the particles later dephased with the wake and slowly fell out of the simulation box.

The total amount of charge trapped within each simulation is plotted in Figure A.8. For the 2D simulations we did not observe a dramatic difference in the number of trapped charge-per-unit-length for each laser energy, but in the 3D case there is an order of magnitude difference in the 500 TW case. In addition, after approximately 0.6cm the trapped charge of the 3D simulation drops due to many of the particles dephasing with the wake and slowly fell out of the simulation box. This is because of a unique population of particles trapped in the 3D, 500 TW simulation that forms a second peak in the spectrums of particles trapped in the first bucket. This second bunch of trapped particles peaked at $0.21GeV$, 2.1mm into the plasma and the difference in the energy spectrums are presented in Figure A.9.

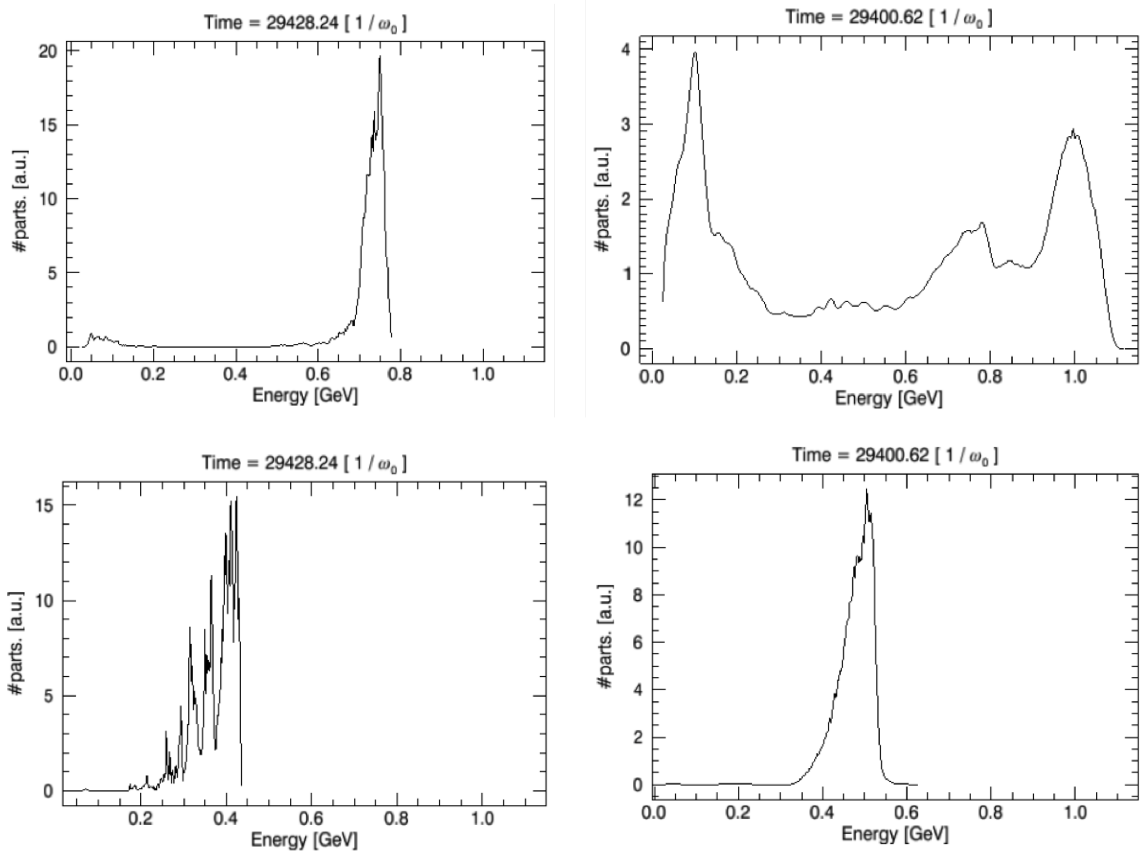

Figure A.9: The spectrums of the trapped particles 0.37cm into the plasma, for the 2D (left) and 3D (right) cases of the 500 TW (top) and 100 TW (bottom) simulations. In the 3D, 500 TW case there is a second population of trapped electrons, which makes for a very different energy spectrum.

The purpose of this subsection was to highlight the differences we observed between the 2D and 3D simulations of the two-stage ionization injection simulations. There is much room for studying the reasons for these deviations given the complexity of this problem and the degree to which the simulated geometry affects them, but this will be left as potential work for future research.

A.3 Conclusion

The two stage ionization injection scheme has been proven to be an effective method of producing a low energy spread beam in both experiment and in simulations. We presented 2D and 3D Cartesian geometry simulations which verify the validity of the method as well as explore the capabilities of the Callisto laser system. In addition, we explored key differences and observations between the 2D and 3D geometries, which may later prove to be important in understanding the complex manner in which the simulation geometry affects the LWFA problem. These latter observations were a major motivation for developing the quasi-3D algorithm as it can capture "3D" physics in a much faster, less expensive geometry. We have recently added ionization in to the quasi-3D algorithm and it would be illuminating to use it to revisit the simulations in this Appendix for comparison.

Appendix B

Formation of Ultrarelativistic Electron Rings

B.1 Introduction

Preliminary results from the two-stage ionization injection simulations (most of whose results were presented in Appendix A) showed the unexpected formation of electron rings. These simulations showed that a laser intensity enhancement as the laser evolves leads to a wake where there is sheath splitting and the formation of a hollow toroidal pocket in the electron density around the wake behind the first wake bucket. The rings are formed in a complex process involving the acceleration of particles trapped in the second bucket maneuvering around the potential behind the first bucket, and to ultimately fall into the first bucket after transforming into a ring. The importance of these findings were not well understood until experiments demonstrated that Gaussian laser pulses can produce highly relativistic spatial rings of electrons in addition to the on-axis electron beams [105]. These experiments were conducted using the Ti:sapphire Callisto laser system at the Lawrence Livermore National Laboratory. After these findings these simulation results were revisited to better understand the process.

Past literature proposed various potential possibilities concerning the use of such relativistic electron rings, highlighting their potential importance. Electron rings were proposed for the acceleration of ions in conventional RF accelerators[106], as improved drivers for PWFAs of positrons[107], and they have been used in RF accelerators as compact collimators for proton bunches[108]. Simulations have shown that high-energy electron rings may be formed by donut-shaped wakes driven by Laguerre-Gaussean laser pulses[109], but the results presented here show that they are possible with Gaussian laser pulses as well.

Due to their unique importance, the results for the original 3D OSIRIS simulation that showed the injection and formation of the electron ring will be presented here in its own Appendix. In section B.2, we will present the results and the basic description of the trapping process. In section B.3 we will summarize the results and postulate future directions of relevant research.

B.2 Simulation Results

The 3D OSIRIS simulation in which the ring-injection was first observed was that of a two-stage ionization LWFA scheme similar to the one presented in Appendix A. The density profile for the two-stage scheme in this case is figure in Figure B.1, and is differentiated largely by a longer injection stage. The simulation was conducted over 10mm in total length of plasma. This was a simulation of a 40 TW laser with a spot size of $W_0 = 15\mu m$ and $FWHM = 60fs$ ($a_0 = 2.3$). The density of the fully ionized He plasma was approximately $n_p = 3.0 \times 10^{18} cm^{-3}$, and was 0.5% doped with N in the injection stage. $4000 \times 300 \times 300$ cells were used in total, with 2 particles per cell for each gas. Quadratic particle shapes were used, along with current smoothing and compensation.

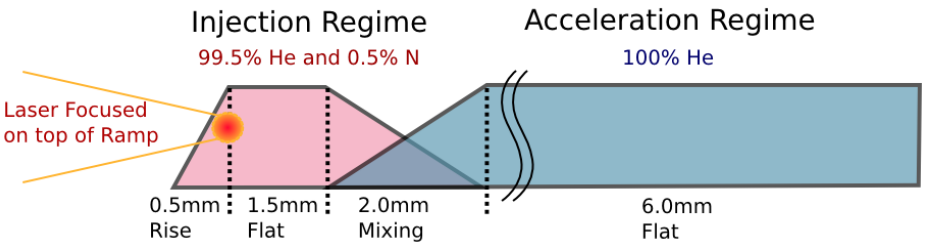

Figure B.1: A pictorial representation of the density of the two-stage LWFA scheme in which we found the injection of electron rings. The pure injection regime ramps up for about 0.5mm and flattens for another 1.0mm until it gradually ramps down into the acceleration regime in a 0.5 mm mixing region. The acceleration regime continues for another 6mm. We did not simulate a down ramp in the acceleration regime as we have in the previous Appendix.

As can be recalled from Sections 2.7 and 2.8, a particle can undergo a minimum change in the trapping potential $\Delta\Psi \equiv \Psi_f - \Psi_i \approx -1$ in order to be trapped. More exactly, this

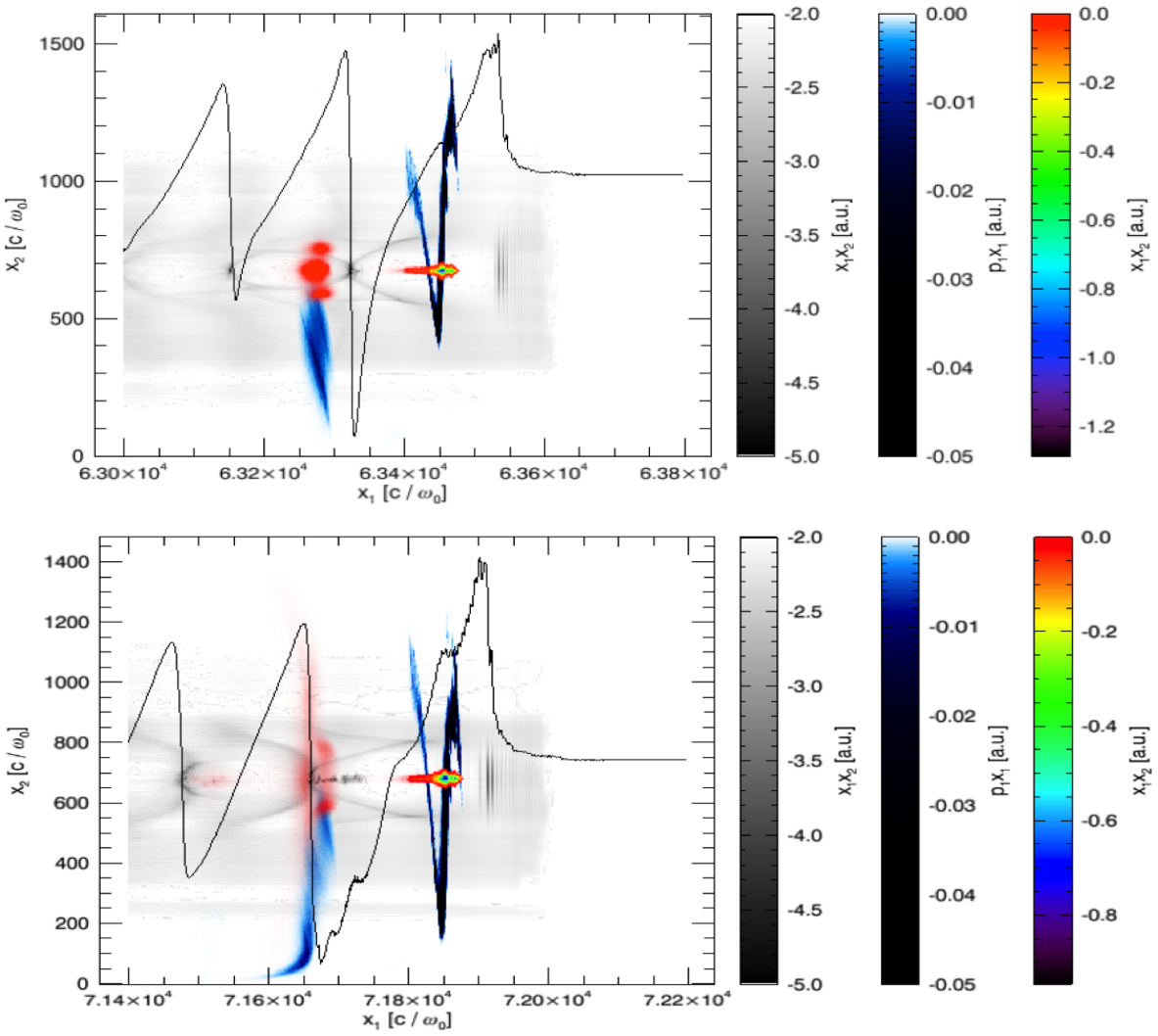

Figure B.2: The density plots and a E_1 lineout pertaining to the first two bubbles in a ionization-injected LWFA simulation at 8.0mm into the plasma (top) and 9.1mm into the plasma (bottom). The Greyscale shows the density cross section of the He (forming the wake), and the rainbow axis displays the density of the N^6 and N^7 electrons (which form the trapped particles). The blue-white scale is the p_1x_1 plot of the trapped particles, showing the relative momentum of the trapped particles at each point along the z-axis.

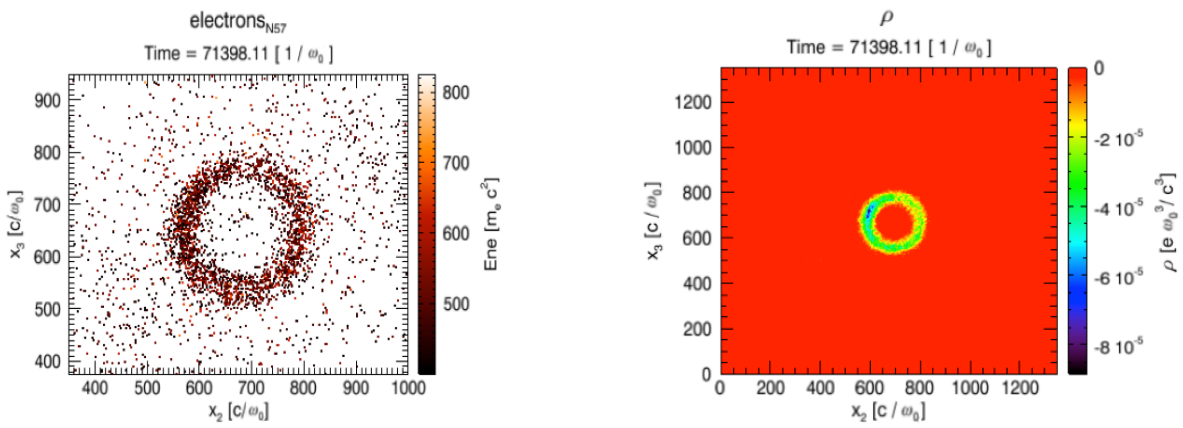

Figure B.3: The raw particle data for the x_1x_2 positions (left) and the cross-sectional density profile (right) of the trapped particle ring shown on the bottom plot of Figure B.2. This is at 9.1mm into the plasma.

expression is given by Equation 2.57, given by

$$\Delta\Psi = \frac{\sqrt{1+p_\perp^2}}{\gamma_\phi} - 1,$$

where $\gamma_\phi \equiv 1/\sqrt{1-v_\phi^2}$. One advantage of the ionization-injection method is that particles being born in the center of the laser pulse have a high Ψ_f, and therefore a smaller potential drop is necessary in order to trap them. As explained in the previous Appendix, this is the reason for which a comparatively small normalized laser amplitude of $a_0 \approx 1.6$ has been shown to trap in the ionization injection scheme, whereas $a_0 \gtrsim 4.0$ is necessary in order to trap particles in a pre-ionized plasma. However, if the phase velocity v_ϕ of the wake is reduced by any mechanism, trapping with a smaller drop in trapping potential is possible.

Electrons born early in the laser pulse have a smaller Ψ_i and often do not satisfy the trapping condition in the first bucket, even as the laser amplitude is set such as the electrons born in the center of the pulse is being successfully trapped in the first bucket. These electrons still have a chance of becoming trapped in the second bucket if the wake is evolving[110, 111]. The wake can evolve from beam loading of the trapped electrons[112], or from the ponderomotive force enhancement from self-focusing and photon deceleration of the laser[113]. These effects cause the radius of the bucket to increase and the potential minimum to fall backward

with respect to the laser pulse, thus reducing the effective phase velocity, and it's effect is greater in each successive bucket[114].

Figure B.2 displays the elections that have been trapped in the first and the second buckets of the two-stage ionization-injection simulation presented in this Appendix - one at 8mm into the plasma and the other at 9.1mm into the plasma. The trapped electrons (N^6 and N^7 electrons, which are separated as their own distinct electron population in the OSIRIS simulation), which are shown in rainbow colors, are distinguished from the He electrons that have been ionized to form the wake, which are shown in grey scale. At 8mm into the plasma, the particles trapped in the first bucket has been completely dephased, but there is also a population of electrons that are trapped in the second bucket that is beginning to split into what appears to be three segments. This plot is a 2D cross-section of a fully 3D Cartesian simulation, and upon closer examination what we see in Figure B.2 is in fact a cross section of a toroidal population of the trapped particles splitting away from a central, spherical population. This population of electrons have fallen into a potential well that is formed by the splitting of the narrow He electron sheath. This splitting of the narrow sheath is typical of a LWFA in the blowout regime, where it is not as well defined as a PWFA in the same regime. Plotting the data similarly at 9.1mm, slightly passed the dephasing length, we show that this toroidal population of electrons continue to travel forward with respect to the wake, ultimately to fall into the first bucket. The on-axis population of the electrons in the second bucket, in contrast, begins to decelerate within the potential peak between the buckets. An x-y cross section at the location of the electron ring 9.1mm into the plasma is presented in Figure B.3, both as a scatter plot of the raw macroparticle positions, and as a cross-sectional plot of the combined N^6 and N^7 electron density. These electrons are shown to fall fully into the first bucket in Figure B.4 by the time the laser travels 9.6mm into the plasma.

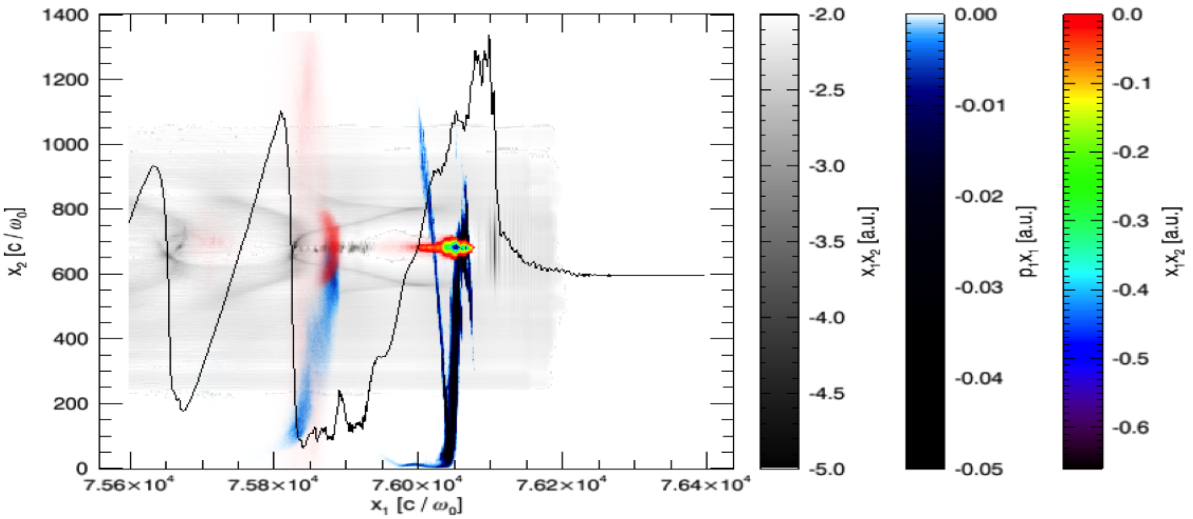

Figure B.4: The density plots and a E_z lineout pertaining to the first two bubbles in a ionization-injected LWFA simulation at 9.6mm into the plasma. The Greyscale shows the density cross section of the He (forming the wake), and the rainbow axis displays the density of the N^6 and N^7 electrons (which form the trapped particles). The blue-white scale is the p_1x_1 plot of the trapped particles, showing the relative momentum of the trapped particles at each point along the z-axis.

B.3 Conclusion

Experiments conducted using the Callisto laser system has shown that 200 TW, 60 fs pulse focused 750 μm inside a 10 mm long gas cell target ($\sim$ 3 times the ideal dephasing length for the electron density) containing a composition that varied from a pure He plasma to a mixture of He and N, can produce an ultrarelativistic electron ring that propagates in free space over a meter-scale distance upon exiting the plasma[105]. Upon discovering the reality of this physical phenomena, these two-stage ionization-injection simulation results were revisited to give a physical explanation the processes that led to those results. The formation of the rings was seen to involve a complex process of particles trapped in the second bubble falling into a pocket of the wake potential produced by the sheath splitting characteristic of LWFAs in the blowout regime, and then passing through into the first bucket after a dephasing length. Based on this explanation, there is potential for improving the mechanism of producing an ultrarelativistic ring in a future experiments.

Pollock et al. states that in order to use the produced rings for applications, the ratio of the ring to the axial current must be increased - a possibility being the use of a density down ramp. The laser pulse may also be spectrally tailored to let the bubble length expand from laser evolution, or a density down ramp may be used to expand the bubble in an accordion effect.

References

[1] R. G. Hemker. *Particle-In-Cell Modeling of Plasma-Based Accelerators in Two and Three Dimensions*. PhD thesis, University of California, Los Angeles, 2000.

[2] R. A. Fonseca, L. O. Silva, F. S. Tsung, V. K. Decyk, W. Lu, C. Ren, W. B. Mori, S. Deng, S. Lee, and T. Katsouleas. Osiris: A three-dimensional, fully relativistic particle in cell code for modeling plasma based accelerators. *Lecture Notes in Computer Science*, 2331:342–351, 2002.

[3] A. F. Lifschitz, X. Davone, E. Lefebvre, J. Faure, C. Rechatin, and V. Malka. Particle-in-cell modelling of laser-plasma interaction using fourier decomposition. *Journal of Computational Physics*, 228(5):1803–1814, 2009.

[4] W. Lu, M. Tzoufras, C. Joshi, F. S. Tsung, W. B. Mori, J. Vieira, R. A. Fonseca, and L. O. Silva. Generating multi-gev electron bunches using single stage laser wakefield acceleration in a 3d nonlinear regime. *Physical Review Special Topics - Accelerators and Beams*, 10(061301), 2007.

[5] T. Tajima and J. M. Dawson. Laser Electron-Accelerator. *Physical Review Letters*, 43(4):267–270, 1979.

[6] E. Esarey, P. Sprangle, J. Krall, and A. Ting. Overview of plasma-based accelerator concepts. *IEEE Transactions on Plasma Science*, 24(2):252–288, Apr. 1996. International Workshop on 2nd-Generation Plasma Accelerators, Kardamyli, Greece, Jun. 26-30, 1995.

[7] P. Chen, J. M. Dawson, R. W. Huff, and T. Katsouleas. Acceleration of electrons by the interaction of a bunched electron-beam with a plasma. *Physical Review Letters*, 54(7):693–696, 1985.

[8] A. Seryi, M. Hogan, S. Pei, T. Raubenheimer, P. Tenenbaum, T. Katsouleas, C. Huang, C. Joshi, W. Mori, and P. Muggli. A concept of plasma wake field acceleration linear collider (pwfa-lc). SLAC-PUB-13766, 2009.

[9] J. M. Dawson. Nonlinear Electron Oscillations in a Cold Plasma. *Physical Review*, 113(2):383–387, 1959.

[10] A. I. Akhiezer and R. V. Polovin. Theory of wave motion of an electron plasma. *Soviet Physics, JETP*, 3(5):696–705, 1986.

[11] Ian Blumenfeld, Christopher E. Clayton, Franz-Josef Decker, Mark J. Hogan, Chengkun Huang, Rasmus Ischebeck, Richard Iverson, Chandrashekhar Joshi, Thomas Katsouleas, Neil Kirby, Wei Lu, Kenneth A. Marsh, Warren B. Mori, Patric Muggli, Erdem Oz, Robert H. Siemann, Dieter Walz, and Miaomiao Zhou. Energy doubling of 42 GeV electrons in a metre-scale plasma wakefield accelerator. *Nature*, 445(7129):741–744, Feb. 15 2007.

[12] J. B. Rosenzweig, B. Breizman, T. Katsouleas, and J. J. Su. Acceleration and focusing of electrons in two-dimensional nonlinear plasma wake fields. *Physical Review A (Statistical Physics, Plasmas, Fluids, and Related Interdisciplinary Topics)*, 44:R6189–92, 15 Nov. 1991.

[13] W. B. Mori, T. Katsouleas, C. B. Darrow, C. E. Clayton, C. Joshi, J. M. Dawson, C. B. Decker, K. Marsh, and S. C. Wilks. Laser wakefields at ucla and llnl. *Conference Record of the IEEE Particle Accelerator Conference, Accelerator Science and Technology*, 1:564–566, 1991.

[14] W. B. Mori, V. K. Decyk, T. C. Katsouleas, D. W. Forslund, R. D. Ferraro, and E. Horowitz. Full-scale numerical experiment to test a future plasma-based accelerator. Submitted to NSF as part of the U.S. High Performance Computing and Communications Program, 1992.

[15] V. Malka, S. Fritzler, E. Lefebvre, M. M. Aleonard, F. Burgy, J. P. Chambaret, J. F. Chemin, K. Krushelnick, G. Malka, S. P. D. Mangles, Z. Najmudin, M. Pittman, J. P. Rousseau, J. N. Scheurer, B. Walton, and A. E. Dangor. Electron acceleration by a wake field forced by an intense ultrashort laser pulse. *Science*, 298(5598):1596–1600, Nov. 22 2002.

[16] A. Pukhov and J. Meyer-ter Vehn. Laser wake field acceleration: the highly non-linear broken-wave regime. *Applied Physics B-Lasers and Optics*, 74(4-5):355–361, Apr. 2002.

[17] F. S. Tsung, R. Narang, W. B. Mori, C. Joshi, R. A. Fonseca, and L. O. Silva. Near-GeV-energy laser-wakefield acceleration of self-injected electrons in a centimeter-scale plasma channel. *Physical Review Letters*, 93(18), Oct. 29 2004.

[18] S. P. D. Mangles, C. D. Murphy, Z. Najmudin, A. G. R. Thomas, J. L. Collier, A. E. Dangor, E. J. Divall, P. S. Foster, J. G. Gallacher, C. J. Hooker, D. A. Jaroszynski, A. J. Langley, W. B. Mori, P. A. Norreys, F. S. Tsung, R. Viskup, B. R. Walton, and K. Krushelnick. Monoenergetic beams of relativistic electrons from intense laser-plasma interactions. *Nature*, 431(7008):535–538, Sep. 30 2004.

[19] C. G. R. Geddes, C. Toth, J. van Tilborg, E. Esarey, C. B. Schroeder, D. Bruhwiler, C. Nieter, J. Cary, and W. P. Leemans. High-quality electron beams from a laser wakefield accelerator using plasma-channel guiding. *Nature*, 431(7008):538–541, Sep. 30 2004.

[20] J. Faure, Y. Glinec, A. Pukhov, S. Kiselev, S. Gordienko, E. Lefebvre, J. P. Rousseau, F. Burgy, and V. Malka. A laser-plasma accelerator producing monoenergetic electron beams. *Nature*, 431(7008):541–544, Sep. 30 2004.

[21] W. P. Leemans, B. Nagler, A. J. Gonsalves, Cs. Toth, K. Nakamura, C. G. R. Geddes, E. Esarey, C. B. Schroeder, and S. M. Hooker. GeV electron beams from a centimetre-scale accelerator. *Nature Physics*, 2(10):696–699, Oct. 2006.

[22] S. Kneip, S. R. Nagel, S. F. Martins, S. P. D. Mangles, C. Bellei, O. Chekhlov, R. J. Clarke, N. Delerue, E. J. Divall, G. Doucas, K. Ertel, F. Fiuza, R. Fonseca, P. Foster, S. J. Hawkes, C. J. Hooker, K. Krushelnick, W. B. Mori, C. A. J. Palmer, K. Ta Phuoc, P. P. Rajeev, J. Schreiber, M. J. V. Streeter, D. Urner, J. Vieira, L. O. Silva, and Z. Najmudin. Near-GeV Acceleration of Electrons by a Nonlinear Plasma Wave Driven by a Self-Guided Laser Pulse. *Physical Review Letters*, 103(3), Jul. 17 2009.

[23] C. E. Clayton, J. E. Ralph, F. Albert, R. A. Fonseca, S. H. Glenzer, C. Joshi, W. Lu, K. A. Marsh, S. F. Martins, W. B. Mori, A. Pak, F. S. Tsung, B. B. Pollock, J. S. Ross, L. O. Silva, and D. H. Froula. Self-Guided Laser Wakefield Acceleration beyond 1 GeV Using Ionization-Induced Injection. *Physical Review Letters*, 105(10), Sep. 1 2010.

[24] P. A. Walker, N. Bourgeois, W. Rittershofer, J. Cowley, N. Kajumba, A. R. Maier, J. Wenz, C. M. Werle, S. Karsch, F. Gruener, D. R. Symes, P. P. Rajeev, S. J. Hawkes, O. Chekhlov, C. J. Hooker, B. Parry, Y. Tang, and S. M. Hooker. Investigation of GeV-scale electron acceleration in a gas-filled capillary discharge waveguide. *New Journal of Physics*, 15, Apr. 26 2013.

[25] S. F. Martins, R. A. Fonseca, W. Lu, W. B. Mori, and L. O. Silva. Exploring laser-wakefield-accelerator regimes for near-term lasers using particle-in-cell simulation in Lorentz-boosted frames. *Nature Physics*, 6(4):311–316, Apr. 2010.

[26] R. A. Fonseca, L. O. Silva, F. S. Tsung, V. K. Decyk, W. Lu, C. Ren, W. B. Mori, S. Deng, S. Lee, T. Katsouleas, and J. C. Adam. OSIRIS: A three-dimensional, fully relativistic particle in cell code for modeling plasma based accelerators. In Sloot, P and Tan, CJK and Dongarra, JJ and Hoekstra, AG, editor, *Computational Science-ICCS 2002, PT III, Proceedings*, volume 2331 of *Lecture Notes in Computer Science*, pages 342–351, Heidelberger Platz 3, D-14197 Berlin, Germany, 2002. Univ Amsterdam, Sect Computat Sci; Sharcnet, Canada; Univ Tennessee, Dept Comp Sci; Power Comp & Commun BV; Elsevier Sci Publ; Springer Verlag; HPCN Fdn; Natl Supercomp Facilities; Sun Microsyst Inc; Queens Univ, Sch Comp Sci, Springer-Verlag Berlin. International Conference on Computational Science, Amsterdam, Netherlands, Apr. 21-24, 2002.

[27] A. Davidson, A. Tableman, W. An, F. S. Tsung, W. Lu, J. Vieira, R. A. Fonseca, L. O. Silva, and W. B. Mori. Implementation of a hybrid particle code with a PIC description in r-z and a gridless description in phi into OSIRIS. *Journal of Computational Physics*, 281:1063–1077, Jan. 15 2015.

[28] C. Joshi, W. B. Mori, T. Katsouleas, J. M. Dawson, J. M. Kindel, and D. W. Forslund. Ultrahigh Gradient Particle-Acceleration by Intense Laser-Driven Plasma-Density Waves. *Nature*, 311(5986):525–529, 1984.

[29] P. Sprangle, E. Esarey, J. Krall, and G. Joyce. Propagation and Guiding of Intense Laser-Pulses in Plasmas. *Physical Review Letters*, 69(15):2200–2203, Oct. 12 1992.

[30] C. A. Coverdale, C. B. Darrow, C. D. Decker, W. B. Mori, K. C. Tzeng, K. A. Marsh, C. E. Clayton, and C. Joshi. Propagation of Intense Subpicosecond Laser-Pulses Through Underdense Plasmas. *Physical Review Letters*, 74(23):4659–4662, Jun. 5 1995.

[31] P. Chen, J. M. Dawson, R. W. Huff, and T. Katsouleas. Acceleration of Electrons by the Interaction of a Bunched Electron-Beam With a Plasma. *Physical Review Letters*, 54(7):693–696, 1985.

[32] G. Z. Sun, E. Ott, Y. C. Lee, and P. Guzdar. Self-Focusing of Short Intense Pulses in Plasmas. *Physics of Fluids*, 30(2):526–532, Feb. 1987.

[33] W. P. Leemans, B. Nagler, and A. J. Gonsalves. Gev electron beams from a centimetre-scale accelerator. *Nature Physics*, 2(10):696–699, 2006.

[34] N. A. M. Hafz, T. M. Jeong, I. W. Choi, S. K. Lee, K. H. Pae, V. V. Kulagin, J. H. Sung, T. J. Yu, K. H. Hong, T. Hosokai, J. R. Cary, D. K. Ko, and J. Lee. Stable generation of gev-class electron beams from self-guided laser-plasma channels. *Nature Photonics*, 2(9):571–577, 2008.

[35] X. M. Wang, R. Zgadzaj, N. Fazel, Z. Y. Li, S. A. Yi, X. Zhang, W. Henderson, Y. Y. Chang, R. Korzekwa, H. E. Tsai, C. H. Pai, H. Quevedo, G. Dyer, E. Gaul, M. Martinez, A. C. Bernstein, T. Borger, M. Spinks, M. Donovan, V. Khudik, G. Shvets, T. Ditmire, and M. C. Downer. Quasi-monoenergetic laser-plasma acceleration of electrons to 2 gev. *Nature Communications*, 4(1988), 2013.

[36] W. Lu, C. Huang, M. Zhou, W. B. Mori, and T. Katsouleas. Nonlinear theory for relativistic plasma wakefields in the blowout regime. *Phys. Rev. Lett.*, 96:165002, Apr. 2006.

[37] S. Gordienko and A. Pukhov. Scalings for ultrarelativistic laser plasmas and quasimonoenergetic electrons. *Physics of Plasmas*, 12(4), Apr. 2005.

[38] E. Oz, S. Deng, T. Katsouleas, P. Muggli, C. D. Barnes, I. Blumenfeld, F. J. Decker, P. Emma, M. J. Hogan, R. Ischebeck, R. H. Iverson, N. Kirby, P. Krejcik, C. O'Connell, R. H. Siemann, D. Walz, D. Auerbach, C. E. Clayton, C. Huang, D. K. Johnson, C. Joshi, W. Lu, K. A. Marsh, W. B. Mori, and M. Zhou. Ionization-induced electron trapping in ultrarelativistic plasma wakes. *Physical Review Letters*, 98(8), Feb. 23 2007.

[39] A. Pak, K. A. Marsh, S. F. Martins, W. Lu, W. B. Mori, and C. Joshi. Injection and Trapping of Tunnel-Ionized Electrons into Laser-Produced Wakes. *Physical Review Letters*, 104(2), Jan. 15 2010.

[40] C. McGuffey, A. G. R. Thomas, W. Schumaker, T. Matsuoka, V. Chvykov, F. J. Dollar, G. Kalintchenko, V. Yanovsky, A. Maksimchuk, K. Krushelnick, V. Yu. Bychenkov, I. V. Glazyrin, and A. V. Karpeev. Ionization Induced Trapping in a Laser Wakefield Accelerator. *Physical Review Letters*, 104(2), Jan. 15 2010.

[41] J. Faure, C. Rechatin, A. Norlin, A. Lifschitz, Y. Glinec, and V. Malka. Controlled injection and acceleration of electrons in plasma wakefields by colliding laser pulses. *Nature*, 444(7120):737–739, Dec. 7 2006.

[42] P. Tomassini, M. Galimberti, A. Giulietti, D. Giulietti, L. A. Gizzi, L. Labate, and F. Pegoraro. Laser wake field acceleration with controlled self-injection by sharp density transition. *Laser and Particle Beams*, 22(4):423–429, Dec. 2004. International Workshop on Laser and Plasma Accelerators, Portovenere, Italy, Sep. 29-Oct. 03, 2003.

[43] A. J. Gonsalves, K. Nakamura, C. Lin, D. Panasenko, S. Shiraishi, T. Sokollik, C. Benedetti, C. B. Schroeder, C. G. R. Geddes, J. van Tilborg, J. Osterhoff, E. Esarey, C. Toth, and W. P. Leemans. Tunable laser plasma accelerator based on longitudinal density tailoring. *Nature Physics*, 7(11):862–866, Nov. 2011.

[44] C. G. R. Geddes, K. Nakamura, G. R. Plateau, Cs. Toth, E. Cormier-Michel, E. Esarey, C. B. Schroeder, J. R. Cary, and W. P. Leemans. Plasma-density-gradient injection of low absolute-momentum-spread electron bunches. *Physical Review Letters*, 100(21), May 30 2008.

[45] K. Schmid, A. Buck, C. M. S. Sears, J. M. Mikhailova, R. Tautz, D. Herrmann, M. Geissler, F. Krausz, and L. Veisz. Density-transition based electron injector for laser driven wakefield accelerators. *Physical Review Special Topics-Accelerators and Beams*, 13(9), Sep. 7 2010.

[46] X. Xu. in preparation and in personal communication, 2016.

[47] J. M. Dawson. Particle Simulation of Plasmas. *Reviews of Modern Physics*, 55(2):403–447, 1983.

[48] Charles K. Birdsall and A. Bruce Langdon. *Plasma Physics Via Computer Simulation*. McGraw Hill Higher Education, 1984.

[49] W. Lu, C. Huang, M. M. Zhou, W. B. Mori, and T. Katsouleas. Limits of linear plasma wakefield theory for electron or positron beams. *Physics of Plasmas*, 12(6), Jun. 2005.

[50] P. Mora and T. M. Antonsen. Kinetic modeling of intense, short laser pulses propagating in tenuous plasmas. *Physics of Plasmas*, 4(1):217–229, Jan. 1997.

[51] P. Sprangle, E. Esarey, and A. Ting. Nonlinear-Theory of Intense Laser-Plasma Interactions. *Physical Review Letters*, 64(17):2011–2014, Apr. 23 1990.

[52] D. H. Whittum. Transverse two-stream instability of a beam with a Bennett profile. *Physics of Plasmas*, 4(4):1154–1159, Apr. 1997.

[53] W. K. H. Panofsky and W. A. Wenzel. Some Considerations Concerning the Transverse Deflection of Charged Particles in Radio-Frequency Fields. *Review of Scientific Instruments*, 27(11):967, 1956.

[54] M. Tzoufras, W. Lu, F. S. Tsung, C. Huang, W. B. Mori, T. Katsouleas, J. Vieira, R. A. Fonseca, and L. O. Silva. Beam loading by electrons in nonlinear plasma wakes. *Physics of Plasmas*, 16(056705), 2009.

[55] W. B. Mori. The physics of the nonlinear optics of plasmas at relativistic intensities for short-pulse lasers. *IEEE Journal of Quantum Electronics*, 33(11):1942–1953, Nov. 1997.

[56] C. D. Decker, W. B. Mori, K. C. Tzeng, and T. Katsouleas. Evolution of ultra-intense, short-pulse lasers in underdense plasmas. *Physics of Plasmas*, 3(5, 2):2047–2056, May 1996. 37th Annual Meeting of the Division-of-Plasma-Physics of the American-Physical-Society, Louisville, KY, Nov. 06-10, 1995.

[57] I. Kostyukov, A. Pukhov, and S. Kiselev. Phenomenological theory of laser-plasma interaction in "bubble" regime. *Physics of Plasmas*, 11(11):5256–5264, Nov. 2004.

[58] C. D. Decker and W. B. Mori. Group-velocity of large-amplitude electromagnetic-waves in a plasma. *Physical Review Letters*, 72(4):490–493, Jan. 24 1994.

[59] C. D. Decker and W. B. Mori. Group-velocity of large-amplitude electromagnetic-waves in a plasma. *Physical Review E*, 51(2):1364–1375, Feb. 1995.

[60] C. D. Decker, W. B. Mori, and T. Katsouleas. Particle-in-cell simulations of raman forward scattering from short-pulse high-intensity lasers. *Physical Review E*, 50(5):R3338–R3341, Nov. 1994.

[61] C. Huang, V. K. Decyk, M. Zhou, W. Lu, and W. B. Mori. Quicpic: a highly efficient fully parallelized pic code for plasma-based accelration. *Journal of Physics: Conference Series*, 46:190–199, 2006.

[62] Weiming An, Viktor K. Decyk, Warren B. Mori, and Thomas M. Antonsen, Jr. An improved iteration loop for the three dimensional quasi-static particle-in-cell algorithm: QuickPIC. *Journal Of Computational Physics*, 250:165–177, Oct. 1 2013.

[63] D. F. Gordon, W. B. Mori, and T. M. Antonsen. A ponderomotive guiding center particle-in-cell code for efficient modeling of laser-plasma interactions. *IEEE Transactions on Plasma Science*, 28(4):1224–1232, Aug. 2000.

[64] J. L. Vay. Noninvariance of space- and time-scale ranges under a Lorentz transformation and the implications for the study of relativistic interactions. *Physical Review Letters*, 98(13), Mar. 30 2007.

[65] J. L. Vay, C. G. R. Geddes, E. Cormier-Michel, and D. P. Grote. Effects of hyperbolic rotation in Minkowski space on the modeling of plasma accelerators in a Lorentz boosted frame. *Physics of Plasmas*, 18(3), Mar. 2011.

[66] S. F. Martins, R. A. Fonseca, J. Vieira, L. O. Silva, W. Lu, and W. B. Mori. Modeling laser wakefield accelerator experiments with ultrafast particle-in-cell simulations in boosted frames. *Physics of Plasmas*, 17(5), May 2010. 51st Annual Meeting of the

Division-of-Plasma-Physics of the American-Physics-Society, Atlanta, GA, Nov. 02-06, 2009.

[67] C. Benedetti, C. B. Schroeder, E. Esarey, and W. P. Leemans. Efficient modeling of laser-plasma accelerators using the ponderomotive-based code inf&rno. In *proceedings of ICAP2012*, 2012.

[68] Xinlu Xu, Peicheng Yu, Samual F. Martins, Frank S. Tsung, Viktor K. Decyk, Jorge Vieira, Ricardo A. Fonseca, Wei Lu, Luis O. Silva, and Warren B. Mori. Numerical instability due to relativistic plasma drift in EM-PIC simulations. *Computer Physics Communications*, 184(11):2503–2514, Nov. 2013.

[69] P. Yu, X. Xu, V. K. Decyk, W. An, J. Vieira, F. S. Tsung, R. A. Fonseca, W. Lu, and L. O. Silva. Modeling of laser wakefield acceleration in lorentz boosted frame using em-pic code with spectral solver. *Journal of Computational Physics*, 266(1):124–138, 2014.

[70] Brendan B. Godfrey and Jean-Luc Vay. Numerical stability of relativistic beam multidimensional PIC simulations employing the Esirkepov algorithm. *Journal of Computational Physics*, 248:33–46, Sep. 1 2013.

[71] S. Corde, C. Thaury, A. Lifschitz, G. Lambert, K. Ta Phuoc, X. Davoine, R. Lehe, D. Douillet, A. Rousse, and V. Malka. Observation of longitudinal and transverse self-injections in laser-plasma accelerators. *Nature Communications*, 4, Feb. 2013.

[72] B. Marder. A Method For Incorporating Gauss Law Into Electromagnetic Pic Codes. *Journal Of Computational Physics*, 68(1):48–55, Jan. 1987.

[73] A. B. Langdon. On Enforcing Gauss Law In Electromagnetic Particle-In-Cell Codes. *Computer Physics Communications*, 70(3):447–450, Jul. 1992.

[74] C. K. Birdsall and A. B. Langdon. *Plasma physics via computer simulation*. The Adam Hilger series on plasma physics. McGraw-Hill, 1985.

[75] J. M. Dawson. The electrostatic sheet model for a plasma and its modification to finite-size particles. In B. Alder, S. Fernbach, and M. Rotenberg, editors, *Methods in computational physics. IX. Plasma physics*, pages 1–28. Academic, London, UK, 1970 1970.

[76] B. B. Godfrey and Mission Research Corp Albuquerque NM. *The IPROP Three-Dimensional Beam Propagation Code*. Defense Technical Information Center, 1985.

[77] B. B. Godfrey, M. M. Campbell, and Mission Research Corp Albuquerque NM. *IVORY: A Three-Dimensional Beam Propagation Code*. Defense Technical Information Center, 1982.

[78] P. Yu, X. Xu, A. Davidson, A. Tableman, T. Dalichaouch, M. D. Meyers, F. S. Tsung, V. K. Decyk, F. Fiuza, J. Vieira, R. A. Fonseca, W. Lu, L. O. Silva, and W. B. Mori. Lorentz boosted frame simulation of laser wakefield acceleration in quasi-3d geometry. *Journal of Computational Physics*, in revision, 2016.

[79] G. S. Constantinescu and S. K. Lele. A highly accurate technique for the treatment of flow equations at the polar axis in cylindrical coordinates using series expansions. *Computer Physics Communications*, 183(1):165–186, 2002.

[80] F. S. Tsung. personal communication, 2016.

[81] K. S. Yee. Numerical solution of initial boundary value problems involving maxwell's equations in isotropic media. *Antennas and Propagation, IEEE Transactions on*, 14(3):302–307, 1966.

[82] T. Z. Esirkepov. Exact charge conservation scheme for Particle-in-Cell simulation with an arbitrary form-factor. *Computer Physics Communications*, 135(2):144–153, Apr. 1 2001.

[83] John Villasenor and Oscar Buneman. Rigorous charge conservation for local electromagnetic field solvers. *Computer Physics Communications*, 69:306–316, 1992.

[84] D. H. Whittum, W. M. Sharp, S. S. Yu, M. Lampe, and G. Joyce. Electron-hose instability in the ion-focused regime. *Physical Review Letters*, 67(8):991–994, Aug. 19 1991.

[85] C. Huang, W. Lu, M. Zhou, C. E. Clayton, C. Joshi, W. B. Mori, P. Muggli, S. Deng, E. Oz, T. Katsouleas, M. J. Hogan, I. Blumenfeld, F. J. Decker, R. Ischebeck, R. H. Iverson, N. A. Kirby, and D. Walz. Hosing instability in the blow-out regime for plasma-wakefield acceleration. *Physical Review Letters*, 99(25), Dec. 21 2007.

[86] S. Mallat. *A Wavelet Tour of Signal Processing*. Academic Press, London, UK, 1998.

[87] D. F. Gordon, B. Hafizi, R. F. Hubbard, J. R. Penano, P. Sprangle, and A. Ting. Asymmetric self-phase modulation and compression of short laser pulses in plasma channels. *Physical Review Letters*, 90(21), May 30 2003.

[88] C. Ren, B. J. Duda, R. G. Hemker, W. B. Mori, T. Katsouleas, T. M. Antonsen, and P. Mora. Compressing and focusing a short laser pulse by a thin plasma lens. *Physical Review E*, 63(2, 2):art. no.–026411, Feb. 2001.

[89] J. Faure, Y. Glinec, J. J. Santos, F. Ewald, J. P. Rousseau, S. Kiselev, A. Pukhov, T. Hosokai, and V. Malka. Observation of laser-pulse shortening in nonlinear plasma waves. *Physical Review Letters*, 95(20), Nov. 11 2005.

[90] M. Tzoufras, F. S. Tsung, W. B. Mori, and A. A. Sahai. Improving the Self-Guiding of an Ultraintense Laser by Tailoring Its Longitudinal Profile. *Physical Review Letters*, 113(24), Dec. 9 2014.

[91] B. J. Duda and W. B. Mori. Variational principle approach to short-pulse laser-plasma interactions in three dimensions. *Physical Review E*, 61(2):1925–1939, 2000.

[92] P. Sprangle, J. Krall, and E. Esarey. Hose-Modulation Instability of Laser-Pulses In Plasmas. *Physical Review Letters*, 73(26):3544–3547, Dec. 26 1994.

[93] J. Tonge, J. May, W. B. Mori, F. Fiuza, S. F. Martins, R. A. Fonseca, L. O. Silva, and C. Ren. A simulation study of fast ignition with ultrahigh intensity lasers. *Physics of Plasmas*, 16(5), May 2009. 50th Annual Meeting of the Division of Plasma Physics of the American-Physical-Society, Dallas, TX, FEB 01, 2008.

[94] F. Fiuza, M. Marti, R. A. Fonseca, L. O. Silva, J. Tonge, J. May, and W. B. Mori. Efficient modeling of laser-plasma interactions in high energy density scenarios. *Plasma Physics and Controlled Fusion*, 53(7), Jul. 2011.

[95] J. May, J. Tonge, F. Fiuza, R. A. Fonseca, L. O. Silva, C. Ren, and W. B. Mori. Mechanism of generating fast electrons by an intense laser at a steep overdense interface. *Physical Review E*, 84(2, 2), Aug. 3 2011.

[96] Dan Haberberger, Sergei Tochitsky, Frederico Fiuza, Chao Gong, Ricardo A. Fonseca, Luis O. Silva, Warren B. Mori, and Chan Joshi. Collisionless shocks in laser-produced plasma generate monoenergetic high-energy proton beams. *Nature Physics*, 8(1):95–99, Jan. 2012.

[97] L. Yin, B. J. Albright, H. A. Rose, K. J. Bowers, B. Bergen, and R. K. Kirkwood. Self-Organized Bursts of Coherent Stimulated Raman Scattering and Hot Electron Transport in Speckled Laser Plasma Media. *Physical Review Letters*, 108(24), Jun. 12 2012.

[98] B. J. Winjum, J. E. Fahlen, F. S. Tsung, and W. B. Mori. Anomalously Hot Electrons due to Rescatter of Stimulated Raman Scattering in the Kinetic Regime. *Physical Review Letters*, 110(16), Apr. 15 2013.

[99] B. B. Afeyan and E. A. Williams. Unified Theory Of Stimulated Raman-Scattering And 2-Plasmon Decay In Inhomogeneous Plasmas - High-Frequency Hybrid Instability. *Physical Review Letters*, 75(23):4218–4221, Dec. 4 1995.

[100] J. B. Rosenzweig, A. M. Cook, A. Scott, M. C. Thompson, and R. B. Yoder. Effects of ion motion in intense beam-driven plasma wakefield accelerators. *Physical Review Letters*, 95(19), Nov. 4 2005.

[101] Peicheng Yu, Xinlu Xu, Adam Tableman, Viktor K. Decyk, Frank S. Tsung, Frederico Fiuza, Asher Davidson, Jorge Vieira, Ricardo A. Fonseca, Wei Lu, Luis O. Silva, and Warren B. Mori. Mitigation of numerical Cerenkov radiation and instability using a hybrid finite difference-FFT Maxwell solver and a local charge conserving current deposit. *Computer Physics Communications*, 197:144–152, Dec. 2015.

[102] Stuart P. D. Mangles, Alec G. R. Thomas, Claudio Bellei, A. E. Dangor, Christos Kamperidis, Stefan Kneip, Sabrina R. Nagel, Louise Willingale, and Zulfikar Najmudin. Self-guided wakefield experiments driven by petawatt-class ultrashort laser pulses. *IEEE Transactions on Plasma Science*, 36(4, 4):1715–1721, Aug. 2008.

[103] B. B. Pollock, C. E. Clayton, J. E. Ralph, F. Albert, A. Davidson, L. Divol, C. Filip, S. H. Glenzer, K. Herpoldt, W. Lu, K. A. Marsh, J. Meinecke, W. B. Mori, A. Pak,

T. C. Rensink, J. S. Ross, J. Shaw, G. R. Tynan, C. Joshi, and D. H. Froula. Demonstration of a Narrow Energy Spread, similar to 0.5 GeV Electron Beam from a Two-Stage Laser Wakefield Accelerator. *Physical Review Letters*, 107(4), Jul. 18 2011.

[104] M. V. Ammosov, N. B. Delone, and V. P. Krainov. Tunnel ionization of complex atoms and of atomic ions in an alternating electromagnetic field. *Soviet Physics - JETP*, 64:1191–4, Dec. 1986.

[105] B. B. Pollock, F. S. Tsung, F. Albert, J. L. Shaw, C. E. Clayton, A. Davidson, N. Lemos, K. A. Marsh, A. Pak, J. E. Ralph, W. B. Mori, and C. Joshi. Formation of Ultrarelativistic Electron Rings from a Laser-Wakefield Accelerator. *Physical Review Letters*, 115(5), Jul. 31 2015.

[106] J. D. Lawson. Electron Ring Accelerators a Cheap Path to Very High Energy Protons. *Nature*, 218(5140):430–&, 1968.

[107] B. E. Blue, C. E. Clayton, C. L. O'Connell, F. J. Decker, M. J. Hogan, C. Huang, R. Iverson, C. Joshi, T. C. Katsouleas, W. Lu, K. A. Marsh, W. B. Mori, P. Muggli, R. Siemann, and D. Walz. Plasma-wakefield acceleration of an intense positron beam. *Physical Review Letters*, 90(21), May 30 2003.

[108] G. Stancari, A. Valishev, G. Annala, G. Kuznetsov, V. Shiltsev, D. A. Still, and L. G. Vorobiev. Collimation with Hollow Electron Beams. *Physical Review Letters*, 107(8), Aug. 17 2011.

[109] J. Vieira and J. T. Mendonca. Nonlinear Laser Driven Donut Wakefields for Positron and Electron Acceleration. *Physical Review Letters*, 112(21), May 27 2014.

[110] S. Y. Kalmykov, A. Beck, S. A. Yi, V. N. Khudik, M. C. Downer, E. Lefebvre, B. A. Shadwick, and D. P. Umstadter. Electron self-injection into an evolving plasma bubble: Quasi-monoenergetic laser-plasma acceleration in the blowout regime. *Physics of Plasmas*, 18(5), May 2011. 52nd Annual Meeting of the APS Division of Plasma Physics, Chicago, IL, 2010.

[111] S. A. Yi, V. Khudik, S. Y. Kalmykov, and G. Shvets. Hamiltonian analysis of electron self-injection and acceleration into an evolving plasma bubble. *Plasma Physics and Controlled Fusion*, 53(1, SI), Jan. 2011.

[112] M. Tzoufras, W. Lu, F. S. Tsung, C. Huang, W. B. Mori, T. Katsouleas, J. Vieira, R. A. Fonseca, and L. O. Silva. Beam loading in the nonlinear regime of plasma-based acceleration. *Physical Review Letters*, 101(14), Oct. 3 2008.

[113] S. Y. Kalmykov, A. Beck, X. Davoine, E. Lefebvre, and B. A. Shadwick. Laser plasma acceleration with a negatively chirped pulse: all-optical control over dark current in the blowout regime. *New Journal of Physics*, 14, Mar. 15 2012.

[114] T. Katsouleas. Physical-Mechanisms in The Plasma Wake-Field Accelerator. *Physical Review A*, 33(3):2056–2064, Mar. 1986.